# Université de Paris

École doctorale Bio Sorbonne Paris Cite ED562

Laboratoire Institut Imagine- INSERM UMR1163,

Génétique des troubles du neurodéveloppement

"Cellular Modelling of a new type of Pontocerebellar Hypoplasia caused by a defect in the multiple inositol-polyphosphate phosphatase 1 gene"

Par Ekin UCUNCU

Thèse de doctorat de Génétique

Dirigé par Vincent CANTAGREL

Présentée et soutenue publiquement le 9/11/2020

Devant un jury composé de :

| | |
|---|---|
| Prof Christophe ERNEUX | Rapporteur |
| Dr Anselme PERRIER | Rapporteur |
| Prof Nadia-BAHI BUISSON | Examinateur |
| Dr Lydie BURGLEN | Examinateur |
| Dr Vincent CANTAGREL | Directeur de thèse |

Except where otherwise noted, this work is licensed under
https://creativecommons.org/licenses/by-nd/3.0/fr/

UNIVERSITE DE PARIS

ECOLE DOCTORALE BIO SORBONNE PARIS CITE

THESE pour obtenir le grade de

DOCTEUR DE UNIVERSITE DE PARIS

# "Cellular Modelling of a new type of Pontocerebellar Hypoplasia caused by a defect in the multiple inositol-polyphosphate phosphatase 1 gene"


Présentée par

Ekin UCUNCU

Institut Imagine- INSERM UMR1163

Génétique des troubles du neurodéveloppement


Membres du jury:

| | |
|---|---|
| Prof Christophe ERNEUX | Rapporteur |
| Dr Anselme PERRIER | Rapporteur |
| Prof Nadia-BAHI BUISSON | Examinateur |
| Dr Lydie BURGLEN | Examinateur |
| Dr Vincent CANTAGREL | Directeur de thèse |

*dedicated to my two grandfathers…*

# ACKNOWLEDGEMENT

I would like to deeply thank Dr Vincent Cantagrel for accepting me as a PhD candidate and giving me the opportunity to work in the field that I am really passionate about. Together, we have faced the challenges of working with iPSCs and indeed I am so grateful for his patience, understanding and guidance throughout this four year. Thank you so much for enriching my vision and helping me to develop my scientific thinking, I really appreciated it.

I would like to sincerely thank Prof Christophe Erneux, Dr Anselme Perrier, Prof Nadia-Bahi Buisson and Dr Lydie Burglen for being part of my thesis committee. Truly, I am honoured that my PhD work will be evaluated by the experts in the field of our study. Thank you very much indeed for the time and effort you will devote in advance.

I would like to express my warmest appreciation to Prof Adolfo and Miranda Wilson, for their continuous support and guidance. Your contribution has been invaluable for my project and I am so grateful to be able to work with you. Thank you so much for your warm welcome during my stay in the UCL and precious scientific discussions we had together.

To my three "Imaginary" mothers: Karine, Nathalie and Corinne. I don't know how I could do without you this four year… I don't want to even think about it. It is so hard to express my feelings here in couple of sentence, but I would like to thank you from the bottom of my heart for your continuous support and endless help throughout my PhD.

Karine, I have never met someone like you that can always see the positive sides within a problem. You cannot imagine how much energy you gave me by passing by my office every day to see if I am ok, by sending me messages during the weekends or during your vacation. Thank you so much for taking care of me. You will be always "my queen with magical hands". Thank you for being how you are.

Nathalie, without you, I never would have become the person I am now. You made me reach my dreams and truly I don't know how I can express my thankfulness to you. I will never forget the hours, weekends I spent with you in the L2, learning iPSCs, looking under the microscope to see beautiful colonies and mostly helping me to solve the challenges I face. Every time, I felt like I cannot handle the stress any more, I run to you, with the tears on the way. And each time, you made me feel like I was at home with your lovely smile. You cannot imagine how precious those moments were. Thank you for being my angel, I will miss you so deeply.

Corinne, you cannot imagine how you helped me to get through the challenges I faced, with your positive energy and your "esprit" full of love. Thank you so much for all.

Karthi, you know that my list is super long for you, as I thank you probably couple of times per day. We have been together in such a difficult journey and shared every day, same frustrations. Each time, one of us was less frustrated than the other, which made us go over the challenges one by one. I would like to thank you from the bottom of my heart for creating this supportive environment, helping each other in every minute and in every sense 7/24 hours. Nothing would be possible without you. Thank you for being how you are.

Nami, your continuous help in the project and your endless positivity and smile helped me tremendously in advancing in the project. Thank you so much for being our "Superman".

Céline, you cannot imagine how you made me so happy every time I see you in the elevator or corridors. I will never forget the moments we spent in the L2 and your endless help. Thank you so much for all.

Nami, Sonny, Julien and Dani: I have never met someone like you that can bring so much positivity, love and joy in an environment. Without you, I would never been able to adapt so easily to our laboratory. Thank you so much for all of those beautiful moments. I already missed you so much from the moment you all left, which was truly detrimental for me….

Giulia, you cannot imagine how you helped me during this four year with your endless positivity and love. Together, we faced so much difficulties, being the only iPSC student in our laboratories. Every time I see you in the L2 or during the yoga sessions, you made me feel like I was not alone in this PhD endeavour. Thank you for this beautiful friendship full of support and love.

Floriane, truly I have never met someone like you that can take care of everyone 7/24 hours, no matter how busy you are. Thank you so much for your endless help, and being also my angel.

I would like to deeply thank Marie-Claude and Jeanne for their patience and endless help throughout my PhD. I really appreciate all the administrative challenges you had to face for me and all the urgent orders we had to pass together. Thank you for all.

I would like to also thank Amine, Moussa, Alexis and Roger for asking me every day how I am. It truly helped me to start the day with a positive energy, which made feel like we are all like a big family. I will miss all of you.

Anna, Stefania, Caro, Marta, Lucas, Satish, Emilie and Daniel: Thank you so much for being so friendly with me every time I come across you in the Institute. The little conversations we had together was so valuable for me. I would like to specially thank Lucas, for all of his support. You made me so happy every time I saw you.

I would like to thank Marion, for her positive energy from the moment she joined to our laboratory. Thank you so much for listening to me and helping me to reduce my stress during the writing stage of my thesis. Your encouragement really saved my life.

Also, I would like to thank to everyone who joined to our yoga sessions with Giulia. It was lovely to see you all of you on Friday afternoons, sharing an hour full of peacefulness, where we can forget our problems, at least for an hour.

In a broader frame, I would like to thank to everyone in the Imagine Institute for creating such a friendly environment. I feel so lucky to be part of this Institute.

To my two sweethearts, Dani and Pedro: Simply, thank you for bringing life in my PhD life. Truly, I feel so lucky to have met you. I will never forget how you helped me to go over many challenges and how you took care of me no matter where you are. You cannot imagine how you changed my life. Nothing would be the same without you. Thank you from the bottom of my heart for being so massively beautiful, loving you…

Lastly, I would like to deeply thank all of my friends and my family for their continuous encouragement, support and endless prayers, especially within this last semester. I am so lucky to have all of you in my life.

# ABSTRACT

Developmental defects of the cerebellum cause both motor and cognitive symptoms. They are highly heterogeneous at the genetic level and most cases are not diagnosed yet. Pontocerebellar hypoplasia (PCH) is a group of rare recessive disorders, characterized mainly by degeneration and lack of proper development of the pons and the cerebellum. Clinical features vary widely, including 13 subtypes, and the genetic basis is still not known for all of the subtypes. In this disease, early-onset neurodegeneration intersects with neurodevelopment and pathological mechanisms are poorly understood. Recently, we identified 8 PCH patients from six independent families, all harbouring loss of function (LOF) mutations in a novel disease-causing gene: multiple inositol-polyphosphate phosphatase 1 (*MINPP1*). All of the 8 patients shared a never described neuroradiological phenotype that includes basal ganglia involvement, hence pointing out a new PCH subtype. Strikingly, the inositol polyphosphate metabolism pathway has been directly involved neither in human brain development nor in any Mendelian disorders. Thus, this study sought to model *MINPP1*-PCH using cellular and mouse models, including HEK293 cells, iPSCs and *Minpp1*$^{-/-}$ mice.

To assess the effect of PCH-associated *MINPP1* mutations, we started our project by generating a knock-out model for *MINPP1* in HEK293 cells. *MINPP1*$^{-/-}$ HEK293 cells showed a proliferation defect, which was partially rescued by overexpression of wild type (WT) MINPP1. Contrastingly, overexpression of MINPP1 missense PCH variants did not rescue the proliferation phenotype, indicating that all of the missense variants tested are deleterious for protein function and hence suggesting a LOF. To better understand the involvement of LOF of *MINPP1* in PCH aetiology, we then derived iPSCs from one of the patients harbouring homozygous early-truncating mutations in *MINPP1*. Subsequently, to have an isogenic control, we generated *MINPP1*$^{-/-}$ iPSCs. To obtain the disease relevant cell types, we further differentiated them towards neuronal lineage. Interestingly, both *MINPP1* mutant lines displayed delayed neuronal differentiation associated with enhanced apoptosis. To better understand the biochemical mechanisms underlying these defects, we performed inositol metabolic radiolabelling to quantify intracellular inositol phosphate levels during differentiation. Intriguingly, both *MINPP1* mutant lines exhibited a disruption in inositol phosphate homeostasis, with a robust increase in $IP_6$ levels during differentiation. Hence, these data showed that the absence of MINPP1 leads to $IP_6$ accumulation during neural differentiation.

Next, we tried to understand how this biochemical defect related to a ubiquitous enzyme could cause these neurological phenotypes. Given $IP_6$'s strong ion-chelating characteristic, we hypothesize that $IP_6$ accumulation in some cellular compartments could chelate some divalent cations and cause an intracellular depletion of these free ions. Such depletion could alter neuronal differentiation and enhance neuronal degeneration. In support of this hypothesis, *MINPP1*$^{-/-}$ HEK293 cells showed a robust decrease in free intracellular $Ca^{2+}$ and $Fe^{3+}$ levels, while displaying a marked increase in $IP_6$ levels. Hence, these data suggested that $IP_6$ accumulation leads to a disruption in intracellular cation homeostasis. To assess its involvement and further characterize such mechanism, a mouse model KO for the *Minpp1* gene was created in the lab. In line with the results from HEK293 cell model, *Minpp1*$^{-/-}$ mouse neural progenitors showed a marked decrease in free intracellular $Ca^{2+}$ levels. Thus, these data suggest the involvement of $IP_6$-mediated chelation as the underlying cause of *MINPPI*-PCH pathology.

Hence, this study provides novel insights into the genetic, molecular and phenotypic spectrum of PCH by demonstrating for the first time the involvement of an abnormal inositol phosphate metabolism as a cause of PCH and a human developmental disorder.

# RESUME

Les anomalies du développement du cervelet sont associées à des troubles cognitifs et moteurs, et, pour une part importante des patients atteints, il n'y a pas de diagnostic moléculaire. Parmi ces anomalies, les hypoplasies pontocérébelleuses (HPC) sont des maladies rares, très sévères, caractérisées par un développement incomplet du cervelet et du tronc cérébral. En plus de ces défauts structurels du cerveau postérieur, les patients atteints présentent également une microcéphalie progressive, indiquant une atteinte du cortex cérébral. En raison du caractère progressif sévère de cette maladie, la plupart des patients meurent à la naissance ou pendant l'enfance. Souvent dans les HPC, les mécanismes neurodéveloppementaux et neurodégénératifs interagissent dans l'étiologie de la maladie. Il existe une grande variabilité dans les caractéristiques cliniques, et 13 sous-types d'HPC ont été définis. Actuellement, plus de 20 gènes ont été identifiés comme responsables, et il est intéressant de noter que presque tous sont impliqués dans des processus ubiquitaires. Alors que la plupart d'entre eux agissent dans la synthèse de l'ARNt et le métabolisme de l'ARN, les autres sont impliqués dans des processus cellulaires non connectés, notamment la biosynthèse du GTP et le trafic intracellulaire des vésicules. Cependant, il reste de nombreux cas pour lesquels la base génétique est inconnue et de nombreux sous-types restent sans doute à identifier. Dans ce contexte, notre laboratoire cherche à identifier de nouvelles causes génétiques d'HPC et à mieux comprendre les mécanismes moléculaires impliqués dans l'étiologie de la maladie.

Récemment, nous avons identifié chez des patients avec HPC des mutations bi-alléliques dans le gène *MINPP1* (*pour multiple inositol-polyphosphate phosphatase 1*), qui n'avait jusqu'alors jamais été impliqué dans cette pathologie. Ces mutations ont été identifiées chez huit patients, issus de six familles différentes, et elles sont soit tronquantes, soit faux-sens. Ces patients présentent tous une image typique à l'IRM reconnaissable de par l'atteinte des ganglions de la base. *MINPP1* est impliqué dans le métabolisme du phosphate d'inositol et code pour une phosphatase qui métabolise principalement l'inositolhexakisphosphate ou $IP_6$. Aucun rôle dans le développement du cerveau n'était cependant rapporté pour ce gène. Étonnamment, de façon générale, la voie métabolique des inositol phosphates n'avait jamais été impliquée dans des maladies congénitales, ni dans le développement cérébral. Mon projet de thèse a visé à établir des modèles d'étude de la maladie à l'aide de cellules HEK293, de cellules souches pluripotentes induites humaines (CSPi) ainsi que d'un modèle murin invalidé pour *Minpp1*.

Pour évaluer l'effet des variants de *MINPP1* identifiés chez les patients HPC, nous avons commencé notre projet en générant un modèle de cellules HEK293 invalidées pour *MINPP1*. Lors de la génération des cellules HEK293 *MINPP1*$^{-/-}$, nous avons remarqué que celles-ci poussent nettement plus lentement que les cellules témoins. Afin de mieux caractériser ce phénotype, nous avons quantifié au cours du temps le nombre de cellules viables en utilisant le test colorimétrique MTT. Conformément à notre observation initiale, après 48 heures de culture, les cellules HEK293 *MINPP1*$^{-/-}$ ont montré une diminution de 30% de leur taux de croissance par rapport aux cellules témoins. Pour valider la spécificité de cet effet, nous avons surexprimé de manière transitoire la forme sauvage du gène *MINPP1* dans les cellules HEK293 *MINPP1*$^{-/-}$. Dans ces conditions nous avons observé une restauration partielle mais significative de la croissance cellulaire. Pour tester si le défaut de croissance observé dans les cellules HEK293 *MINPP1*$^{-/-}$ était dû à une augmentation de la mort cellulaire, nous avons évalué le taux d'apoptose par marquage à l'Annexine-V. Pendant 48 heures de culture cellulaire, le nombre de particules positives d'Annexine-V $^{+}$ est resté comparable entre les cultures de contrôle et de cellules HEK293 invalidées pour *MINPP1*. Ces analyses montrent que la perte de MINPP1 n'affecte pas l'apoptose dans les cellules HEK293 et suggèrent que le phénotype de croissance observé dans les cellules HEK293 *MINPP1*$^{-/-}$ est dû à un défaut de prolifération. Nous avons ensuite mis à profit ce phénotype de prolifération du KO MINPP1 pour déterminer

l'effet de variants faux-sens de MINPP1 sur la fonction protéique. Pour cela, nous avons surexprimé de manière transitoire dans les cellules HEK293 *MINPP1*$^{-/-}$ deux variants faux-sens différents identifiés chez des patients (Y53D, E486K) et déterminé leur taux de croissance à l'aide du test MTT. Après 48 heures de culture, le taux de croissance des cellules HEK293 *MINPP1*$^{-/-}$ surexprimant l'un ou l'autre des variants faux-sens reste comparable aux cellules *MINPP1*$^{-/-}$, indiquant que ces deux variants faux-sens MINPP1 sont incapables de sauver le phénotype de prolifération. Ces expériences démontrent ainsi que les deux variants faux-sens de MINPP1 testés entraînent une perte de fonction de MINPP1, et que celle-ci est bien à l'origine d'une forme spécifique d'HPC.

Afin d'établir un modèle cellulaire plus pertinent pour l'étude de la maladie, nous avons dérivé des cellules souches pluripotentes induites humaines (CSPi) à partir de cellules provenant de patients HPC porteur d'une mutation tronquante dans *MINPP1*. Parallèlement, nous avons généré des CSPi invalidées pour *MINPP1* via la technologie CRISPR/Cas9. Nous avons confirmé tout d'abord l'absence de la protéine MINPP1 dans l'ensemble de ces lignées CSPi. Nous avons ensuite contrôlé leur qualité par différents tests. Nous avons ainsi confirmé le maintien de la pluripotence en réalisant une immunofluorescence et une cytométrie en flux pour les marqueurs OCT4, SOX2, SSEA-4 et TRA-1-81. Nous avons également confirmé leur potentiel de différenciation dans les trois feuillets embryonnaires. Enfin, nous avons évalué l'intégrité génomique de nos lignées CSPi en effectuant une analyse de CGH 60K. Cette analyse n'a pas révélé d'anomalies chromosomiques évidentes. Dans l'ensemble, cette étude de caractérisation nous a permis de confirmer la qualité de nos modèles CSPi.

Compte tenu du phénotype de prolifération observé dans les cellules HEK293 invalidée pour *MINPP1*, nous avons ensuite déterminé si nos lignées mutantes pour *MINPP1* présentent une prolifération altérée, par un test basé sur l'incorporation de BrdU. Le pourcentage de cellules $BrdU^+$ était comparable entre les CSPi contrôles et mutantes (provenant de patients et *MINPP1*$^{-/-}$), montrant que la perte de MINPP1 n'affecte pas la prolifération dans les CSPi. Nous avons également quantifié le niveau d'apoptose dans les lignées CSPi mutantes pour *MINPP1* à l'aide d'un test TUNEL, une méthode utilisée pour détecter les cassures d'ADN double brin. L'analyse n'a révélé aucune différence significative dans les niveaux d'apoptose entre les lignées CSPi.

Nous avons ensuite testé l'effet de la perte de fonction de MINPP1 sur la capacité de différenciation neuronale. Les expériences d'induction de différenciation neuronale ont montré une forte augmentation dans le pourcentage des progéniteurs neuronaux par rapport aux cellules témoins. Celle-ci s'accompagne d'une diminution dans le pourcentage des neurones positifs pour Tuj1, suggérant un retard sévère de différenciation neuronale, aussi bien dans les lignées dérivées de patients que les lignées mutées par CRISPR. De plus, nous avons observé une augmentation de la mort cellulaire dans ces lignées lors de cette différenciation.

Par la suite, nous avons testé un mécanisme biochimique pouvant expliquer comment la perte de fonction de MINPP1 pouvait affecter la différenciation neuronale et la survie cellulaire. Des études précédentes avaient montré que le substrat principal de MINPP1 est l'$IP_6$. En accord avec cela, nous avons pu mesurer une accumulation d'$IP_6$ dans notre modèle de cellules HEK293 invalidées pour *MINPP1*. Nous avons également quantifié les inositol phosphates intracellulaires lors de la différenciation neuronale des cellules CSPi et observé une augmentation du taux d'$IP_6$ pour les lignées mutantes pour *MINPP1*. L'$IP_6$ étant un fort chélateur, nous avons émis l'hypothèse que cette accumulation d'$IP_6$ causait un déséquilibre dans l'homéostasie d'ions intracellulaires, connus pour jouer un rôle dans la survie cellulaire et la différenciation neuronale. C'est le cas par exemple du calcium et les ions ferreux. En accord avec cette hypothèse, les cellules HEK293 *MINPP1*$^{-/-}$ montraient une forte diminution de $Ca^{2+}$ cytosolique. Pour évaluer si ce phénotype pouvait avoir un impact sur la signalisation $Ca^{2+}$, nous avons évalué la réponse des cellules HEK293 *MINPP1*$^{-/-}$ à la mobilisation $Ca^{2+}$ à partir

du réticulum endoplasmique (RE). Pour cela, nous avons traité les cellules mutantes avec de la caféine, qui induit la libération de $Ca^{2+}$ du RE via les récepteurs de la ryanodine (RyR). En réponse à la caféine, les cellules *MINPP1*$^{-/-}$ présentaient une diminution drastique de la mobilisation du $Ca^{2+}$ du RE par rapport aux cellules témoins, suggérant la réduction des niveaux de $Ca^{2+}$ stocké dans le RE. Nous avons pu sauver ce phénotype en sur-exprimant la forme sauvage de MINPP1, démontrant ainsi sa spécificité. En conclusion, ces résultats démontrent que la perte de fonction de *MINPP1* a un impact sur l'homéostasie du calcium dans le réticulum endoplasmique. Par ailleurs, nous avons mesuré le fer libre intracellulaire dans les lysats de cellules HEK293 *MINPP1*$^{-/-}$, en utilisant un test colorimétrique dans lequel le fer ferreux est détecté en formant un complexe coloré avec de la ferrozine. Pour mesurer également le fer ferrique libre, nous avons inclus un réducteur de fer dans les lysats cellulaires. Nous avons effectué ces mesures dans des conditions de milieu enrichi en fer, conditions nécessaires pour rendre apparents les phénotypes de carence en fer. Conformément à notre hypothèse initiale, dans des conditions de fer élevé, nous avons observé une déplétion de 60% des niveaux de fer intracellulaire libre total dans les cellules HEK293 *MINPP1*$^{-/-}$, par rapport aux cellules témoins. L'ensemble de ces données montrent un déséquilibre dans les taux d'ions intracellulaires suite à la perte de fonction de MINPP1 et suggèrent l'implication de la chélation médiée par $IP_6$ comme cause sous-jacente de la pathologie.

Pour mieux comprendre le rôle de *MINPP1*dans le développement du cerveau in vivo, nous avons généré des souris KO pour le gène orthologue murin *Minpp1*. Nous avons pu montrer que les souris *Minpp1*$^{-/-}$ présentent une réduction légère mais significative du poids du cerveau au stade post-natal P21. Une diminution du poids moyen du cerveau est également détectée à 11 mois, mais reste comparable à celle observée à P21, suggérant une absence de progressivité du phénotype. Par conséquent, ces observations montrent une réduction du poids du cerveau chez les souris *Minpp1*$^{-/-}$, susceptible de résulter d'un défaut précoce survenant au cours du développement. Pour mieux caractériser ce phénotype cérébral, nous avons ensuite analysé histologiquement le cervelet et le cortex cérébral de souris *Minpp1*$^{-/-}$ à P21. Les analyses histologiques avec coloration à l'hématoxyline et à l'éosine n'ont pas révélé de différences majeures dans l'architecture du cortex cérébelleux ou cérébral entre les souris sauvages et *Minpp1*$^{-/-}$. Cependant, nous avons détecté une diminution légère mais significative d'environ 10% de l'épaisseur corticale chez les souris *Minpp1*$^{-/-}$ à P21. Par conséquent, bien que notre modèle de souris nécessite une caractérisation plus approfondie, ces observations initiales suggèrent que la perte de fonction de *Minpp1* affecte le développement du cortex cérébral de la souris.

Ensuite, nous avons cherché à identifier une cause potentielle du phénotype cortical observé dans les souris *Minpp1*$^{-/-}$. Utilisant un autre modèle murin, une précédente étude avait montré que la perte de fonction de *Minpp1* chez la souris entraîne une accumulation d'$IP_6$, comme nous l'avons observé dans les cellules humaines HEK293 et dérivées de CSPi. Considérant les phénotypes de déplétion cationique que nous avons détectés dans notre modèle cellulaire HEK293, nous avons émis l'hypothèse que la perte de Minpp1 pourrait avoir un impact sur la physiologie des cations dans le cerveau de la souris, altérant le bon développement du cortex cérébral. Pour évaluer cette hypothèse, nous avons exploré l'effet de l'absence de Minpp1 sur l'homéostasie du $Ca^{2+}$ dans les progéniteurs neuraux corticaux embryonnaires à E14.5. Conformément à notre modèle cellulaire HEK293 *MINPP1*$^{-/-}$, nous avons observé une forte diminution des niveaux de $Ca^{2+}$ dans les progéniteurs neuraux corticaux mutés pour *Minpp1* par rapport aux cellules sauvages. La perte de Minpp1 a donc également un impact majeur sur la disponibilité de $Ca^{2+}$ libre dans les progéniteurs neuraux corticaux de souris. Ce résultat suggère l'existence d'un mécanisme pathologique lié à la perte de MINPP1 conservé entre espèces, et impliquant une homéostasie cationique défectueuse, due à une accumulation de $IP_6$.

En conclusion, mon travail de thèse a permis de démontrer un rôle critique de MINPP1 dans la régulation du métabolisme des inositol phosphates, de la physiologie cationique cellulaire et du développement du cerveau humain. Ce projet a permis d'identifier un nouveau gène de HPC et les mécanismes biochimiques et cellulaires associés et ainsi de démontrer, pour la première fois, l'implication d'une anomalie du métabolisme des inositol phosphates dans les HPC et, plus généralement, dans une maladie congénitale. Cette étude met ainsi en lumière le métabolisme de ces inositol phosphates comme une voie cruciale à explorer à l'avenir pour une meilleure compréhension du neurodéveloppement et des processus neurodégénératifs précoces.

# TABLE OF CONTENTS

**ABSTRACT** ..... **3**

**RESUME** ..... **4**

**LIST OF ABBREVIATIONS** ..... **12**

**INTRODUCTION** ..... **16**

**CHAPTER ONE: CEREBELLUM** ..... **17**

1.1 Cerebellum ..... 17

1.2 The cerebellar circuitry ..... 18

1.3 Cerebellum Development ..... 20

1.4 Cerebellar malformation disorders ..... 24

**CHAPTER TWO: PONTOCEREBELLAR HYPOPLASIA** ..... **26**

2.1 Pontocerebellar hypoplasia (PCH) ..... 26

2.2 Typical structural brain abnormalities in PCH ..... 30

2.3 Distinct neurodevelopmental and neurodegenerative features of PCH subtypes ..... 32

2.4 Genetic causes and molecular basis of PCH ..... 34

**CHAPTER THREE: PCH DISEASE MODELLING** ..... **39**

3.1 PCH Disease Modelling ..... 39

3.2 PCH-mouse models ..... 39

3.3 PCH-disease modelling with iPSCs ..... 44

**CHAPTER FOUR: INOSITOL PHOSPHATES** ..... **63**

4.1 Inositol Phosphates (IPs) and their metabolism in mammalians ..... 63

4.2 The subcellular distribution of IPs in mammalians: focus on $IP_5$ and $IP_6$ ..... 69

4.3 Inositol phosphates in brain physiology ..... 71

4.4 $IP_6$: the most abundant inositol phosphate with unique characteristics ..... 78

4.5 Roles and mode action of $IP_6$ in mammalian cells ..... 80

**CHAPTER FIVE: MINPP1** ..... **85**

5.1 *MINPP1*: transcripts, isoforms and protein domains ..... 85

5.2 Evolutionary relationship of MINPP1 ..... 86

5.3 Back in 90's: From I(1,3,4,5)$P_4$ 3-Phosphatase to MINPP1 ..... 88

5.4 How MINPP1 meets its substrates *in vivo*? ..... 89

5.5 Physiological Function of MINPP1 ..... 94

**CHAPTER SIX: AIM OF THE STUDY** ..... **97**

**MATERIALS AND METHODS** ..... **98**

**RESULTS** ..... **112**

**1.1 Defects in *MINPP1* gene cause a distinct subtype of PCH.** ..... **112**

**1.2 Assessing the effect of PCH-associated *MINPP1* mutations using HEK293 cells** ..... **117**

1.2.1 *MINPP1* missense PCH variants affect protein level without obvious alteration of the glycosylation status of MINPP1. ..... 117

1.2.2 MINPP1 loss leads to a proliferation defect without affecting apoptosis in HEK293 cells. ..... 119

1.2.3 *MINPP1* missense PCH variants do not rescue proliferation defect of *MINPP1* KO…….....121
1.2.4 MINPP1 loss tends to alter extracellular inositol phosphate metabolism in HEK293 cells.....122
1.2.5 MINPP1 loss leads to an altered intracellular inositol phosphate metabolism with a marked increase in $IP_6$ levels in HEK293 cells.....123
1.2.6 The impact of *MINPP1* missense PCH mutations on cellular enzyme activity 124
1.2.7 Under high iron condition, MINPP1 loss alters iron homeostasis by depleting free intracellular iron in HEK293 cells.....126
1.2.8 MINPP1 loss alters calcium homeostasis by depleting the calcium pools in the cytosol and the ER in HEK293 cells.....129
1.2.9 Summary of the findings obtained from our HEK293 cell models .....132

**1.3 Insights into the function of *MINPP1* on mammalian brain development.....133**
1.3.1 Minpp1 loss leads to a reduction in brain weight and cerebral cortical thickness in P21 mouse.....133
1.3.2 Minpp1 loss reduces intracellular free $Ca^{2+}$ levels in E14.5 mouse cortical neural progenitors. .....134
1.3.3 The summary of the findings obtained from our *Minpp1*$^{-/-}$ mouse model .....136

**1.4 Unravelling *MINPP1*-PCH disease mechanisms using iPSCs .....137**
1.4.1 MINPP1 loss does not affect proliferation and apoptosis in iPSCs.....140
1.4.2 MINPP1 loss leads to a delayed neuronal differentiation in iPSCs associated with an increased rate of early-onset apoptosis. .....141
1.4.3 MINPP1 loss leads to an abnormal cellular inositol phosphate metabolism with an accumulation of $IP_6$ during early stages of neural differentiation of iPSCs. .....146
1.4.4 The summary of the findings obtained from our *MINPP1*-PCH iPSC models .149

**CONCLUSION .....150**

**DISCUSSION.....151**

**1.1 PCH14: the first brain disorder caused by an altered inositol phosphate metabolism.....151**

**1.2 The consequences of $IP_6$ accumulation on cellular physiology.....152**
1.2.1 Hypothesis on the subcellular localization of the accumulated $IP_6$.....152
1.2.2 The impact of $IP_6$ accumulation on cellular cation homeostasis: revealing a previously unappreciated phenotype.....153

**1.3 The brain-specific effects of the loss of function of *MINPP1* .....154**
1.3.1 Insights from *Minpp1*$^{-/-}$ mice .....154
1.3.2 Insights from *MINPP1*-iPSCs models .....155
1.3.3 *MINPP1*-iPSCs models: suitable for the study of *MINNP1-PCH*.....156

**1.4 The impact of defective MINPP1-mediated inositol phosphate metabolism on neuronal differentiation and survival .....156**
1.4.1 Specificities in the inositol phosphate metabolism of neural cells .....157
1.4.2 The impact of $IP_6$-mediation cation chelation .....158

**1.5 Conclusion and Perspectives.....161**

**REFERENCES.....164**

**APPENDIX-PUBLICATIONS.....191**

# LIST OF FIGURES

**Figure 1.** Functional organization of the human cerebellum .....18
**Figure 2.** The cortico-cerebellar network and the local circuit in the human cerebellum .....19
**Figure 3.** Schematic illustrations showing the patterning of the cerebellar primordium during embryonic mouse development .....21
**Figure 4.** Timeline of Purkinje and granule cell development in human and mouse .....22
**Figure 5.** Schematic representation depicting the key cellular events during postnatal development of the mouse cerebellar cortex .....24
**Figure 6.** Midline sagittal brain magnetic resonance images (MRI) showing the key features of cerebellar malformation disorders .....25
**Figure 7.** Typical structural brain abnormalities in PCH .....31
**Figure 8.** Schematic overview showing the overlapping pathology between PCH subtypes .33
**Figure 9.** Pie-chart indicating the proportion of PCH patients per PCH-related pathological pathway. .....34
**Figure 10.** Neurodegenerative features of neonatal lethal Clp1-kinase-dead (*Clp1*$^{K/K}$) knock-in embryos .....41
**Figure 11.** Early studies setting up the stage for transcription factor-mediated cellular reprogramming .....45
**Figure 12.** Overview of the iPSC reprogramming and differentiation .....47
**Figure 13.** Overview of iPSC-based disease modelling .....48
**Figure 14.** Key stages of neural development *in vivo* and neural differentiation *in vitro* .....51
**Figure 15.** Schematic diagram showing the patterning of the developing neural tube along the A-P and D-V axes .....53
**Figure 16.** Comparison of genetically-matched and unmatched study design in iPSC-based disease modelling .....58
**Figure 17.** Overview of the CRISPR-Cas9-mediated DSB repair mechanism .....59
**Figure 18.** Structure of the myo-inositol and nomenclature of the inositol phosphates .....63
**Figure 19.** Schematic representation showing the main enzymes and inositol phosphates involved in the lipid-dependent inositol phosphate metabolic pathway .....66
**Figure 20.** Schematic representation of the lipid-independent inositol phosphate metabolic pathway .....69
**Figure 21.** Overview of the IP3-dependent $Ca^{2+}$ signalling pathway .....72
**Figure 22.** Molecular structure of $IP_6$ and its binding capacity .....78
**Figure 23.** Schematic representation of the *MINPP1* transcripts and MINPP1 protein .....85
**Figure 24.** Phylogenetic tree and multiple sequence alignment of MINPP1 from different species .....88
**Figure 25.** Schematic representation of the proposed metabolic activity and subcellular localization of MINPP1 in mammalian cells .....93
**Figure 26.** Biallelic mutations in *MINPP1* cause a distinct PCH phenotype .....114
**Figure 27.** Family pedigrees and *in silico* prediction analysis of the missense *MINPP1* variants .....116
**Figure 28.** *MINPP1* missense PCH variants affect protein stability without altering glycosylation status of MINPP1 .....119
**Figure 29.** PCH-associated mutations of *MINPP1* impact cell proliferation without affecting apoptosis in HEK293 cells .....120
**Figure 30.** The extracellular and intracellular inositol phosphate metabolism in HEK293 cellular models of PCH-associated *MINPP1* mutations .....126
**Figure 31.** Under high iron condition, MINPP1 loss alters iron homeostasis by depleting free intracellular iron levels in HEK293 cells .....128

**Figure 32.** MINPP1 loss alters intracellular $Ca^{2+}$ homeostasis by depleting cytosolic calcium levels in HEK293 cells.....131
**Figure 33.** Generation and characterization of CRISPR-Cas9 *Minpp1*$^{-/-}$ mouse .....135
**Figure 34.** Schematic illustration of our study design for modelling *MINPP1*-PCH using iPSCs.....138
**Figure 35.** Characterization of patient-derived (CerID-30-2) and *MINPP1*$^{-/-}$ iPSCs.....140
**Figure 36.** MINPP1 loss does not affect proliferation and apoptosis in iPSCs .....141
**Figure 37.** Flow cytometry analysis of patient-derived (CerID-30-2) and *MINPP1*$^{-/-}$ iPSCs following dual SMAD inhibition-based neural induction .....142
**Figure 38.** MINPP1 loss leads to a delayed neuronal differentiation in iPSCs associated with an increased rate of apoptosis .....146
**Figure 39.** MINPP1 loss disrupts cellular inositol phosphate metabolism with an accumulation of IP6 during neural differentiation of iPSCs.....148
**Figure 40.** Schematic illustration showing the study model .....159

# LIST OF TABLES

**Table 1.** PCH subtypes.....28
**Table 2.** Differential diagnosis of PCH.....29
**Table 3.1.** Clinical information of the patients with variants in *MINPP1* .....115
**Table 3.2.** *MINPP1* variants identified in the different cohorts.....116

# LIST OF ABBREVIATIONS

5-HT: 5-hydroxytryptamine
AAV: Adeno-associated viruses
ADAR1: Adenosine deaminase acting on RNA-1
ADAT1: Adenosine deaminase tRNA Specific-1
Akt: AKT Serine/Threonine Kinase 1
$Al^{3+}$: Aluminium
AlCAr: Acetyl-L-carnitine
AMP: Adenosine monophosphate
AMPA: α-amino-3-hydroxy-5-methyl-4-isoxazolepropionic acid
AMPD2: Adenosine monophosphate deaminase 2
Ampd3: Adenosine monophosphate deaminase 3
ANOVA: Analysis of variance
APC: Allophycocyanin
ATCC: American type culture collection
ATXN2: Ataxin 2
ATXN7: Ataxin 7
AU-rich element: Adenylate-uridylate-rich element
BCA: Bicinchoninic acid
BDNF: Brain-derived neurotrophic factor
bFGF: basic fibroblast growth factor
BGH: Bovine growth hormone
BMI1: B lymphoma Mo-MLV insertion region 1 homolog
BMP: Bone morphogenetic protein
BrdU: Bromodeoxyuridine 5-bromo-2'-deoxyuridine
BSA: Bovine serum albumin
C57BL/6: C57 black 6
C57BLKS/J: C57 Black Kaliss J
$Ca^{2+}$: Calcium
$CaCl_2$: Calcium chloride
CADD: Combined annotation dependent depletion
Cas9: CRISPR-associated protein 9
CASK: Calcium/calmodulin dependent serine protein kinase
cDNA: complementary DNA
CEBP: CCAAT enhancer binding protein
CGH: Comparative genomic hybridization
CHMP1A: Charged multivesicular body protein 1A
CLP1: Cleavage factor polyribonucleotide kinase subunit 1
$CO_2$: Carbon dioxide
COASY: Coenzyme A synthase
ConA: Concanavalin A
Corl2: SKI family transcriptional corepressor 2
Cre: cyclic recombinase
CRISPR: Clustered regularly interspaced short palindromic repeat
dbSNP: Single nucleotide polymorphism database
DKC1: Dyskerin pseudouridine synthase-1
DMSO: Dimethyl sulfoxide
DNA: Deoxyribonucleic acid

E.coli: *Escherichia coli*
EB: Embryoid body
EDTA: Ethylenediaminetetraacetic acid
EGFR: Embryonic growth factor receptor
En1: Engrailed homeobox 1
En2: Engrailed homeobox 2
ExAC: Exome aggregation consortium
EXOSC: Exosome component
FAC: Ferric Ammonium Acetate
FACS: Fluorescence-activated cell sorting
$Fe^{2+}$: Ferrous ion
$Fe^{3+}$: Ferric ion
FGF: Fibroblast growth factor
FGF2: Fibroblast growth factor 2
FGF8: Fibroblast growth factor 8
FITC: Fluorescein isothiocyanate
FKRP: Fukutin-related protein
FKTN: Fukutin
FOXG1: Forkhead box protein G1
GABA: Gamma aminobutyric acid
GATA1: GATA-binding protein-1
GATK: Genome analysis tool kit.
Gbx2: Gastrulation brain homeobox 2
GDNF: Glial cell-derived neurotrophic factor
GFP: Green fluorescent protein
GnomAD: Genome aggregation database
gRNA: guide RNA
GTP: Guanosine-5'-triphosphate
HCl: Hydrochloric acid
Hek293: Human embryonic kidney 293T cells
HEPES: 4-(2-hydroxyethyl)-1-piperazineethanesulfonic acid
HNK1: Human natural killer-1
HPLC: High performance liquid chromatography
HRP: Horseradish peroxidase
IGF-1: Insulin-like growth factor-1
IMP: Inosine monophosphate
INDEL: Insertion or deletion
iNeurons: induced neurons
INK4A: Cyclin-dependent kinase inhibitor-2A
iPSCs: induced pluripotent stem cells
ISPD: Isoprenoid synthase domain containing
ITPR1: Inositol 1,4,5-trisphosphate receptor type-1
KCl: Potassium chloride
kDA: kilodalton
KIRREL2: Kirre-like nephrin family adhesion molecule 2
Klf4: Kruppel-like factor 4
$KMnO_4$: Potassium permanganate
KO: Knock-out
LARGE: LARGE xylosyl- and glucuronyltransferase 1
LDN: Low-dose naltrexone

LOF: Loss of function
MAF: Minor allele frequency
Math1: Atonal homolog 1
MBOP: Myelin-associated oligodendrocyte basic protein
MBP: Myelin basic protein
$Mg^{2+}$: Magnesium
$MgCl_2$: Magnesium chloride
MRI: Magnetic resonance imaging
mRNA: Messenger RNA
MTT: Methylthiazolyldiphenyl-tetrazolium bromide
MyOD: Myoblast determination protein 1
NaCl: Sodium chloride
NADPH: Nicotinamide adenine dinucleotide phosphate
$NaH_2PO_4$ : Monosodium phosphate
$NaHCO_3$: Sodium bicarbonate
NaOH: Sodium hydroxide
NCAD: N-cadherin
NeuN: Neuronal nuclei
NF-κB: Nuclear factor kappa B
NMDA: N-Methyl-d-aspartate
NT-3: Neurotrophin-3
O.D: Optical density
OCT4: Octamer-binding transcription factor 4
OMIM: Online Mendelian inheritance in man
OrG: Orange-R
OTX2: Orthodenticle homeobox 2
PAGE: Polyacrylamide gel electrophoresis
PAX2: Paired box-2
PAX5: Paired box-5
PAX6: Paired box-6
PAX8: Paired box-8
PBS-T: Phosphate-buffered saline with tween-20
PBS: Phosphate-buffered saline
PCLO: Piccolo presynaptic cytomatrix protein
PCR: Polymerase chain reaction
PE: R-phycoerythrin
PFA: Paraformaldehyde
PI3K: Phosphoinositide 3-kinases
PKC: Protein Kinase C
PMM2: Phosphomannomutase 2
PNGase: Peptide N-glycosidase
POMGnT1: Protein O-mannose beta-1,2-N-acetylglucosaminyltransferase
POMT1: Protein O-mannosyltransferase 1
POMT2: Protein O-mannosyltransferase 2
PSA-NCAM: Polysialylated neuronal cell adhesion molecule
Ptch1: Protein patched homolog-1
PTF1A: Pancreas associated transcription factor-1a
RA: Retinoic acid
Rab: Ras-related in brain
RARS2: Arginyl-tRNA synthetase 2

Rb: Retinoblastoma protein
RELN: Reelin
RNA: Ribonucleic acid
ROCK: Rho-associated protein kinase inhibitor
SAX-HPLC: Strong anion-exchange high performance liquid chromatography
s.d.: standard deviation
SDS: Sodium dodecyl sulfate
SEPSECS: O-phosphoseryl-tRNA(Sec) selenium transferase
sgRNA: single guide RNA
SHH: Sonic hedgehog
SIFT: Sorting intolerant from tolerant
SLC25A46: Solute carrier family 25 member 46
SNP: Single nucleotide polymorphisms
SOX2: Sex determining region Y-box 2
SSEA-4: Stage-specific embryonic antigen-4
SynCAMs: Synaptic cell adhesion molecules
TBC1D23: TBC1 domain family member 23
Tbr1: T-box brain transcription factor 1
TGF-β: Transforming growth factor beta
TIDE: Tracking of indels by decomposition
TOE1: Target of EGR1 protein 1
tRNA: transfer ribonucleic acid
TSEN: tRNA Splicing Endonuclease Subunit
TUBA1A: Tubulin alpha-1a
TUBA8: Tubulin alpha-8 chain
TUBB2B: Tubulin beta-2b class IIb
TUBB3: Tubulin beta-3 class III
TUBB5: Tubulin beta-5 chain
TUNEL: Terminal deoxynucleotidyl transferase dUTP nick end labelling
VEGF: Vascular endothelial growth factor
VLDLR: Very-low-density-lipoprotein receptor
VPS51: Vacuolar protein sorting-associated protein 51 homolog
VPS53: Vacuolar protein sorting-associated protein 53 homolog
VRK1: VRK Serine/Threonine Kinase 1
WNT1: Wnt Family Member 1
WT: Wild type
Zli: Zona limitans intrathalamica
$Zn^{2+}$: Zinc

# INTRODUCTION

Human brain is composed of about 100 billion of neurons and a roughly equal number of glial cells, the two cell types that form intricate neural networks in the brain. Proper development of these neural networks requires a tight control of key spatiotemporal processes, including proliferation and differentiation of specific neural lineages, and integration of these specific neural subtypes into neural circuits. Genetic mutations and environmental factors that alter these tightly coordinated events lead to an abnormal development of neural networks, which in turn affects neuronal activity and thereby acquisition and processing of information (e.g. sensory, motor and cognitive) in postnatal brain development, hence leading to neurodevelopmental brain disorders. These heterogeneous disorders cause a serious health issue in our society, affecting >3% of children worldwide. Hence, it is of great interest to identify genetic and molecular basis that can contribute to the wide spectrum of disease pathology. Within this aim, our laboratory has particularly focused on unravelling the basis of brain malformation defects, with a particular interest on the cerebellum. In this line, this study describes the identification and functional characterization of a novel-disease causing gene in a novel subtype of Pontocerebellar Hypoplasia, in an attempt to better understand the pathological mechanisms behind the cerebellar and thereby neurodevelopmental brain malformation defects.

# CHAPTER ONE: CEREBELLUM

## 1.1 Cerebellum

Cerebellum, termed “little brain” in Latin, is the second largest structure of the human brain located inferior to the cerebral cortex and dorsal to the brainstem. It consists of two hemispheres separated in the midline by the cerebellar vermis. As its name suggests, cerebellum accounts for only ~10% of the total human brain mass (Azevedo et al., 2009). Despite its relatively small portion, it consumes ~20% of the whole human brain energy and homes to ~70 billion of neurons, representing 80% of the total number of the neurons in the human brain (Azevedo et al., 2009; Howarth et al., 2010). This remarkable packed structure was initially thought to be solely involved in adaptive motor coordination (Holmes, 1939; Ito, 1984; Manto et al., 2012; Schmahmann, 1997). However, in past three decades, there has been growing recognition of its vital role in non-motor functions, including perception, memory, language, high-order thinking and cognition (reviewed in Schmahmann, 2019; Sokolov et al., 2017). Recently, social behaviour and reward circuitry have been added to this growing list (Carta et al., 2019). As a reflection to its functional heterogeneity, cerebellum has been implicated in various brain disorders, including Autism spectrum disorder, Down Syndrome, Schizophrenia and Alzheimer’s disease (Anderson et al., 2013; Chen and Brandizzi, 2013; Jacobs et al., 2018; Rogers et al., 2013; Sathyanesan et al., 2019). Altogether, scientists now begin to parcellate cerebellum into multiple functional domains and reconsider this remarkable brain structure as “brains’ ultimate control unit of all cortical motor and cognitive tasks” (Figure 1, King et al., 2019; Marek et al., 2018).

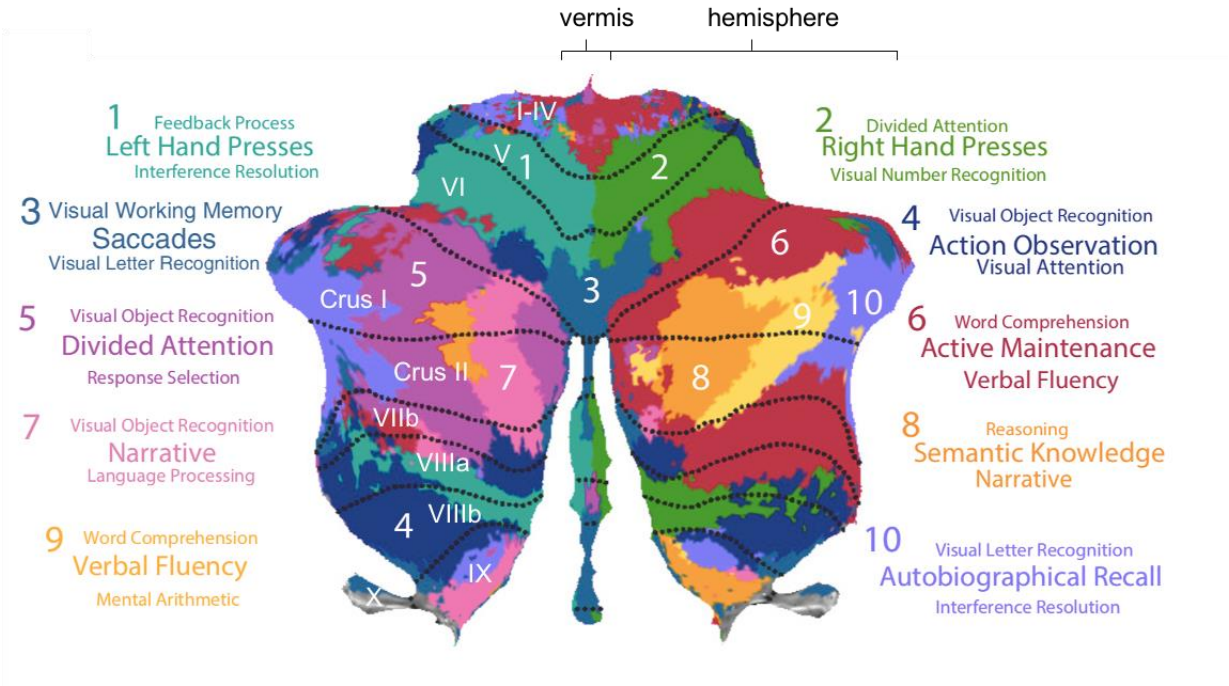


**Figure 1. Functional organization of the human cerebellum (adapted from King et al., 2019).** Ten functional regions are defined through task-based functional MRI. The three characteristics that best describe each region are indicated. The font size depicts the strength of these characteristics. Black dotted lines separate ten cerebellar lobules (numbered I-X). Cerebellar lobule VII is subdivided into Crus I, Crus II and VIIb in the cerebellar hemisphere.

## 1.2 The cerebellar circuitry

Cerebellum forms circuitry between various regions, including cerebral cortex, basal ganglia, hippocampus and spinal cord (reviewed in Bohne et al., 2019; Bostan and Strick, 2018; Diedrichsen et al., 2019). Here, we will focus on the cerebellum-cerebral cortex connection pathways as they have been instrumental in understanding the multiple functionality of the cerebellum (King et al., 2019; Marek et al., 2018, for more information regarding the local circuitry in the cerebellum see Figure 2).

The primary connection pathway between the cerebellum and the cerebral cortex involves via mossy fibres. Indeed, of the 40 millions of axons that leave various areas of the cerebral cortex, including motor and non-motor areas, the majority projects to the pontine nuclei of the brain stem (Figure 2A, Schmahmann and Pandya, 1991; Schmahmann and Pandya, 1993; Schmahmann and Pandya, 1997; Strick et al., 2009; Tomasch, 1969). These pontine projections, termed mossy fibres, innervate distinct cerebellar lobules and synapse onto

~50 billion of granule cells, the main glutamatergic cerebellar cell population (Azevedo et al., 2009). Every granule cell projects its axon, termed parallel fibre, to a single Purkinje cell, the sole output neuron of the cerebellum. In turn, ~15 millions of Purkinje cells convey their output back to cortical input sources via deep cerebellar nuclei (DCN) and thalamus.

The second cortico-cerebellar pathway involves through climbing fibres. Climbing fibres arise from the inferior olive and mainly carry information projected from the sensorimotor complex, which is critical for associative learning (Otis et al., 2012). These climbing fibres synapse on to Purkinje cells, which in turn send inhibitory output to the cells in the DCN (Figure 2B).

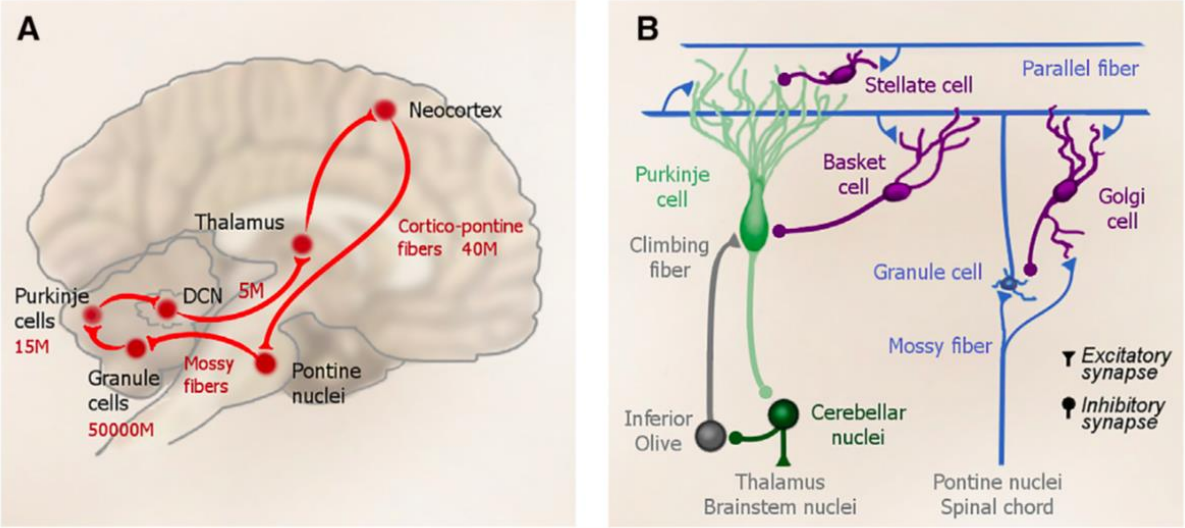


**Figure 2. The cortico-cerebellar network and the local circuit in the human cerebellum (from Diedrichsen et al., 2019). (A) The primary connection pathway between the cerebellum and the** cerebral cortex via mossy fibres**.** M indicates million. **(B)** Circuit network in the cerebellum. Every granule cell receives excitatory signal from 4-5 mossy fibres and in turn sends single parallel fibre to a Purkinje cell. Each Purkinje cell receives input from ~175,000 parallel fibres and also from a single climbing fibre. In turn, Purkinje cells deliver their inhibitory output to the deep cerebellar nuclei (DCN). The inhibitory interneurons (i.e. basket, Golgi and stellate cells) complete the local neuronal network in the cerebellum.

## 1.3 Cerebellum Development

Remarkably, cerebellum is one of the first brain structures to develop but it is one of the last to mature (Wang and Zoghbi, 2001). For instance, in mouse, the cerebellum develops over 30-35 days, starting from early embryonic period and continuing during 3 weeks after birth (Altman and Bayer, 1985; Miale and Sidman, 1961). In human, this developmental process is even more protracted, extending from the early first trimester of gestation until the first postnatal years (Ábrahám et al., 2001; Kiessling et al., 2014; Limperopoulos et al., 2005; Volpe, 2009). Currently, the most available data describing the cellular and molecular aspects of the cerebellum development comes from animal models, particularly rodents (reviewed in (Martinez et al., 2013). Hence, based on insights obtained from these models, cerebellum development is often divided into four main steps. These steps include: (1) formation of the cerebellar territory at the midbrain-hindbrain boundary, (2) establishment of distinct neural progenitor zones and neurogenesis (3) inward migration of the granule cells to their definitive position beneath the Purkinje cell layer (4) formation of cerebellar cytoarchitecture and circuitry. Here, we will limit our description to the timeline of critical cellular events occurring during human and mouse cerebellum development. Such description will help us to better define the highly protracted nature of the human cerebellum development (for more detailed information about the molecular aspects of the cerebellum development see reviews Basson and Wingate, 2013; Martinez et al., 2013; Marzban et al., 2015).

**Formation of the cerebellar territory at the midbrain-hindbrain boundary**

During early embryonic development, the neural tube is progressively regionalized by gradients of signalling molecules that are secreted in a spatiotemporal manner by various developmental signalling centres. These organizing centres are located along the anterior-posterior (A/P) and dorsal-ventral (D/V) axis of the developing neural tube (Kiecker and Lumsden, 2012; Le Dréau and Martí, 2012). For instance, patterning along A/P axis subdivides

neural tube into four primordial regions: the forebrain (prosencephalon), the midbrain (mesencephalon), hindbrain (rhombencephalon) and the spinal cord. Around embryonic day (E) 9.5-11 in mice and 4.5$^{th}$ gestational week in human, cerebellum territory emerges from the dorsal part of the most anterior region of the hindbrain, known as rhombomere-1 (r1) alar plate (Figure 3A, Ábrahám et al., 2001; Kaufman 2000). This region is specified mainly by the signalling centre located at the midbrain-hindbrain boundary, named as isthmus organizer (IsO) (Figure 3A, B, Martinez et al., 1991; Nakamura et al., 2005). At a molecular level, the position of IsO is determined and maintained by a complex network of region-specific transcription factors, including Otx2, Gbx2, En1/2 and Pax2/5/8 (Guo et al., 2007; Joyner et al., 1991; Millet et al., 1999). Once the IsO identity is established, it secretes positional signals such as Fgf8 and Wnt1 (Crossley et al., 1996; Wittmann et al., 2009). A positive feedback loop between these two positional signals maintain the expression of transcription factors such as En2 and Pax2, instructing the induction of cerebellar primordium from r1 alar plate (Sato and Joyner, 2009) .

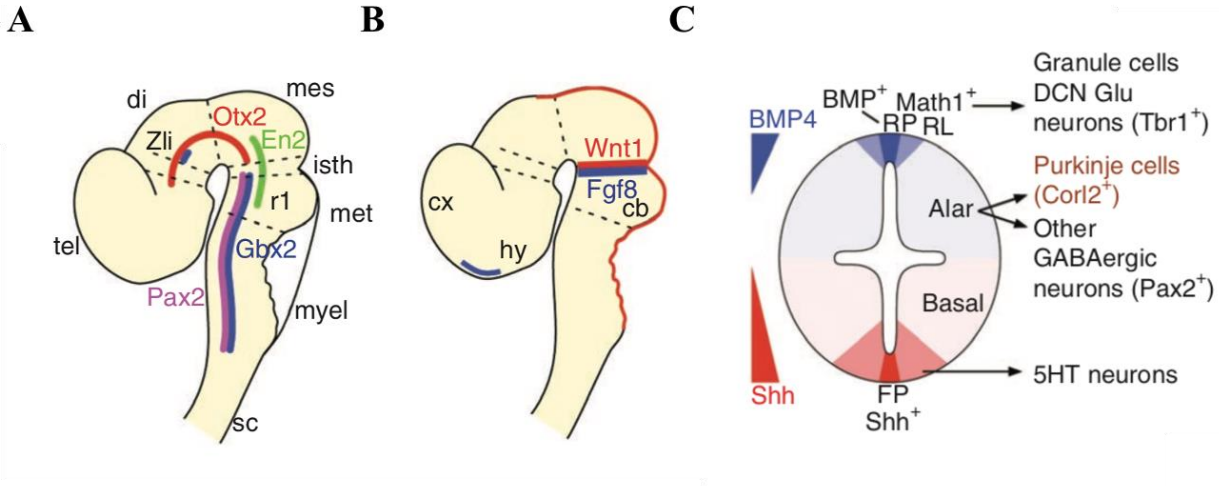


**Figure 3. Schematic illustrations showing the patterning of the cerebellar primordium during embryonic mouse development (from Muguruma et al., 2010). (A)** Isthmic organizer (isth) lies between the mesencephalon (mes) and metencephalon (met) and is specified via differential expression of region-specific transcription factors, including Otx2 and Gbx2. **(B)** The cerebellar primordium arises from the dorsal region of the r1 under the influence of two main isth factors: Fgf8 and Wnt1. **(C)** In the developing cerebellum, neurogenesis takes place in two different zones of the r1 alar plate: Ventral-most region of the r1 alar plate gives rise to GABAergic cerebellar neurons, including Corl2$^{+}$ Purkinje cells and Pax2$^{+}$ GABAergic cerebellar interneurons. Whereas, the dorsal-most region of the r1 alar plate, rhombic lip (RL), gives rise to Math1$^{+}$ progenitors, generating glutamatergic cerebellar neurons, including granule cells and Tbr1$^{+}$ deep cerebellar nuclei glutamatergic (DCN Glu) neurons. BMP4-Shh signalling controls the dorsal-ventral specification of the r1. The r1 basal plate develops into the pons

and generates serotonergic $5HT^+$ neurons. Abbreviations: tel, telencephalon; di, diencephalon; myel, myelencephalon; sc, spinal cord; cx, cortex; hy, hypothalamus; cb, cerebellum. RP, roof plate; FP, floor plate.

**Establishment of distinct neural progenitor zones**

After this initial A/P patterning, two distinct neural stem cell zones begin to form along the dorsoventral axis of the cerebellar primordium: (1) the ventricular zone that lines the lumen of the fourth ventricle and (2) the rhombic lip located at the dorsal tip of the r1 alar plate (Figure 3C). The ventricular zone gives rise to neural progenitors of all GABAergic neurons of the cerebellum (i.e. Purkinje cells, cerebellar interneurons, GABAergic cerebellar nuclei neurons) (Leto et al., 2006). Whereas, the neural progenitors of all glutamatergic cerebellar neurons (i.e. granule cells, unipolar brush cells, deep cerebellar nuclei neurons) are generated from the rhombic lip (Englund et al., 2006; MacHold and Fishell, 2005).

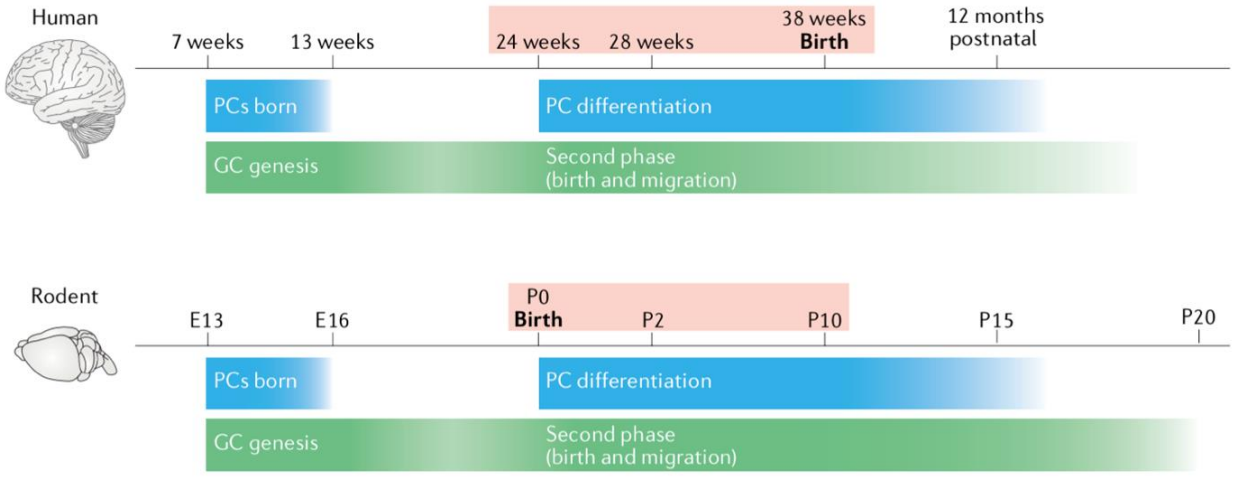


**Figure 4. Timeline of Purkinje and granule cell development in human and mouse (from Sathyanesan et al., 2019).** Pink shading marks the window of timeline in which the neurogenesis reaches a peak in the developing cerebellum. In human, this period corresponds to the gestational weeks 24-40, whereas in the mouse it corresponds to the first postnatal weeks. Abbreviations: PC, Purkinje cell; GC, granule cell; E, embryonic day.

**Timeline of Purkinje and granule cell development**

Purkinje cells, the principle GABAergic neurons of the cerebellum, arise around E13 in mouse and 7$^{th}$ gestational week in human (Figure 4, Rakic and Sidman, 1970). Progressively, they migrate radially from the ventricular zone towards cerebellar cortex, forming the Purkinje cell layer. The Purkinje cell layer continues to thicken until the first 2 postnatal weeks in mouse and 1$^{st}$ postnatal year in human. On the one hand, the development of the granule cells starts with the migration of the granule cell progenitors (GCP) from the rhombic lip over the surface of the cerebellum, forming the external granule layer (EGL). In mouse, the proliferation of GCP occurs in EGL between E17.5- P16 and is mainly coordinated by the underlying Purkinje cell layer via Shh signalling (Figure 4, Altman and Bayer, 1979; Dahmane and Ruiz I Altaba, 1999; Miale and Sidman, 1961). In human, this developmental process begins at the 10$^{th}$ gestational week and continues until the first postnatal months (Ábrahám et al., 2001; Kiessling et al., 2014). Particularly, a massive proliferation in the EGL occurs during gestational weeks 24-40, leading to a five-fold increase in the human cerebellar size (Limperopoulos et al., 2005; Volpe, 2009).

**Inward migration of the granule cells beneath the Purkinje cell layer**

Following the differentiation of GCP into granule cells, granule cells exit cell cycle and migrate ventrally to their definitive position beneath the Purkinje cell layer, forming the internal granule layer (IGL) (Figure 5). In mouse, this developmental process continues until P20, whereas in human it extends beyond the 11$^{th}$ postnatal month (Ábrahám et al., 2001; Kiessling et al., 2014; Miale and Sidman, 1961). In human, by the end of the second postnatal year, EGL disappears and cerebellar size continues to increase until adolescence (Sussman et al., 2016; Tiemeier et al., 2010).

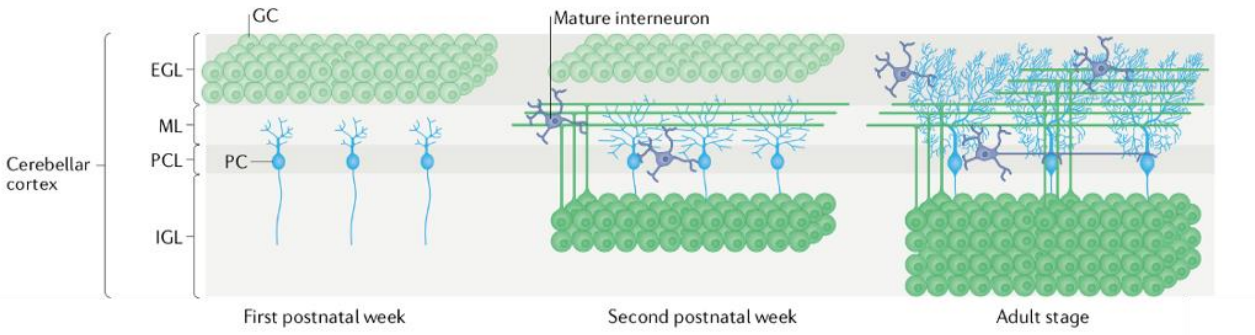


**Figure 5. Schematic representation depicting the key cellular events during postnatal development of the mouse cerebellar cortex (from Sathyanesan et al., 2019).** During the first postnatal week, the proliferation in the external granule layer (EGL) (light green) continues. Within the same timeline, Purkinje cells start differentiating in the Purkinje cell layer (PCL). During the second-postnatal week, granule cells continue to migrate from the external granule layer (EGL) (light green) to the internal granule layer (IGL) (dark green). Meanwhile, Purkinje cells develop extensively, forming complex dendritic arbours in PCL. Also, within the same timeline, cerebellar interneurons differentiate and migrate to the cerebellar cortex from the cerebellar white matter. During the late-stage of the cerebellum development, EGL disappears and interneurons integrate into the cerebellar neuronal network. In the adult, cerebellar circuitry reaches maturity. Abbreviations: ML, Molecular layer; GC, granule cell.

Overall, the development of human cerebellum is highly protracted compared to mouse. This protracted developmental time line makes cerebellum susceptible to a wide range of neurodevelopmental and early-onset neurodegenerative disorders, including complex developmental brain disorders (e.g. autism spectrum disorder and Down syndrome) and cerebellar malformation disorders (e.g. Pontocerebellar Hypoplasia (PCH) and Joubert syndrome). For our specific focus, the next section will introduce the latter group of disorders.

## 1.4 Cerebellar malformation disorders

Cerebellar malformation disorders are a group of rare heterogeneous disorders resulting in either small, large or abnormally shaped cerebellum (reviewed in Basson and Wingate, 2013; Haldipur and Millen, 2019). They display variable degrees of structural defects in the cerebellar vermis and hemispheres (Figure 6). Owing to cerebellum's functional heterogeneity, these disorders are often associated with impairments in the development of multiple functions, including motor, communication and cognition. They are primarily classified based on the major involvement of the cerebellum or both the cerebellum and the brain stem (Aldinger and

Doherty, 2016). Examples for the former group are Dandy-Walker malformation and Poretti–Boltshauser syndrome (PBS) (Figure 6). On the one hand, the latter group includes Pontocerebellar Hypoplasia (PCH), Joubert syndrome and Cobblestone brain malformation disorder (COB) (Figure 6). These cerebellar malformation disorders are further characterized based on the genetic causes, clinical and brain imaging features. For our purpose, the following section will explain in detail PCH, our disease of interest.

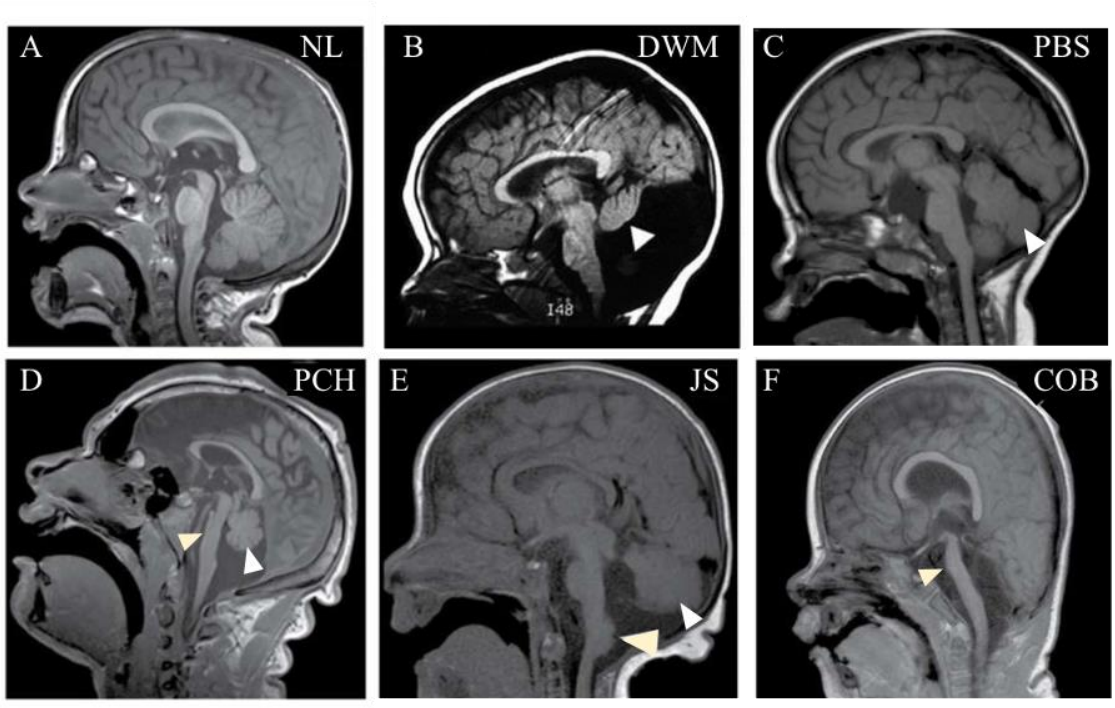


**Figure 6. Midline sagittal brain magnetic resonance images (MRI) showing the key features of cerebellar malformation disorders (adapted from Aldinger and Doherty, 2016; Haldipur and Millen, 2019). (A)** Unaffected individual for comparison. **(B)** Dandy-Walker malformation (DWM) with small and rotated cerebellar vermis (arrowhead). **(C)** Poretti–Boltshauser syndrome (PBS) with abnormally shaped cerebellum (arrowhead), termed as cerebellar dysplasia. **(D)** Pontocerebellar hypoplasia (PCH) with abnormally small cerebellum (white arrowhead) and pons (yellow arrowhead). **(E)** Joubert syndrome with small cerebellum (white arrowhead) and dorsally displaced cervicomedullary junction (yellow arrowhead), the region where the brainstem continues as the spinal cord. **(F)** Cobblestone brain malformation disorder with absent vermis and profoundly small pons (yellow arrowhead). Abbreviation: NL, normal.

# CHAPTER TWO: PONTOCEREBELLAR HYPOPLASIA

## 2.1 Pontocerebellar hypoplasia (PCH)

Pontocerebellar hypoplasia (PCH) is a heterogeneous group of rare recessive disorders, characterized mainly, but not exclusively, by degeneration and lack of proper development of the pons and the cerebellum. The term PCH originally appeared over a century ago in a report of Brun, where he initially defined the disorder as stunted growth of the cerebellum (Brun, 1917). The following reports in early 1920s, re-defined PCH as "hypoplasia ponto-neocerebellaris" to describe a number of patients presenting underdeveloped cerebellum and pons, with signs of prenatal-onset degeneration (Bakker and Bouman, 1924; Koster, 1926). In light of this latter definition, in 1928, Krause provided the first clinical details of a patient with PCH presenting additional features, including jerking movements of limbs, swallowing difficulties and spasticity (Krause, 1929). Later on, starting from the report of Norman in 1960, various studies reported PCH patients with severe spinal motor neurodegeneration (Chou et al., 1990; Goutieres et al., 1977; Kamoshita et al., 1990; Norman, 1961). Meanwhile, in 1990, Barth et al. introduced a group of 7 patients from 5 related families, presenting PCH with microcephaly and voluntary movement defects (Barth et al., 1990). Altogether, the high incidence in the number of PCH patients with distinct phenotypes highlighted the need for a diagnostic classification of the disorder. Indeed, in 1993, PCH1 and PCH2 were introduced as the first two subtypes of PCH (Barth, 1993). The former, is initially distinguished by a spinal motor neurodegeneration with a decrease in muscle tone. The latter, is mainly defined by swallowing impairments and almost complete absence of voluntary movement and cognitive development (Barth, 1993). Over the past 25 years, the classification has been extended to 13 subtypes, based on genetic defects, clinical, neuropathological and neuroradiological phenotypes (Table 1, Uwineza et al., 2019; van Dijk et al., 2018a; van Dijk et al., 2018b). While the clinical features vary widely within and between PCH subtypes, almost all of the subtypes

involve progressive degeneration in the various brain structures, including cerebellum, pons and cerebral cortex, with varying degree of severity. Additional clinical features include motor and cognitive impairments, epilepsy, ataxia, swallowing, feeding and respiratory difficulties, axonal motor and sensory peripheral neuropathy. Owing to the progressive nature of these symptoms, most of the patients die after birth or during infancy and childhood. Altogether, PCH represents a severe neurodevelopmental and neurodegenerative disorder that occurs mainly with a prenatal-onset and follows a progressive course. Based on the known molecular causes, PCH is mostly caused by defects in ubiquitous cellular processes, including RNA metabolism and tRNA synthesis (Table 1). Yet, the genetic basis is still not known for all of the PCH cases and many subtypes remain to be identified. Therefore, it is of great interest to identify new causes of PCH to better understand the molecular mechanisms implicated in the disease aetiology. Indeed, to this extent our study has contributed to the phenotypic spectrum and genetic diagnosis of PCH by introducing a distinct PCH subtype caused by mutations in a novel disease-causing gene: *MINPP1*, a gene involved in inositol phosphate metabolism.

It is worth to note that along with the 13 PCH subtypes, a large group of disorders are diagnosed with PCH (Table 2). These include congenital disorders of glycosylation 1a (CDG1a), *CASK*, *RELN* and *VLDLR* associated disorders, certain tubulin-related disorders and dystroglycanopathies. However, it remains unclear as to why this group of disorders are not classified as PCH.

**Table 1. PCH subtypes (adapted from van Dijk et al., 2018b).**

| Subtype | Distinctive features | Subcategory | Gene | Gene Function | OMIM number | Key references |
|---|---|---|---|---|---|---|
| **PCH1** | Spinal motor neuron degeneration, muscle weakness, hypotonia, respiratory insufficiency, corpus collosum Hypoplasia | PCH1A | *VRK1* | Neuronal migration | (#607596) | (Gonzaga-Jauregui et al., 2013; Renbaum et al., 2009; Stoll et al., 2016) |
| | | PCH1B | *EXOSC3* | mRNA degradation | (#614678) | (Eggens et al., 2014; Rudnik-Schöneborn et al., 2013; Wan et al., 2012) |
| | | PCH1C | *EXOSC8* | mRNA degradation | (#616081) | (Boczonadi et al., 2014) |
| | | PCH1D | *EXOSC9* | mRNA degradation | (#618065) | (Burns et al., 2018) |
| | | | *SLC25A46** | Mitochondrial fission and fusion | (#610826) | (Van Dijk et al., 2017; Wan et al., 2016) |
| **PCH2** | Generalized clonus, impaired swallowing, dystonia, chorea, severe forms of progressive microcephaly | PCH2A | *TSEN54* | tRNA splicing | (#277470) | (Budde et al., 2008; Namavar et al., 2011a; Sánchez-Albisua et al., 2014) |
| | | PCH2B | *TSEN2* | tRNA splicing | (#612389) | (Bierhals et al., 2013; Budde et al., 2008) |
| | | PCH2C | *TSEN34* | tRNA splicing | (#612390) | (Budde et al., 2008) |
| | | PCH2D | *SEPSECS** | Selenocysteine synthesis | (#613811) | (Agamy et al., 2010; Iwama et al., 2016; Pavlidou et al., 2016) |
| | | PCH2E | *VPS53* | Membrane trafficking | (#615851) | (Feinstein et al., 2014) |
| | | PCH2F | *TSEN15* | tRNA splicing | (#617026) | (Breuss et al., 2016) |
| **PCH3** | Facial dysmorphism, optic atrophy | | *PCLO** | Regulation synaptic protein & vesicle formation | (#608027) | (Ahmed et al., 2015; Durmaz et al., 2009; Rajab et al., 2003) |
| **PCH4** | Severe form of PCH2, micrencephaly, congenital contractures, inferior olivary nuclei hypoplasia/ atrophy, polyhydramnios, neonatal death | | *TSEN54* | tRNA splicing | (#225753) | (Budde et al., 2008) |
| **PCH5** | Identical to PCH4 | | *TSEN54* | tRNA splicing | (#610204) | (Namavar et al., 2011b; Patel et al., 2006) |
| **PCH6** | Hypotonia, seizures, elevated CSF lactate, progressive supratentorial atrophy | | *RARS2** | Arginyl tRNA synthetase | (#611523) | (Cassandrini et al., 2013; Edvardson et al., 2007) |
| **PCH7** | DSD, thin corpus callosum, enlarged ventricles | | *TOE1* | RNA processing | (#614969) | (Lardelli et al., 2017) |
| **PCH8** | Non-progressive/ non-degenerative PCH, thin corpus callosum | | *CHMP1A* | Regulation INK4A | (#614961) | (Mochida et al., 2012) |
| **PCH9** | Abnormal muscle tone, impaired swallowing, corpus callosum hypoplasia, 'figure 8' configuration of brainstem | | *AMPD2* | Regulation GTP synthesis | (#615809) | (Accogli et al., 2017; Akizu et al., 2013a; Marsh et al., 2015; Marsh et al., 2017) |
| **PCH10** | Abnormal muscle tone, seizures, spinal motor neuron degeneration, mild cerebellar hypoplasia/atrophy, thin corpus callosum | | *CLP1* | tRNA splicing | (#615803) | (Karaca et al., 2014; Schaffer et al., 2014) |
| **PCH11** | Non-progressive/ non-degenerative PCH, corpus callosum hypoplasia | | *TBC1D23* | Intracellular vesicle transport | (#617695) | (Ivanova et al., 2017; Marin-Valencia et al., 2017) |
| **PCH12** | Severe prenatal symptoms, micrognathia, arthrogryposis | | *COASY* | Coenzyme A synthesis | (#618266) | (van Dijk et al., 2018a) |
| **PCH13** | Facial hypotonia, small hippocampus, thin corpus callosum | | *VPS51* | Membrane trafficking | (#618606) | (Uwineza et al., 2019) |

PCH subtypes with postnatal onset neurodegeneration are marked with *. Abbreviations: DSD, disorders of sex development.

**Table 2. Differential diagnosis of PCH (from van Dijk et al., 2018b).**

| Disorders | Distinctive Features | Gene(s) involved | Key references |
|---|---|---|---|
| **Congenital disorder of Glycosylation Ia (CDGIa)** | **Clinical:** neonatal onset multi organ failure, dysmorphic features, ataxia. Microcephaly<br>**MRI:** global PCH with superimposed atrophy, supratentorial atrophy, ventriculomegaly, delayed myelinisation | *PMM2* | (Barone et al., 2014; De Lonlay et al., 2001; Feraco et al., 2012) |
| **CASK- related disorders** | **Clinical:** facial dysmorphism, sensorineural hearing loss, ophthalmologic abnormalities. Developmental progress in a subgroup of patients. No MND or chorea. Progressive microcephaly.<br>**MRI:** variable degree of PCH, equally affecting hemispheres and vermis. Cortical malformations can be present. | *CASK* | (Burglen et al., 2012; Hackett et al., 2010; Moog et al., 2015; Najm et al., 2008) |
| **Tubulin defects** | **Clinical:** DD, seizures. Progressive microcephaly.<br>Optic atrophy in some cases.<br><br>**MRI:** cortical malformations (e.g. lissencephaly, polymicrogyria) with cerebellar hypoplasia and brainstem malformations | *TUBA1A , TUBB2B, TUBB3, TUBB5, TUBA8* | (Fry et al., 2014; Jaglin and Chelly, 2009; Kumar et al., 2010) |
| **RELN & VLDLR mutations** | **Clinical:** Severe DD, hypotonia, epilepsy, nystagmus.<br>In VLDLR: non-progressive ataxia, quadrupedal gait.<br>**MRI:** lissencephaly, severe PCH and abnormal hippocampus, milder in VLDLR. | *RELN, VLDLR* | (Boycott et al., 2005; Hong et al., 2000; Valence et al., 2016) |
| **α- dystroglycan related dystrophies (WWS, MEB, Fukuyama congenital muscular dystrophy)** | **Clinical:** severe DD, muscle weakness with increased CK, ophthalmologic abnormalities.<br>WWS at the severest end of the spectrum.<br>**MRI:** cobblestone lissencephaly, PCH, congenital hydrocephalus. | *POMT1, POMT2 POMGnT1, LARGE, FKTN, FKRP, ISPD FKR* | (Boycott et al., 2005; Hong et al., 2000; Valence et al., 2016) (Clement et al., 2008) |
| **X-linked Hoyeraal-Hreidarsson syndrome** | **Clinical:** IUGR, microcephaly, failure to thrive, progressive bone marrow failure, aplastic anaemia, combined immunodeficiency,<br>**MRI:** PCH, delayed myelinisation, focal high intensities in brainstem and thalamus, subcortical calcifications. | *DKC1* | (Knight et al., 1999; Sznajer et al., 2003) |
| **Paediatric onset Spinocerebellar Ataxia** | **Clinical:** Ataxia, developmental progress, some cases with retinitis pigmentosa or cone-rod dystrophy.<br>**MRI:** Ponto cerebellar hypoplasia/atrophy, no supratentorial atrophy. | *ITPR1, ATXN7, ATXN2* | (Donis et al., 2015; Poretti et al., 2015; Singh et al., 2014; Storey, 2014; van Dijk et al., 2017) |

Abbreviations: MND, motor neuron degeneration; DD, developmental delay; CK, creatine kinase; WWS, Walker-Warburg syndrome; MEB, Muscle eye brain disease; IUGR, Intrauterine growth retardation; DC, dyskeratosis congenital.

## 2.2 Typical structural brain abnormalities in PCH

Neuropathology, neuroradiology and head circumference measurements provide insights into the structural brain abnormalities seen in PCH. For instance, the study of perinatal and neonatal post-mortem brain tissues from PCH patients, often reveal morphological and cytological abnormalities in the developing cerebellum and the pons. These abnormalities include changes in the shape and foliation of the cerebellum, increase in the number of pyknotic cells and reduction in the number of neurons in the cerebellum and pons. Thereby, PCH is typically associated with a prenatal-onset neurodegeneration mechanism, as typically seen in PCH4 caused by mutations in *TSEN54* (Barth et al., 2007; Namavar et al., 1993; Namavar et al., 2011a).

Along with the histopathology analysis, follow-up MRI scans provide insights into the nature of volume loss detected in the cerebellum and pons of the patients with PCH. Indeed, when the cerebellum and pons display a normal shape but a reduced volume size, these conditions are referred to as cerebellar and pontine hypoplasia, respectively (Poretti et al., 2015; van Dijk et al., 2018b) . Often, these hypoplastic conditions are static and thereby imply an abnormally developed cerebellum and pons. On the one hand, when the cerebellum and pons progressively reduce in volume, this condition is referred to as cerebellar and pontine atrophy, respectively, often reflecting their degeneration. While the distinction between these hypoplastic and atrophic conditions seems evident in theory, this is often very challenging in practice, especially in PCH in which neurodevelopmental and neurodegenerative defects intersect prenatally. Thereby, in most of the PCH subtypes, the cerebellar and pontine growth defects are labelled as “hypoplasia/atrophy”, indicating the involvement of both neurodevelopmental and neurodegenerative features. Moreover, in most of the PCH subtypes, the cerebellum typically appears in a “dragon fly configuration”, in which flattened cerebellar hemispheres represent “the wings” and the relatively spared vermis represents “the body”, as

typically seen in the coronal MRI of the patients with *TSEN54-PCH* (Figure 7). Hence, in PCH, often cerebellar hemispheres are more affected than the cerebellar vermis.

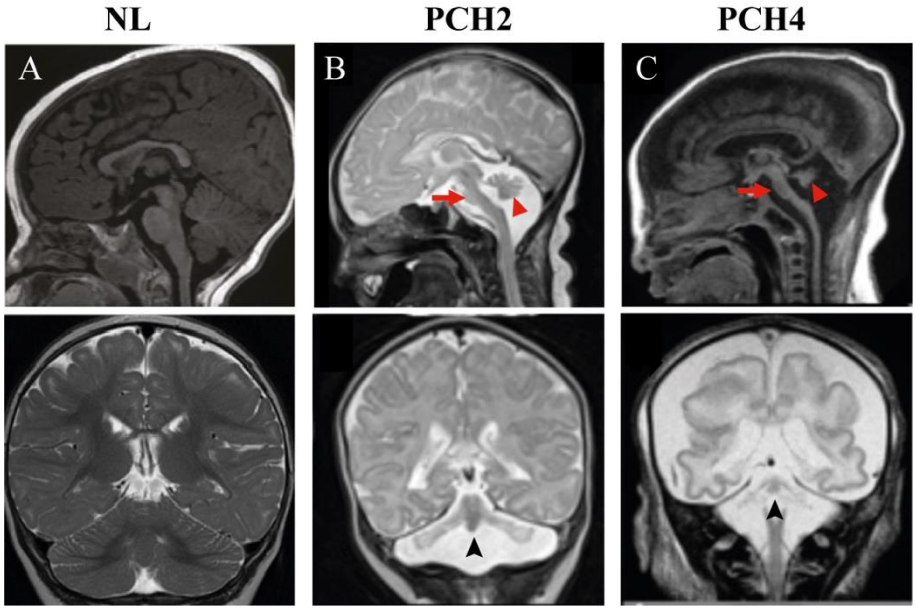


**Figure 7. Typical structural brain abnormalities in PCH (adapted from Appelhof et al., 2019; Haldipur and Millen, 2019).** Midline-sagital (top) and coronal (bottom) brain MRIs of a healthy individual **(A)** and patients with PCH2 **(B)** and PCH4 **(C)**, both carrying loss of function mutations of *TSEN54*. Sagittal MRIs show variable degree of pontine (red arrow) and the cerebellar atrophy/hypoplasia (red arrowhead). The cerebral involvement is also clearly seen in PCH4. Coronal MRIs display the typical "dragon fly pattern" of the cerebellum, with severe flattening of the cerebellar hemispheres and relative sparing of the vermis (black arrowhead). Abbreviation: NL, normal.

Along with these hindbrain growth defects, follow-up MRI scans and head circumference (HC) measurements also reveal reduction in the total brain volume in most of the patients with PCH. Indeed, when the brain volume decrease is static and visible at birth, this condition is referred to as congenital microcephaly, reflecting the abnormally developed brain (Haldipur and Millen, 2019; van Dijk et al., 2018b). On the one hand, when the total brain volume loss is progressive, this condition is referred to as progressive microcephaly and implies the early-onset degeneration of various brain structures, cerebral and cerebellar cortex being the most profoundly affected. Most of the PCH subtypes results in the latter condition with a marked cerebral and cerebellar atrophy (Table 1).

Altogether, PCH is often associated with (1) prenatal-onset hypoplasia/atrophy of the cerebellum and pons, (2) “dragon fly configuration” of the cerebellum and (3) progressive microcephaly, hence indicating the involvement of both neurodevelopmental and neurodegenerative mechanisms.

## 2.3 Distinct neurodevelopmental and neurodegenerative features of PCH subtypes

Besides the above-mentioned structural brain phenotypes commonly seen in PCH, additional and variable neurodevelopmental and neurodegenerative features can distinguish multiple PCH subtypes (Table 1, Figure 8). For instance, many PCH subtypes additionally present neuroradiological defects in the corpus callosum, the brain structure that connects the left and right side of the cerebral hemispheres. Indeed, while PCH1, PCH9 and PCH11 are characterized by severe corpus callosum hypoplasia, several other PCH subtypes (i.e. PCH7, PCH8 and PCH10) display a thinner corpus callosum compared to the healthy individuals (see Table 1). Therefore, the development of the corpus callosum is also affected in many PCH subtypes.

Furthermore, PCH1 and PCH10 additionally present spinal motor neurodegeneration (Figure 8, Boczonadi et al., 2014; Eggens et al., 2014; Gonzaga-Jauregui et al., 2013; Renbaum et al., 2009; Wan et al., 2012). For instance, both of these subtypes involve severe forms of axonal motor peripheral neuropathy. In line with this neuropathy, histopathological analysis often reveal hypomyelination and almost complete loss of motor neurons in the spinal cord of the patients with PCH1 (Boczonadi et al., 2014; Eggens et al., 2014; Gonzaga-Jauregui et al., 2013; Renbaum et al., 2009; Wan et al., 2012). Thus, PCH1 and PCH10 involve both central and peripheral nervous system defects.

PCH4 and PCH5 additionally involve hypoplasia/atrophy of the inferior olivary nuclei and progressive micrencephaly, the latter defined as abnormally small brain (Table 1).

Moreover, histopathological autopsy analysis show almost complete absence of Purkinje cells and dentate nucleus in the cerebellar sections of the patients with either of the subtypes (Namavar et al., 2011b; Patel et al., 2006; Rudaks et al., 2011). Thereby, PCH4 and PCH5 involve the severest form of neonatal brain growth defects in PCH, as a result of the severe progressive micrencephaly phenotype.

Interestingly, PCH8 and PCH11 differ from other PCH subtypes by their non-progressive and non-degenerative form of PCH (Ivanova et al., 2017; Marin-Valencia et al., 2017; Mochida et al., 2012). Thereby, they are recognized by their entirely neurodevelopmental origin.

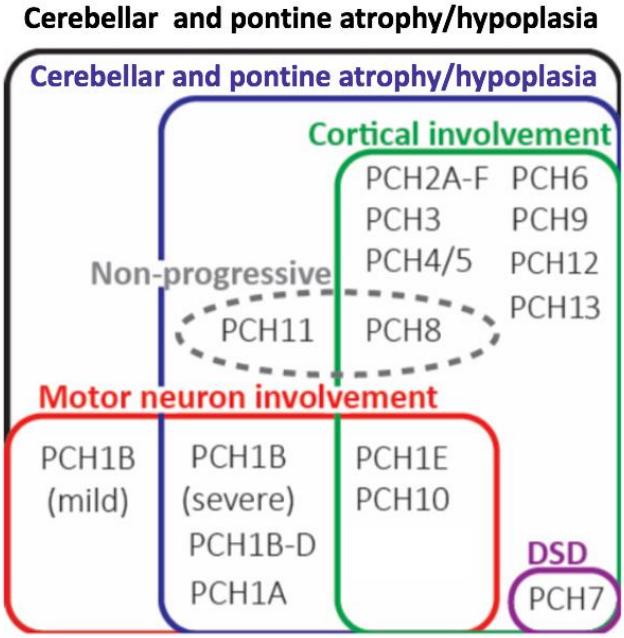


**Figure 8. Schematic overview showing the overlapping pathology between PCH subtypes (adapted from Appelhof et al., 2019).** Abbreviation: DSD, disorders of sex development.

Lastly, it is worth to note that none of the 13 PCH subtypes are associated with neurodegeneration in the basal ganglia and thalamus, the two features typically detected in the *MINPP1*-PCH patients within this study.

Altogether, PCH subtypes involve a broad spectrum of neurodevelopmental and prenatal- onset neurodegenerative features, affecting mainly, but not exclusively, the proper growth and development of the hindbrain. In an attempt to better understand the underlying molecular mechanisms, the next section will focus on the genetic and molecular basis of PCH.

## 2.4 Genetic causes and molecular basis of PCH

Having a recessive inheritance, PCH is so far found to be caused by mutations in more than 20 genes, interestingly almost all involved in ubiquitous cellular processes (Table 1). Indeed, while nine of them (i.e. *TSEN15, TSEN2, TSEN34, TSEN54, CLP1, RARS2, EXOSC3, EXOSC8, TOE1)* act in tRNA synthesis and RNA metabolism, the remaining is involved in various unconnected cellular processes, including GTP biosynthesis, cell cycle regulation and membrane trafficking (Table 1, Figure 9). Although, it remains unclear how defects in these ubiquitous processes can solely result in PCH, a number of studies have shed light on the possible molecular mechanisms underlying the genetic causes of PCH. To this extent, the following part of this section will explain the molecular basis of PCH by mainly focusing on the studies that functionally characterized the disease-causing gene mutations. These will include the ones leading to progressive forms of PCH (e.g. *CLP1, EXOSC8, AMPD2)* and non-progressive forms of PCH (i.e. *TBC1D23* and *CHMP1A*) (marked in asterisks in Figure 9).

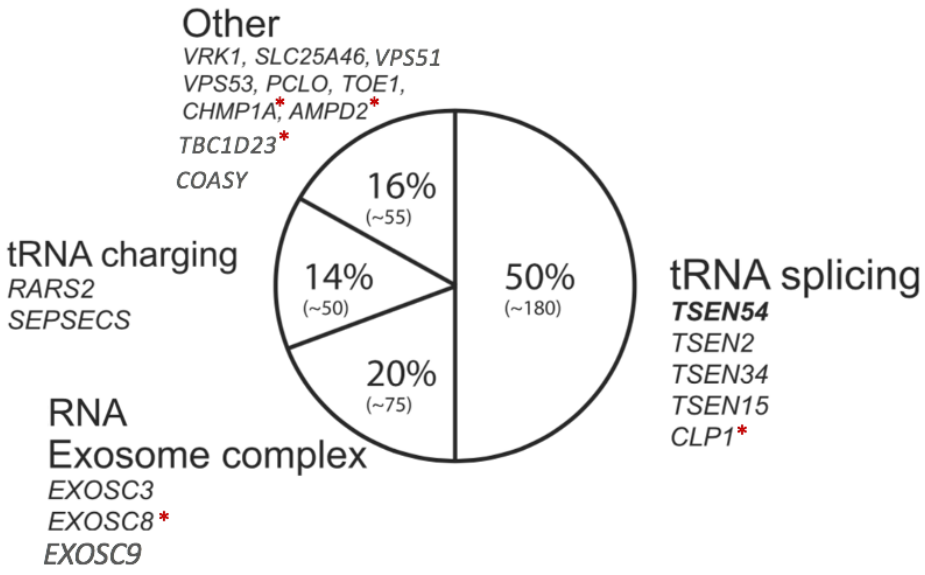


**Figure 9. Pie-chart indicating the proportion of PCH patients per PCH-related pathological pathway (adapted from van Dijk et al., 2018b).** Patient numbers are calculated based on the published reports.

**Molecular basis of progressive forms of PCH**

For instance, defects in tRNA splicing has been suggested to cause PCH10 following the identification of 9 unrelated families carrying the same homozygous missense mutation in *CLP1,* a gene encoding the RNA kinase component of the TSEN complex involved in tRNA splicing (Karaca et al., 2014; Schaffer et al., 2014). Interestingly, PCH10-*CLP1* mutation impairs the binding of CLP1 to TSEN complex, without affecting its protein levels. As a potential consequence of this binding defect, neurons-derived from patient fibroblasts (iNeurons) showed accumulation of pre-tRNAs, indicating a perturbed tRNA splicing (Schaffer et al., 2014) .To assess whether such accumulation can be toxic for neuronal cell survival, patient iNeurons were overexpressed with pre-tRNAs and tested for cell viability (Schaffer et al., 2014). Surprisingly, no signs of toxicity was detectable under these conditions. However, under oxidative stress, patient fibroblasts overexpressed with partially processed tRNA fragments showed reduced cell viability while no effect is seen in control fibroblasts. Thus, these findings have suggested that accumulation of incompletely processed tRNAs, rather than their unprocessed forms, perturbs the survival of patient cells. Thus, although cell type specific effects remains to be determined, misprocessing of pre-tRNAs due to loss of CLP1 function has been proposed as the underlying molecular basis of PCH10. In the following section, neurodegenerative mechanisms associated with PCH10 will be explained through *Clp1*-kinase dead mutant mice (see section 3.2).

In addition to the defective tRNA splicing, altered mRNA metabolism has also been proposed as the cause of PCH following the discovery of PCH1-causing homozygous missense mutations in *EXOSC8,* leading to almost complete loss of its expression (Boczonadi et al., 2014). *EXOSC8* encodes a component of the RNA exosome complex involved in the degradation of AU-rich element (ARE) containing-mRNA. Thereby, expression of various ARE transcripts were studied to assess the effect of mutant-EXOSC8 in patient myoblasts.

Interestingly, patient cells showed a specific upregulation of ARE-containing myelin-related genes, including *MBP* and *MOBP*. Considering the observation that *EXOSC8*-PCH1 patients display severe hypomyelination in the brain and the spinal cord, these findings suggested that imbalance between ARE and non-ARE containing myelin-related mRNA transcripts due to impaired *EXOSC8* activity could be the underlying cause of this progressive form of PCH. To this extent, it would be interesting to assess whether PCH patients with LOF *EXOSC3 and EXOSC9* mutations also display a similar mRNA metabolic activity defect (Table 1).

Along with the RNA-related pathogenic mechanisms, defects in protein translation due to impaired GTP biosynthesis has also been associated with the progressive form of PCH, following the identification of PCH9-causing loss of function mutations in *AMPD2*, a gene involved in the conversion of AMP to IMP (Akizu et al., 2013). As a potential consequence of this genetic defect, under physiological concentrations of adenosine, the building block of AMP, neural progenitor cells (NPCs) derived from patient iPSCs displayed severe phenotypes, including a dramatic reduction in GTP levels, a reduced cell viability and robust defects in global protein synthesis. Interestingly, following treatment with AlCAr, an analogue of AMP, patient NPCs fully restored these phenotypes. Thereby, these findings have suggested that AMPD2-dependent defective GTP biosynthesis and protein synthesis are likely to be the underlying cause of PCH9 (for more in depth discussion on *AMPD2*-PCH9 disease modelling see section 3.2).

**Molecular basis of non-progressive forms of PCH**

While the progressive forms of PCH are shown to be caused by defects in RNA metabolism and protein synthesis, non-progressive forms are associated with abnormal cell cycle regulation and membrane trafficking (Ivanova et al., 2017; Marin-Valencia et al., 2017; Mochida et al., 2012). For instance, PCH8 is caused by loss of function mutations in *CHMP1A*, a chromatin modelling gene involved in the recruitment of BMI1 to promoters of cyclin-

dependent kinase inhibitor genes. As a potential consequence of this genetic defect, patient-derived lymphoblastoid cell lines showed reduced cell proliferation compared to control cell lines. To reveal the underlying mechanisms of this proliferation defect, expression of *BMI1*-target genes were assessed in patient and control cells. Interestingly, patient cells revealed upregulation only in one of the *BMI1*-target genes: *INK4A*. This specific de-repression phenotype is further confirmed by chromatin immunoprecipitation (ChIP) assays, in which patient cells showed reduced binding of BMI1 solely at *INK4A* promoter. As INK4A inhibition is known to be necessary for neural stem cell proliferation, these findings suggested that PCH8 is likely to be caused by defects in CHMP1A-mediated neural stem cell cycle progression (Bruggeman et al., 2005; Coulter et al., 2018).

Furthermore, impaired vesicle trafficking has also been associated with a non-progressive form of PCH, following the discovery of PCH11-causing homozygous truncating mutations in *TBC1D23*, a gene involved in Rab-mediated membrane trafficking (Ivanova et al., 2017; Marin-Valencia et al., 2017). To assess the effect of mutant TBC1D23 on vesicle trafficking, patient and control fibroblasts were transfected with GFP-tagged vesicle peptides and monitored via live imaging. Remarkably, vesicles in patient fibroblasts displayed altered anterograde and retrograde movement with reduced velocity. Thus, defective TBC1D23-mediated membrane trafficking has been suggested to be causal in PCH11. To this extent, it is interesting to note that other vesicle-trafficking related genes, including *VPS51* and *VPS53*, are also found to be causative of PCH (Table 1).

Altogether, while the exact molecular mechanisms behind the genetic defects involved in PCH remains incomplete, it is interesting to observe that PCH is mainly caused by defects in ubiquitous cellular processes, with its progressive forms mostly associated with RNA and protein synthesis defects and non-progressive forms with dynamic cellular processes, including

cell proliferation and membrane trafficking. In light of these molecular basis of PCH, the next section moves on to the PCH-disease models.

# CHAPTER THREE: PCH DISEASE MODELLING

## 3.1 PCH Disease Modelling

Animal and cellular models of PCH have been key in establishing the causality between genotype and phenotype. For instance, zebrafish knockdown models of various PCH-causing genes (i.e. *exosc3, exosc8, toe1, tsen54, clp1, slc25a46, chmp1a, tbc1d23)* recapitulated key disease features, including small brain size and impaired hindbrain and forebrain development, which were largely rescued following co-injection with the wild-type mRNA of the relevant gene (Boczonadi et al., 2014; Lardelli et al., 2017; Marin-Valencia et al., 2017; Mochida et al., 2012; Schaffer et al., 2014; Wan et al., 2012; Wan et al., 2016). Interestingly, while zebrafish models of PCH adequately reflect some of the human conditions, mouse models of PCH display milder forms of human disease phenotypes. Nevertheless, they have provided important insights into neurodevelopmental and neurodegenerative mechanisms of PCH. Along with these animal models, recently, induced pluripotent stem cells (iPSCs) have started to become an alternative cellular model, enabling one to uncover patient-specific PCH pathology. To this extent, our study has taken an advantage of these two latter models in an attempt to investigate the effect of loss of function of *MINPP1* in PCH causing mechanisms. Hence, for our purpose, this section will start by introducing the neurodegenerative and neurodevelopmental mouse models of PCH. Next, it will explain iPSCs technology and its relevance to PCH modelling.

## 3.2 PCH-mouse models

### Neurodegenerative mouse models of PCH

Mouse models of PCH9 and PCH10 represent the main neurodegenerative mouse models of PCH. The former initially involved *Ampd2* KO mouse following the identification of patients with PCH9 carrying loss of function mutations in *AMPD2*, a gene encoding an AMP deaminase (Akizu et al., 2013). However, unlike in *AMPD2* mutant patients, *Ampd2* KO mice

presented no major structural brain abnormalities. The absence of a discernible brain phenotype in *Ampd2* KO has raised the possibility of a functional redundancy between *Ampd2* and its paralog *Ampd3.* Indeed, *Ampd2* and *Ampd3* double-knock-out (DKO) mice displayed a slightly reduced brain size compared to their wild-type littermates. In line with this mild phenotype, histological analysis of *Ampd2/3* DKO mice revealed little signs of neurodegeneration, detecting some pyknotic cells in the cerebellum, cerebral cortex and hippocampus after P14. Such a mild neurodegenerative brain phenotype seen in *Ampd2/3* DKO has raised the question of whether it is due to the effects of genetic-background or species differences in AMP deaminase activity (for more details on the function of *AMPD2* see previous section 2.4)

In addition to *Ampd2/3 DO* mouse, other neurodegenerative mouse models of PCH involve *Clp1*-kinase-dead ($Clp1^{K/K}$) knock-in mice, including a viable one on a CBA/J background and a neonatal lethal one on a C57BL/6 background (Hanada et al., 2013; Karaca et al., 2014). Interestingly, both of these mice models were initially characterized by severe spinal motor neurodegeneration and reported to have no major structural brain abnormalities (Hanada et al., 2013). Later on, identification of *CLP1* mutant patients with PCH10 have questioned whether initial characterization studies had missed a brain phenotype in these *Clp1* mutant mice models, considering the fact that both the patient and mouse mutation leads to defective CLP1/Clp1 function (for more details on the function of *CLP1* see previous section 2.4). Indeed, by analysing the brain weight and performing MRI-3D brain reconstruction, both of the $Clp1^{K/K}$ mice models were found to display a mild reduction in the brain weight, volume and cortical thickness. These phenotypes became significant by 2 months and embryonic day (E) 18.5 on a viable and lethal background, respectively (Karaca et al., 2014) . In correlation with these brain phenotypes, immunofluorescence analysis revealed reduction in the number of $NeuN^+$ neurons in the neocortex of the 3 months-old $Clp1^{K/K}$ mice. Similarly, $Clp1^{K/K}$ E18.5 embryos on a lethal background showed reduced number of $Tbr1^+$ neurons in the cortical plate,

while retaining a comparable number of Pax6$^{+}$ and Ki67$^{+}$ neuronal progenitor cells (Figure 10, (Karaca et al., 2014)). Importantly, increased number of apoptotic cells was also detected throughout the brain of *Clp1*$^{K/K}$ E18.5 embryos, revealing an enhanced cell death in *Clp1*$^{K/K}$ lethal mice (Figure 10). Surprisingly, unlike *CLP1* mutant patients, none of the *Clp1*$^{K/K}$ mouse models show any structural and immunohistochemical abnormalities in the cerebellum. Altogether, the characterization of these *Clp1* mouse models identified mild forms of microcephaly with a reduced number of neurons and a potential increased number of apoptotic cells in the cerebral cortex.

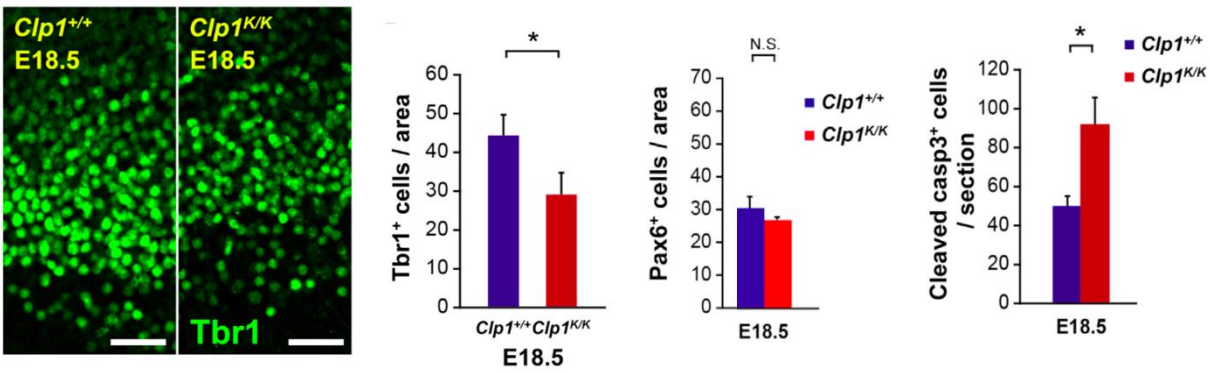


**Figure 10. Neurodegenerative features of neonatal lethal Clp1-kinase-dead (*Clp1*$^{K/K}$) knock-in embryos (from Karaca et al., 2014)**. Clp1$^{K/K}$ E18.5 embryos show reduced number of Tbr1$^{+}$ neurons in the cortical plate and a marked increase in the number of cleaved caspase 3$^{+}$ apoptotic cells throughout the coronal brain sections. The number of Pax6$^{+}$ neuronal progenitors remain comparable between the Clp1 mutant and wild type mice.

To conclude, while the PCH9 mouse model (*Ampd2/3 DO*) shows little signs of neurodegeneration in the cerebellum and cerebral cortex, PCH10 mouse models (*Clp1*$^{K/K}$ knock-in mice) display a slightly more severe phenotype affecting majorly the cerebral cortex. The question as to why these mouse models display milder forms of human neurodegenerative brain phenotypes remains as a mystery.

**Neurodevelopmental mouse models of PCH**

Interestingly, compared to the neurodegenerative mouse models of PCH mentioned above, neurodevelopmental mouse models of PCH (i.e. those of PCH8 and *CASK*-PCH) have more closely mimicked the human condition, hence revealing more in depth insights into potential neurodevelopmental mechanisms associated with PCH (Coulter et al., 2018; Mori et al., 2019). For instance, like *CHMP1A* mutant patients with PCH8, *Chmp1a* KO mice presented severe cerebellar hypoplasia with a relatively moderate microcephaly at birth (Coulter et al., 2018). In correlation with these brain phenotypes, immunofluorescence analysis revealed a marked reduction in the number of mitotic cerebellar granule cell precursors (GCP) in *Chmp1a* KO P0 pups, with a relatively moderate decrease in the number of mitotic cerebral cortical progenitors at E14.5. In an attempt to unravel the molecular mechanism underlying these proliferation defects, Coulter and his colleagues analysed the Shh signalling in the cerebellum as Shh is known to be an important mitogen for neuronal progenitors, including GCP. Indeed, *in situ* hybridization analysis showed a marked reduction in the expression of *Ptch1*, a negative regulator of Shh signalling, in the cerebellum of the *Chmp1a* KO mice at P0. Moreover, ELISA analysis revealed a considerable decrease in Shh levels in the cerebrospinal fluid (CSF) of the *Chmp1a* KO mice at E14.5. Supportive to these data, *Chmp1a* KO microcephaly phenotype was rescued in *Chmp1a* null: *Ptch1* heterozygous mice, in which Shh signalling is genetically engineered to be enhanced *in vivo*. Hence, this characterization study showed that SHH-mediated neural progenitor proliferation defect is the underlying cause of the hypoplastic brain phenotypes seen in *Chmp1a* KO mice.

Along with the *Chmp1a* KO mouse, heterozygous *Cask*-KO mouse model have shed light on the pathophysiology of various neurodevelopmental disorders associated with genetic defects in *CASK*, including *CASK*-PCH (Table 2, Burglen et al., 2012; Hayashi et al., 2012; Mori et al., 2019; Najm et al., 2008). *CASK* is located on X-chromosome and encodes a membrane-associated guanylate kinase that contains an additional N-terminal calcium/calmodulin kinase like domain. *In vitro*, CASK is shown to have pre- and post-synaptic functions such as binding various synaptic proteins involved in cell adhesion (i.e. neurexin, SynCAMs), regulation of ion channels (i.e. $Ca^{2+}$ channels and voltage-gated sodium channels) and transcription of NMDA receptor (Biederer et al., 2002; Hata et al., 1996; Hsueh et al., 2000; Schuh et al., 2003; Wang et al., 2004). However, the function of CASK in the brain has remained elusive. The initial mouse model for CASK-related disorders involves the *Cask KO* mice, which died soon after birth without showing any obvious structural brain abnormalities (Atasoy et al., 2007) . In order to study the impact of this gene defect on postnatal brain development, Mori et al. have used the previously generated heterozygous female *Cask*-KO mice (Mori et al., 2019). Indeed, $Cask^{+/-}$ female mice displayed smaller cerebellar cortex, mimicking the human disease condition. In addition to this brain phenotype, the balance between excitatory/inhibitory postsynaptic currents were shown to be disrupted in $Cask^{+/-}$ pyramidal neurons, analysed on brain cortical sections at P14. To assess whether such synaptic defect arose during neural development or after synapse formation, *Cask* was conditionally knocked-out in the cerebral cortex at P10. This was assessed by injecting AAV-GFP-Cre vector into the somatosensory cortex of the *Cask*-floxed mice. Interestingly, analysis of postsynaptic currents at P24-28 did not reveal any alteration in the *Cask* conditional KO neurons. Hence, these data suggested that Cask deficiency leads to an imbalance in the excitatory/inhibitory system during mouse neural development.

Altogether, defects in neural progenitor proliferation and synaptic transmission have been suggested as the main neurodevelopmental phenotypes underlying mouse models of PCH8, and *CASK*-PCH respectively. Having explained both the neurodegenerative and neurodevelopmental mouse models of PCH, the following part of this section will turn to iPSCs technology and iPSC-based PCH models.

## 3.3 PCH-disease modelling with iPSCs

### 3.3.1 Cellular reprogramming and iPSC technology

The landmark discovery that somatic cells can be reprogrammed back to pluripotency have led to the innovation of embryonic stem cell-like pluripotent cells, named as iPSCs, that are characterized mainly by their unlimited self-renewal capacity and robust potential to differentiate into any cell type in the body (Takahashi and Yamanaka, 2006; Takahashi et al., 2007). The concept of induced pluripotency emerged following a series of seminal studies on cellular plasticity that go back over 50 years (Figure 11). Indeed, the first example of nuclear reprogramming came in early 1960s by ground-breaking study of Sir John Gurdon, where he successfully generated fully developed frogs by transferring the nucleus of a somatic cell into an enucleated oocyte, a technique called as somatic cell nuclear transfer (SCNT) (Gurdon, 1963; Gurdon, 1962). Decades later, several other groups succeeded in cloning mouse and sheep via SCNT, expanding the finding of Gurdon to mammals (Wakayama et al., 1998; Wilmut et al., 1997). Indeed, these seminal findings have shown for the first time that a nucleus of a somatic cell can be reprogrammed back to an embryonic state if placed in a suitable cytoplasmic environment. However, whether somatic cells can be reprogrammed back to an embryonic state remained elusive. Decades later, studies performing somatic cell (i.e. fibroblasts and T lymphocytes) fusion with embryonic stem cells (ESCs) showed that this is indeed the case (Cowan et al., 2005; Tada et al., 2001). Interestingly, in addition to providing evidence for cellular reprogramming, these studies have also supported the idea that ESCs

possess diffusible reprogramming factors that are capable of erasing the identity of a somatic cell. The strong evidence that these reprogramming factors are likely to be transcription factors came from early transdifferentiation studies, where ectopic expression of a single transcription factor was shown to convert one cell type to another (Davis et al., 1987; Kulessa et al., 1995; Xie et al., 2004). One seminal example of this involves myoblast master regulator, MyOD, whose enforced expression was sufficient to transform mouse fibroblasts to myoblasts (Davis et al., 1987) .

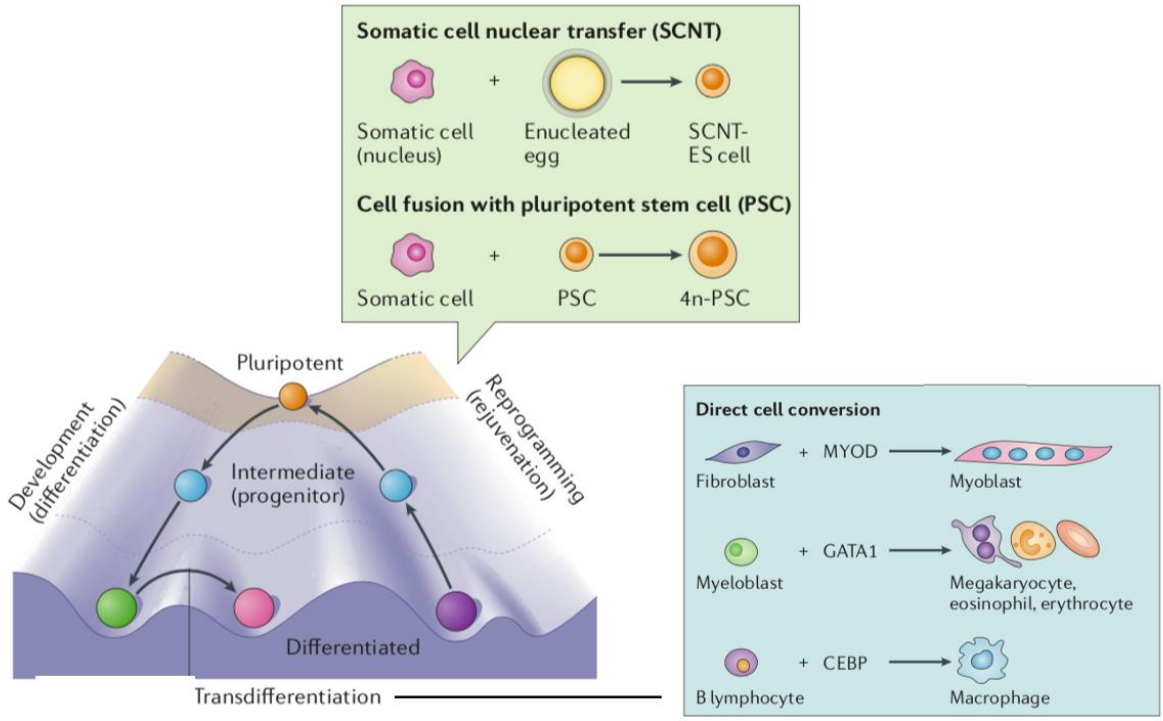


**Figure 11. Early studies setting up the stage for transcription factor-mediated cellular reprogramming (from Takahashi and Yamanaka, 2016).** The first examples of nuclear and cellular reprogramming came from studies involving somatic cell nuclear transfer (SCNT) and somatic cell fusion assays with pluripotent stem cells (PSC). These experiments have demonstrated for the first time that somatic cells can be reprogrammed back to pluripotency. In the meanwhile, early transdifferentiation studies provided strong evidence that transcription factors can change the cellular fate of a somatic cell. Hence, these seminal findings have led to the discovery of reprogramming transcription factors capable of inducing pluripotency in somatic cells.

Overall, these landmark studies have set the stage for Yamanaka and Takahashi to identify candidate reprogramming factors by selecting 24 transcription factors that are highly and specifically expressed in embryonic stem cells (Takahashi and Yamanaka, 2006). Remarkably, simultaneous ectopic expression of all 24 candidate genes in mouse embryonic fibroblasts have led to the formation of embryonic stem cell-like colonies. By eliminating one transcription factor at a time, Yamanaka and his group narrowed down the list of 24 genes to a minimal set of 4 reprogramming factors (Oct4, Sox2, Klf4 and c-Myc), here after referred to as OSKM factors, and showed that the combination of these OSKM factors induce pluripotency when retrovirally overexpressed in mouse embryonic and adult fibroblasts (Takahashi and Yamanaka, 2006). The resulting pluripotent cells were shown to display morphological, phenotypical and molecular properties of mouse ESCs, representing the first examples of iPSCs. Within a year, two researcher groups, including Yamanaka's team, have independently reported the derivation of iPSCs from human fibroblasts (Takahashi et al., 2007; Yu et al., 2007). While the incredible potential of iPSCs was immediately recognized, their poor reprogramming efficiency, reproducibility and signs of genomic instability have created a bottleneck, restricting their usability. Thereby, since the discovery of iPSCs, much effort has been devoted to overcome these challenges and indeed significant progress has been made to improve the quality of iPSCs in terms of transcriptional signatures, epigenetic status, genomic, self-renewal and pluripotent stability. This is achieved mostly by optimizing iPSCs reprogramming methodologies (e.g. reprogramming cocktails and their delivery strategies), somatic cell sources, cell culture conditions and iPSC characterization procedures (Figure 12, for more in depth discussion see the following reviews Li and Belmonte, 2016; Takahashi and Yamanaka, 2016).

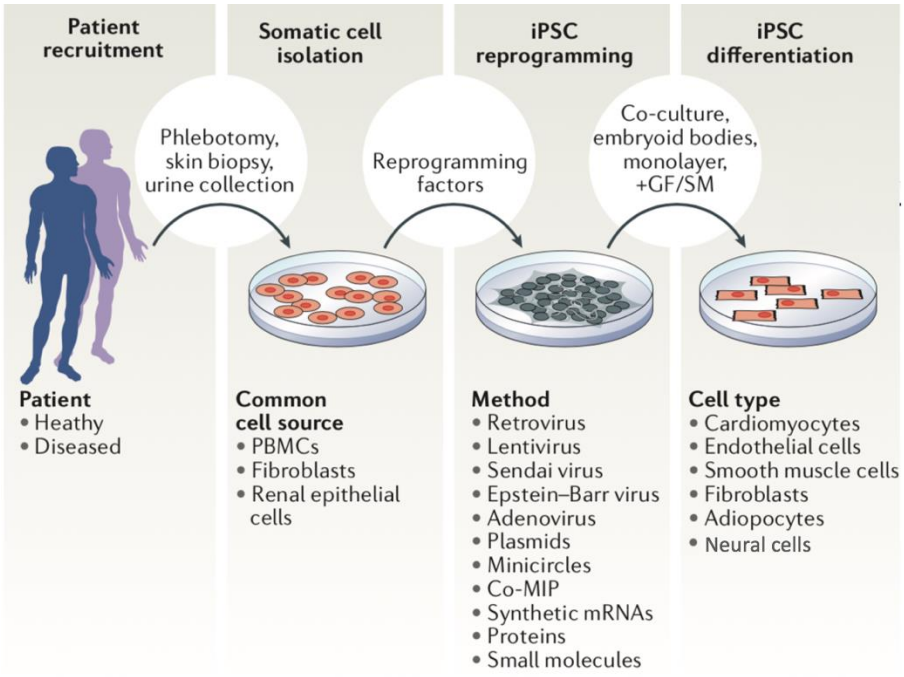


**Figure 12. Overview of the iPSC reprogramming and differentiation (from Chen et al., 2016).** Following isolation, patient somatic cells can be reprogrammed into iPSCs by exogenously expressing reprogramming factors via different reprogramming delivery methods. The resultant iPSCs can be further differentiated into cell type of interest, allowing one to study disease mechanisms in a human disease-relevant cell type. Abbreviations: PBMCs, peripheral blood mononuclear cells; GF, growth factors, SM, small molecules.

### Challenges of iPSC reprogramming

Despite the advances mentioned above, iPSC reprogramming still remains as a very inefficient and imperfect process which can result in partially reprogrammed iPSCs, hence highlighting the need for their careful characterization prior to any differentiation study (Carey et al., 2011; Volpato and Webber, 2020), for more in depth discussion see section 3.3.3). Moreover, there are still many unanswered questions about the underlying mechanisms of this astounding phenomenon, impeding the development of more efficient cell reprogramming protocols. For instance, while the initial reprogramming steps involved in reverting a fully differentiated cell to a pluripotent one have started to be uncovered, still very less is known about the molecular events required for the maintenance of the pluripotent state of iPSCs (Buganim et al., 2013).

**iPSCs vs. ESCs**

In spite of the challenges mentioned above, when genetically and sex matched, human iPSCs were shown to be molecularly and functionally equivalent to their gold standard, human ESCs, hence making iPSCs as a powerful alternative cellular model (Choi et al., 2015). And more importantly, unlike ESCs, the derivation of iPSCs does not require destruction of the human embryos, thereby avoiding the ethical concern associated with the use of ESCs. Rather, iPSCs can be derived from any somatic cells from any individual, with the order of easy accessibility being skin fibroblasts, blood cells and urine-derived cells. Hence, owing to these advantages, iPSCs have become the preferred option for various applications, including disease modelling, cellular therapy and drug discovery (Figure 13).

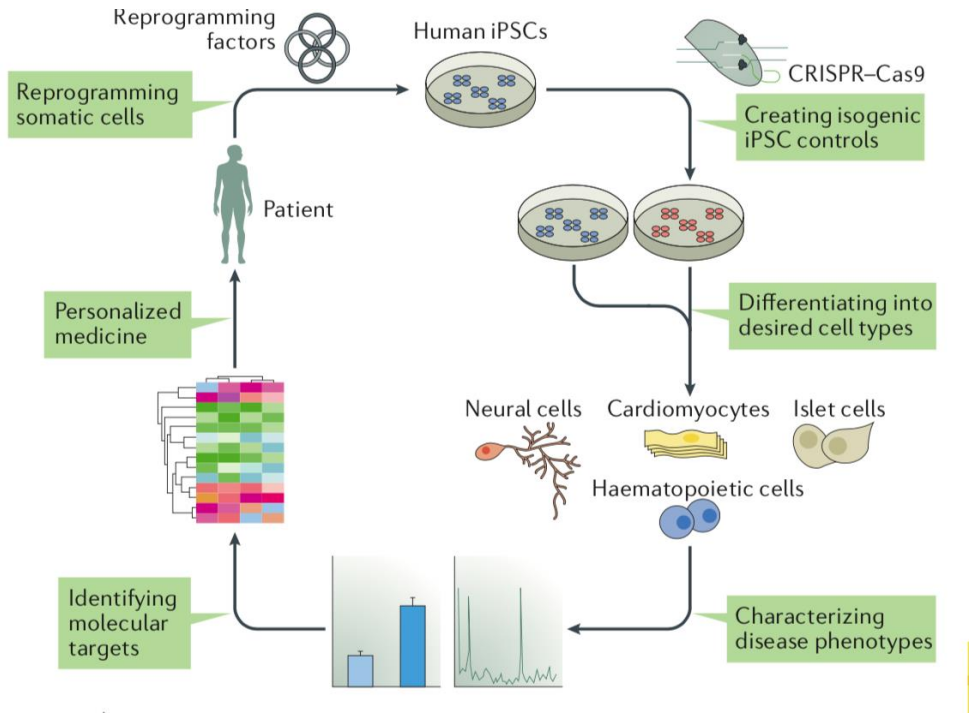


**Figure 13. Overview of iPSC-based disease modelling (from Shi et al., 2017).** Disease modelling using iPSCs starts with the derivation of iPSC lines from patient somatic cells, followed by the generation of genetically-matched isogenic control iPSC lines via gene editing technologies such as CRISPR-Cas9. Subsequently, iPSCs lines are differentiated into disease-relevant cell types, allowing one to identify disease-causing molecular and cellular mechanisms which can serve as a potential therapeutic target.

**Modelling brain disorders with iPSCs**

Particularly, iPSCs technology has reshaped modelling of brain disorders by the development of defined 2D and 3D neural differentiation protocols, hence providing a unique source for otherwise inaccessible human brain cells (reviewed in Kelava and Lancaster, 2016). Indeed, in many neurodevelopmental and neurodegenerative brain disorders, iPSC model systems have revealed insights into patient-specific cellular and molecular disease mechanisms that were previously not captured by studying post-mortem tissues, neural cancer cell lines and mouse models. For instance, by using iPSCs derived from lissencephaly patients, Kriegstein and his group uncovered a severe mitotic defect in outer radial glia cells (oRG cells), a neural progenitor population that is largely absent in the rodents but essential for human neocortical development (Bershteyn et al., 2017). Moreover, advents in genome editing technologies have further advanced iPSC-based disease modelling, enabling the study of various genetic brain disorders in an isogenic cellular setting (reviewed in Hockemeyer and Jaenisch, 2016). However, despite these advances, remaining caveats include high-variability between iPSCs lines, incapacity of iPSC-derived brain cells to mature into adult-like states and lack of robust differentiation protocols for the generation of various neural subtypes, including cerebellar neural cells (for more in depth discussion see the following two sections). Nevertheless, iPSC models developed in our study have enabled us to investigate pathological mechanism underlying *MINPP1*-PCH in a human disease-relevant cell type. Having briefly defined iPSCs technology, the following sections will focus on iPSC-based neural differentiation and study design strategies important to our study.

### 3.3.2 Neural differentiation from iPSCs

Neuroembryology studies on amphibian and mouse models have provided insights into molecular and morphological mechanisms underlying key stages of early neurodevelopment. Extrapolating these developmental stages *in vitro* have enabled the development of 2D and 3D

neural differentiation protocols from iPSCs, the former being important to our study. 2D differentiation protocol is established mainly in a four-step process: (1) neural induction, (2) specification of neuroepithelial cells to region-specific neural progenitor subtypes, (3) neuronal/glial differentiation and (4) their functional maturation (Tao and Zhang, 2016) (Figure 14). Here, we will first introduce the main strategies behind the first step as it will be important to understand the neural induction methods used in this study to model *MINPP1*-PCH with iPSCs. We will then briefly define the latter steps to explain the current challenges in directing iPSCs towards cerebellar neurons. Such explanation will help to better understand the reason why iPSC-based PCH modelling studies, including ours, have hitherto mostly taken the strategy of generating non-cerebellar cells from patients with a major cerebellar phenotype.

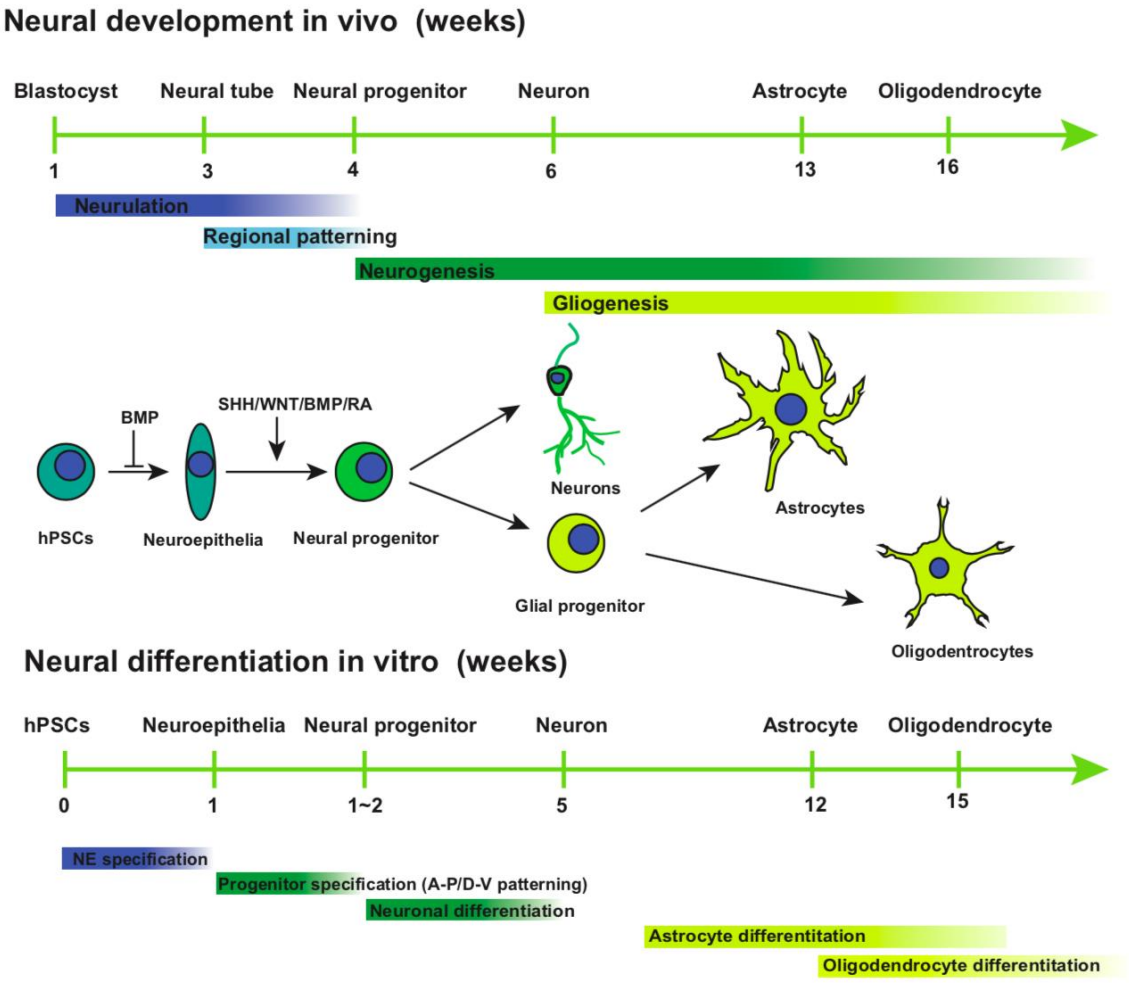

**Figure 14. Key stages of neural development *in vivo* and neural differentiation *in vitro* (from Tao and Zhang, 2016).** iPSCs resemble the inner cell mass (ICM) of the blastocyst. In the presence of neural-inducing molecules (e.g.BMP inhibitors), iPSCs differentiate into neuroepithelial cells, corresponding to their *in vivo* counterparts that form the neural plate and later the neural tube *in vivo.* Neuroepithelial cells are further specified into region-specific neural progenitor subtypes in the presence of morphogen gradients (e.g. SHH, WNT, BMP, RA) that provide positional identity along the anterior-posterior (A/P) and dorsal-ventral (D/V) of the developing neural tube. Regionally patterned neural progenitors are then further differentiated into functionally specialized neural subtypes.

## 1. Neural induction

The first step in guiding iPSCs towards neural lineage involves neural induction (Figure 14). *In vivo*, this stage refers to the process by which ectodermal cells on the dorsal portion of the embryo acquire a neural fate and differentiate into neuroectodermal precursor cells, known as neuroepithelial cells (reviewed in Rogers et al., 2009)). During this process, neuroepithelial cells expand and form the neural plate, the structure which later folds into neural tube during the 3$^{rd}$ and 4$^{th}$ week of gestation. Neural induction is triggered when the cells of the primitive node, an important developmental signalling centre, moves underneath the ectoderm and secretes molecules that inhibit BMP signalling (e.g. Noggin, Chordin and Follistatin) and activate FGF pathway (e.g. FGF1, FGF2 and FGF4), the two opposing signalling pathways involved in specification of neuroectoderm from ectoderm (Fainsod et al., 1997; Hongo et al., 1999; Piccolo et al., 1996; Rogers et al., 2009; Zimmerman et al., 1996). In an attempt to mimic this *in vivo* environment, neural induction protocols were initially developed using ESCs and relied on the ability of the ESC suspension aggregates, termed as embryoid body (EB), to differentiate into neuroectodermal lineage in response to neural-inducing molecules, including FGF ligands and BMP inhibitors. For instance, the first protocol was developed by culturing ESC-derived EBs on an adhesive substrate under a chemically defined media with FGF2 (Zhang et al., 2001). Upon culture, an increase in the number of small and elongated cells became apparent in the centre of differentiating ESC-derived EBs, resembling the *in vivo* development of the neural plate. These elongated cells displayed neuroepithelial cell features, including columnar cell morphology and expression of neuroectoderm (e.g. PAX6 and NCAD)

and neural stem cell markers (e.g. NESTIN, MUSASHI-1, PSA-NCAM) (Pankratz et al., 2007; Zhang et al., 2001). Hence, this first report has provided important insights into sequence of events leading to the generation of neuroepithelial cells. However, one considerable drawback of this method was the wide size variability in ESC-derived EBs, leading to variation in neural induction efficiency. To overcome this problem, several different strategies have been developed. For instance, Sasai's group provided a better control over the variation in EB size by re-aggregating a defined number of dissociated ESCs in round-bottom well plates (Eiraku et al., 2008). On the one hand, other studies sought to bypass embryoid body stage by developing a monolayer culture system. One such method was developed by Gerrard et al., where EDTA-dissociated ESCs were shown to differentiate into $PAX6^+$ neuroepithelial cells under serum-free conditions with Noggin, a BMP inhibitor (Gerrard et al., 2005). A succeeding study by Studer's group provided a more efficient, robust and fast neural induction method by culturing single ESCs under serum-free media supplemented with Noggin and SB431542, an inhibitor of Activin/TGF-β signalling pathway involved in several stages of differentiation, including suppression of meso-endodermal fates (Chambers et al., 2009; Smith et al., 2008). As both BMP and TGF-β signalling pathways involve SMAD proteins as signalling transducers, Studer's group named their approach as "dual-SMAD inhibition method" (Chambers et al., 2009). Remarkably, following dual-SMAD inhibition >80% of the ESCs were shown to differentiate to $PAX6^+$ neuroepithelial cells, compared to <10% when single factor is used. Thus, dual-SMAD inhibition greatly improved neural conversion of ESCs. Altogether, these four independent strategies have set the basis for the development of neural induction methods from iPSCs. In our study, we have used the two monolayer culture strategy developed by Gerard et al. and Studer's group.

Before introducing the second step in neural differentiation from iPSCs, it is important to note that, along with the generation of neuroepithelial cells, neural induction protocols have

also mimicked the regional identity of the early-born neuroepithelial cells *in vivo*. Indeed, during *in vivo* neural induction, neural plate is specified first in the head region. Correspondingly, regardless of the neural induction method used, neuroepithelial cells differentiated from iPSCs initially exhibited transiently anterior brain markers (e.g. PAX6, FOXG1 and OTX2), a key information that set up the stage for the development of strategies for the second step in neural differentiation from iPSCs (Chambers et al., 2009; Eiraku et al., 2008; Pankratz et al., 2007; Zhang et al., 2001).

**2. Specification of neuroepithelial cells to region-specific neural progenitor subtypes**

Following neural induction, the second step in neural differentiation from iPSCs involves the specification of the early-stage neuroepithelial cells to region-specific neural progenitor subtypes (Figure 14). This is achieved by mimicking the neural tube development *in vivo*. During this morphological process, neuroepithelial cell fates are determined by gradients of signalling molecules, known as morphogens, that are secreted in a spatial and temporal manner by various developmental signalling centres found along the anterior-posterior and dorsal-ventral axis of the developing tube (Kiecker and Lumsden, 2012; Le Dréau and Martí, 2012) (Figure 15).

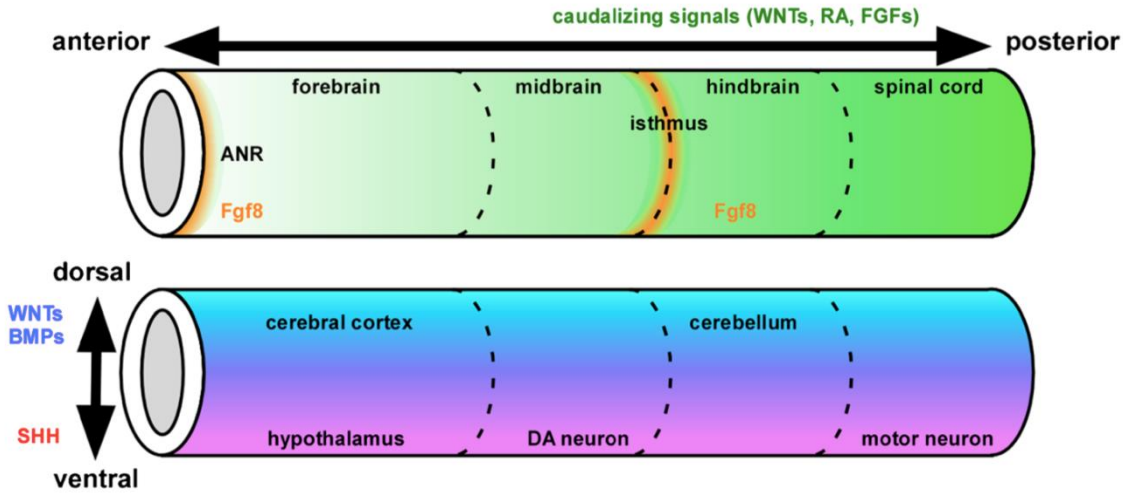


**Figure 15. Schematic diagram showing the patterning of the developing neural tube along the A-P and D-V axes (from Muguruma, 2018).** Morphogen gradients involved during this developmental process are represented by colour gradients. Cerebral cortex arises from the most anterior and dorsal part of the neural plate, whereas the cerebellum develops from the dorsal region of the most anterior part of the hindbrain. Abbreviations: ANR, anterior neural ridge; DA, dopaminergic; RA, retinoic acid.

Hence, to generate neural progenitors with a specific regional identity *in vitro*, neural differentiating cell cultures are treated with particular morphogens in a specific concentration at a specific time point (i.e. during neural induction, neural plate or neural rosette stage) (Li et al., 2009; Tao and Zhang, 2016). This strategy of patterning neuroepithelial cells along the A-P and D-V axes *in vitro* has been very efficient for deriving neural progenitor populations that are located at the most anterior/posterior and dorsal/ventral parts of the neural tube. For instance, in the absence of any morphogens, nearly pure population of cerebral cortical progenitors are generated from early-stage neuroepithelial cells of anterior identity (Figure 15, Espuny-Camacho et al., 2013). However, such strategy has been challenging for specifying the ones located in between the ends. One example, includes progenitors emerging from the cerebellar region of the neural tube, owing to its location at the dorsal region of the rostral hindbrain (Figure 15). *In vivo*, this region is known to be specified mainly via morphogens FGF8 and WNT1 that are secreted from the developmental signalling centre located between the hindbrain and midbrain boundary, known as isthmic organizer (Guo et al., 2007; Joyner et al., 1991; reviewed in Leto et al., 2015). However, surprisingly, *in vitro* FGF8 and WNT1 had little effect in specifying early-stage neuroepithelial cells to cerebellar progenitors, with an efficiency of only 15% (Muguruma et al., 2010). To overcome this poor specification, several strategies have been developed, initially using ESCs and later adapting to iPSCs. For instance, several groups additionally used FGF2 and RA, two factors previously reported to be involved in cerebellar patterning *in vivo* (Erceg et al., 2010; Nayler et al., 2017; Sundberg et al., 2018). In contrast, Sasai's group took a completely different approach, where they patterned EB-like aggregates to the isthmic organizer fate by using two moderate caudalizing morphogens (i.e. FGF2 and insulin) during neural induction stage (Ishida et al., 2016; Muguruma et al., 2015). Such indirect strategy, recapitulated the *in vivo* isthmic organizer signalling microenvironment, enabling the induction of endogenous cerebellar patterning programme (e.g. 30%

KIRREL2$^{+}$/PTF1A$^{+}$/EN2$^{+}$) in EB-like aggregates. Further optimization of this protocol allowed the generation of EN1$^{+}$ iPSC-derived cerebellar progenitors at an efficiency between 70-90% (Watson et al., 2018). However, despite these progress, the further specification of these cells into GABAergic and glutamatergic cerebellar progenitor subtypes has become the next hurdle in cerebellar differentiation protocols from iPSCs. Indeed, *in vivo* these two main progenitor populations are generated from different regions of the developing cerebellum (see section 1.3). However, currently available protocols do not use a directed differentiation strategy to generate these progenitor subtypes. In contrast, they are based on a heterogeneous differentiation process, during which the desired progenitor population is enriched mainly by cell sorting (Ishida et al., 2016; Silva et al., 2020; Sundberg et al., 2018; Wang et al., 2015; Watson et al., 2018). However, such strategy remains quite inefficient at least for Purkinje progenitors that arise from the GABAergic progenitor population, representing only the 14-28% of the differentiating iPSCs prior to cell sorting (Ishida et al., 2016; Silva et al., 2020; Sundberg et al., 2018; Wang et al., 2015; Watson et al., 2018). And indeed, the efficiency of generating other cerebellar progenitor subtypes remains unexplored with the exception of a recently published paper reporting the presence of 46-49% of granule cell progenitors arising from the iPSCs-derived glutamatergic progenitor population (Silva et al., 2020). Hence, there is still a bottleneck in generating pure and efficient cerebellar progenitor subtypes from iPSCs, hindering the generation of efficient and robust cerebellar differentiation protocols. Indeed, given this context, currently most of the PCH modelling studies with iPSCs, including our study, have circumvented this limitation by directing patient-derived iPSCs towards cerebral cortical progenitors, one of the most robust and efficient neural differentiation strategy from iPSCs (reviewed in Wiethoff et al., 2015) . While such strategy does not allow the direct study of cerebellar-PCH phenotypes, it provides the opportunity to study PCH cortical phenotypes, which gives important clues to the aetiology of PCH.

### 3-4. Differentiation and functional maturation of neural subtypes

The latter two steps in neural differentiation from iPSCs involve the differentiation and functional maturation of neural subtypes from region-specific neural progenitors. For instance during cortical neuronal differentiation, iPSC-derived cerebral cortical neural progenitors progressively exit cell cycle and acquire glutamatergic transmitter identity. Following terminal differentiation, post-mitotic cortical neurons mature over a couple of weeks or months until they acquire functional electrophysiological and synaptic properties. These processes are achieved either under standard neuronal culture conditions supplemented with neuronal survival factors (e.g. BDNF, GDNF, NT3) or with co-culture systems (Bardy et al., 2015; Johnson et al., 2007; Tao and Zhang, 2016). For instance, for differentiation and maturation of the Purkinje neurons, iPSC-derived Purkinje progenitors are co-cultured with mouse-granule cells or human foetal cerebellar slices over a period of more than 2 months (Ishida et al., 2016; Sundberg et al., 2018; Wang et al., 2015; Watson et al., 2018). However, such co-culture system greatly introduces variability to the procedure, hence introducing another challenge in cerebellar differentiation protocols. Indeed, currently only two studies have been able to use this strategy to model cerebellar disease with iPSC-derived Purkinje neurons (Ishida et al., 2016; Sundberg et al., 2018) .

It is worth to note that, currently all published iPSCs-derived neurons resemble the transcriptomic profile of those in the foetal brain (Handel et al., 2016). While such embryonic state does not introduce a major problem for modelling developmental disorders, it poses a great challenge for modelling adult neurodegenerative disorders. In an attempt to overcome this challenge, several approaches have been followed to induce ageing in iPSC-derived neurons. The most common one involves exposing iPSC-derived neurons to cellular stressors, such as toxins and reactive oxygen species (reviewed in Studer et al., 2015). Indeed, in various

neurodegenerative disease modelling studies, such strategy enables patient-specific iPSC-derived neurons to present pathological phenotypes.

To conclude, modelling cerebellar and neurodegenerative conditions with iPSCs is still on its early stage due to lack of robust cerebellar differentiation protocols from iPSCs and the technical limitations to mature iPSC-derived brain cells beyond their foetal stage. So far, iPSC-based PCH modelling studies have circumvented these challenges by following a cortical neuronal differentiation protocol and inducing aging stress in their iPSC models, respectively, the former approach taken by our study.

### 3.3.3 Study design in iPSC-based disease modelling

Disease modelling using iPSCs requires a careful study design, as one needs to clearly distinguish disease-related phenotypes from unpredictable experimental outcomes arising from line-to-line variability (Ardhanareeswaran et al., 2017; Hockemeyer and Jaenisch, 2016; Volpato and Webber, 2020). Although often ignored, such variation between individual iPSCs lines is mostly caused by differences in their genetic background and cellular changes resulting from reprogramming process (Carey et al., 2011; Soldner et al., 2011). To this extent, this section will address how these two main cell-line-to-cell-line differences can be minimized. And, in the meanwhile, it will introduce the study design used in this study for modelling *MINPP1*-PCH with iPSCs.

**Genetic background variability**

Individual iPSCs lines, apart from their disease status, exhibit highly variable features, the most important being the genetic background. However, this confounding effect is often neglected by most of the monogenic disease modelling studies, in which disease-causing mechanisms are assessed by matching patient-derived iPSC line with iPSC lines generated from non-disease affected individuals (Figure 16A). However, this study design introduces confusion over whether the observed phenotypic differences between differentiated

counterparts of these cell lines are due to disease-causing mutations and/or genetic background variability.

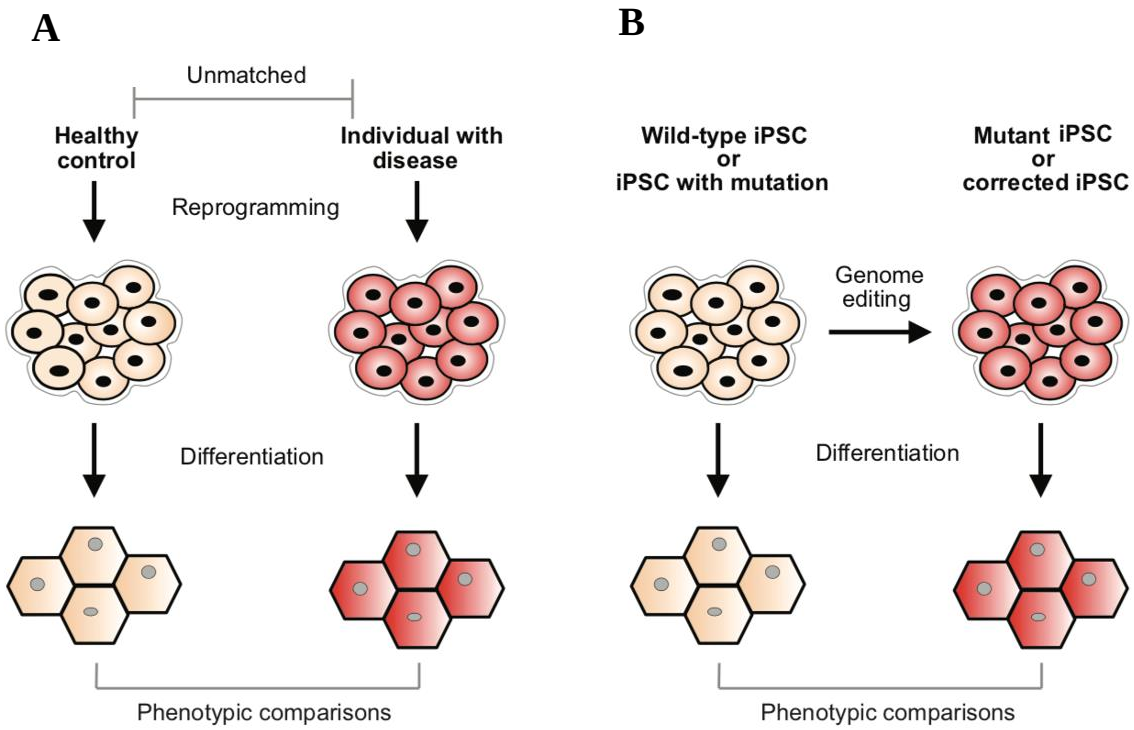


**Figure 16. Comparison of genetically-matched and unmatched study design in iPSC-based disease modelling (from Musunuru, 2013). (A)** When investigating the phenotypic effects of disease-causing genes, patient derived iPSCs are often matched with iPSCs that are generated from non-disease affected individuals. However, such study design fails to distinguish disease-relevant phenotypes from line-to-line variations, arising largely due to the genetic background effects. **(B)** Recent advances in gene editing technology allows the creation of isogenic cell lines that differ only at the disease causing mutation, allowing one to establish direct causality between genotype and phenotype.

To ensure valid disease modelling, the most robust study design would be to provide genetically-matched control iPSC lines that differ only in disease-causing mutations, known as isogenic control cell lines (Figure 16B). This can be achieved either by introducing specific mutations into non-disease affected iPSC lines or correcting disease-causing mutations in patient-derived iPSCs. Indeed, recent advances in genome editing have enabled the generation of such isogenic control cell lines, CRISPR-Cas9 technology being the most efficient, specific and easy-to-use system (Byrne et al., 2014; Chen et al., 2015; Hockemeyer and Jaenisch, 2016a; Jinek et al., 2012). This technology is successfully adapted from bacterial adaptive immune system that uses RNA-guided nucleases to cleave pathogenic DNA (Jinek et al., 2012;

Zetsche et al., 2015). Hence, by simply specifying guide-RNA (gRNA) to a genetic locus of interest, one can easily direct Cas9, the nuclease of the CRISPR type-2 system, to introduce double strand break (DSB) at a target genomic locus (Ran et al., 2013; Zetsche et al., 2015) (Figure 17). In the absence of exogenous DNA-repair template, DSB is repaired via error-prone non-homologous end joining (NHEJ) DNA repair pathway, in which insertions or deletions (indels) are often made during the re-ligation process of DSB (Perez et al., 2008; Ran et al., 2013). Thereby, this strategy is mostly used to generate gene knockouts, as indels introduced in coding exon often result in frameshift mutations and premature stop codons. On the one hand, in the presence of exogenous-DNA repair template, Cas9-generated DSB is repaired by homology directed repair (HDR) pathway (Chen et al., 2011). This editing strategy is mostly used to introduce or correct patient-specific mutations. Hence, although several caveats remain such as Cas9 off-target effects and low repair efficiency of HDR, CRISPR-Cas9 technology has re-shaped gene editing in iPSCs, allowing one to study disease-causing mutations in an isogenic background (Hockemeyer and Jaenisch, 2016).

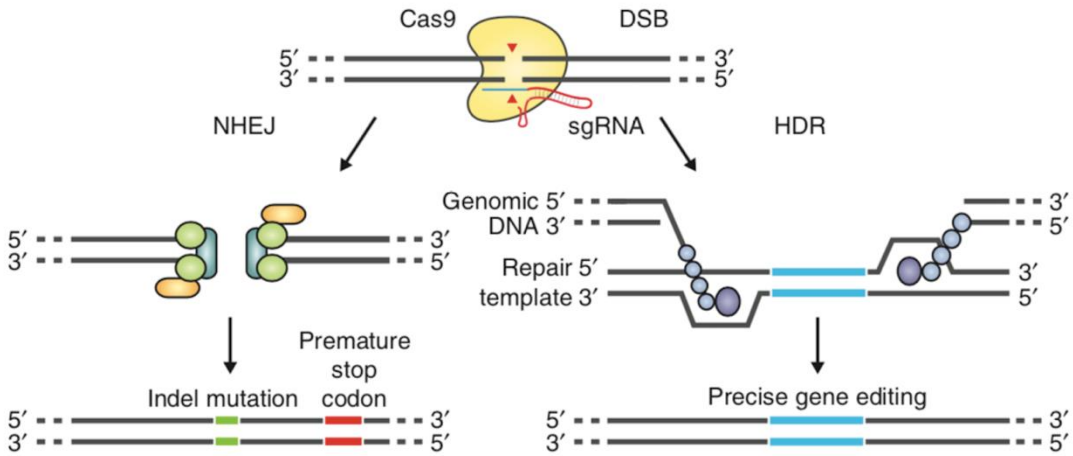


**Figure 17. Overview of the CRISPR-Cas9-mediated DSB repair mechanism (from Ran et al., 2013)** Double strand break (DSB) generated by Cas9/gRNA complex can be repaired either via the error prone non-homologous end joining (NHEJ) or the precise homology directed repair (HDR) DNA repair pathway. The former often introduces indel mutations which can result in frameshifts and premature stop codon when religating the ends of the DSB break. Thereby, this strategy is often used to knock out a gene of interest. On the one hand, the latter pathway introduces specific nucleotide modifications at a target locus in the presence of an exogenous repair template containing the desired mutation flanked by the homology arms. Thereby, HDR pathway is often used to introduce patient-specific mutations at a target genomic locus. Abbreviation: sgRNA, single guide-RNA.

In our study, to establish direct causality between loss of function of *MINPP1* and its PCH-causing phenotypic effects, we generated the following two iPSC-based *MINPP1*-PCH models: a patient-derived iPSC line harbouring early-truncating mutation in *MINPP1* and a CRISPR-Cas9 *MINPP1* knock-out iPSC line derived from a non-disease affected individual. The latter model allowed us to mimic patient-mutation in an isogenic cellular setting, hence overcoming the issue of genetic background variability between patient-derived and control iPSC lines.

**Reprogramming-based variability**

Reprogramming-based variability represents another big challenge for iPSC-based disease modelling studies, as cellular differences caused by reprogramming process (e.g. the degree of epigenetic reprogramming and level of reprogramming-induced genetic alterations) often lead to variation in the quality of iPSC lines (Carey et al., 2011; Maherali and Hochedlinger, 2008; Volpato and Webber, 2020). For instance, in our study, iPSCs lines are generated using different reprogramming methods, affecting the reprogramming efficiency and pluripotency potential of iPSC lines. Hence, to ensure valid disease modelling, it is important to perform the following characterization assays in order to properly asses the quality of an iPSC line via: (1) characterization of pluripotency via detection of pluripotency markers (e.g. SOX2, OCT4, SSEA-4, NANOG and TRA1-81) and via embryoid body (*in vitro*) or teratoma formation *(in vivo)* assays to assess the differentiation potential into three germ layers (endoderm, mesoderm and ectoderm) (2) characterization of genomic integrity via whole genome single nucleotide polymorphism (SNP) or comparative genomic hybridization (CGH) array.

### 3.3.4 iPSC-based PCH models

Modelling PCH with iPSCs has not yet become a routine approach given the limitations discussed previously in the section 3.3.2. Indeed, only two studies have hitherto modelled PCH using iPSCs, following either a 2D cortical or 3D cerebral organoid differentiation strategy due to the lack of robust cerebellar differentiation protocols (Akizu et al., 2013; Coulter et al., 2018). Here, we will briefly discuss both studies, starting from the one that took the 2D differentiation strategy to study the pathological mechanisms in PCH10. As mentioned in the section 2.4, PCH10 is caused by mutations in *AMPD2*, a gene involved in the purine biosynthesis by converting AMP to IMP (Akizu et al., 2013). As *de novo* purine biosynthesis is known to be highly active in proliferating cells, Akizu et al., modelled *AMPD2*-PCH by generating cortical neural progenitor cells (NPCs) from iPSC lines derived from patients and unaffected individuals. It is important to note that the group captured disease-relevant neurodegenerative phenotypes only by subjecting patient-derived NPCs to a metabolic stress induced by adenosine treatment. Indeed, under this cell culture condition, patient-derived (NPCs) displayed a dramatic reduction in cell survival, GTP levels and severe defects in global protein synthesis. The former phenotype is rescued following overexpression of *AMPD2* cDNA in patient-derived NPCs, indicating the specificity of the disease-causing genetic defect. Furthermore, following treatment with AlCAr, an analogue of AMP, patient-derived NPCs were shown to restore all the three phenotypes mentioned above. Altogether, modelling *AMPD2*-PCH with iPSCs allowed Akizu and his colleagues to unravel patient-specific disease mechanisms and in the meanwhile have provided the opportunity to identify potential treatment strategy for this early-onset neurodegenerative PCH subtype.

Along with a 2D cellular model, a 3D cerebral organoid model has also been used to study PCH pathogenesis (Coulter et al., 2018). Interestingly, like in the 2D model-mentioned above, defects in neural progenitors are also found to be central in cerebral organoids KO for

the PCH8-causing gene, *CHMP1A*. For instance, by performing immunostaining, Coulter et al. found a 65% decrease in $PAX6^+$ progenitor cell area in early-differentiated *CHMP1A* KO cerebral organoids. In line with this immunostaining data, RNA sequencing revealed down regulation in progenitor marker genes (e.g. *SOX1, SOX2, HES5)*. Importantly, these defects in progenitor maintenance were mirrored by a 130% increase in CTIP-positive postmitotic neuron area, along with the upregulation in early-neuronal differentiation genes (e.g. *DCX*, *NRXN1*, *SYT4*). Hence, this initial characterization allowed Coulter et al. to study PCH pathogenesis at a human-tissue level, revealing insights into defective brain development due to impaired progenitor maintenance and early-neuronal differentiation.

To conclude this section, mouse and iPSC-based PCH models have provided important insights into neurodevelopmental and neurodegenerative mechanisms underlying PCH-relevant phenotypes. While the former has allowed the study of disease-causing genetic defects in an *in vivo* environment, the latter has provided insights into human-specific disease phenotypes. To this extent, in our study we have developed both of these models in an effort to unravel disease mechanisms underlying *MINPP1*-PCH. In an attempt to better describe the role of MINPP1 in inositol phosphate metabolism, the next section moves on to inositol phosphates with a particular focus on inositol hexakisphosphate ($IP_6$), the main substrate of MINPP1.

# CHAPTER FOUR: INOSITOL PHOSPHATES

## 4.1 Inositol Phosphates (IPs) and their metabolism in mammalians

Inositol phosphates (IPs) are vital metabolic and signalling molecules omnipresent in eukaryotic cells (Irvine and Schell, 2001). Their building block, *myo*-inositol, here after referred to as inositol, is chemically stable unlike glucose or ribose (Saiardi, 2017). Thereby, the arrangement of phosphate groups around its six-carbon-sugar ring provides an ideal scaffold for the generation of a vast family of phosphorylated molecules, including lipid-bound inositol phosphates, known as phosphatidylinositols, and inositol phosphates, referred to as "soluble" due to their ability to dissolve in water-based acid solutions (Figure 18, Irvine and Schell, 2001).

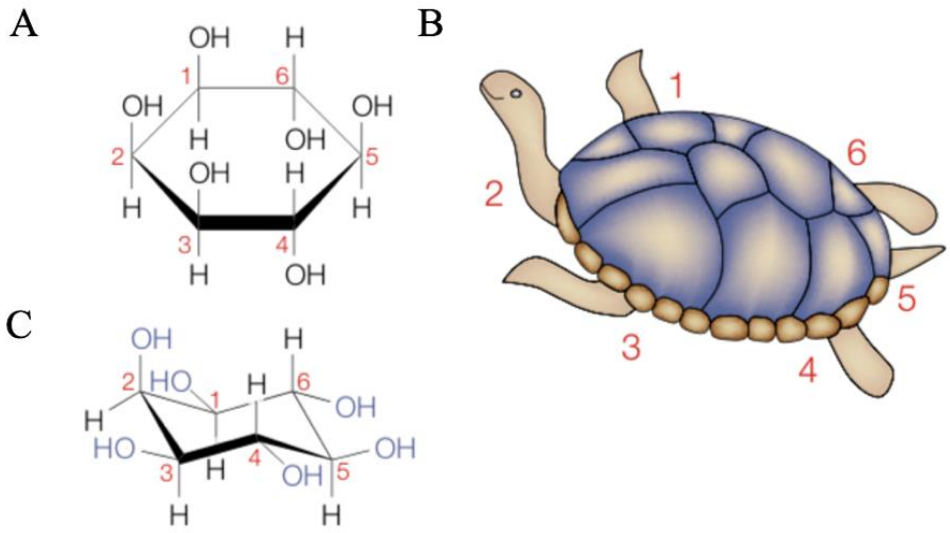


**Figure 18. Structure of the myo-inositol and nomenclature of the inositol phosphates (from Irvine and Schell, 2001)**. Inositol is a carbohydrate with the formula $C_6H_{12}O_6$. It has nine stereoisomers, myo-inositol being the most common. **(A, C)** The diagrams show the structure of the myo-inositol in Haworth **(A)** and chair **(C)** configuration. The chair configuration represents the most thermodynamically stable conformation of the myo-inositol *in vivo*. **(B)** The carbon atoms on the myo-inositol ring are numbered in a counter-clock wise manner by following Agranoff's turtle (Thompson, 1980). Inositol phosphates are named based on the position of the hydroxyl group(s) that is/are phosphorylated.

Inositol phosphate molecules have received a considerable attention after the discovery of inositol 1,4,5-trisphosphate ($IP_3$) as $Ca^{2+}$ mobilizing-messenger (Berridge et al., 2000; Mikoshiba et al., 1993; Streb et al., 1983). To date, more than 30 distinct inositol phosphates have been identified in eukaryotic cells, each resolved based on their negative charged determined by the number and position of the phosphate group(s) present on their inositol-ring (Figure 18, Azevedo and Saiardi, 2006; Irvine and Schell, 2001)). However, many more members of this family are believed to exist, given the capacity of the inositol-phosphate complex to generate 64 unique inositol phosphates (York, 2006). Hence, inositol phosphates comprise a highly complex family of signalling molecules, with many more yet to be discovered. As a reflection to their high complexity, a vast array of inositol phosphate kinases and phosphatases have been identified in various organisms, including yeast, plants and animals, revealing important insights into the biosynthesis of the inositol phosphates (reviewed in Irvine and Schell, 2001; Saiardi et al., 2018; Tsui and York, 2010). Over the last four decades, most studies of the inositol phosphate metabolism have performed *in vivo* metabolic radiolabelling, using exogenous [$^3$H]-inositol as a tracer to monitor the changes in the intracellular inositol phosphates levels (Azevedo and Saiardi, 2006; Stevenson-Paulik et al., 2006). This traditional method has been instrumental in identifying the inositol phosphate metabolic pathway originating from the extracellularly imported inositol, here after referred to as lipid-dependent inositol phosphate metabolic pathway. In this section, we will start by explaining this metabolic network. Subsequently, we will introduce the recently discovered lipid-independent metabolic pathway that originates from the endogenously synthesized inositol phosphates (Desfougères et al., 2019). Such background will help to better understand the function of *MINPP1*, the PCH-causing gene identified in this study.

### 4.1.1 Lipid-dependent inositol phosphate metabolic pathway

The lipid-dependent inositol phosphate metabolic pathway uses lipid derived-$IP_3$ as a precursor for the generation of a wide variety of inositol phosphates (Irvine and Schell, 2001). Hence, this network begins with the synthesis of phosphatidylinositol (PI), resulting from the incorporation of the inositol into the cell-membrane via phosphatidylinositol synthase (PI-synthase) (Figure 19, Antonsson, 1997). The resulting IP is then phosphorylated by a set of kinases (i.e. 1-phosphatidylinositol 4-kinase (PI-kinase) and phosphatidylinositol-4-phosphate-5-kinase (PIP-kinase)), leading to the sequential formation of phosphatidylinositol-4-phosphate (PIP) and phosphatidylinositol-4,5-bisphosphate ($PIP_2$), respectively (Rameh et al., 1997; Roth, 2004). The latter serves as a precursor for $IP_3$ and diacylglycerol (DAG), generated by phospholipase-C (PLC) (Berridge, 1993; Hokin, 1985; Majerus, 1992; Mitsunori Fukuda and Katsuhiko Mikoshiba, 1997; Nishizuka, 1986). The majority of the PLC-generated $IP_3$ is then dephosphorylated sequentially by a set of phosphatases, including inositol polyphosphate 5-phosphatases (INPP5A) and inositol polyphosphate 1-phosphatases (INPP1), yielding the formation of the lower phosphorylated inositol phosphates: inositol 1,4-bisphosphate ($IP_2$) and inositol 4-monophosphate (IP), the latter being recycled back to inositol by inositol mono-phosphatase-1(IMPA1) (Connolly et al., 1987; Hermosura et al., 2000; Majerus et al., 1999; Verjans et al., 1994).

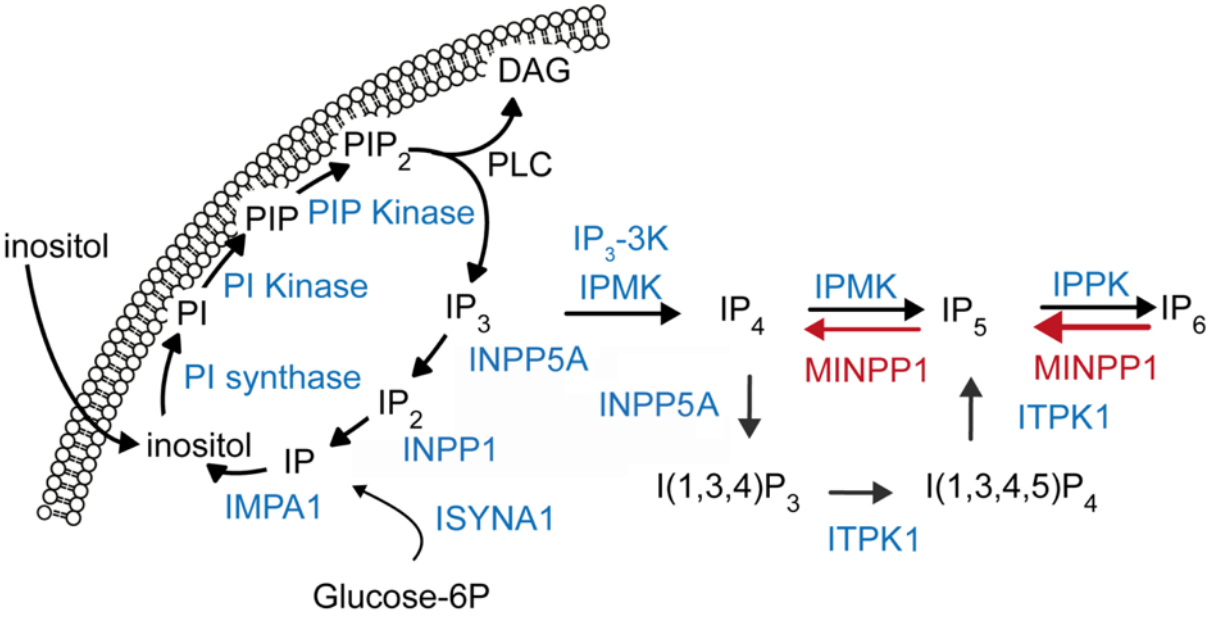


**Figure 19. Schematic representation showing the main enzymes and inositol phosphates involved in the lipid-dependent inositol phosphate metabolic pathway.** This pathway depicts the inositol phosphate synthesis and inositol cycle, originating from the incorporation of the inositol into the cell membrane**.** The thickness of the red arrow depicts the strength of the MINPP1 activity.

Alternative to the $PIP_2$-derived IP, in most mammalian cells, IP can also be de novo synthesized from glucose-6-phosphate (G6P) by inositol 3-phosphate synthase (ISYNA1), giving rise to inositol 3-monophosphate (I(3)P) (Donahue and Henry, 1981). Its further dephosphorylation by IMPA1, yields the production of endogenous inositol, which in turn enters to the lipid-dependent inositol phosphate metabolic cycle (Berridge and Irvine, 1989). For our interest, it is worth to mention that cortical neurons do not express ISYNA1 (Di Daniel et al., 2006). Thus, they acquire inositol solely from the extracellular fluid.

**ITPK1 and IPMK metabolic paths**

While PLC-generated $IP_3$ generates lower phosphorylated inositol phosphates, it also serves the basis for the synthesis of higher phosphorylated inositol phosphates, known as inositol polyphosphates (Figure 19). This is achieved via two main metabolic routes, known as ITPK1 and IPMK metabolic paths (Saiardi et al., 2018). The former starts with the phosphorylation of the lipid-derived $IP_3$ by inositol 1,4,5-trisphosphate 3-kinase (IP3-3K), yielding inositol 1,3,4,5-tetrakisphosphate ($IP_4$) (Batty et al., 1985; Irvine et al., 1986; Yang et

al., 1999). The resulting $IP_4$ is then catalysed by INPP5A, generating inositol 1,3,4-trisphosphate ($I(1,3,4)P_3$) (Connolly et al., 1987; Hermosura et al., 2000; Ramos et al., 2019). For our interest, it is worth nothing that INPP5A is highly abundant in the cerebellum and is involved in the progression of spinocerebellar ataxias type 17 (Liu et al., 2020).

INPP5A-generated ($I(1,3,4)P_3$) then serves as the main substrate for inositol-tetrakisphosphate 1-Kinase (ITPK1), synthesizing the 1,3,4,5,6-pentakisphosphate ($IP_5$), the most abundant $IP_5$ isomer in eukaryotic cells (Ho et al., 2002; Mitchell et al., 2008; Saiardi and Cockcroft, 2008). The resulting $IP_5$ can also be dephosphorylated by its producing-enzyme ITPK1 and by multiple inositol-polyphosphate phosphatase 1 (MINPP1), generating inositol 3,4,5,6-tetrakisphosphate ($I(3,4,5,6)P_4$) and inositol 1,4,5,6-tetrakisphosphate ($I(1,4,5,6)P_4$), respectively (Chi et al., 2000a; Ho et al., 2002; Mitchell et al., 2008; Saiardi and Cockcroft, 2008; Shears, 2009; Windhorst et al., 2013a).

As an alternate to the ITPK metabolic route, IPMK path occurs through the sequential phosphorylation of $IP_3$ by inositol-polyphosphate multikinase (IPMK), yielding $IP_5$ (Odom et al., 2000; Saiardi et al., 1999). Thus, while the ITPK1 and IPMK metabolic routes involve a different set of enzymes, both of them starts with the lipid-derived $IP_3$ and results in the production of $IP_5$.

The resulting $IP_5$, generated from either of these two pathways, serves as a substrate for inositol pentakisphosphate 2-kinase (IPPK), synthesizing the fully-phosphorylated and the most abundant inositol polyphosphate in eukaryotic cells inositol hexakisphosphate ($IP_6$) (Ives et al., 2000).While the further phosphorylation of $IP_6$ leads to the formation of the higher-phosphorylated inositol polyphosphates, known as inositol pyrophosphates, its dephosphorylation by MINPP1 generates inositol 1,2,4,5,6-pentakisphosphate ($IP(1,2,4,5,6)_5$) (Ali et al., 1993; Chi et al., 2000a; Stephens et al., 1993; Wilson et al., 2013; Windhorst et al., 2013). $IP_6$ is also shown to be catalysed *in vitro* by IP6 kinases (IP6Ks) through its 1-

phosphatase activity following a decrease in the cellular ATP/ADP ratio (Wundenberg et al., 2014). Nevertheless, MINPP1 remains as the primary-$IP_6$ catalysing enzyme *in vivo* (Chi et al., 2000).

Thus, given the number of enzymes and their respective metabolic activities, the lipid-dependent inositol phosphate metabolic pathway represents a complex network, relying mainly on exogenously-acquired inositol to produce the whole spectrum of inositol phosphates from inositol-lipid-derivatives. As of our interest, it is worth to note that among the enzymes involved in this pathway, MINPP1 is one of the least understood, owing to its predominant localization in the ER and its substrates predominantly in the cytosol (for more in depth discussion see section 5.4).

### 4.1.2 Lipid-independent inositol phosphate metabolic pathway

As an alternative to the network described above, Saiardi and his colleagues have recently identified the lipid-independent inositol phosphate metabolic route, originating from the endogenously synthesized IP (Figure 20, Desfougères et al., 2019). Indeed, the group has developed a novel strategy to differentiate the inositol phosphates derived from the two inositol sources (i.e. exogenously acquired and endogenously synthesized). This was achieved by analysing the differences in the inositol phosphate profile obtained through traditional inositol metabolic labelling [$^3$H], detecting the exogenous inositol source, and polyacrylamide gel electrophoresis (PAGE) mass assay, detecting the both inositol sources. Such experimental design revealed ITPK1 as the key enzyme involved in the conversion of G6P-derived-IP to higher phosphorylated forms. Hence, this study have provided important insights into the metabolism of endogenously produced IPs. Nevertheless, as cortical neurons cannot convert glucose to IP, due to the absence of ISYNA1, this metabolic network is not our priority in this study (Di Daniel et al., 2006).

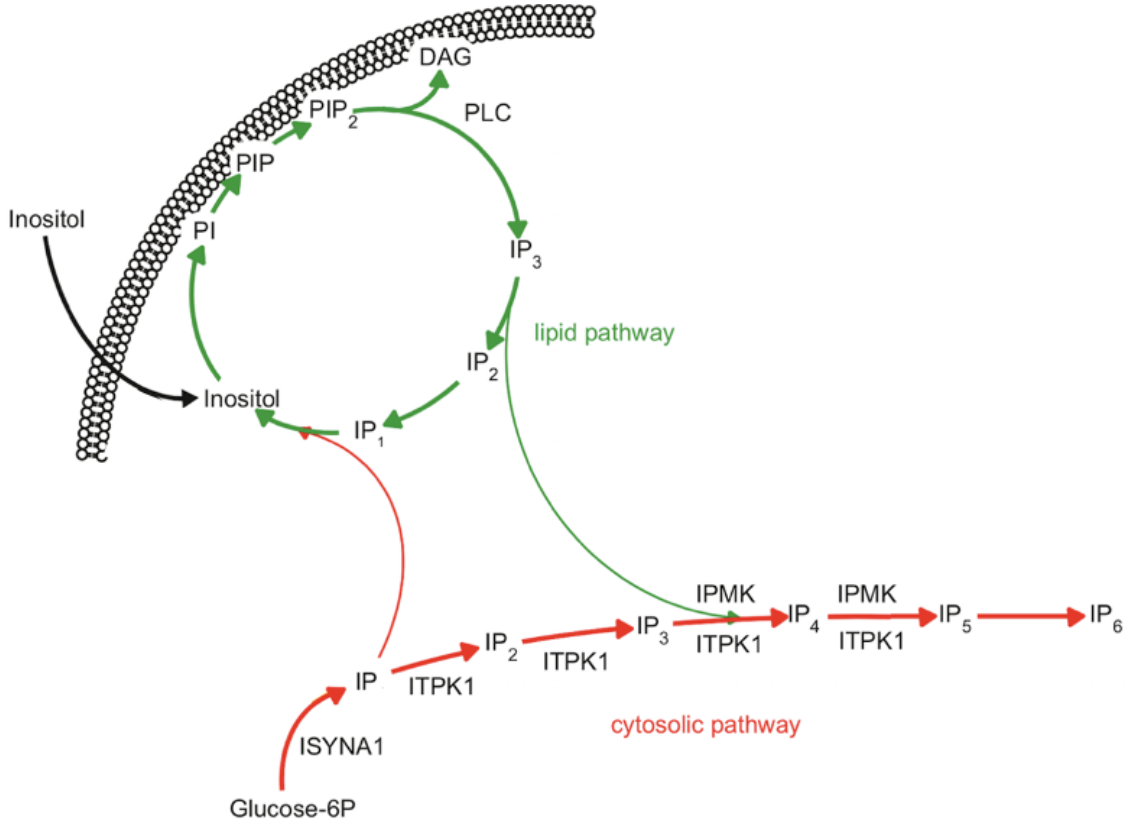


**Figure 20. Schematic representation of the lipid-independent inositol phosphate metabolic pathway (from Desfougères et al., 2019).** This pathway starts with the conversion of glucose-6 phosphate (G6P) to IP and continues with the synthesis of higher phosphorylated inositol phosphates by ITPK1.

## 4.2 The subcellular distribution of IPs in mammalians: focus on $IP_5$ and $IP_6$

In an attempt to better understand the physiological function and metabolic activity of inositol phosphates *in vivo*, various studies have sought to define the subcellular distribution of these soluble molecules. To this extent, a number of methods were developed to selectively permeabilize the cell membrane without disrupting the intracellular organelles in which inositol phosphates might be present (Michell et al., 1992; Stuart et al., 1993; Stuart et al., 1994). Regardless the method used, most of the inositol phosphates were released in parallel with cytosolic markers, suggesting that these soluble molecules are mostly concentrated in the cytosol. Interestingly, ≤10-20% of the $IP_5$ and $IP_6$ levels were shown to be retained following the release of all cytosolic markers, suggesting that a small percentage of these inositol polyphosphates might be present in other subcellular pools (Stuart et al., 1994). However, no

study has been able to identify such pools due to the technical challenges in assessing the inositol phosphate levels in each intracellular organelles. Nevertheless, several studies of inositol phosphate metabolism have suggested the presence of multiple intracellular inositol phosphates pools in mammalian cells. For instance, York and his group, have argued the presence of two metabolic reservoirs for $IP_5$ and $IP_6$ pools, including a stable one and the one that become accessible to inositol phosphate-metabolizing enzymes following G-protein activation (Otto et al., 2007). Moreover, recently, Saiardi and his colleagues have raised the possibility that lipid-dependent and independent inositol metabolic pathways might be compartmentalized differently (Desfougères et al., 2019). Furthermore, studies working on the subcellular distribution of inositol phosphate-metabolizing-enzymes have favoured the presence of different intracellular inositol phosphates pools. Indeed, while the majority of the enzymes are shown be cytosolic or membrane-bound facing the cytosol, some of them are found in other intracellular organelles such as the nucleus and the ER. For instance, while PLC, IPMK and IP6K-isoform-1 are shown to be both nuclear and cytosolic, IP6K-isoform-2 are found to be predominantly nuclear, suggesting the presence of inositol polyphosphates in the nucleus (Cocco et al., 2001; Malabanan et al., 2016; Nalaskowski et al., 2002; Resnick et al., 2005; Saiardi et al., 2001; York, 2006b). Moreover, the predominant localization of MINPP1 in to the ER lumen, has questioned the existence of intracellular ER pools for its substrates, being mainly $IP_5$ and $IP_6$ (Ali et al., 1993; Craxton et al., 1995). Indeed, in supportive to this proposition, our study has also favoured the presence of inositol phosphates in the ER, following the detection of altered inositol phosphate levels in *MINPP1* mutant cells.

Thus, while inositol phosphates have been considered mainly as cytosolic in the mammalian cells, several studies have left open the possibility that inositol phosphates might be localized in multiple intracellular pools.

## 4.3 Inositol phosphates in brain physiology

Inositol phosphates influence almost every cellular processes, including proliferation, calcium signalling and ion channel regulation (Irvine and Schell, 2001). They are particularly important for the brain, owing to their involvement in various key processes during brain development and function. As a consequence, imbalance in the brain inositol levels has been reported in various brain disorders, further implying an important role for inositol and its downstream effectors in brain physiology. For instance, altered inositol levels have been detected in the brains of patients with schizophrenia, Down syndrome, Alzheimer's disease (AD), bipolar (BPD) and autism spectrum disorder (ASD) (Berry et al., 1995; Davanzo et al., 2001; Frey et al., 1998; Friedman et al., 2003; Griffith et al., 2008; Kato et al., 1991; Kato et al., 1994; McLaurin et al., 1998; Moore et al., 1999; Rumpel et al., 2003; Shimohama et al., 1998; Shimon et al., 1997; Shimon et al., 1998; Vasconcelos et al., 2008; Wellard et al., 2003; Yildiz et al., 2001). Moreover, inositol deficiency during embryogenesis has been shown to cause neural tube defects in rat and mouse (Cockroft, 1988; Cockroft et al., 1992). In addition, it is worth mentioning that the brain displays the highest inositol concentration (5–50 mM) in the human body, about 100 times higher than those in blood and other tissues, thus further suggesting its high demand for inositol and inositol-containing molecules (Michaelis et al., 1993). In light of these information, this section will first introduce in detail the known-physiological activities of $IP_3$ in a first part and then other key inositol phosphates in a second part during brain development and function.

### 4.3.1 $IP_3$ as an intracellular $Ca^{2+}$ mobilizer in the brain

As the best-well characterized inositol phosphate, $IP_3$ functions primarily as an intracellular $Ca^{2+}$ mobilizer in the brain, via $IP_3$-dependent-$Ca^{2+}$ signalling pathway (Figure 21). This pathway starts with the binding of an agonist (e.g. growth factors, neurotransmitters) to the G protein-coupled receptors (GPCR) or the protein tyrosine kinase-linked receptors

(PTKRs), which triggers the activation of PLC-β or PLC-γ1, respectively (Berninger et al., 1993; Cocco et al., 2015). The activated-PLC then metabolizes $PIP_2$ to form both DAG and $IP_3$, the latter mobilizing the intracellular calcium stores from the ER to the cytosol upon binding to $IP_3$ receptors ($IP_3$Rs) (Streb et al., 1983). In turn, $IP_3$-induced-$Ca^{2+}$ release generates transient increase in the cytosolic $Ca^{2+}$ concentration, leading to the formation of $Ca^{2+}$ spikes (Berridge, 1990; Berridge, 2007). The spatial and temporal activation of this signalling pathway over a longer period triggers a continuous series of $Ca^{2+}$ spikes, giving rise to $Ca^{2+}$ oscillations that are vital for various dynamic processes during the brain development and function.

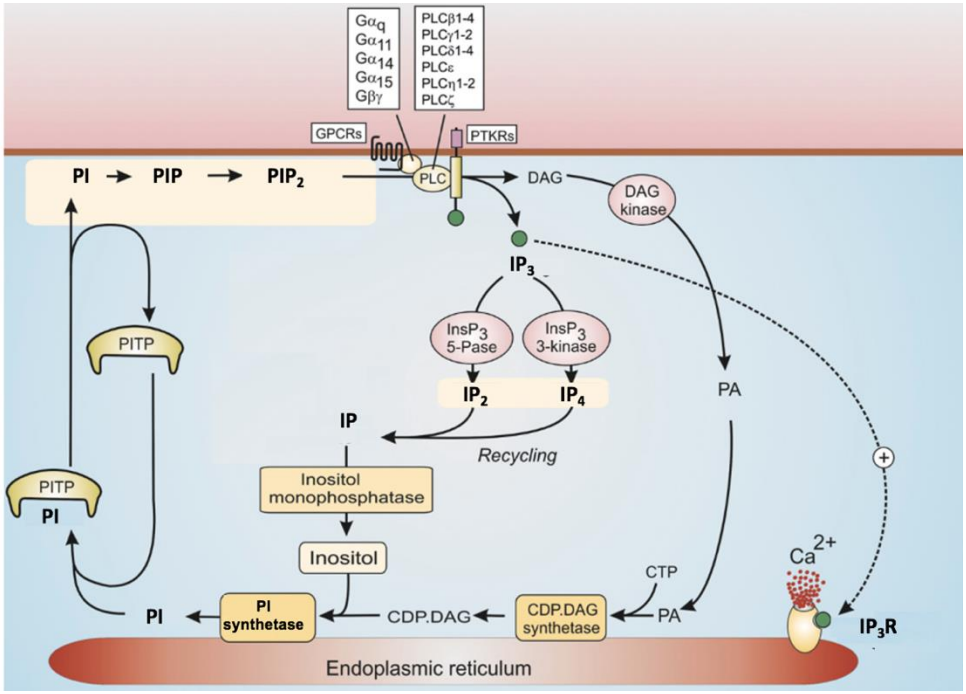


**Figure 21. Overview of the $IP_3$-dependent $Ca^{2+}$ signalling pathway (from Berridge, 2016).** The pathway starts with the activation of G protein-coupled receptors (GPCRs) or protein tyrosine kinase-linked receptors (PTKRs), which in turn stimulates different phospholipase C (PLC) isoforms, being PLC-β for the former and PLC-γ1 for the latter. Following stimulation, PLC synthesizes diacylglycerol (DAG) and $IP_3$ from phosphatidylinositol 4,5-bisphosphate ($PIP_2$). $IP_3$ then diffuses into the cytosol and binds to $IP_3$ receptors ($IP_3$Rs) to release $Ca^{2+}$ from the endoplasmic reticulum (ER), which in turn stimulates distinct downstream signalling pathways involved in different cellular processes, including proliferation, differentiation and migration. The $IP_3$-dependent $Ca^{2+}$ signalling pathway is maintained through the recycle of both $IP_3$ and DAG. While the recycle of $IP_3$ enables the supply of inositol required for the synthesis of phosphatidyl inositol (PI), the recycle of DAG back to its precursor (i.e. cytidine diphosphate diacylglycerol (CDP-DAG)) allows the reformation of PI and then $PIP_2$, the latter being the substrate of PLC. Abbreviations: (PA), phosphatidic acid; (PITP), phosphatidylinositol transfer proteins (PITPs).

**Roles of $IP_3$-dependent $Ca^{2+}$ signalling during the brain development**

$IP_3$-dependent-$Ca^{2+}$signalling regulates various neural developmental processes, including proliferation, neurogenesis, axonal and dendritic growth. For instance, during early neocortical development, PLC-γ1-$IP_3$-$Ca^{2+}$ cascade modulates the proliferation of radial glial cells by inducing spontaneous intercellular $Ca^{2+}$ waves along the ventricular zone (Weissman et al., 2004). As corticogenesis proceeds, PLC-β-$IP_3$-$Ca^{2+}$ pathway regulates the neurogenesis of radial glial cells by generating $Ca^{2+}$ oscillations in response to the neurogenic-inducer factor present in the cerebrospinal fluid (Takeo et al., 2016). In the course of axonal growth, PLC-γ1-$IP_3$-$Ca^{2+}$ signalling directs the turning of growth cone by increasing cytosolic $Ca^{2+}$ concentration at the proximal side of the guidance cues, such as nerve growth (NGF) and brain-derived neurotrophic factor (BDNF)) (Akiyama et al., 2009; Li et al., 2005). Furthermore, during postnatal brain development, NGF-activated PLC-γ1-$IP_3$-$Ca^{2+}$ signalling enhances dendritic growth by elevating $Ca^{2+}$ levels at the site of the dendritic branch points (Koizumi et al., 1999).

**Roles of $IP_3$-dependent $Ca^{2+}$ signalling in neuronal activity**

$IP_3$-dependent-$Ca^{2+}$ signalling influences multiple neuronal activities, including neuronal excitability, synaptic transmission and plasticity. Indeed, following activation by D2 dopaminergic or metabotropic glutamate G-protein-coupled receptors (mGLURs), PLC-β-$IP_3$-$Ca^{2+}$ cascade modulates the activity of L-type voltage-gated calcium channels and thus contributes to the generation of action potential in various neurons, such as cerebellar granule cells, neocortex pyramidal cells, striatal neurons (De Waard et al., 1992; Hernádez-López et al., 2000; Yamamoto et al., 2005). Moreover, in hippocampal neurons, this signalling cascade regulates the function of post-synaptic AMPA receptors by modulating the post-synaptic $Ca^{2+}$ dynamics (Bashir et al., 1993; Harvey and Collingridge, 1992; Kelly et al., 2005). Furthermore, PLC-γ1-$IP_3$-$Ca^{2+}$ signalling enhances BDNF-induced neural activity and synaptic plasticity in

various neurons, including cerebellar granule cells and CA1 pyramidal neurons (Amaral and Pozzo-Miller, 2007; Li et al., 1999; Pradhan et al., 2019).

**Roles of $IP_3$-dependent $Ca^{2+}$ signalling in the brain function**

$IP_3$-dependent-$Ca^{2+}$ pathway contributes to many brain functions, including memory and brain rhythms. Indeed, it regulates memory formation in various neurons (e.g. Purkinje cells, hippocampal mossy fibres and prefrontal cortex neurons) by activating the long-term depression (LTD), a process by which synaptic connections between neurons weakens in an activity-dependent manner (Brennan et al., 2008; Hernjak et al., 2005; Inoue et al., 1998; Yamazaki et al., 2011). Furthermore, during sleep-wake cycles, PLC-β-$IP_3$-$Ca^{2+}$ signalling cascade regulates brain rhythms by enhancing the activity of $Ca^{2+}$-activated-non-selective-cation channels (CANs) in reticular activating system (RAS) (Berridge, 2014; Partridge and Valenzuela, 1999).

**Brain disorders associated with altered $IP_3$-dependent-$Ca^{2+}$ signalling**

Notably, in supportive to the above background, alterations in $IP_3$-dependent-$Ca^{2+}$ signalling are involved in the onset of many brain disorders, including AD, Huntington's disease (HD), spinocerebellar ataxia (SCA), epilepsy, schizophrenia, and ASD. For instance, in AD, enhanced $IP_3$-dependent-$Ca^{2+}$ signalling activity leads to an excessive activation of LTD, resulting in the memory loss (Demuro and Parker, 2013; Ferreiro et al., 2004; Jensen et al., 2013). Moreover, in HD and many forms of SCA, altered sensitivity of IP3Rs leads to an abnormal elevation in the cytosolic $Ca^{2+}$ levels, contributing to the synaptic loss and progressive neurodegeneration in striatal neurons and Purkinje cells, respectively (Bauer et al., 2011; Bezprozvanny, 2011; Brown and Loew, 2015; Fedorenko et al., 2014; Schorge et al., 2010; Tang et al., 2003). For the scope of this study, it is interesting to note that a single variant in type-1 IP3R (*ITPR1*) has been identified in a patient with PCH, suggesting also the involvement of $IP_3$-dependent calcium in PCH aetiology (van Dijk et al., 2017). Moreover,

during epileptic seizures, a large release of glutamate triggers an enhanced $IP_3$-dependent-$Ca^{2+}$signalling, leading to imbalances in the activity of excitatory and inhibitory neurons (DeLorenzo et al., 2007; Nagarkatti et al., 2008; Pal et al., 2001). Meanwhile, in schizophrenia, abnormal expression of PLC-β leads to a decline in $IP_3$-dependent-$Ca^{2+}$ signalling activity, altering the brain rhythms (Park et al., 2015). Lastly, a marked decline in $IP_3$-dependent-$Ca^{2+}$ mobilization resulting in an abnormal formation of synapses has been observed in AD (Gilman et al., 2011; Ma et al., 2013; Schmunk et al., 2015).

Indeed, taken together, $IP_3$-dependent-$Ca^{2+}$ signalling participates in various aspects of brain development and function and consequently subtle changes in its activity lead to severe disease states. Thereby, $IP_3$ is vital for maintaining proper brain physiology.

### 4.3.2 The role of other inositol phosphates in the brain physiology

In contrast to $IP_3$, relatively few studies have explored the functional role of inositol polyphosphates in the brain, leaving an incomplete picture of their action in the brain physiology. In this regard, the following part of this section will first introduce the suggested $IP_4$-based signalling in neurons. Next, it will explain the physiological events that are associated with changes in $IP_5$ and $IP_6$ levels during brain development and neuronal activity. The explanation of the latter will be particularly important for this study, as $IP_5$ and $IP_6$ are known to be the main substrate of *MINPP1*, PCH causing gene identified in this study.

**$IP_4$ in brain physiology**

$IP_4$ has been proposed to modulate ion channel activation in neurons, however the physiological significance of this modulation has remained elusive. For instance, early *in vitro* studies in hippocampal CA1 pyramidal neurons have suggested that $IP_4$, the product of ITPKA, $IP_3$-3K isoform A, can activate voltage-gated calcium channels (VGCC) to induce long-term potentiation (LTP), a process by which synaptic connections enhances long-lastingly (Mailleux et al., 1991; Szinyei et al., 1999; Takazawa et al., 1990; Tsubokawa et al., 1996). However,

characterization analysis of *Ip3k*$^{-/-}$ mouse models have raised concerns regarding the physiological relevance of such regulation, as while one model showed enhanced LTP in the CA1 layer of the hippocampus with a 75% reduction in $IP_4$ levels, the other one displayed reduced LTP in the CA3 layer of the hippocampus via a mechanism independent of *Ip3k* kinase activity (Kim et al., 2009; Jun et al., 1998). Thereby, the physiological significance of $IP_4$-mediated-VGCC activation has remained elusive. Meanwhile, the $IP_4$ isoform, I(3,4,5,6)$P_4$, the substrate of ITPK1, is found to inhibit calcium-activated chloride channel 3 (CIC-3) in neonatal hippocampal neurons (Mitchell et al., 2008). However, no further study has explored the functional relevance of this regulation.

While, the functional role of $IP_4$ in the brain remains as a mystery, it should be mentioned that $IP_4$ is known to bind various proteins, including PKB and GTPase-activating proteins (GAPs), the latter known to be highly abundant in the brain (Cullen et al., 1995; Jia et al., 2007). Given their key role in multiple cellular processes (e.g. proliferation and apoptosis), it is likely that $IP_4$ plays as an important cofactor in various aspects of brain development and physiology (Kim et al., 2003; Tschopp et al., 2005).

**$IP_5$ and $IP_6$ in brain physiology**

Alterations in $IP_5$ and $IP_6$ levels have been found to be necessary for proper brain development, neuronal differentiation and survival. For instance, the initial data for the former emerged from embryonically lethal *Ipmk* knock-out (ko) mouse model that displayed various morphological defects, including abnormal neural tube folding (Frederick et al., 2005). In correlation with the role of Ipmk as an $IP_6$ synthesizing enzyme from $IP_3$, *Ipmk* knock-out ES cells exhibited almost complete ablation in $IP_5$ and $IP_6$ synthesis, without showing major alterations in $IP_3$-dependent $Ca^{2+}$ signalling. Thereby, these in vivo findings have suggested that $IP_5$ and $IP_6$ are important for early brain development. In correlation with this *in vivo* data, Saiardi and his group identified a potential role for $IP_5$ and $IP_6$ in early neuronal differentiation

by studying inositol phosphate metabolism and their synthesizing enzyme, IPPK, during early stages of neuronal differentiation of PC12 cells, a classical neuronal rat cell model (Loss et al., 2013). Interestingly, following exposure to NGF, PC12 cells displayed enhanced IPPK protein levels, followed by a robust increase in $IP_5$ and $IP_6$ levels. In correlation to these findings, knock-down of IPPK during first stages of neuronal differentiation resulted in neurite outgrowth defects in PC12 cells, which was rescued following overexpression of IPPK. Thereby, these findings indicate that changes in $IP_5$ and $IP_6$ levels are necessary for the early stages of NGF-mediated neuronal differentiation.

Interestingly, the same study also found that at later stages of neuronal differentiation, IPPK protein levels were reduced markedly in PC12 cells, to a level lower than the one in undifferentiated cells (Loss et al., 2013). Interestingly, PC12 and superior cervical ganglion (SCG) neurons transfected with IPPK showed axonal degeneration and nuclear fragmentation, whereas no signs of neurodegeneration were detected in neurons transfected with kinase-dead IPPK mutant. Thereby, these findings revealed that low $IP_5$-$IP_6$ synthesizing activity is essential for neuronal survival.

Hence, taken together, these studies suggest that $IP_5$ and $IP_6$ dynamics contribute to the proper brain development, early neuronal differentiation and survival. However, "how" remains as a question.

Moreover, several studies also proposed that alterations in $IP_6$ levels affect neuronal excitation and neurotransmission in hippocampal neurons (Yang et al., 2001; Yang et al., 2012). However, as these studies monitored the neuronal activity following intracellular injection of exogenous $IP_6$, the physiological significance of them remains uncertain (for more in depth discussion see section 4.5).

Altogether, inositol phosphates represent a wide family of signalling and regulatory molecules that are essential for proper brain development and function: $IP_3$ being a vital $Ca^{2+}$

mobilizer and inositol polyphosphates displaying a great potential to regulate various physiological processes in brain development, with many more yet to be discovered. To this extent, our study will contribute to a better understanding of the effect of MINPP1-dependent $IP_6$ levels in neuronal differentiation. Hence, for our interest, the next section will move on to explain the characteristics of $IP_6$, the main substrate of MINPP1.

## 4.4 $IP_6$: the most abundant inositol phosphate with unique characteristics

While the physiological role of $IP_6$ in the brain remains elusive, $IP_6$ is considered to be an important metabolite and signalling molecule in eukaryotic cells by virtue of its unique characteristics. For instance, $IP_6$ is the most abundant inositol phosphate in eukaryotic cells, with cellular concentrations reaching up to 100 μM in mammalian cells and 0.5mM in amoeba *Dictyostelium discoideum* (Bunce et al., 1993; Pisani et al., 2014; Szwergold et al., 1987). In plants, $IP_6$, known as phytic acid, accumulates in seeds and accounts for 65–90% of the total phosphorous content. It is also abundant in cereals and legumes, reaching up to 6.4% of their total weight (Harland and Oberleas, 1987; Reddy et al., 1982). Thereby, $IP_6$ is highly concentrated in eukaryotic cells and all edible-seeds used in food products.

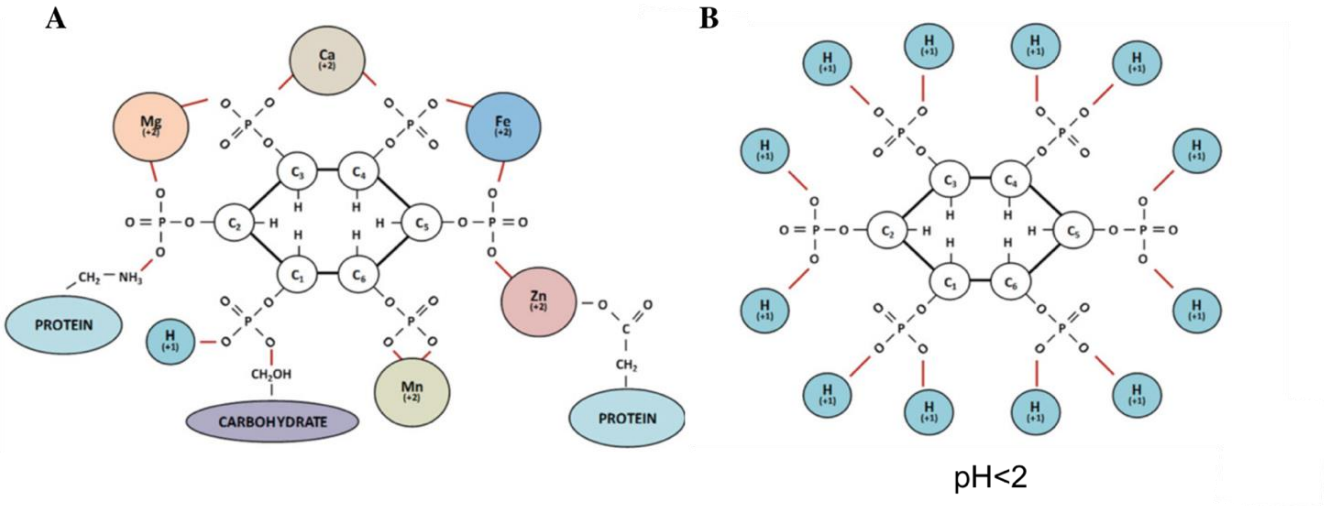


**Figure 22. Molecular structure of $IP_6$ and its binding capacity (from Vieira et al., 2018). (A)** $IP_6$ is unique among inositol phosphates by virtue of its highly anionic characteristic, making $IP_6$ a strong chelator. It strongly binds divalent cations (e.g. $Ca^{2+}$, $Mg^{2+}$, $Fe^{3+}$, $Fe^{2+}$, $Zn^{2+}$), proteins, carbohydrates and $H^+$ ions. **(B)** In a highly acidic environment (pH<2), $H^+$ protons occupy all the $IP_6$ binding sites, rendering $IP_6$ with a less potential to bind other compounds.

Moreover, given its fully-phosphorylated form, $IP_6$ differs from other inositol phosphates by its highly polar and chemically stable nature. Indeed, these two characteristics enable $IP_6$ to form high-affinity complexes with polyvalent cations, including $Mg^{2+}$, $Ca^{2+}$, $Al^{3+}$, $Fe^{3+}$, $Fe^{2+}$ and $Zn^{2+}$ (Figure 22, Hawkins et al., 1993; Mali et al., 2006; Poyner et al., 1993; Torres et al., 2005; Veiga et al., 2006). However, the chemistry of these $IP_6$-cation complexes is poorly studied, hindering the complete understanding of their physiological relevance in cells. Nevertheless, the available biophysical data suggest that under cytosolic conditions, $IP_6$ is predominantly associated with $Mg^{2+}$ species, forming neutral complexes that remain soluble up to 49 μM (Torres et al., 2005; Veiga et al., 2006). Beyond this concentration barrier, all of the $IP_6$-cation complexes are expected to form insoluble precipitates at cytosolic pH and salt conditions (Torres et al., 2005; Veiga et al., 2006). Hence, any $IP_6$ in excess of 49 μM is assumed to exist in protein bound form (Veiga et al., 2006). Thus, $IP_6$ is recognized as a strong chelator for a variety of polyvalent cations whilst their physiological interactions remains elusive.

Another characteristic that makes $IP_6$ distinct from other inositol phosphates is its strong antioxidant ability. Indeed, $IP_6$ possesses a unique phosphate grouping at position 1, 2 and 3 (axial-equatorial-axial) that allows the formation of specific interactions with iron, inhibiting its capacity to catalyse the production of hydroxyl radicals (Hawkins et al., 1993). Thereby, $IP_6$ is a natural antioxidant, impeding formation of radical oxygen species (ROS) (Graf and Eaton, 1985; Vucenik and Shamsuddin, 2006).

Taken together, $IP_6$ possesses unique characteristics by virtue of its cellular abundance, strong chelating and antioxidant nature.

## 4.5 Roles and mode action of $IP_6$ in mammalian cells

Unravelling the cellular role of $IP_6$ has been challenging due to difficulties in providing physiologically relevant experimental conditions for the study of this highly polar and abundant inositol phosphate molecule (Shears, 2001). Nevertheless, $IP_6$ has been shown to influence a wide range of unconnected cellular processes, including exocytosis, endocytosis, $Ca^{2+}$ channel regulation, cell cycle progression, ubiquitylation, RNA editing, mRNA export and DNA repair (Monserrate and York, 2010; Shamsuddin and Bose, 2012). Moreover, an extensive number of studies have argued the beneficial effects of dietary $IP_6$ in various pathological conditions, including cancer, liver injury, diabetes, kidney stone formation, calcification and Alzheimer's pathology (Anekonda et al., 2011; Bhowmik et al., 2017; Brehm and Windhorst, 2019; Lee et al., 2006; Shamsuddin and Bose, 2012; Taylor et al., 2004; Vucenik and Shamsuddin, 2006). However, its contribution to the majority of these physiological and pathological processes still remains doubtful and unclear due to various concerns, including experimental artefacts, poorly studied cellular mechanisms and controversies in the $IP_6$ field. Within this background, this section will start by introducing the proposed physiological roles of $IP_6$ in mammalian cells. Subsequently, it will explain the controversy in the field regarding the mode of action of $IP_6$ in treatment of pathological conditions. This explanation will be helpful to understand why our study have particularly avoided the use of exogenous $IP_6$ while investigating the inositol phosphate metabolism in *MINPP1* mutant cells.

**Proposed role of $IP_6$ in endocytosis and exocytosis**

Studies using intracellular $IP_6$-microinjection assays, have suggested that $IP_6$ plays a role in exocytosis and endocytosis by binding and regulating the activity of various proteins involved in vesicle-trafficking, including synaptotagmin-1, dynamin-1 and adaptors of clathrin-mediated endocytosis (Høy et al., 2002; Høy et al., 2003; Larsson et al., 1997; Sasakawa et al., 1993; Yang et al., 2012). However, interpretation of these findings remains

challenging due to the potential experimental artefacts arising from $IP_6$ micro-injection assays, such as ion chelation and non-specific association of $IP_6$ with proteins in response to physiologically irrelevant environment created following $IP_6$ injection (Shears, 2001). In addition to these concerns, another challenge faced by these studies is the uncertainty in the specificity of the $IP_6$ action (Shears, 2001). Indeed, they failed to consider the possibility that other inositol phosphates or inositol lipids can compete for $IP_6$-protein binding sites and thereby regulate vesicle-trafficking activity. Hence, the functional significance and specificity of the role of $IP_6$ in endocytosis and exocytosis remain doubtful and incomplete.

**The potential role of $IP_6$ in cell cycle progression**

Changes in intracellular $IP_6$ levels have been shown to influence cell cycle progression. For instance, upon stimulation of rat thymocytes with concanavalin-A, an inducer of thymocyte proliferation, a rapid and transient increase in $IP_6$ and $IP_5$ levels were detected by HPLC analysis (Guse et al., 1993). The concentration of both of these inositol polyphosphates remained constant during the S phase, followed by a long-term increase during G2 and M phases. Interestingly, during both of these cell cycle phases, the biosynthesis of $IP_6$ was recorded to be higher than that of $IP_5$. Nevertheless, these data have suggested that $IP_6$ and $IP_5$ may be necessary for proper cell cycle progression in rat thymocytes. However, the underlying mechanism and contribution of $IP_6$ per se remain unknown.

**The potential role of $IP_6$ in ubiquitylation**

$IP_6$ has been suggested to modulate the activity of cullin-RING ligase family (CRLs), responsible for the one-fifth of the mammalian ubiquitylation (Scherer et al., 2016). Indeed, coimmunoprecipitation assays found that IPPK (i.e. $IP_6$ synthase) binds to cullins, including Cul1 and Cul4A. Interestingly, knockdown of IPPK in HEK cells, abolished the binding of these cullins to their inhibitors, known as CSN2. In correlation with the role of IPPK as an $IP_6$ synthase, this binding defect was rescued by the addition of $IP_6$ into cell lysates, suggesting a

potential regulatory role for $IP_6$ in stabilizing the cullin-CSN2 assembly. However, the physiological consequence of this modulation remains to be elucidated.

**The potential role of $IP_6$ in RNA editing and mRNA export**

Promising studies have favoured the role of $IP_6$ in RNA editing and mRNA export as a cofactor. For instance, ion electrospray mass spectrometry and crystal structure analysis revealed that $IP_6$ binds to the core catalytic domain of RNA editing enzymes: ADAR2 and ADAT1 (Macbeth et al., 2005). Interestingly, ADAR2 and ADAT1 proteins expressed in *ipk1Δ* yeast mutant, lacking $IP_6$ production, failed to edit *in vitro* their mRNA and tRNA substrates, respectively (e.g. glutamate receptor B pre-mRNA and adenosine 37 in tRNA). Thereby, these data highlighted the potential role of $IP_6$ in mRNA and tRNA editing.

Moreover, $IP_6$ has been also shown to participate in mRNA export following its binding to Gle-1, a key mRNA export factor. In yeast, this interaction has been shown to enhance the activation of the DEAD-box protein Dbp5, an ATPase providing directionality to the messenger ribonucleoprotein (mRNP) (Alcázar-Román et al., 2006; Weirich et al., 2006). Indeed, a recent study revealed that this regulatory cascade is also conserved in human cells (Adams et al., 2017).

**The potential role of $IP_6$ in DNA repair machinery**

Interestingly, via a mutational analysis, $IP_6$ binding sites are also identified in Ku heterodimer (Ku70/Ku80), the main component of the non-homologous end-joining (NHEJ) pathway involved in double strand repairing mechanism (Cheung et al., 2008; Hanakahi et al., 2000). Subsequently, Ku $IP_6$-binding mutants were shown to display impaired *in vitro* NHEJ activity, suggesting that $IP_6$ may be necessary for efficient NHEJ (Cheung et al., 2008). However, whether such mechanism exists *in vivo* remains unknown.

Taken together, while $IP_6$ has been suggested to play a role in various cellular processes, it remains unclear whether $IP_6$ per se participates in these processes *in vivo.*

**Mode of action of extracellular $IP_6$**

In addition to the suggested cellular roles mentioned above, an extensive field of research has reported the beneficial effects of dietary $IP_6$ in treatment of various pathological conditions, including cancer, liver injury, diabetes, kidney stone formation, calcification and Alzheimer's pathology, the former being the most studied (Anekonda et al., 2011; Bhowmik et al., 2017; Brehm and Windhorst, 2019; Lee et al., 2006; Shamsuddin and Bose, 2012; Taylor et al., 2004; Vucenik and Shamsuddin, 2006). For instance, a large number of study found that exogenous supply of $IP_6$ at high concentration (≥70 μM) prevents cancer cell growth *in vitro* and *in vivo* (Brehm and Windhorst, 2019; Shamsuddin and Bose, 2012). Furthermore, such growth inhibitory effect was shown to influence multiple signalling pathways (e.g. PI3K/Akt, TGF-β, NF-κB, EGFR, IGF-1, PKC, VEGF), expression of various tumour suppressor and cell-cycle genes (e.g. p53, p21, p27, Rb) and many cellular processes (e.g. telomerase activity, proliferation, apoptosis, cell adhesion and migration). However, the mode of action of $IP_6$ per se has remained doubtful due to the following observation and findings: (1) First of all, $IP_6$ cannot diffuse across the cell membrane due to its high polar structure. (2) Furthermore, no $IP_6$ transporters have been identified so far. Indeed, in support of these observations, a highly specific and sensitive assays (i.e. enzyme-based-$IP_6$ mass assay and $TiO_2$-purification of inositol polyphosphates) detected no $IP_6$ in the human plasma and urine (Letcher et al., 2008; Wilson et al., 2015). More importantly, key studies feeding rats with [$^3$H]-$IP_6$ showed its hydrolysis in the gut and detected only [$^3$H]-inositol and [$^3$H]-IP in the plasma and urine (Eiseman et al., 2011; Sakamoto et al., 1993; Wise and Gilburt, 1982). In line of these observations, currently, two possible models have been suggested for the anti-cancer effects seen following the supply of exogenous $IP_6$: (1) $IP_6$ can serve as a source of inositol following its hydrolysis in the gut by phytases, the bacteria homologue of MINPP1. Indeed, in supportive to this model, various studies have showed that inositol and $IP_6$ display a comparable tumour-

growth inhibitory activity, highlighting the anti-cancer capacity of the inositol (Fu et al., 2016; Vucenik and Shamsuddin, 2006; Vucenik et al., 1995). (2) Or else, $IP_6$ can act as a strong chelator of minerals. Thereby, high concentrations of $IP_6$ can deplete key cations in the cell culture medium and in the gut (Brehm and Windhorst, 2019; Letcher et al., 2008; Wilson et al., 2015; Windhorst et al., 2013). Hence, both of these models clearly pointed out that secondary effects are responsible for the observed anti-cancer effects rather than the $IP_6$ per se. Consequently, this observation has also raised concern as to the physiological relevance of the studies that use extracellular $IP_6$ to investigate the role of $IP_6$ in cellular physiology. To this extent, in our study we have particularly avoided using extracellular $IP_6$ while studying the role of MINPP1 inositol phosphate metabolism, unlike the previous report that took an $IP_6$ inositol phosphate labelling strategy while studying this inositol polyphosphatase (Windhorst et al., 2013).

Altogether, having introduced inositol phosphates with a particular focus on $IP_6$, the last section will move on to MINPP1 in an effort to better understand the physiological function of this enzyme.

# CHAPTER FIVE: MINPP1

## 5.1 *MINPP1*: transcripts, isoforms and protein domains

As a PCH-causing gene identified in this study, *MINPP1* localizes to chromosome 10q23.3 and encodes three transcripts, each giving rise to one protein isoform (Figure 23A). The transcript-variant-1, NM_004897.5, contains all the five exons of *MINPP1* and translates into the longest protein isoform of 487 amino acids. The transcript variant-2 encodes a protein isoform with distinct C-terminus of 312 amino acids. And, the transcript variant-3 contains a distinct N-terminus of 286 amino acids. Among these three transcripts, the transcript-variant-1 is the mostly expressed (based on GTEx). Hence, the rest of the thesis will focus on the transcript-variant-1 and its protein isoform and thereby for simplicity will use "*MINPP1* and MINPP1" to refer to these two terms, respectively.

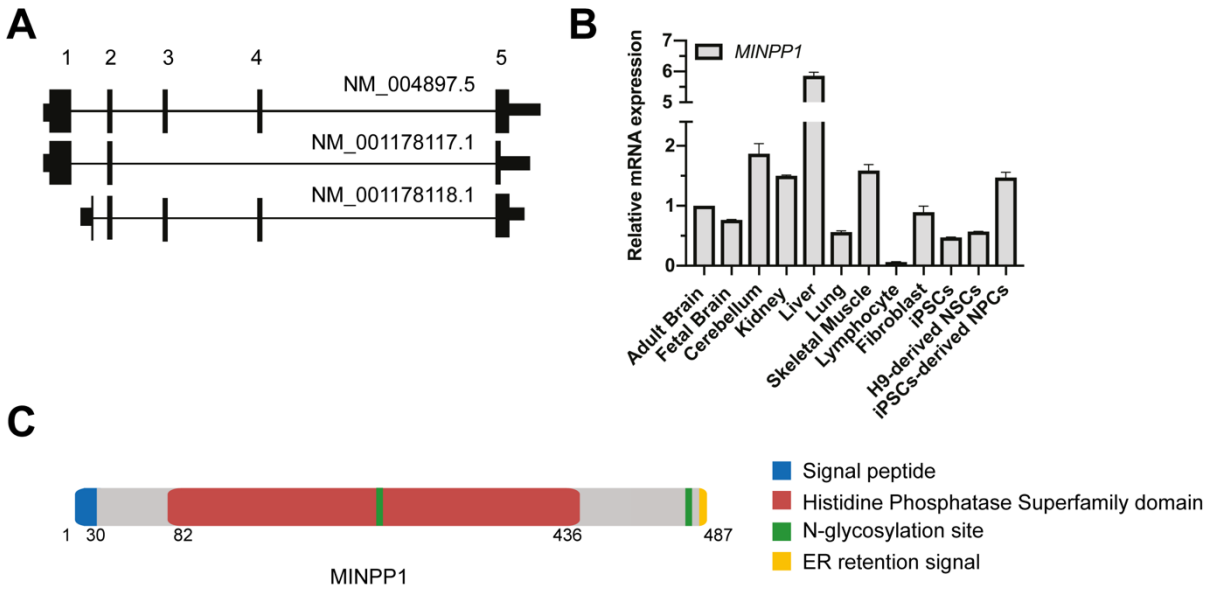


**Figure 23. Schematic representation of the *MINPP1* transcripts and MINPP1 protein. (A)** Transcript variants NM_004897.5, NM_001178117.1 and NM_001178118.1 are depicted, respectively. Exon numbers for the longest isoform NM_004897.5 are indicated above the schematic representation. **(B)** Quantitative PCR analysis of *MINPP1* expression, normalized with *ACTB*, in human cells and tissues. **(C)** Predicted protein domains of MINPP1, the protein isoform of the transcript NM_004897.5. Abbreviations used: Neural Stem Cells (NSCs); Neuronal Progenitor Cells (NPCs).

*MINPP1* is widely expressed in the developing and adult mouse, and rat, as well as in human tissues (Chi et al., 1999; Chi et al., 2000a; Craxton et al., 1997, Figure 23B). MINPP1 has two main functional domains that provide important insights into its distinct features among inositol phosphates (Figure 23C). For instance, unlike other inositol phosphate-related phosphatases, MINPP1 contains the conserved RHGXRXP histidine phosphatase motif and hence is a member of the histidine phosphatase superfamily. Within this family, it falls into the same branch as phytases, the bacteria homologue of MINPP1, based on the sequence homology, common evolutionary origin and functional similarity in the hydrolysis of $IP_6$ (Caffrey et al., 1999; Kilaparty et al., 2014; Rigden, 2008). Thus, these characteristics predict MINPP1 as an $IP_6$-phosphatase.

Apart from the histidine phosphatase motif, MINPP1 is also unique among inositol phosphate-related enzymes by the presence of KDEL-ER retention motif at its C terminal. This motif allows proteins to be retained in the ER by a retrieval mechanism mediated by KDEL receptors present on vesicles shuttling between the ER and the cis-Golgi. Thus, the presence of such motif in MINPP1 predicts its subcellular localization to the ER lumen (Chi et al., 1999; Kilaparty et al., 2014, for more in depth discussion see section 5.4). In addition to these two motifs, MINPP1 has also two N-linked glycosylation sites, whose functional significance remains unknown.

Thus, at first glance, these protein domains describe this enzyme as an ER-resident $IP_6$-phosphatase.

## 5.2 Evolutionary relationship of MINPP1

In an attempt to assess whether the predicted features of MINPP1 possess functionally-relevant evolutionary patterns, various studies focused on unravelling the evolutionary relationship of MINPP1 (Caffrey et al., 1999; Chi et al., 1999; Kilaparty et al., 2014). Indeed, in a seminal study, Kilaparty and her colleagues revealed the wide distribution of MINPP1

across a broad range of taxa by identifying homologous MINPP1 sequences from 40 species (Kilaparty et al., 2014). The phylogenetic tree constructed based on these homologous sequences revealed two major clades, representing the lower and higher organisms, respectively. Indeed, while lower organisms (e.g. bacteria, fungi, plants and insects) appeared to be more closely related to each other, they displayed only 20-30% sequence similarity with their human homolog (Figure 24). In contrast, higher organisms (e.g. amphibians, fish, birds and mammals) showed higher divergence among themselves, with a relatively higher sequence similarities with MINPP1, being 50-90%. Despite these differences in evolutionary pattern between the lower and higher organisms, RHGXRXP histidine phosphatase motif appeared to be fully conserved among all of the 40 species examined, revealing MINPP1 as a highly conserved histidine phosphatase.

Meanwhile, KDEL retention motif were shown to be highly conserved solely in higher organisms, with the few exceptions of *Danio rerio* and *Hydra magnipapillata*, in which KDEL is varied into RNTEL and KKTEL, respectively. Thus, such conservation pattern reveals the evolutionary adaptability of Minpp1 to an ER sub-localization.

In light of this phylogenetic context, the next section will focus on the discovery of MINPP1 in mammalians.




**Figure 24. Phylogenetic tree and multiple sequence alignment of MINPP1 from different species (from Kilaparty et al., 2014).** Dendrogram shows phylogenetic tree of MINPP1 homologous sequences from 40 species. The tree is clustered into two cladograms, revealing divergence in MINPP1 sequence homology between lower and higher organisms.

## 5.3 Back in 90's: From I(1,3,4,5)$P_4$ 3-Phosphatase to MINPP1

The discovery of $IP_3$ as a $Ca^{2+}$ mobilizing second messenger in 1983, has ignited an explosion of interest in enzymes involved in $IP_3$ metabolism (Irvine and Schell, 2001; Streb et al., 1983). Among these enzymes, I(1,3,4,5)$P_4$ 3-phosphatase has received a particular attention in the early 1990's for its potential role in regulating $IP_3$ levels. Various cell-free systems have been shown to metabolize I(1,3,4,5)$P_4$ to $IP_3$, suggesting the presence of I(1,3,4,5)$P_4$ 3-phosphatase in multiple cell-free extracts, including porcine brain extracts and human erythrocyte membranes (Coughney et al., 1988; Cullen et al., 1989; Cunha-Melo et al., 1988;

Dean and Moyer, 1988; Estrada-Garcia et al., 1991; Hodgson and Shears, 1990; Höer et al., 1988; Höer et al., 1990; Oberdisse et al., 1990; Shears, 1990). However, it's widely-varying enzyme activity in different mammalian cell-free extracts, raised concerns about its physiological significance (Hodgson and Shears, 1990; Shears, 1990). Shears' group provided a seminal explanation to these puzzling findings by identifying the two potent *in vitro* inhibitors of I(1,3,4,5)$P_4$ 3-phosphatase: $IP_5$ and $IP_6$ (Hughes and Shears, 1990). Given the high abundance of $IP_5$ and $IP_6$ in mammalian cells, this finding suggests that $IP_5$ and $IP_6$ contribute to the endogenous inhibition of I(1,3,4,5)$P_4$ 3-phosphatase activity in cell-free extracts. In a subsequent study, the same research group purified rat liver I(1,3,4,5)$P_4$ 3-phosphatase from its endogenous inhibitors and study its kinetic properties. Surprisingly, they found that I(1,3,4,5)$P_4$ 3-phosphatase display 3 and 400 fold higher affinity for I(1,3,4,5,6)$P_5$ and $IP_6$, respectively, than I(1,3,4,5)$P_4$ (Nogimori et al., 1991). Thus, these intriguing findings conclude that $IP_5$ and $IP_6$ are indeed *in vitro* substrates of the I(1,3,4,5)$P_4$ 3-phosphatase, rather than inhibitors. Thereupon, Shears and his colleagues suggested the term 'multiple inositol polyphosphate phosphatase' (MIPP) for the enzyme previously known as I(1,3,4,5)$P_4$ 3-phosphatase (Craxton et al., 1995). Later on, this original abbreviation is replaced with MINPP1, multiple inositol-polyphosphate phosphatase 1, along with increasing number of studies on this puzzling enzyme.

## 5.4 How MINPP1 meets its substrates *in vivo*?

### Early subcellular fractionation studies

The identification of three inositol phosphates as in *vitro* substrates of MINPP1, has raised a host of new questions about the physiological activity of this enigmatic enzyme in mammalian cells: Does MINPP1 have access to all the three substrates *in vivo*? If so, which of the three inositol phosphates is/are more likely to be the *in vivo* substrates of the enzyme? To provide answers to these questions, a number of studies aimed to initially identify subcellular

localization of MINPP1 in different cell types. By studying I(1,3,4,5)$P_4$ 3-phosphatase activity in human erythrocyte subfractions, Estrada and his colleagues detected the enzyme activity solely in saponin-permeabilised red blood cell ghost preparations, suggesting that MINPP1 is an integral membrane protein facing the cytoplasmic face of the human erythrocyte plasma membrane (Estrada-Garcia et al., 1991). Given the atypical characteristics of mature erythrocytes, devoid of nucleus and most organelles, Shears' group sought to assess the enzyme activity in rat liver subcellular fractions in order to better predict the localization of MINPP1 in most other cell types (Ali et al., 1993; Craxton et al., 1995). Indeed, unlike human erythrocytes, Shears and colleagues detected the highest I(1,3,4,5)$P_4$ 3-phosphatase activity in the soluble portion of the microsomal fraction, showing that rat hepatic MINPP1 majorly resides in ER lumen. As a molecular explanation to the latter biochemical data, subsequent cloning studies revealed conserved C-terminal ER retention motif in plant, chick and mammalian MINPP1 and thereby characterized MINPP1 as a luminal ER-resident protein (Caffrey et al., 1999; Chi et al., 1999; Craxton et al., 1997; Romano et al., 1998).

**Assessing the *in vivo* substrates of Minpp1 in a *Minpp1*$^{-/-}$ mouse model**

The distinct subcellular I(1,3,4,5)$P_4$ 3-phosphatase activity in human erythrocytes and rat hepatic cells have led to the question of whether both enzymes are encoded by *MINPP1*. To address this point, Chi et al. generated a knock out mouse model for *Minpp1* and studied the *in vitro* $IP_4/IP_5$ 3-phosphatase activity in *Minpp1*$^{-/-}$ mice erythrocyte and brain extracts (Chi et al., 2000). Interestingly, in both extracts, MINPP1 activity was undetectable, indicating that both plasma membrane and ER-based inositol polyphosphate phosphatase are encoded by *Minpp1*. Such intriguing finding has brought confusions over the physiological substrates of both membrane bound and ER-resident MINPP1 proteins, for the following two major reasons: Firstly, as mature erythrocytes do not synthesize inositol phosphates, due to a lack of an activated phospholipase-C, Chi et al.'s finding has impeded the understanding of how

membrane-bound-MINPP1 can dephosphorylate inositol polyphosphates in red blood cells. Secondly and more challengingly, the compartmentalization of the MINPP1 in ER in most of the other cell types have made it difficult to assess how this enzyme can gain access to the inositol polyphosphates pools that are known to be primarily located in the cytosol. Although no further studies have been conducted to resolve the former problem, apart from proposing 2,3-BPG as an alternative substrate for membrane-bound-MINPP1, Chi et al. focused on the latter issue and investigated whether inositol polyphosphates are indeed *in vivo* substrates of ER-resident MINPP1 (Chi et al., 2000; Cho et al., 2008). To this end, the group performed $^{3}$H-inositol metabolic labelling on wild-type and *Minpp1*$^{-/-}$ mouse embryonic fibroblasts (MEFs) and further resolved extracted-inositol phosphates with HPLC. Intriguingly, $IP_5$ and $IP_6$ were increased in *Minpp1*$^{-/-}$ MEFs, by 45 and 35%, respectively, compared to the wild type cells. To better assess the role of ER-resident-Minpp1 in inositol polyphosphate homeostasis, Chi et al. introduced a tagged version of Minpp1 into *Minpp1*$^{-/-}$ MEFs and confirmed the co-localisation of the exogenous Minpp1 with the ER marker ConA. Overexpression of Minpp1 in *Minpp1*$^{-/-}$ MEFs reduced $IP_5$ and $IP_6$ levels by 35 and 65%, respectively, thus restoring the inositol polyphosphate homeostasis. Hence, these seminal findings showed for the first time that ER-enzyme Minpp1 regulate $IP_5$ and $IP_6$ pools *in vivo* and these two inositol polyphosphates are physiological substrates of Minpp1 in MEFs (Chi et al., 2000), Figure 25). However, how the substrates can get access to this enigmatic ER-enzyme in murine cells has remained elusive.

**Subcellular fractionation studies of MINPP1 in a human cell line**

While the above question left unanswered, more than a decade later, with the increase number of studies working on the anticancer effects of extracellularly-added-$IP_6$, Mayr and his group reconsidered to study the intracellular distribution pattern of MINPP1 in a human carcinoma cell line: H1299 (Windhorst et al., 2013). By performing western-blot on different subcellular fractions, interestingly, they revealed the highest level of MINPP1 in the fraction

enriched with the Golgi marker “Golph”, while the second highest level was detected in the fractions containing ER, endosome and lysosome (Figure 25). The presence of MINPP1 in various organelles of the secretory pathway, prompted Mayr and his group to check if MINPP1 is secreted. Indeed, western blot analysis of cell culture medium of H1299 revealed a MINPP1 band that is 4kDA larger than the band detected in whole cell lysate. Mayr and his group then moved one step further and generated MINPP1 knock down H1299 cell lines to study the $IP_6$-phosphatase activities of both intracellular and secreted MINPP1. Instead of performing radioactive metabolic labelling, they treated both knock down and control cell lines with 30µM $IP_6$ and analysed intracellular and extracellular inositol phosphate levels with HPLC. Knock down cells displayed reduced intracellular $IP_5/IP_6$ ratio and intriguingly lower concentrations of extracellular $IP_3$ and $IP_2$, in comparison to the control cell lines. Based on these data, Mayr and his colleagues suggested distinct $IP_6$-phosphatase activities for intracellular and secreted version of MINPP1 in H1299 cell lines: the former mainly catalysing $IP_6$ to $IP_5$ and the latter majorly dephosphorylating extracellular $IP_6$ to $IP_3$ and $IP_2$ (Figure 25). This conclusion, however, was later challenged by the seminal study of Wilson et al., demonstrating the absence of $IP_6$ in human biofluids, thus raising great concerns about the physiological relevance of Windhorst et al.'s study (Wilson et al., 2015).

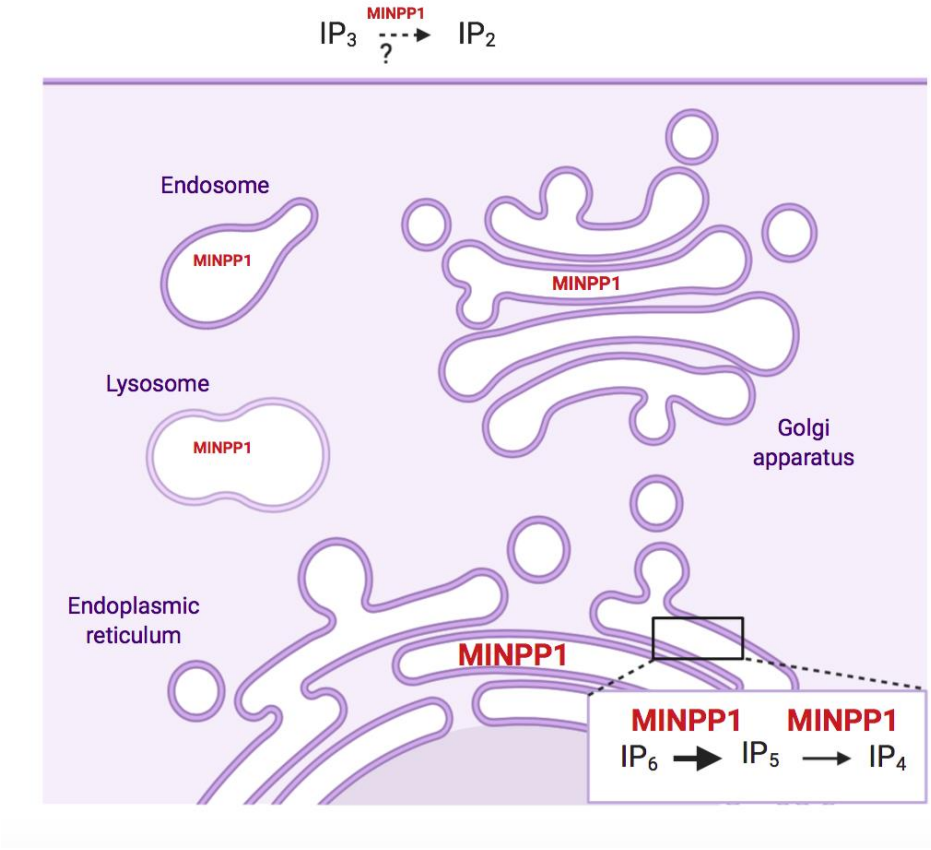


**Figure 25. Schematic representation of the proposed metabolic activity and subcellular localization of MINPP1 in mammalian cells.** Early subcellular fractionation studies in rat liver revealed Minpp1 as an ER-resident protein. In accordance, inositol labelling studies in mouse embryonic fibroblasts, found $IP_6$ and $IP_5$ as the main *in vivo* substrates of ER-resident Minpp1. Hence, Minpp1 is recognized as an ER resident protein responsible for the metabolism of $IP_6$ and $IP_5$. The thickness of the black arrow depicts the strength of the MINPP1 activity. Recently, subcellular fractionation studies in human carcinoma cell line found the presence of MINPP1 in the ER, Golgi and to a lower extent in the endosome and lysosome fractions. Meanwhile, western blot analysis revealed MINPP1 band in the cell culture medium of the human carcinoma cell line, proposing Minpp1 as a secretory protein. Furthermore, $IP_6$ inositol labelling studies suggested that secretory Minpp1 is responsible for the degradation of $IP_6$ to $IP_3$ and $IP_2$, respectively. However, the physiological relevance of this latter finding has been challenged by the absence of $IP_6$ in biofluids. The font size depicts the abundance of MINPP1.

Thereby, given the above discussion, much uncertainty still remains about the subcellular localization of MINPP1 and its access to its inositol polyphosphate substrates in mammalian cells, leaving a set of questions, including: Does MINPP1 display cell-type specific 3-phosphatase activities and subcellular pattern? Are there multiple intracellular or extracellular inositol polyphosphate pools in mammalian cells? Although addressing to each of these question is beyond the scope of this study, here we sought to better assess the cell-type specific

activity of MINPP1 by studying its metabolic activity in multiple human cell types, including fibroblasts, HEK293T cells, iPSCs and their neuronal differentiated counterparts.

## 5.5 Physiological Function of MINPP1

Despite the unclarity about how MINPP1 meets its substrates *in vivo*, the observation that MINPP1 is the only $IP_6$-phosphatase *in vivo* has suggested a fundamental physiological role for this enzyme. Thereby, many studies have explored the expression pattern of *Minpp1* and its protein levels during various physiological processes, including bone development, mouse embryogenesis and cellular stress responses (Caffrey et al., 1999; Chi et al., 2000a; Kilaparty et al., 2016; Reynolds et al., 1996; Romano et al., 1998). For instance, Minpp1 has been suggested to play a role in osteogenesis after its discovery in a differential display analysis of gene expression in chick growth plate chondrocytes (Caffrey et al., 1999; Reynolds et al., 1996). This initial finding was later supported by various *in situ* hybridization and immunohistochemistry analysis, detecting enriched Minpp1 mRNA and protein levels in lower proliferative and upper hypertrophic zone of chick and rat growth plates (Caffrey et al., 1999; Reynolds et al., 1996; Romano et al., 1998). Despite this high expression pattern, surprisingly, histological and molecular analysis revealed comparable bone development between *Minpp1*$^{-/-}$ and wild type mice, thereby leaving the physiological function of Minpp1 in chondrocytes as a mystery (Chi et al., 2000).

In addition to chondrocyte maturation, Minpp1 has also been questioned for its potential role in mouse embryogenesis following in situ hybridization analysis, showing enhanced *Minpp1* RNA levels in mouse visceral endoderm and foetal liver at stages E7.5-8 and E12.5-14.5, respectively (Chi et al., 2000). Surprisingly, notwithstanding the preceding, *Minpp1*$^{-/-}$ mice were viable and presented no major structural and physiological abnormalities over a 2-year follow-up period (Chi et al., 2000). Although *Minpp1*$^{-/-}$ mice awaits more thorough characterization, the absence of a detectable phenotype at first glance, has raised the possibility

of functional redundancy of murine Minpp1. Indeed, to this extent, Chi et al. revealed $IP_4/IP_5$ 3-phosphatase activity in *Minpp1*$^{-/-}$ erythrocyte extracts whose elution position differed from the one corresponding to Minpp1 in wild type extracts (Chi et al., 2000). The identification of such distinct enzyme activity has suggested for a potential compensatory mechanism for the loss of Minpp1. However, unlike in *Minpp1*$^{-/-}$ erythrocytes, Chi et al. could not detect such enzyme activity in other extracts of *Minpp1* deficient mice, including liver and brain (Chi et al., 2000). Hence, these data have argued that functional redundancy is unlikely to explain the lack of an obvious phenotype in *Minpp1*$^{-/-}$ mice. Interestingly, in our study, we have identified a mild brain phenotype in our *Minpp1*$^{-/-}$ mice model, a phenotype that was overlooked by Chi and his colleagues.

**MINPP1 as an apoptotic stress-response-protein**

The absence of a detectable phenotype in *Minpp1*$^{-/-}$ mice, have led to the question of whether Minpp1 loss can cause subtle phenotypic changes at cellular level. Kilaparty et al. addressed this issue by studying Minpp1 levels under various apoptotic stresses, following increased number of studies working on the apoptotic effects of extracellularly-added-inositol-polyphosphates (Agarwal et al., 2009; Kilaparty et al., 2016; Singh et al., 2003). Interestingly, Kilaparty et al. revealed increased Minpp1 levels in different mammalian cell lines, including PanC1, SW40 and MC3T3-E1, upon induction of apoptosis via a etoposide, wortmannin and ER-stress (Kilaparty et al., 2016). To further assess the correlation between Minpp1 and apoptosis, the group generated Minpp1 knock down MC3T3-E1 mammalian cell lines and measured etoposide-induced-apoptosis through the release of cytochrome-c from the mitochondria to the cytosol. Interestingly, in contrast to the control cells, no cytochrome-c was detected in the cytosolic fractions of *Minpp1* knock down cell lines, suggesting for a suppressed apoptosis. Along with the cytochrome-c data, caspase-3 activity was also reported to be unaffected in *Minpp1* knock down cell lines upon etoposide-induced-apoptosis. Thus, these

findings have suggested important insights into the distinct physiological role of Minpp1 as a apoptotic stress-response-protein. However, whether deregulation of such physiological function can lead to a pathological condition has remained totally elusive.

**Mipp1 in epithelial cell migration**

While the physiological function of Minpp1 in high order organisms has remained unclear, a seminal study in Drosophila identified a fundamental role for *mipp1* in epithelial cell migration during tracheal development (Cheng and Andrew, 2015). Indeed, fluorescent in situ hybridization analysis revealed enriched *mipp1* expression at the distal tip of migrating tracheal branches in an FGF-dependent manner. In correlation with this dynamic expression profile, *mipp1*$^{KO}$ embryos displayed perturbed tracheal morphogenesis with reduced number of filopodia, which is rescued by overexpressing minpp1 in *mipp1*$^{KO}$ embryos. As the underlying mechanism for this mipp1-mediated cell migration, Chen et al. proposed the ability of mipp1 to deplete extracellular $IP_6$ , previously shown as the *in vitro* blocker of FGF signalling (Morrison et al., 1994). However, whether such extracellular $IP_6$ pools exist in drosophila and, if yes, whether *mipp1*$^{KO}$ display an altered $IP_6$ extracellular levels during tracheal development remain totally ambiguous. Thereby, the question of how Minpp1 involves in tracheal cell migration of drosophila remains unanswered.

Overall, given the above literature, the physiological function of MINPP1 *in vivo* remains totally elusive. To this extent, our study has provided new insights into its physiological role during neuronal differentiation and brain development.

# CHAPTER SIX: AIM OF THE STUDY

This study aims to model a new subtype of Pontocerebellar Hypoplasia caused by a defect in a novel-disease causing gene: multiple inositol-polyphosphate phosphatase 1 (*MINPP1*). To achieve this aim, the study had the following objectives, each developed separately in the result section:

1) to describe the identification of *MINPP1* as a novel PCH type causing gene
2) to assess the effect of PCH-associated *MINPP1* mutations on protein stability, function and cellular physiology using HEK293T as a cellular model
3) to provide initial insights into the effect of loss of function of *MINPP1* on mammalian brain development by generating and studying a *Minpp1*$^{-/-}$ mice model
4) to investigate the effect of loss of function of *MINPP1* on PCH causing mechanisms using patient-derived and CRISPR-Cas9 mediated *MINPP1*$^{-/-}$ iPSCs

In a broader frame, this study aims to provide novel insights into the genetic, molecular and phenotypic spectrum by demonstrating for the first time the involvement of an abnormal inositol phosphate metabolism as a cause of PCH.

# MATERIALS AND METHODS

## 1. Patients recruitment and investigation

The patients from families CerID-09, CerID-11 and CerID-30 included in this project were referred to the Departments of Paediatric Neurology and Genetics of the Necker Enfants Malades Hospital. Family TR-PCH-01 was recruited by the French Reference Centre for Cerebellar Malformations and Congenital Diseases at Trousseau Hospital. Patients from families PCH-2456 and PCH-2712 were referred for neurological or genetic assessment at the National Research Centre in Cairo and Hacettepe University Medical Faculty Department of Paediatric Neurology in Turkey. Written informed consents have been obtained both from the participants and the legal representatives of the children.

## 2. Method for Sequencing, Variant Filtering and Prioritization

This part of the study has been carried out with the help of Nami Altin, Michael Nicouleau and the collaborators from the University of California San Diego and Sorbonne University.

### 2.1 Families CerID-09, 11 and 30:

Genomic DNA was extracted from peripheral blood cells. Exome capture was performed as previously described (Chemin et al., 2018; Megahed et al., 2016). Agilent Sure Select Human All Exon (54Mb Clinical Research Exome) libraries were prepared. Barcoded exome libraries were pooled and sequenced with a HiSeq2500 system (Illumina). After demultiplexing, sequences were aligned to the reference human genome hg19 using the Burrows-Wheeler Aligner (BWA). Variants were annotated and analysed using the Polyweb software interface designed by the Bioinformatics Platform of University Paris Descartes. Variants were filtered to less than 1% minor allele frequency in population databases and with MAF <0.001 in our sequenced cohort that include more than 15000 exomes. Manual curation of the known PCH genes (for the gene list see Chemin et al. Brain 2018) was first performed

to exclude a known genetic cause. Variants were then prioritized by the suspected mode of inheritance, OMIM status and *in silico* prediction tools (Mutation Taster (Schwarz et al. Nature Methods. 2014); SIFT and Polyphen (McLaren et al. Genome Biology. 2016); CADD score (Rentzsch et al. Nucleic Acids Res. 2018). Sanger sequencing of the patient and her parents was performed to confirm the variants and co-segregation using a 3500xl genetic analyser (4405633; Applied Biosystems).

### 2.2 Family TR-PCH-01

Patient TR-PCH-01-1 was part of a replication cohort of 100 patients with congenital or early-onset cerebellar defects that includes 21 PCH cases. This cohort was investigated using a targeted gene panel. This panel includes 184 known genes involved in congenital cerebellar anomalies (list available upon request), and 13 candidate genes, including *MINPP1*. Samples were prepared using Blood DNA and the SeqCap EZ Choice preparation kit (Roche) and sequenced on an Illumina MiSeq sequencer using 2 × 150 bp sequencing kits. The Basespace cloud computing platform (with BWA 2.1 and GATK Unified Genotyper 1.6) and the Variant Studio v.3.0 software provided by Illumina were used. Other known PCH genes were excluded for TR-PCH1-1. Pathogenicity of variants was ascertained according to the ACMG (American College of Medical Genetics) criteria. The segregation was confirmed by Sanger sequencing in the index case, both parents and unaffected sibling.

### 2.3 Families PCH-2456 and PCH-2712

Blood DNA was extracted using Qiagen reagents (Qiagen Inc., USA) and whole exome sequencing was performed on all affected family members using the Illumina HiSeq2500 which yields 100 bp paired-end reads covering 80% of the exome at 20X. GATK best practices pipeline was used for SNP and INDEL variant identification. Variants were prioritized by allele frequency (<0.1% MAF in our exome database of over 5000 individuals), conservation and predicted effect on protein function. The variants were predicted to be disease causing and were

absent from 1000 Genomes, ExAC and gnomAD. Sanger sequencing confirmed segregation according to a strict recessive mode of inheritance in all genetically informative and available family members.

### 3. Maintenance and Culture of iPSCs, Fibroblasts and HEK293 Cells

All human cell culture and storage protocols were performed with approval from French Research Ministry (DC 2015-2595, 09/05/2016) and all participants provided written consent. iPSC lines Ctrl-D10 and CerID-30-2 were generated by Duke iPSC Share Resource Facility, using RNA-based reprogramming method. CerID-30-2 and Ctrl-D10 were derived from unrelated individuals. Ctrl-D10 iPSC line was derived from BJ fibroblasts of a non-disease affected male new born (ATCC cell line, CRL-2522). The control iPSC line (IMAGINi004, referred to as Ctrl-I004 in this study) was generated by Imagine Institute iPSC Platform, using non-integrating Sendai virus approach (CytoTune-2.0). All iPSC lines were shown to display embryonic pluripotency markers OCT4, SOX2, SSEA-4 and TRA-1-81, no obvious chromosomal abnormalities (CGH array 60K, data not shown) and differentiate into mesoderm and endoderm lineage following embryoid body formation, assessed as previously described (Menara et al., 2020). Additionally, no obvious differences in proliferation and apoptosis were observed among all the iPSC lines. iPSCs were maintained in vitronectin-coated (10 µg/ml; 07180, STEMCELL) 3.5 cm dishes (353001, Falcon) in complete mTeSR-1 medium (STEMCELL, 85850) supplemented with 1% Penicillin-Streptomycin (PS) (15140122, Gibco) in a humidified incubator (5% $CO_2$, 37 °C). The media were replaced daily and iPSCs were mechanically passaged with ROCK inhibitor Y-27632 (10 µM; 72304, STEMCELL) every 7-8 days, with a 1:3 split ratio. Human primary fibroblasts and HEK293T (HEK293) cells were cultured in Dulbecco's modified Eagle medium (DMEM) (11965092, Gibco) supplemented with 10% Foetal Bovine Serum (FBS) (16000044, Gibco) and 1% PS in a humidified incubator (5% $CO_2$, 37 °C).

## 4. Generation of genome edited *MINPP1*$^{-/-}$ HEK293 and iPSCs

*MINPP1*$^{-/-}$ HEK293 and iPSC lines were generated via a CRISPR-Cas9 genome editing strategy, as previously described (Medina-Cano et al., 2018). Generation of *MINPP1*$^{-/-}$ HEK293 has been carried out by Daniel-Medina Cano. Briefly, sgRNAs targeting the first exon of MINPP1 transcript variant 1 (NM_004897.5) were designed on CRISPOR website (http://crispor.tefor.net/) and further cloned into the pSpCas9(BB)-2A-GFP plasmid (PX458, 48138, Addgene). For the generation of *MINPP1*$^{-/-}$ HEK293 clones, transfection of pSpCas9(sgRNA)-2A-GFP into HEK293 cells was performed with Lipofectamine 2000 (11668019, Invitrogen), as per manufacturer's instructions (2.5 µg of DNA per well of a 6-well plate). Two days post-transfection, single GFP$^{+}$ HEK293 cells were sorted into 96 well plates by Fluorescence-activated cell sorting (FACS) (BD FACSAria II SORP, BD Biosciences). Indel mutations of clones were detected by Sanger sequencing, and target editing efficiency was assessed by TIDE analysis (https://tide-calculator.nki.nl/; data not shown).

The following sgRNA resulted in the highest indel-editing frequencies (88-90%): 5'-CACCGTGAGAACTACGGCCGCCTGG-3'. Thereby, *MINPP1* KO HEK293 cell clones generated using this sgRNA were used for the experiments.

For the generation of *MINPP1*$^{-/-}$ iPSCs clones, transfection of pSpCas9(sgRNA)-2A-GFP into iPSC line (Ctrl-I004) was performed using Amaxa 4D-Nucleofector X-Unit (AAF-1002X, Lonza) according to manufacturer's instructions. The above-mentioned sgRNA is used for the generation of *MINPP1*$^{-/-}$ iPSCs clones.

Briefly, iPSCs were pre-treated with Y-27632 (10 µM) for 1 hour and further dissociated into single cell suspension with Accutase (STEMCELL, 07920). 4 x$10^{5}$ iPSCs were nucleofected per 20 µl nucleocuvette strip, using P3 Primary Cell 4D X Kit S (V4XP-3032, Lonza), 1µg DNA per reaction, and the program CA-137. After nucleofection, iPSCs were seeded on vitronectin pre-coated 12-well plates and cultured in complete mTeSR-1 medium

supplemented with Y-27632 (10 μM). Two days post-transfection, $GFP^+$ iPSCs (22%) were sorted by FACS and plated at low densities of 1-2x$10^4$ cells per 6cm dish (Falcon, 353037) in mTeSR-1 medium supplemented with Y-27632 (10 μM). The single cell cloning efficiency was recorded as 0.05%.

After 12-16 days, a subset of individual colonies (~15) was processed for DNA extraction using Quick-DNA/RNA Miniprep Plus Kit (D7003, Zymo) and Sanger sequenced. Out of 15 clones, 3 clones are found to be CRISPR-edited. Target editing efficiencies were assessed by TIDE analysis and recorded to be between 88 and 92% (https://tide-calculator.nki.nl/; data not shown). Subsequent TA cloning and sequencing demonstrated that both alleles of each clone are mutated, confirming the homozygous knock-out state. After clonal selection and expansion, no unusual chromosomal abnormalities were detected by CGH array (60K, data not shown). Validation of *MINPP1*$^{-/-}$ iPSC clones were further assessed by the absence of MINPP1 by western blot.

## 5. Cloning of MINPP1 variants into plasmids

This part of this study has been carried out by Nami Altin. The MINPP1 cDNA (transcript NM_004897.5) sequence was isolated by PCR from human brain cDNA. The PCR product was then ligated into the FLAG-HA-pcDNA3.1 vector (52535, Addgene). The mutations c.157T>G and c.1456G>A were incorporated in to the wild type plasmid with QuickChange Lightning Site-Directed Mutagenesis Kit (210515, Agilent). One Shot TOP10 chemically competent *E. coli* (C404006, Invitrogen) were then transformed with the resulting plasmid. Colony PCR was performed on plasmids by using T7 promoter/BGH-reverse primers and clones were sequenced by Sanger sequencing to check sequence reliability.

## 6. Transient transfection of MINPP1 missense variants into Hek293 cells

Transient transfection of MINPP1 missense variants into Hek293 cells was performed using Amaxa 4D-Nucleofector X-Unit (AAF-1002X, Lonza) according to manufacturer's

instructions. In brief, 2 x$10^5$ HEK293 cells were nucleofected per 20µl nucleocuvette strip, using P3 Primary Cell 4D X Kit S (V4XP-3032, Lonza), 1µg DNA per reaction, and the program CA-137.

## 7. Generation of stable HEK293 cell lines

HEK293 cells were transfected with either FLAG-HA-empty or FLAG-HA-MINPP1 plasmids by performing lipofection with the Lipofectamine 3000 reagent (Invitrogen, L3000015) as per manufacturer's instructions (2.5 µg of DNA per well of a 6-well plate und) under serum-free media. Six hours post-transfection, the media were replaced with normal HEK293 cell culture growth media. Two days post-transfection, the cell culture media were replaced with the media supplemented with the selection antibiotic geneticin (0.6mg/ml, Life, 10131027) and continued to be replaced twice a week until the cells in the 6 well plate reach high confluence. At high confluence, the cells were passaged and continued to be cultured for two to three weeks with the cell culture media supplemented with the geneticin (0.6mg/ml). The selection of clones was assessed by checking the presence of MINPP1 with Western-blot.

## 8. Generation of *Minpp1*$^{-/-}$ mice

*Minpp1*$^{-/-}$ mice were generated with the aid of LEAT platform of Imagine Institute by using a CRISPR/Cas9 system. In this study, animals were used in compliance with the French Animal Care and Use Committee from the Paris Descartes University (APAFIS#961-201506231137361). Guide RNAs (sgRNAs) targeting the first exon of the gene were designed via the CRISPOR (http://crispor.tefor.net/). C57Bl/-J female mice (4 weeks old) were super ovulated by intraperitoneal injection of 5 IU PMSG (SYNCRO-PART® PMSG 600 UI, Ceva) followed by 5 IU hCG (Chorulon 1500 UI, Intervet) at an interval of 46-48 hours and mated with C57BL/6J male mice. The next day, zygotes were collected from the oviducts and exposed to hyaluronidase (H3884, Sigma-Aldrich) to remove the cumulus cells and then placed in M2 medium (M7167, Sigma-Aldrich) into a CO2 incubator (5% CO2, 37 °C). SgRNAs were

hybridized with Cas9 (Wild type) protein and injected into the pronucleus of the C57Bl/6J zygotes. Surviving zygotes were placed in KSOM medium (MR-106-D, Merck-Millipore) and cultured overnight to two-cell stage and then transferred into the oviduct of B6CBAF1 pseudo-pregnant females. The generated knockouts were validated by Sanger sequencing combined with tide TIDE analysis (https://tide-calculator.nki.nl/; data not shown). All *Minpp1*-/- mice were backcrossed with C57BL/6J mice to remove potential off-targets. Mice characterization was performed by Karthyayani Rajamani.

## 9. E14.5 Mouse Neural Progenitor Cell Culture

Cerebral cortices (both halves) from E14.5 mice were dissected in Dulbecco Phosphate Balanced Salt Solution, carried out by Karthyayani Rajamani (DPBS, 14190250, Gibco). All procedures were done at room temperature, unless otherwise stated. Cortices were then incubated for 15 minutes at 37 °C in neurocult basal medium (STEMCELL, 05700) with Trypsin (1/100, 25300062, Gibco) and DNase I (1/1000, 79254, Qiagen). Next, neurocult basal medium with 10% FBS was added to the mixture to deactivate the Trypsin. The mixture was then triturated with fire polished Pasteur pipettes to obtain a homogenous mixture of cells. The cells were then centrifuged for 5 minutes at 300xg, washed twice and finally resuspended in neurocult medium with proliferation supplement (STEMCELL, 05701), endothelial growth factor (EGF) (20 ng/ml, PHG0314, Gibco) and 1% PS. Cells were then plated on poly-L-lysine (0.01 mg/ml, P6282, Sigma) and laminin (10 µg/ml; Gibco, 23017015) pre-coated dishes. Cells were passaged post 5 days of culture. All experiments were performed before passage 3.

## 10. Differentiation of iPSCs into neural lineage via dual-SMAD inhibition

iPSCs were differentiated towards neural lineage by following the dual-SMAD inhibition neural induction protocol, as previously described (Chambers et al., 2009; Boissart et al., 2013; Medina-Cano et al., 2018). Briefly, iPSCs were manually dissociated into big clumps and floated in non-coated dishes in neural induction media N2B27 (1:1 mix of DMEM-F12

(31331093, Gibco) and Neural Basal Medium (1103049, Gibco)) supplemented with N2 (07156, STEMCELL), NeuroCult SM1 without vitamin-A (05731, STEMCELL), bFGF (10 ng/ml, PHG0264, Invitrogen) and dual-SMAD inhibition small molecules SB431542 (20 μM, 72232, STEMCELL) and LDN193189 (HCl) (500 nM, 72146, STEMCELL). After 6 hours, embryoid body (EB)-like structures were seeded on polyornithine (0.1 mg/ml, P4957, Sigma) and laminin (4 μg/ml) pre-coated 3.5 cm dishes. The media were changed every 3 days. At day 12-15, the neural rosettes were manually or enzymatically passaged on to polyornithine-laminin-pre-coated dishes and cultured in N2B27 medium supplemented with bFGF (10 ng/ml), EGF (10 ng/ml, PHG0314, Invitrogen) and BDNF (20 ng/ml, 78005, STEMCELL). At confluence, cells were passaged with a density of $5x10^4/cm^2$ and the media was supplemented with Y-27632 (10μM) on the day of passage. Neuroectodermal origin of the emerging neural progenitor-like cells was assessed by HNK1/P75 Flow cytometry.

## 11. Differentiation of iPSCs into neural lineage via Noggin

iPSCs were differentiated into neural lineage by following Gerrard et al.'s protocol (Gerrard et al., 2005). In brief, iPSCs were dissociated into small clumps with Accutase and seeded on polyornithine (0.1 mg/ml, P4957, Sigma) and laminin (4 μg/ml) pre-coated 4-well-plates (179820, Nunc) and cultured in mTSER supplemented with Y-27632 (10 μM). The day after, cell culture media were changed to N2B27 medium (1:1 mix of DMEM-F12 (31331093, Gibco) and Neural Basal Medium (1103049, Gibco)) supplemented with N2 (17502048, Gibco), B27 (17504044, Gibco), Noggin (100 ng/ml, 78060.1, STEMCELL), Y-27632 (10 μM) and 1% PS. The media were replaced every 3 days.

## 12. Inositol Labelling and SAX-HPLC Analysis

This part of this study was carried out with the help of Adolfo Saiardi and Miranda Wilson at the University College London. HEK293 cells and fibroblasts were plated at 10,000 cells/well on 6-well plates and radiolabelled for 5 days with 5 μCi/ml *myo*-[$^3$H]-inositol (1 mCi,

NET114A001, Perkin Elmer) in inositol-free DMEM medium (DML13-500, Caisson) supplemented with dialyzed FBS (Gibco,26400-044) and 1%PS. One quarter of the media was replaced with fresh medium containing 5 μCi/ml [$^3$H]-inositol on day 2. For iPSCs and their day 7 neurally-differentiating counterparts, the inositol metabolic radiolabelling was performed for 3 days and inositol-free DMEM media were supplemented with either bFGF (10 ng/ml, PHG0264, Invitrogen) or Noggin (100 ng / ml, 78060.1, STEMCELL), respectively. For in vitro overexpression studies, the inositol metabolic radiolabelling was performed for 3 days, followed by lipofectamine-based transfection into HEK293 cells in the presence of 5 μCi/ml *myo*-[$^3$H]-inositol. One day post-transfection, the inositol phosphates were extracted. Extraction of inositol phosphates was performed according to published protocol (Azevedo and Saiardi, 2006). Briefly, cells were incubated on ice with 1 M perchloric acid and 5 mM EDTA for 10 minutes followed by the collection of extracts and an overnight neutralisation step with 1 M potassium carbonate. Inositol phosphates were then separated by strong anion-exchange high-performance liquid chromatography (SAX-HPLC). The peaks ([$^3$H]-$IP_n$) were identified based on comparison to standards according to a previously published study (Azevedo and Saiardi, 2006). The radioactivity within each fraction was measured with a beta counter, after addition of 4 ml of scintillation fluid (Ultima-Flo AP LCS-mixture; Packard).The data are presented as percentage of total radioactivity in the inositol-lipid fraction, obtained by incubating the post-extraction cells with 0.1% NaOH and 0.1% SDS overnight at room temperature. Inositol labelling and SAX-HPLC analysis have been carried out by Adolfo Saiardi and Miranda Wilson.

## 13. *In vitro* phytase Assay

The *in vitro* phytase assay was carried out by Miranda Wilson and Adolfo Saiardi and performed as previously described (Wilson et al., 2015). Briefly, 4 nmol of $IP_6$ was added to 1 ml of conditioned media from control and *MINPP1*$^{-/-}$ HEK293 cells and further incubated for

0, 2, 4 and 6 hours at 37 °C. The samples were then mixed with Orange G loading dye and resolved by 35% PAGE followed by toluidine blue staining.

## 14. Analysis of extracellular inositol phosphates

This part of this study has been carried out by Adolfo Saiardi and Miranda Wilson. For analysis of extracellular inositol phosphates, cells were labelled for 5 days with [3H]-inositol as indicated above. Media were collected and centrifuged at 300xg for 5 minutes to remove cell contaminants. Perchloric acid was added to the supernatant to final 1 M. The acidified medium was incubated on ice for 10 minutes before centrifugation at 18,000 xg to remove precipitates. Inositol phosphates in the supernatant were then purified using titanium dioxide beads (Wilson and Saiardi, 2018). Briefly, 4 mg beads were added to the media extracts and the samples rotated at 4°C for 15 minutes. Beads were washed twice in 1 M perchloric acid, before elution with ammonium hydroxide. Radiolabelled inositol phosphates in the purified media extracts were separated by SAX-HPLC as before, and radioactivity in each fraction measured with a beta counter.

## 15. MTT Proliferation Assay

Cells were cultured with Methylthiazolyldiphenyl-tetrazolium bromide (MTT) (0.5 mg/ml, M5655, Sigma) for 1.5 hours. Then, MTT and the cell culture medium were removed and 100% dimethyl sulfoxide (100 µl/well) was added to dissolve the formazan crystals. Next, the cell culture plate was left to shake for 15-30 minutes in the dark at room temperature, followed by transfer of the samples into flat-bottom 96-well microtiter plate (655101, Greiner). The optical density was read on a microplate reader at 560 nm (1681135, Bio-Rad).

## 16. BrdU Proliferation Assay

Initially, the cells were incubated with 10 µM BrdU labelling solution (B5002-1G, Sigma) for 6 hours at 37 °C in a $CO_2$ incubator. The cells were further thoroughly washed thrice with PBS and fixed with 4% paraformaldehyde for 15 minutes. Permeabilization of the

cells were performed using 0.25% PBS-Triton-X-100 for 10 minutes. After 3 washes with PBS, DNA hydrolysis was achieved by incubating the cells with 2 M HCL for 30 minutes at 37 °C. Further, the cells were neutralized with 0.1 M sodium borate buffer (pH 8.5) for 30 minutes at room temperature. Cells were thoroughly washed with PBS and immunostaining of the cells with BrdU antibody (1:250, ab6326, Abcam) was carried out as previously mentioned in the immunofluorescence section.

## 17. TUNEL Apoptosis Assay

The apoptosis is measured using the Click-iT TUNEL Alexa Fluor 594 Imaging Assay (C10246, Thermofischer) according to manufacturer's instructions. For a positive control, cells are treated with tunicamycin (10 µg/ml, 3516/10, Biotechne) for 6 hours to induce apoptosis (data not shown). For quantification analysis, a minimum of 5 fields per replicate were analysed in ImageJ. The percentage of $TUNEL^+$ cells were counted relative to the total number of $Hoechst^+$ cells per field which was comparable (i.e. $Hoechst^+$) between replicates and conditions.

## 18. Cell Proliferation and Apoptosis Assay with Incucyte-Live-Imaging System

Cells were seeded on 96-well plate (4379, Essen Bioscience) and cultured with Annexin-V (1:200, 4641, Essen Bioscience) containing media inside the IncuCyte® Live Cell Analysis System (Essen Bioscience). Three images per well were taken with phase contrast and red fluorescence channels every 2 hours for a total of 48 hours, using 20x objective. Images were then analysed with Incucyte-Zoom software, by defining a mask with the basic analyser. The same mask was applied to all time points.

## 19. Quantification of free intracellular $Ca^{2+}$ levels

Cells were plated at 25,000 cells/well on flat-bottom 96-well plates (Greiner, 655088). After 24 to 48 hours in culture, the cells were loaded with Fluo-4-AM (5 mM, F14201, Invitrogen) diluted in assay buffer (NaCl 140 mM, Glucose 11.5 mM, KCl 5.9 mM, $MgCl_2$ 1.4

mM, $NaH_2PO_4$ 1.2 mM, $NaHCO_3$ 5 mM, , HEPES 10 mM, pH 7.4) with or without $CaCl_2$ (1.8 mM) to a final concentration of 5 μM. After 30 minutes of incubation in a humidified incubator (5% $CO_2$, 37 °C), the loading medium was removed and the cells were washed twice with the assay buffer. Then, the cells were excited at 485nm and emission intensities was recorded at 535nm via a fluorometers (200ProTecan and Tristar LB941) in the presence of assay buffer. The measured fluorescence intensities were then normalised to cell number via MTT proliferation assay. For $Ca^{2+}$ stimulation experiments, Ionomycin (10 μM, I0634-1MG, Sigma) or Caffeine (10 mM, C0750, Sigma) were quickly added to the wells in the presence of assay buffer and fluorescence intensities were recorded every 30 seconds for a minimum of 10 minutes. All the $Ca^{2+}$ stimulation experiments were performed with early batch HEK293 cells (Luo et al., 2005).

## 20. Quantification of intracellular total and free iron levels

The total iron content was measured with a colorimetric ferrozine-based assay according to previous studies (Drecourt et al., 2018; Riemer et al., 2004). Briefly, cells were cultured on 6-well plate (92006, TPP) and incubated with or without ferric ammonium citrate (FAC) (100 μM, RES20400-A702X, Sigma) in serum-free DMEM for 48 hours. Then, the cells were lysed with NaOH (50 mM, 200μl/well) and 50 μl of the lysate was kept apart for protein quantification. The remaining cell lysate was mixed with equal volumes of 10 mM HCl and iron-releasing reagent (HCl 1.4 M, $KMnO_4$ 4.5%) and incubated for 2 hours at 60 °C. Once the samples reached room temperature, 30 μl of iron-detection reagent (6.5 mM ferrozine, 6.5 mM neocuproine, 2.5 M ammonium acetate, and 1 M ascorbic acid) was added to each sample. After 30 minutes of incubation at room temperature, the samples were transferred to flat-bottom 96-well microtiter plate (Greiner, 655101). The optical density was read on a microplate reader at 560 nm (Biorad, 1681135). FAC was used as reference standard. The free iron levels ($Fe^{2+}$ and $Fe^{3+}$) were measured by using the Iron Assay Kit (Abcam, ab83366)

according to manufacturer's instructions. In both iron-detection assays, the data are normalized against the protein levels, quantified via Pierce BCA Protein assay kit (23225, Thermo Scientific).

## 21. Immunofluorescence

Cells were fixed in cold 4% paraformaldehyde for 10 minutes followed by three washes of PBS and permeabilization in 0.25% PBS-Triton-X-100 for 10 minutes. Cells were blocked for 1 hour in 1% BSA and 22.52 mg/ml glycine diluted in 0.1% PBS-Tween-20 (PBST). Cells were then incubated overnight at 4 °C with the following primary antibodies diluted in 1% BSA/0.1% PBST: Anti-PAX6(1:400, 901301, BioLegend), Anti-TUBULIN β-3 (1:1000, 801201, BioLegend), Anti-OCT4 (1:100, sc-5279, Santa-Cruz), Anti-SOX2 (1:1000,AB5603, Millipore), Anti-NESTIN (1:200,N5413, Sigma). After 3 washes with 0.1% PBST, cells were incubated for 1 hour with Alexa-Fluor-coupled secondary antibodies (A21424, A-11034, Invitrogen) diluted 1:500 in 0.1% PBST. Following three washes with 0.1% PBST, cells were then incubated with Hoechst 33342 (H3570, Invitrogen) diluted 1:1000 in 0.1% PBST. After 10 minutes of incubation, cells were washed twice with 0.1% PBST and either kept in PBS or mounted with ProLong™ Diamond Antifade Mountant (P36965, Invitrogen). Images were acquired with CELENA-S Digital Imaging System (CS20001, Logos) and Zeiss Axioplan-2. For quantification analysis, a minimum of 10 fields per replicate were analysed in ImageJ. The percentage of $PAX6^+$ , $TUJ1^+$ or $BrdU^+$ cells were counted relative to the total number of $Hoechst^+$ cells per field which was comparable (i.e. $Hoechst^+$) between replicates and conditions.

## 22. Protein extraction and western blot analysis

Protein extraction, quantification, separation in gel electrophoresis and transfer were performed as described previously (Medina-Cano et al., 2018). Nitrocellulose membranes were blocked either in Odyssey-TM Blocking Buffer (927-50003, LICOR) or in 5% dry milk diluted

in 0.2% PBST for 1 hour and further incubated overnight at 4 °C with the following primary antibodies diluted in either Odyssey-TM Blocking Buffer or 2.5% dry milk diluted in 0.2% PBST: Anti-MINPP1 (1:2000, sc-10399, Santa-Cruz), Anti-β Actin (1:5000, AM4302, Invitrogen). After three washes with 0.2% PBST, the membranes were then incubated for 1 hour at room temperature with HRP (1:10000, sc-2314, sc-2020, Santa-Cruz) or IRDye-coupled (1:10000, 925-68070, 925-32211, LICOR) secondary antibodies. After three washes with 0.2% PBST, the membranes were developed either with HRP (ChemiDoc XRS, Biorad) or Odyssey CLx imaging system (LICOR).

## 23. Glycosylation Studies

The glycosylation status of different MINPP1 mutant forms is checked by following the previously described PnGase F protocol (P0704L, New England BioLabs) (Medina-Cano et al., 2018).

## 24. Statistics

Data were analysed where appropriate with one-way analysis of variance (ANOVA), Two-tailed student's t-test and two-way ANOVA with GraphPad Prism 8. N and n values are detailed in figure legends. "N" refers to independent experiments or animals and "n" refers to technical replicates. All the data are presented as mean ± the standard deviation (s.d.). Statistically significant differences are indicated on the figures by *$p<0.05$, **$p<0.01$, ***$p<0.001$, or ****$p<0.0001$.

# RESULTS

## 1.1 Defects in *MINPP1* gene cause a distinct subtype of PCH.

In an attempt to identify novel genetic causes of PCH, our laboratory has performed whole exome sequencing (WES) for a group of 15 PCH probands that were previously screened negative for mutations in any of the known PCH-causing genes. WES was performed using a trio strategy (i.e. the proband and his/her parents) and then analysed for potentially deleterious rare biallelic variants (see methods for variant filtering and prioritization). Interestingly, in three families, the most likely pathogenic variants were identified in *MINPP1*, a gene that has not been previously associated with any Mendelian disorder. The presence of additional *MINPP1* bi-allelic variants were interrogated in two additional cohorts by research teams in the laboratory of L. Burglen and J. Gleeson. Intriguingly, the analysis revealed three additional families with likely causative variants in *MINPP1*, resulting in a total number of eight PCH children from six unrelated families, all carrying bi-allelic variants in *MINPP1* (Figure 26, Figure 27A, Table 3.1, Table 3.2). These variants include homozygous early-truncating mutations in the families CerID-30 and PCH-2712, compound heterozygous missense and frameshift variants in the family CerID-11, a homozygous missense variant in the endoplasmic reticulum (ER) retention domain of the protein in the family CerID-09, as well as the homozygous missense variants in the histidine phosphatase domain of the protein in the families TR-PCH-01 and PCH-2456.

The early truncating mutations are predicted to cause loss of function of *MINPP1*, either through non-sense mediated mRNA decay or protein truncation (Table 3.2) (Frischmeyer and Dietz, 1999; Kurosaki and Maquat, 2016). Consistently, MINPP1 protein was undetectable in skin fibroblasts obtained from patients of the CerID-30 family, whose mutations are predicted to cause a truncated form of MINPP1 with only 105 amino acids (Figure 26E). Hence, the

absence of MINPP1 in both of the siblings clearly indicated the complete loss of function of *MINPP1* as the cause of the PCH phenotype.

On the one hand, all of the missense variants are predicted to be disease-causing using MutationTaster and SIFT and involve evolutionarily conserved amino acids. (Table 3.2, Figure 26C). In an attempt to better predict the involvement of these missense variants on MINPP1 function, 3D missense structural prediction analysis was performed by using phytase crystal structure of D. castellii as a model. Intriguingly, all the variants involving amino acids that are included in the model (i.e.Tyr53, Phe228, Arg410) are found to introduce structural changes to the MINPP1 protein (Figure 27B). For instance, Tyr53Asp variant disrupts a hydrogen bond with the donor amino-acid Ser299, which is located at the histidine phosphatase domain. Meanwhile, the Phe228Leu substitution breaks a buried hydrogen bond with Lys24, both amino acids located close to the binding site of $IP_6$, the main substrate of the MINPP1. Lastly, the Arg401Gln substitution disrupts a salt bridge formed with the amino-acid Asp318, both amino acids located at the histidine phosphatase domain. Hence, these *in silico* analysis predicted that all the missense variants tested disrupts MINPP1 catalytic activity, and cause a loss of function.

Following the identification of *MINPP1* biallelic variants, interestingly, it became obvious that all of the 8 patients shared a specific and never described neuroradiological phenotype that included the combination of PCH (e.g. pontine and cerebellar atrophy/hypoplasia) and severe atrophies and T2 hypersignals at the level of basal ganglia or thalami (Figure 26A, Table 3.1). Moreover, all of the patients presented almost complete absence of motor and cognitive development, dystonia, vision impairments and progressive or congenital microcephaly with a perinatal or prenatal-onset (Table 3.1). Hence, the independent identification of *MINPP1* biallelic variants in patients with shared and never-described PCH phenotypes supported the fact that defects in *MINPP1* gene cause a distinct PCH subtype.

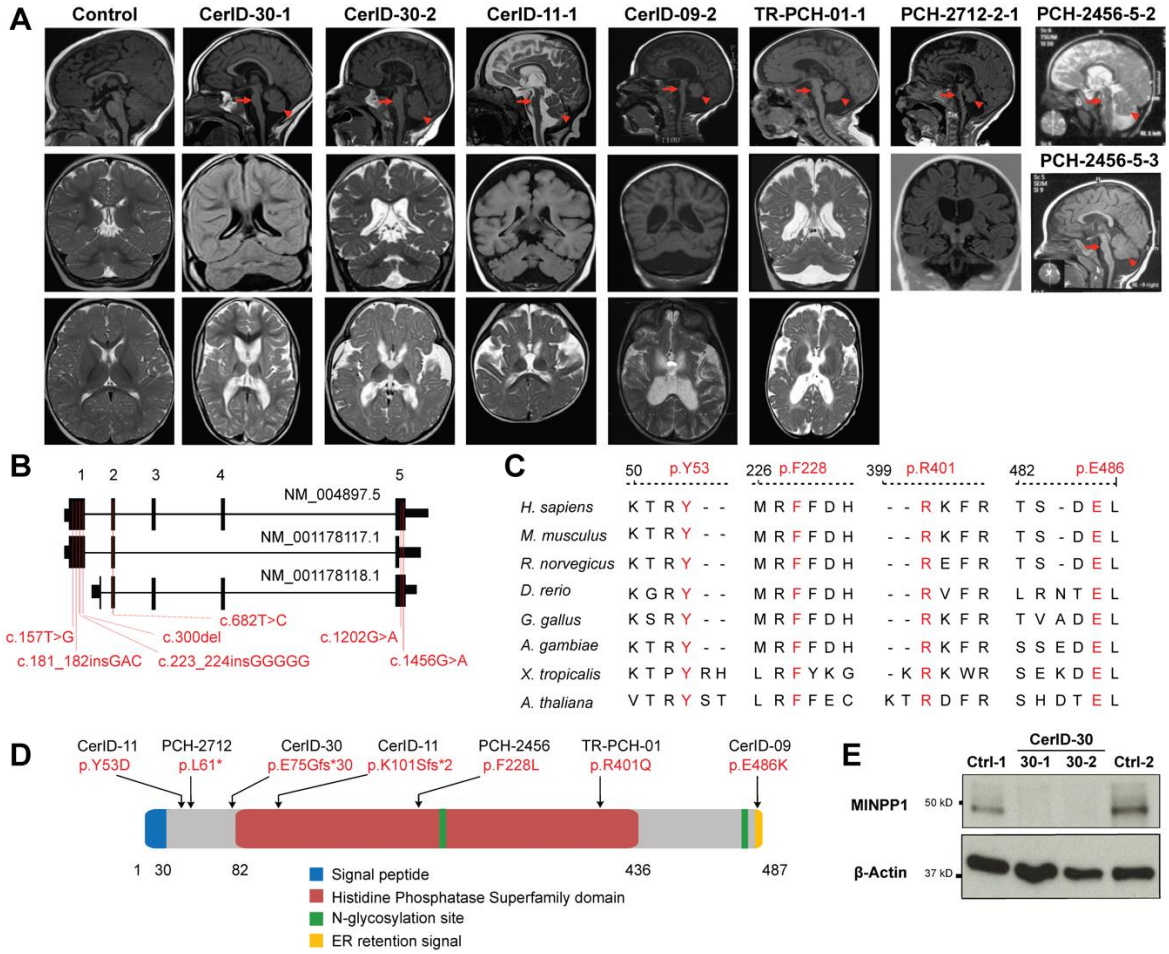


**Figure 26. Biallelic mutations in *MINPP1* cause a distinct PCH phenotype. (A)** Midline sagittal (top), coronal (middle) and axial (bottom) brain MRIs of control and patients from families CerID-30, CerID-11, CerID-09 and TR-PCH-01, respectively. Only sagittal (top) and coronal (middle) brain MRIs were available for the patient from the family PCH-2712 and sagittal brain MRI for the patients from PCH-2456 (top and middle). Sagittal MRIs show variable degree of brain stem (arrow) and cerebellar atrophy/hypoplasia (arrowhead). **(B)** Schematic representation of the *MINPP1* transcripts: NM_004897.5, NM_001178117.1 and NM_001178118.1, respectively. Exon numbers for the longest isoform NM_004897.5 are indicated above the schematic representation. Mutations are shown relative to their cDNA (NM_004897.5) position. **(C)** Multiple-sequence alignment of MINPP1 from different species. Variant amino-acid residues p.Y53, p.F228, p.R401 and p.E486 are evolutionarily conserved. **(D)** Linear schematic representation of MINPP1, showing the position of mutations with respect to predicted protein domains. **(E)** Western blot analysis of MINPP1 level in patient fibroblasts with β-Actin shown as loading control. Patient fibroblasts CerID-30-1 and CerID-30-2 show absent MINPP1. Abbreviations used: Endoplasmic reticulum (ER).

## Table 3.1. Clinical information of the patients with variants in *MINPP1*.

| **Family** | **CerID-30** | | **CerID-09** | **CerID-11** | **TR-PCH-01** | **PCH-2712** | **PCH-2456** | |
|---|---|---|---|---|---|---|---|---|
| Subject | **CerID-30-1** | **CerID-30-2** | **CerID-09-2** | **CerID-11-1** | **TR-PCH-01-1** | **2712-2-1** | **2456-5-2** | **2456-5-3** |
| Gender F/M | F | F | M | F | M | F | M | F |
| Origin (country) | Tunisia | Tunisia | Tunisia | France | France | Turkey | Egypt | Egypt |
| Documented consanguinity | No | No | Yes | No | Yes | Yes -1st cousin parents | Yes -2nd cousin parents | Yes -2nd c cousin parents |
| Age at last follow-up | 12 years | 9 years | 11 years | 18 months | 12 years | 2y10m | 4.5 y | 1.5 y |
| Weight at birth (kg) | 3.2 (M) | 4.2 (+2SD) | 3.2 (M) | 2.4 (-2SD) | 3.710 | 3.0 (M) | 3.4 (M) | 3 (M) |
| Weight at last examination (kg) | 30 (-1,5SD) | 23.4 (-0,5SD) | 16.9 (-4SD) | 10 (-1 DS) | 36 | 10.5 (-2SD) | 10.5 (-3SD) | 8.5 (-3SD) |
| Length at birth (cm) | 50 (M) | 51 (M) | 50.5 (M) | 43.5 (-3SD) | 50 | NA | 49.2 (M) | 47.5 (-1SD) |
| HC at birth (cm) | 34 (M) | 35 (+1SD) | 35 (M) | 30.6 (-3SD) | 36 | 33 (-1SD) | 34 (M) | 32 (-1SD) |
| HC at last examination (cm, age) | 48 cm (8 years; -2SD) | 47 cm (4 years; -2SD) | 47 cm (11 years; -5SD) | 42cm (18 months; -4SD) | -2,55 (18 months) | 41cm (-5SD) | 44.5 (-5SD) | 42 (-3SD) |
| Onset | Perinatal | Perinatal | Perinatal | Prenatal | Perinatal | Perinatal | Perinatal | Perinatal |
| Progressive encephalopathy | No | No | Yes | Yes | No | Yes | Yes | Yes |
| Posture: bedridden (B), sitting (S), walking (W) | B | B | B | B | B | B | B | B |
| Development | | | | | | | | |
| Gross motor (normal/delayed/absent) | Absent | Absent | Absent | Absent | Absent | Absent | Absent | Absent |
| Fine motor (normal/delayed/absent) | Absent | Absent | Absent | Absent | Absent | Absent | Absent | Absent |
| Language (normal/delayed/absent) | Absent | Absent | Absent | Absent | Absent | Absent | Absent | Absent |
| Social (normal/delayed/absent) | Absent | Absent | Absent | Absent | Delayed | Absent | Absent | Absent |
| Seizures | | | | | | | | |
| Epileptic seizures | + | + | + | - | + | + | + | + |
| Onset | 7 years | 4 years | 5 years | - | 1 day | 2 months | 3 months | 5 months |
| Neurological Findings | | | | | | | | |
| Axial hypotonia | + | + | + | + | + | + | + | + |
| Distal hypertonia | + | + | + | + | + | + | + | + |
| Pyramidal signs | Spastic tetraplegia | Spastic tetraplegia | Spastic tetraplegia | Spastic tetraplegia | Spastic tetraplegia | Spastic tetraplegia | Spastic tetraplegia | Spastic tetraplegia |
| Extra-pyramidal signs | + | + | + | + | - | + | + | + |
| Ophthalmological findings | | | | | | | | |
| Nystagmus | + | + | + | + | + | bilateral + | + | + |
| Abnormal ocular movement | + | + | + | + | + | NA | + | + |
| Optic atrophy | + | + | + | - | - | - | + | - |
| VEP/ERG | NA | ERG | VEP | ERG/VEP | NA | | abnormal VEP | |
| Others | Ptosis/cataract | Ptosis/cataract | Blindness | Ptosis | Cataract | abnormal VEP, left eye Ptosis, Cataract | couldn't follow object | - - |
| Investigations | | | | | | | | |
| Metabolic | Normal | Normal | Normal | Normal | Normal | Normal | Normal | Normal |
| EEG | Abnormal | Normal | Normal | Normal | Normal | Abnormal | Abnormal | Abnormal |
| MRI | | | | | | | | |
| Age at last investigation (years (y) ; months (m) ; days(d)) | 2y7m | 8m2d | 1y11m | 8m23d | 4m | 6y8m | 2.5y | 1.5y |
| Cerebellum | Hypoplasia | Hypoplasia | Hypoplasia | Hypoplasia | Hypoplasia | Hypoplasia | Hypoplasia | Hypoplasia |
| Pons | Atrophy | Atrophy | Atrophy | Atrophy | Hypoplasia | Atrophy | Atrophy | Atrophy |
| Cerebral cortex atrophy | Atrophy | Atrophy | Atrophy | Atrophy | - | Atrophy | atrophy | atrophy |
| Ventricles | Enlarged | Enlarged | Enlarged | Enlarged | Enlarged | Enlarged | enlarged | enlarged |
| Corpus callosum | - | - | Thin | NA | - | thin | Thin | Thin |
| Basal Ganglia hypoplasia/atrophy | + | + | + | + | thalamic atrophy | + | + | + |
| Basal ganglia T2 hypersignal | + | + | + | + | thalami | + | - | - |
| Spectroscopy | No lactate abnormality | NA | NA | NA | NA | No lactate abnormality | NA | NA |
| Others (WM defect) | WM periventricular atrophy | WM periventricular atrophy | NA | NA | NA | WM periventricular atrophy | - | - |
| Other symptoms | | | | | | | | |
| Respiratory tract congestion | No | No | Yes | No | Yes | No | Yes | No |
| Apnoea | No | No | No | No | No | No | Yes | No |
| Impaired swallowing | Yes | Yes | Yes | Yes | Yes | Yes | Yes | Yes |
| Joint stiffness | Yes | Yes | Yes | Yes | NA | Yes | Yes | No |
| Skeletal deformities | Scoliosis | Scoliosis | Scoliosis | Scoliosis | Scoliosis | Scoliosis | scoliosis | No |
| Cardiovascular findings | No | No | NA | NA | No | No | No | No |
| Urine screening | Normal | Normal | NA | Normal | Normal | recurrent urinary infection | Normal | Normal |
| Peripheral blood smear | NA | NA | NA | Thrombocytosis | Normal | NA | NA | NA |
| Muscle wasting | Yes | Yes | Yes | Yes | Yes | Yes | Yes | No |
| Facial dysmorphism | Yes | Yes | No | No | Yes | Micrognathia | Non-specific small head, prominent nose, low set ear | Non-specific small head, prominent nose, low set ears |
| Other | NA | NA | Mild Normochromic, normocytic anaemia | Abnormal fat distribution | NA | BAEP: no response | - | - |

Abbreviations: EEG, Electroencephalogram; ERG, abnormal electroretinography; HC, Head Circumference; M, median; NA, Not available.

**Table 3.2. *MINPP1* variants identified in the different cohorts.**

| Family | Genomic Coordinates (GRCh38) | Variant | dbSNP | ExAC | gnomAD | SIFT | Polyphen | Mutation Taster | CADD _PHRED |
|---|---|---|---|---|---|---|---|---|---|
| **CERID-30** | Chr10(GRCh38):g.87505138_ 87505139insGGGGG | NM_004897.4(MINPP1): c.223_224insGGGGG/ p.E75Gfs*30 | - | - | - | - | - | - | - |
| **CERID-11** | Chr10(GRCh38):g.87505072T>G | NM_004897.4(MINPP1): c.157T>G/p.Y53D | - | - | - | Deleterious (0) | Probably damaging (0.978) | Disease causing (prob: 1) | 32 |
| | Chr10(GRCh38):g.87505215del | NM_004897.4(MINPP1): c.300del/p.K101Sfs*2 | - | - | - | - | - | - | - |
| **CERID-09** | Chr10(GRCh38):g.87552470G>A | NM_004897.4(MINPP1): c.1456G>A/p.E486K | - | - | - | Deleterious (0) | Probably damaging (0.94) | Disease causing (prob: 1) | 26.6 |
| **TR-PCH-01** | Chr10(GRCh38):g.87552216G>A | NM_004897.4(MINPP1): c.1202G>A/p.R401Q | rs1381093602 | - | 1 allele count (frequency $3.10^{-6}$ ) | Deleterious (0) | Probably damaging (0.987) | Disease causing (prob: 1) | 33 |
| **PCH-2712** | Chr10(GRCh38):g.87505096_ 87505097insGAC | NM_004897.4(MINPP1): c.181_182insGAC/p.L61* | - | - | - | - | - | - | - |
| **PCH-2456** | Chr10(GRCh38):g.87508380T>C | NM_004897.4(MINPP1): c.682T>C/p.F228L | rs1456945513 | - | - | Deleterious (0) | Probably damaging (0.993) | Disease causing (prob: 1) | 25.8 |

CADD score ⩾ 25 indicates that the variant is among the 0.5% most deleterious substitutions in the protein-coding regions of the human genome.

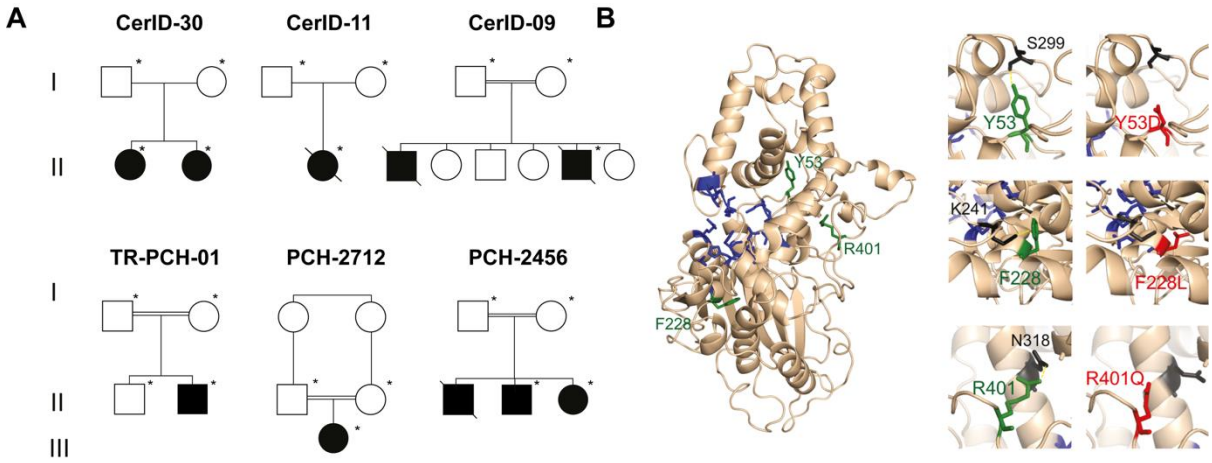


**Figure 27. Family pedigrees and *in silico* prediction analysis of the missense *MINPP1* variants. (A**) Pedigrees of families with mutations in the *MINPP1* gene**.** Individuals subjected to Whole Exome Sequencing (WES) or Sanger Sequencing are indicated with asterisk. Additional DNA samples for family CerID-09 could not be collected for segregation analysis. (**B**) Wild type MINPP1 with amino acids involved in $IP_6$ binding are indicated in blue and amino acids mutated with missense variants are indicated in green. The Missense3D server predicted that all the three missense variants tested cause structural damage.

## 1.2 Assessing the effect of PCH-associated *MINPP1* mutations using HEK293 cells

We started our functional characterization study by determining the effect of PCH-associated *MINPP1* mutations on protein stability, function and cellular physiology. To achieve this, we developed a *MINPP1* KO cellular model in an easily transfectable human cell line: HEK293T(HEK293) cells (Figure 28A). While this model allowed us to reproduce and study the loss of function mutation of the family CerID-30, it also served as a baseline for overexpression studies, providing the opportunity to study patient *MINPP1* missense variants in the absence of endogenous MINPP1. In this study, we focused on the missense variants identified in the family of CerID-09 (i.e. E486K) and CerID-11 (i.e. Y53D). While the former is predicted to impact the subcellular localization of the protein, owing to its location at the ER retention domain, the latter is predicted to disrupt MINPP1 catalytic activity by introducing structural damage at the site of histidine phosphatase domain (see the previous section). Hence, this section will present findings obtained from *MINPP1*$^{-/-}$ HEK293 cells and MINP*P1*$^{-/-}$ HEK293 cells transiently transfected with either of the two missense variants: E486K or Y53D.

### 1.2.1 *MINPP1* missense PCH variants affect protein level without obvious alteration of the glycosylation status of MINPP1.

To determine the effect of *MINPP1* missense variants on protein level, we examined MINPP1 levels in *MINPP1*$^{-/-}$ HEK293 cells overexpressed with either FLAG-tagged-WT, Y53D or E486K MINPP1. Unlike in endogenous protein, western blots revealed two bands in all of the over-expressed MINPP1 forms, hence suggesting for a potential artefact related to the transfected MINPP1 (Figure 28B). Nevertheless, these blots, indicated lower levels of over-expressed missense variant proteins than the WT form, thus suggesting that both of the *MINPP1* missense variants alter the protein level.

We next studied the effect of these *MINPP1* missense variants on the glycosylation status of the protein in an attempt to investigate their potential effect on the protein stability (Lee et al., 2015). To this extent, E486K MINPP1 variant has particularly taken our attention, owing to its close localization to one of glycosylation sites of the protein (N481). Although the glycosylation of MINPP1 has never been studied, as MINPP1 has two predicted N-glycosylation sites (i.e. N242, N481), we treated all of the overexpressed MINPP1 protein extracts (i.e. FLAG-tagged-WT, Y53D and E486K MINPP1) with PNGase, an N-Glycosidase responsible for the removal of N-glycans from proteins (Plummer and Tarentino, 1991). Following treatment, Western blot analysis showed a shift in the endogenous MINPP1, hence showing for the first time that MINPP1 is indeed glycosylated. A similar shift pattern is also observed in both of the MINPP1 missense variants (Figure 28C). Thereby, this data suggested that *MINPP1* missense variants do not seem to have an obvious impact on the glycosylation status of MINPP1, although at this point we cannot totally exclude the slightly different appearance of the E486K MINPP1 under untreated condition.

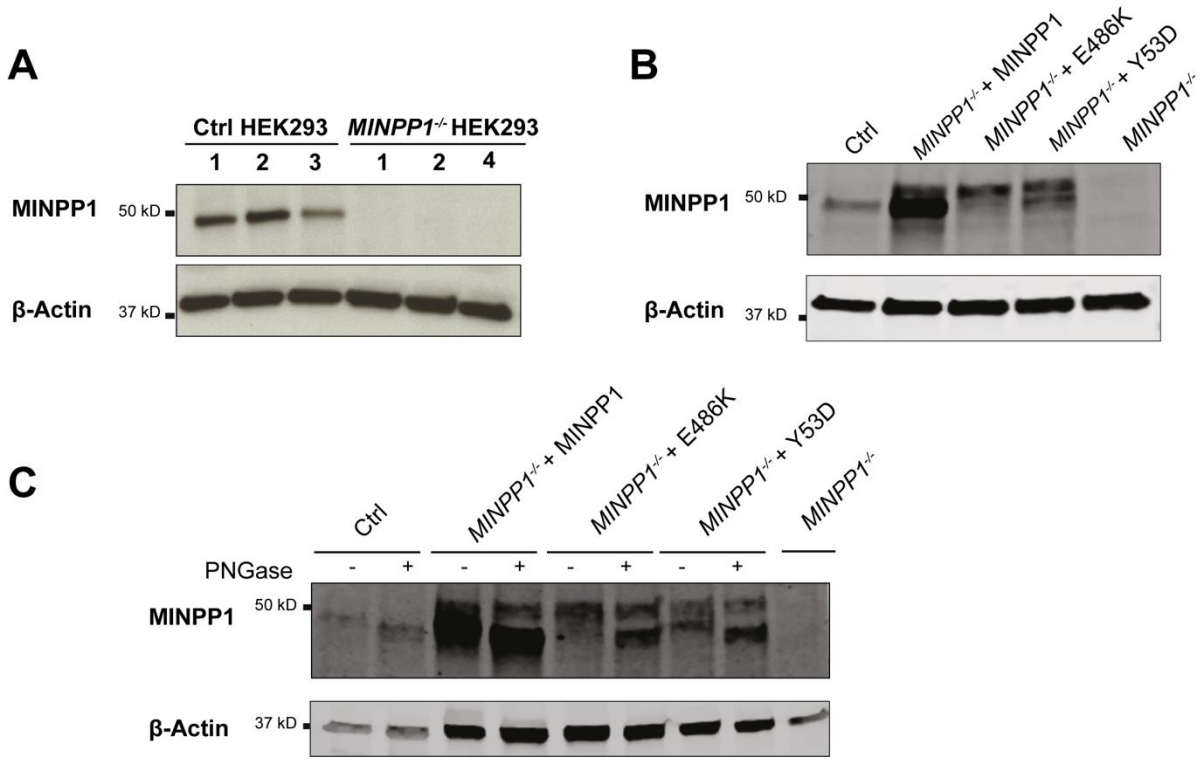


**Figure 28. *MINPP1* missense PCH variants affect protein level without altering glycosylation status of MINPP1. (A)** Western blot analysis of MINPP1 level in HEK293 cells with β-Actin shown as loading control. *MINPP1*$^{-/-}$ HEK293 clones show absent MINPP1. **(B-C)** Western blot data showing the exogenous MINPP1 **(B)** and its glycosylated and de-glycosylated forms **(C)** in *MINPP1*$^{-/-}$ HEK293 cells transiently transfected with plasmids encoding empty vector, wild type, Y53D or E486K mutant MINPP1. MINPP1 is present in control HEK293 cells and absent in *MINPP1*$^{-/-}$ HEK293 cells. β-Actin shown as loading control.

### 1.2.2 MINPP1 loss leads to a proliferation defect without affecting apoptosis in HEK293 cells.

Unexpectedly, following the generation of *MINPP1*$^{-/-}$ HEK293 cells, we noticed that *MINPP1*$^{-/-}$ HEK293 cells were growing much more slowly compared to control cells. In an attempt to better characterize this slow growth phenotype, we determined the number of viable cells over time in control and *MINPP1*$^{-/-}$ HEK293 cultures, using MTT colorimetric assay. This assay is a convenient method to assess the number of viable cells, as it measures cellular mitochondrial-metabolic activity (Mosmann, 1983). Indeed, cells contain NAD(P)H-dependent oxidoreductases that are able to reduce MTT dye into its insoluble form, releasing

a purple colour when dissolved in DMSO. Hence, to assess the cell growth rate with this strategy, we treated control and *MINPP1*$^{-/-}$ HEK293 cells with MTT after 3, 24 and 48 hours of cell-culture and then plotted the absorbance values versus time. At 3hrs, the two cell lines displayed a comparable 560 nm value, confirming an equal initial seeding density (Figure 29A). In line with our initial observation, after 48 hours of culture, *MINPP1*$^{-/-}$ HEK293 cells showed a 30% decrease in their growth rate when compared to the control cells. To assess the specificity of this effect, we transiently overexpressed FLAG-tagged-WT-MINPP1 in *MINPP1*$^{-/-}$ HEK293 cells and found a partial but significant restoration of cell growth, at a transfection efficiency of ~70% (Figure 29B). Hence, overall, these data suggested that MINPP1 loss leads to a growth defect in HEK293 cells.

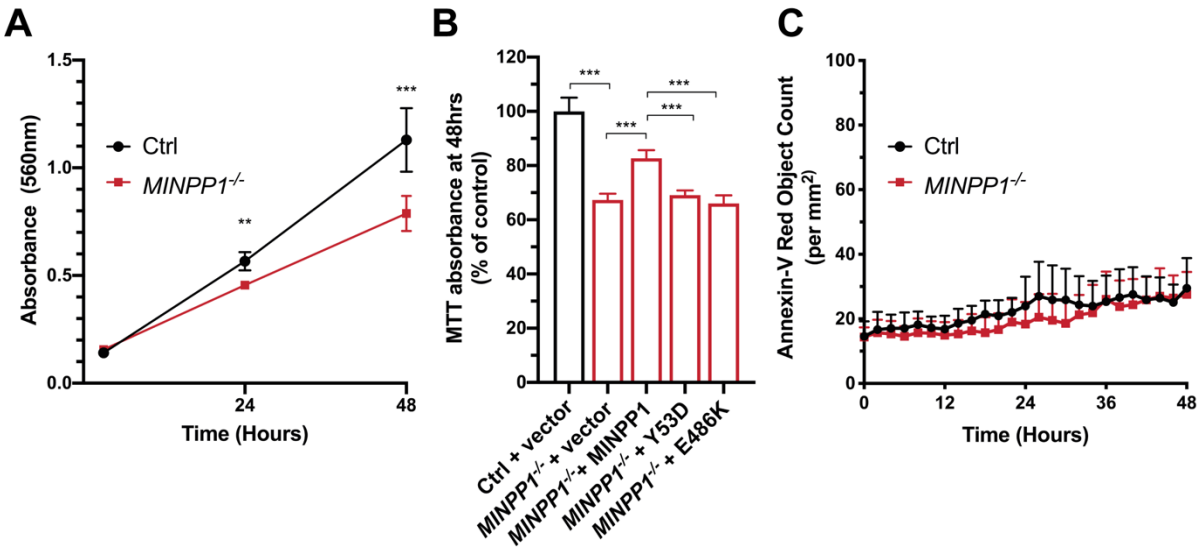


**Figure 29. PCH-associated mutations of *MINPP1* impact cell proliferation without affecting apoptosis in HEK293 cells. (A)** Assessment of cell proliferation of control and *MINPP1*$^{-/-}$ HEK293 cells by MTT assay. For each clone, MTT absorbance was measured 3, 24 and 48 hours post-seeding. Values represent the mean ± s.d. of triplicate determinations from 4 replicates. (n=4, Two-tailed student's t-test, ** and *** indicate p values $p<0.01$ and $P \leq 0.001$, respectively). **(B)** *MINPP1*$^{-/-}$ HEK293 cells were transiently transfected with plasmids encoding empty vector, wild type, Y53D or E486K variant MINPP1. To assess the cell proliferation rate, MTT assay was performed 48 hours post-nucleofection. The data are presented as mean percentage relative to control (Ctrl) ± s.d., with triplicate determinations from four replicates. The normalization was done with 3 hours MTT assay data. (n=4, One-way ANOVA, Tukey's post hoc test, *** indicates the p value $p\leq0.001$). **(C)** Control and *MINPP1*$^{-/-}$ HEK293 were cultured with Annexin-V containing growth media for 48 hours inside the IncuCyte live-cell analysis system, and images were captured with red fluorescence channel to detect Annexin-V positive cells. Graph shows the average ratio (±s.d.) of red cell object count per mm$^2$ (n=3, two-tailed student's t-test, not significant).

To examine whether the observed growth defect in *MINPP1*$^{-/-}$ HEK293 cells is due to a potential cell death, we assessed the apoptosis rate of *MINPP1*$^{-/-}$ HEK293 cells, using Annexin-V fluorescent conjugates. Annexin-V detects externalized phosphatidylserines, a key characteristic of an apoptotic cells (Mariño and Kroemer, 2013; Vermes et al., 1995). Interestingly, during 48-hours of cell culture, the number of Annexin-V$^{+}$ positive particles remained comparable between the cultures of control and *MINPP1*$^{-/-}$ HEK293 cells, showing that MINPP1 loss does not affect apoptosis in HEK293 cells (Figure 29C). Absence of an apoptotic phenotype further suggested that the growth phenotype observed in *MINPP1*$^{-/-}$ HEK293 cells is due to a proliferation defect.

### 1.2.3 *MINPP1* missense PCH variants do not rescue proliferation defect of *MINPP1* KO.

Next, we sought to use this *MINPP1* KO proliferation phenotype to determine the effect of the *MINPP1* missense variants (i.e. Y53D, E486K) on protein function. To achieve this, we transiently overexpressed either of the FLAG-tagged MINPP1 missense variants in *MINPP*$^{-/-}$ HEK293 and assessed their growth rate using MTT assay. After 48 hours of culture, the growth rate between *MINPP1*$^{-/-}$ cells and *MINPP1*$^{-/-}$ cells overexpressing either of the *MINPP1* missense variants remain comparable, indicating that both of the overexpressed MINPP1 missense variants are unable to rescue the *MINPP1* KO proliferation phenotype in HEK293 cells (Figure 29B). Thus, considering a 70% of transfection efficiency, this data showed that both *MINPP1* missense PCH variants result in loss of function of *MINPP1*. Hence, from now on, we will refer to these *MINPP1* missense variants as *MINPP1* missense mutations.

### 1.2.4 MINPP1 loss tends to alter extracellular inositol phosphate metabolism in HEK293 cells.

Before testing the effect of PCH-associated *MINPP1* mutations on cellular enzyme activity, we took advantage of our *MINPP1*$^{-/-}$ HEK293 cell model in order to clarify the recently proposed role of MINPP1 as a secretory phosphatase in a human carcinoma cell line (Windhorst et al., 2013). Hence to elucidate this proposition, we collected conditioned media from both control and *MINPP1*$^{-/-}$ HEK293 cells and incubated them with $IP_6$ for 2 to 6 hours at 37 °C. PAGE analysis after extraction of inositol phosphates, revealed a complete degradation of $IP_6$ in conditioned medium from control cells after 4 hours of incubation (Figure 30A). Conversely, $IP_6$ was still detectable in conditioned medium from *MINPP1*$^{-/-}$ HEK293 cells even after 6 hours of incubation, indicating the absence of an $IP_6$-phosphatase activity. Hence, these data showed that MINPP1 can act also as a secretory phosphatase in HEK293 cells, in addition to its predominant ER-resident phosphatase activity.

To further clarify the activity of MINPP1 as a secreted phosphatase, we performed inositol metabolic radiolabelling in control and *MINPP1*$^{-/-}$ HEK cells and collected their culture media after five days of treatment with tritiated inositol (*myo*-[$^3$H]-inositol) (in collaboration with A.Saiardi UCL, UK). We then acid-extracted extracellular inositol phosphates and separated them into fractions with SAX-HPLC. Next, we measured the radioactivity of each fraction by beta-counter and analysed the extracellular inositol phosphate levels by normalizing to the inositol-lipid fraction. Interestingly, the analysis of *MINPP1*$^{-/-}$ HEK293 culture media showed a marked increase in extracellular $IP_3$ levels, mirrored by a robust decrease in extracellular $IP_2$ levels (Figure 30B). Hence, it can be hypothesized that MINPP1 can convert extracellular $IP_3$ into $IP_2$, rather than the $IP_6$. To this extent, it was interesting to notice that $IP_6$ was absent in the culture media. From a pathological point of view, this analysis also indicated

that MINPP1 loss can have an impact on extracellular inositol phosphate metabolism in HEK293 cells.

### 1.2.5 MINPP1 loss leads to an altered intracellular inositol phosphate metabolism with a marked increase in $IP_6$ levels in HEK293 cells.

To explore the effect of *MINPP1* loss on intracellular inositol phosphate metabolism, the best-characterised metabolic pathway of MINPP1, we performed *myo*-[$^3$H]-inositol metabolic radiolabelling in control and HEK293 *MINPP1*$^{-/-}$ cells, as previously introduced in the above section. Once the exogenously added *myo*-[$^3$H]-inositol enters to the cytosol, it initially follows the phosphatidylinositol pathway to form [$^3$H]-$IP_3$. [$^3$H]-$IP_3$ then serves as a building block for the generation of low and high ordered tritiated inositol phosphates (Figure 30C). To ensure a steady state radiolabelling in all of the inositol phosphate pools, we treated the cells with *myo*-[$^3$H]-inositol for three days. We then proceeded with the analysis of inositol phosphates, as previously explained in the above section. As $IP_5$ and $IP_6$ are known to be the main substrate of MINPP1 in mammalian cells, we initially focused on analysing these inositol polyphosphates in our HEK293 *MINPP1*$^{-/-}$ cell model. Intriguingly, the analysis of *MINPP1*$^{-/-}$ HEK293 cells revealed a 3-fold increase in $IP_6$ levels, with a moderate increase in $IP_5$ levels, when compared to the control cells (Figure 30D). Such a marked increase in $IP_6$ levels was not expected, considering the already high levels of $IP_6$ in normal cells and the previously reported $IP_6$ phenotype in *Minpp1*$^{-/-}$ mice model, displaying an only 1.5 fold increase in $IP_6$ levels (Chi et al., 2000). Hence, these data clearly illustrated the strong impact of MINPP1 loss on cellular $IP_6$ levels in HEK293 cells. Surprisingly, in addition to these findings, we also found a severe decrease in $IP_2$ and IP levels in HEK293 *MINPP1*$^{-/-}$ cells, when compared to the control cells (Figure 30D). To test for the specificity of the $IP_6$ and $IP_2$ phenotypes seen in our *MINPP1*$^{-/-}$ KO model, we transiently overexpressed FLAG-tagged-WT MINPP1 in *MINPP1*$^{-/-}$ HEK293cells after the *myo*-[$^3$H]-inositol metabolic labelling and indeed found almost

complete rescue of $IP_6$ and $IP_2$ levels, at a transfection efficiency of ~70% (Figure 30E, F). Hence, overall, these analysis clearly showed that MINPP1 loss impairs intracellular inositol phosphate metabolism, with a robust increase in $IP_6$ levels in HEK293 cells.

### 1.2.6 The impact of *MINPP1* missense PCH mutations on cellular enzyme activity

Next, we sought to determine the effect of *MINPP1* missense PCH mutations on cellular enzyme activity. To achieve this, we transiently overexpressed FLAG-tagged Y53D or E486K MINPP1 mutant in HEK293 *MINPP1*$^{-/-}$ cells after the *myo*-[$^3$H]-inositol metabolic labelling. We then assessed the effect of these over-expressed MINPP1 mutants on $IP_6$ and $IP_2$ levels. Intriguingly, HEK293 *MINPP1*$^{-/-}$ cells overexpressed with the Y53D mutant phenocopied the $IP_6$ and $IP_2$ phenotypes of *MINPP1* KO, indicating a clear loss enzyme activity for this missense mutant (Figure 30E, F). This result was in line with the previous *in silico* prediction analysis in which Y53D missense mutation is predicted to disrupt MINPP1 catalytic activity by introducing structural damage at the site of histidine phosphatase domain (see previous section 1.1). On the one hand, overexpression of E486K mutant in HEK *MINPP1*$^{-/-}$ cells showed a rescue effect on the $IP_6$ and $IP_2$ levels of HEK293 *MINPP1*$^{-/-}$ cells, indicating that this missense mutant is catalytically active in this over-expression setup (Figure 30 E, F). The observation that E486K mutant does not affect enzyme activity but affects HEK293 cell proliferation, led us to deduce that this missense mutation could impact the regulation of MINPP1.

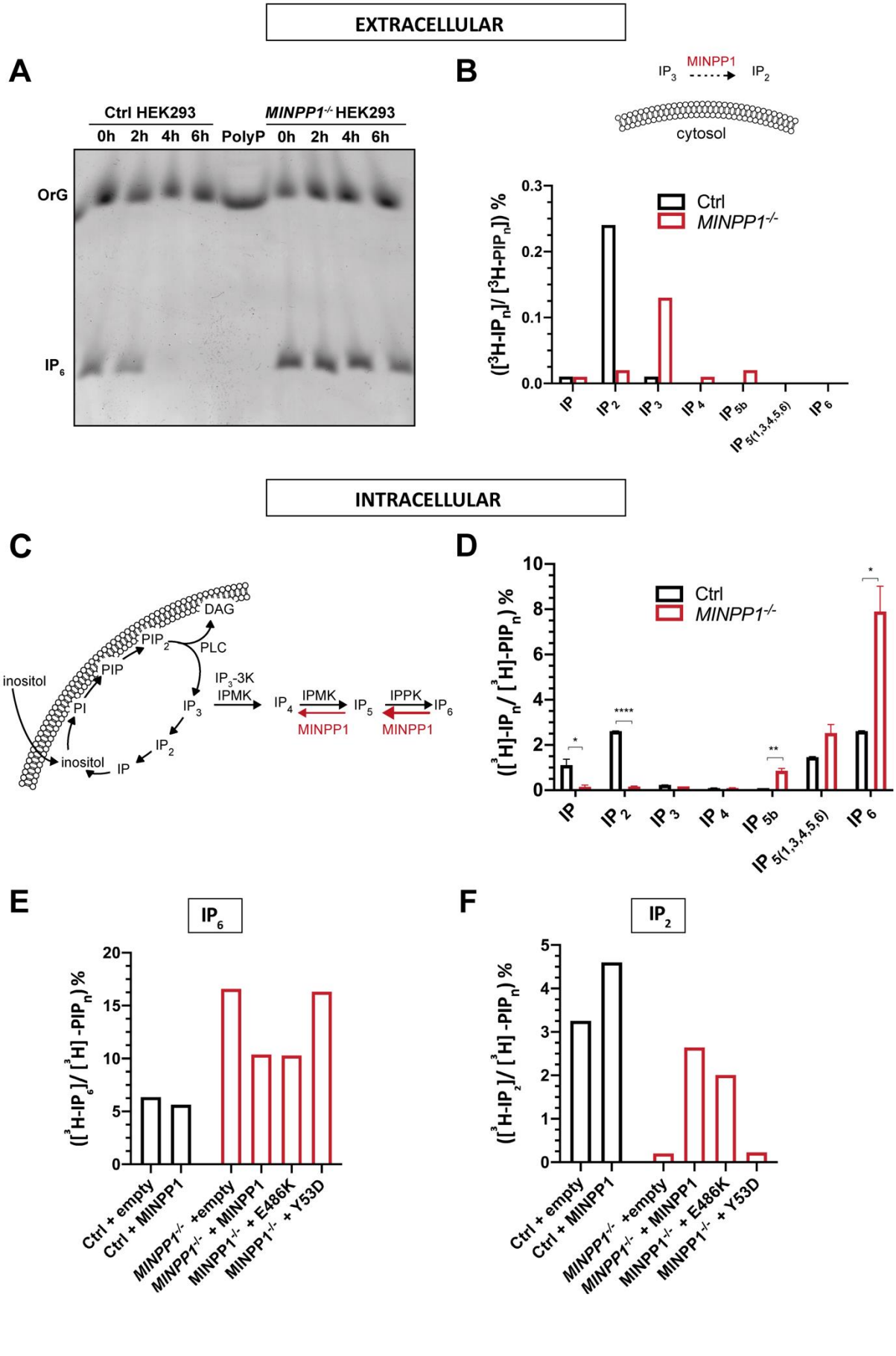
EXTRACELLULAR
A
Ctrl HEK293
MINPP1-/- HEK293
0h 2h 4h 6h PolyP 0h 2h 4h 6h
OrG
IP6
B
IP3 MINPP1 IP2
cytosol
([3H-IPn]/ [3H-PIPn]) %
Ctrl
MINPP1-/-
IP IP2 IP3 IP4 IP5b IP5(1,3,4,5,6) IP6
INTRACELLULAR
C
DAG
PIP2
PLC
PIP
inositol
IP3-3K
IPMK
PI
IP3
IP4
IPMK
IP5
IPPK
IP6
MINPP1
MINPP1
IP2
inositol
IP
D
([3H]-IPn/[3H]-PIPn) %
Ctrl
MINPP1-/-
IP IP2 IP3 IP4 IP5b IP5(1,3,4,5,6) IP6
E
IP6
([3H-IP6]/ [3H] -PIPn) %
Ctrl + empty
Ctrl + MINPP1
MINPP1-/- +empty
MINPP1-/- + MINPP1
MINPP1-/- + E486K
MINPP1-/- + Y53D
F
IP2
([3H-IP2]/ [3H] -PIPn) %
Ctrl + empty
Ctrl + MINPP1
MINPP1-/- +empty
MINPP1-/- + MINPP1
MINPP1-/- + E486K
MINPP1-/- + Y53D

**Figure 30. The extracellular and intracellular inositol phosphate metabolism in HEK293 cellular models of PCH-associated *MINPP1* mutations. (A)** PAGE analysis showing the presence and absence of $IP_6$-phosphatase activity in the conditioned media from control and *MINPP1*$^{-/-}$ HEK293 cells, respectively. 4nmol of $IP_6$ was added to the conditioned media and incubated at 37°C for the time period indicated. The samples were then mixed with Orange G (OrG) loading dye and resolved by PAGE followed by toluidine blue staining. Gel image representative of two independent experiments. Polyphosphate (PolyP) is shown as size ladder. **(B)** SAX-HPLC analysis of inositol phosphates in culture media of control and *MINPP1*$^{-/-}$ HEK293 cells, following inositol radioactive metabolic labelling. Abbreviations: ($IP_2$), inositol bisphosphate; ($IP_3$), inositol 1,4,5-trisphosphate; (MINPP1) Multiple Inositol-Polyphosphate Phosphatase 1**. (C)** Schematic representation of inositol cycle. Abbreviations: (inositol), *myo*-inositol; (PI), phosphatidylinositol; (PIP), phosphatidylinositol phosphate; ($PIP_2$), phosphatidylinositol 4,5-bisphosphate; (DAG), diacylglycerol; (PLC), phospholipase C; (IP), inositol phosphate; ($IP_4$), inositol 1,3,4,5-tetrakisphosphate; ($IP_5$), inositol pentakisphosphate; ($IP_6$), inositol hexakisphosphate ($IP_6$); (IPMK), Inositol Polyphosphate Multikinase; ($IP_3$-3K), I(1,4,5)$P_3$ 3-Kinase; (IPPK), Inositol-Pentakisphosphate 2-Kinase. **(D)** SAX-HPLC analysis of inositol phosphates in control and *MINPP1*$^{-/-}$ HEK293 cells following inositol radioactive metabolic labelling. **(E-F)** SAX-HPLC analysis of $IP_2$ and $IP_6$ in control and *MINPP1*$^{-/-}$ HEK293 cells transiently transfected with plasmids encoding empty vector, wildtype, Y53D or E486K mutant MINPP1 after the *myo*-[$^3$H]-inositol metabolic labelling. The data is representative of two independent experiments. **(B, D, E, F)** The peaks ([$^3$H]-$IP_n$) were identified based on comparison to standards. [$^3$H]-$IP_n$ levels are presented as percentage of total radioactivity in the inositol-lipid fraction ([$^3$H]-$PIP_n$). All error bars represent standard deviation (s.d.). (n=2, Two-tailed student's t-test ; *, **, **** indicate p values $p<0.05$, $p<0.01$, $p \leq 0.0001$, respectively). Abbreviations: IPn, inositol phosphates; $PIP_n$, phosphatidyl inositol phosphates.

### 1.2.7 Under high iron condition, MINPP1 loss alters iron homeostasis by depleting free intracellular iron in HEK293 cells.

Next, we tried to understand how a defective inositol phosphate metabolism could impede cell proliferation and hence cell physiology in HEK293 cells. Considering the strong impact of MINPP1 absence on cellular $IP_6$ levels and the known chelating properties of this molecule for divalent cations (e.g. $Fe^{3+}$, $Ca^{2+}$, $Mg^{2+}$), we hypothesized that an intracellular accumulation of $IP_6$ could deplete intracellular free cations that are essential for cell proliferation in HEK293 cells. Hence based on this hypothesis, we assume that MINPP1 absence can indirectly have consequences on intracellular cation homeostasis in HEK293 cells. Since at physiological pH, $IP_6$ has a strong binding affinity to iron, we first focused on studying the effect of MINPP1 absence on iron homeostasis (Veiga et al., 2006). In normal cells, almost all of the iron (>95%) is protein-bound, most of them being stored mainly in the protein ferritin

(Figure 31A, Crichton, 2001). The remaining iron, referred to as intracellular free or labile iron, is found in its chemically labile, exchangeable and chelatable transitory form (reviewed in Cabantchik, 2014; Hare et al., 2013). Hence, in order to study the effect of MINPP1 loss on both of these iron forms, we measured both the total and free intracellular iron levels in *MINPP1*$^{-/-}$ HEK293 cells, using colorimetric-based assays in which $Fe^{2+}$ is detected by forming stable coloured-complexes with either ferrozine or ferene-S. For some samples, we pre-treated the cell lysates with HCl/$KMnO_4$ at pH 1.4 (Riemer et al., 2004). This treatment enabled the separation of iron from its binding molecules, including proteins and $IP_6$ (Torres et al., 2005) and allows the quantification of total intracellular iron. For other samples, we measured only the free intracellular iron levels using standard lysis at pH 4.6, which maintained proteins and $IP_6$ complexed with iron. Since in many cellular and mouse models, iron accumulation and deficiency phenotypes are only visible in the presence of an excess of iron, we performed these measurements in high iron (provided with ferric ammonium citrate; +FAC) and in low iron (-FAC) conditions (Das et al., 2015; Drecourt et al., 2018; Zheng et al., 2018). Intriguingly, after two days of incubation with FAC, we observed a 1.5-fold increase in the total iron content in *MINPP1*$^{-/-}$ HEK293 cells (Figure 31B). Mirroring this observation, *MINPP1*$^{-/-}$ cells showed a 58% decrease in their total free iron levels, when compared to the control cells (Figure 31C). Hence, these findings suggest that under high iron condition, MINPP1 absence leads to a massive accumulation of complexed iron and depletion of intracellular free iron in HEK293 cells. This conclusion was in line with our hypothesis, suggesting an abnormal cation homeostasis resulting from an increase in $IP_6$-iron chelating activity. Indeed, considering $IP_6$'s higher affinity for $Fe^{3+}$ in comparison to $Fe^{2+}$, it was interesting to observe that the iron depletion phenotype was mainly contributed by a decrease in free cellular $Fe^{3+}$ levels in *MINPP1*$^{-/-}$ cells (Figure 31D, E, Hambidge, 2010; Helmis et al., 2013).

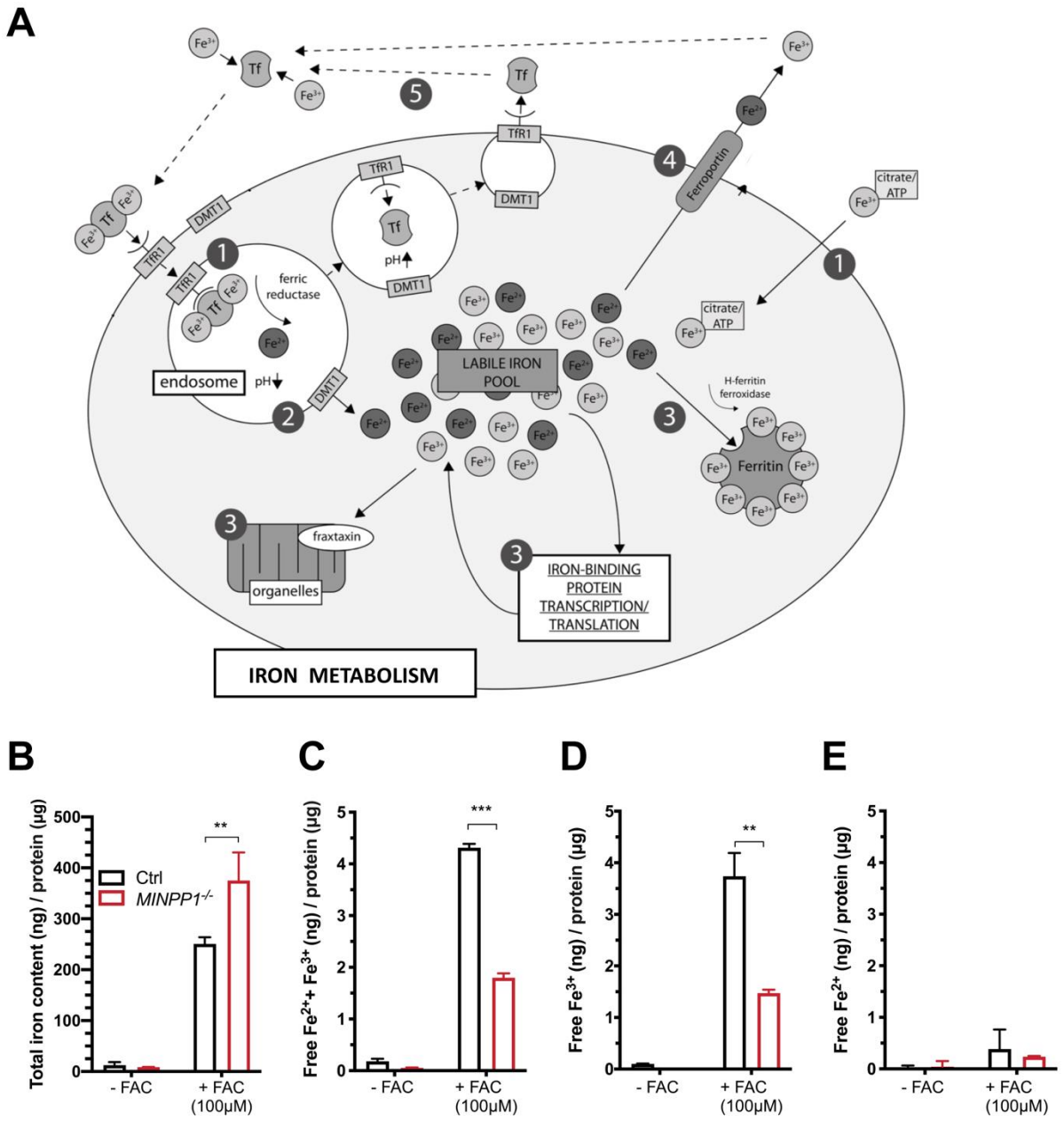


**Figure 31. Under high iron condition, MINPP1 loss alters iron homeostasis by depleting free intracellular iron levels in HEK293 cells. (A)** Diagrammatic representation of the iron metabolism (from Hare et al., 2013). (1) Iron is transported into the cells via transferrin-receptor-(TfR1) mediated endocytosis or citrate/ATP. (2) Once the iron is exported from the endosome via divalent metal transporter-1 (DMT1), it directly contributes to the intracellular free iron pool. The composition of this pool varies depending on the metal concentration, pH and the presence of iron chelators within the environment. (3) In normal cells, almost all of the iron (>95%) is protein-bound, most of them being stored mainly in the protein ferritin. (4) Iron is exported from the cells via the transporter ferroprotein and further recirculated by iron free transferrin. **(B-E)** Quantification of total iron content (**B**), free iron ($Fe^{2+}$ and $Fe^{3+}$) (**C**), $Fe^{3+}$ (**D**) and $Fe^{2+}$ (**E**) levels in extracts from control and *MINPP1*$^{-/-}$ HEK293 cells grown under low (-FAC) and high iron (+FAC, 100 µM) conditions. All values are normalized to the total protein concentration and represent the mean ± s.d (n=3, Two way ANOVA Sidak test, **, *** indicate p values $p<0.01$ and $p<0.001$, respectively).

### 1.2.8 MINPP1 loss alters calcium homeostasis by depleting the calcium pools in the cytosol and the ER in HEK293 cells.

Next, we sought to further explore the effect of MINPP1 absence on cellular cation homeostasis and thereby measured the cytosolic free $Ca^{2+}$ levels in control and *MINPP1*$^{-/-}$ HEK293 cells using FLUO-4-AM calcium binding indicator (Kreitzer et al., 2000). We then normalized the data to the cell number by MTT growth assay. Strikingly, we found an almost 50% decrease in cytosolic free $Ca^{2+}$ levels in *MINPP1*$^{-/-}$ HEK293 cells, when compared to the control cell line, suggesting that MINPP1 loss causes a depletion in cytosolic free $Ca^{2+}$ levels in HEK293 cells (Figure 32B).

To assess whether this depletion phenotype could have an impact on $Ca^{2+}$ signalling and $Ca^{2+}$ ER pool, we evaluated the response of *MINPP1*$^{-/-}$ HEK293 cells to $Ca^{2+}$ mobilisation from the internal stores. Hence, we started our investigation by treating *MINPP1*$^{-/-}$ HEK293 cells with 10 mM caffeine, as it induces $Ca^{2+}$ release from the ER by activating mainly the ryanodine receptors (RyRs) (Figure 32A, Kong et al., 2008). In response to 10 mM caffeine, we observed a significant peak in the cytosolic $Ca^{2+}$ levels within a minute in the control cells. However, we could only detect a slight increase with a sustained plateau in *MINPP1*$^{-/-}$ HEK293 cells (Figure 32C). To better understand this $Ca^{2+}$ mobilization defect, we further studied the response of *MINPP1*$^{-/-}$ cells to ionomycin, as it is known to deplete ER-stored $Ca^{2+}$ by activating $Ca^{2+}$-induced calcium release (CICR) mechanism (Figure 32A, Müller et al., 2013). In response to ionomycin, the control and *MINPP1*$^{-/-}$ HEK293 cells exhibited an initial $Ca^{2+}$ peak with a sustained plateau. However, the relative response to ionomycin stimulation was again significantly decreased in *MINPP1*$^{-/-}$ cells (Figure 32D). This observation prompted us to question whether the observed $Ca^{2+}$ mobilization defects are due to a decrease in the intracellular $Ca^{2+}$ ER stores or due to an inhibition of the calcium entry. In an attempt to provide answer to this question, we repeated both of these studies in the absence of extracellular $Ca^{2+}$

and interestingly obtained similar results for both caffeine and ionomycin data (Figure 32E, F). Hence, these findings suggest that $Ca^{2+}$ mobilization defects seen in *MINPP1*$^{-/-}$ HEK293 cells are due to a decrease in intracellular $Ca^{2+}$ ER stores. In an attempt to assess the specificity of these $Ca^{2+}$ mobilization defects, we generated a stable expression line of WT MINPP1 in *MINPP1*$^{-/-}$ HEK293 cells and indeed found partial but significant restoration in caffeine and ionomycin-induced $Ca^{2+}$ mobilization (Figure 32C-F). Overall, these findings showed that MINPP1 absence impairs calcium homeostasis by reducing intracellular calcium pools in the cytosol and the ER in HEK293 cells. This conclusion was again in line with our initial hypothesis, proposing for a potential abnormal cation homeostasis resulting from an increase $IP_6$-calcium chelation activity. To this extent, owing to MINPP1's predominant localization in the ER, it was interesting for us to observe an ER-$Ca^{2+}$ depletion phenotype in *MINPP1*$^{-/-}$ HEK293 cells.

.

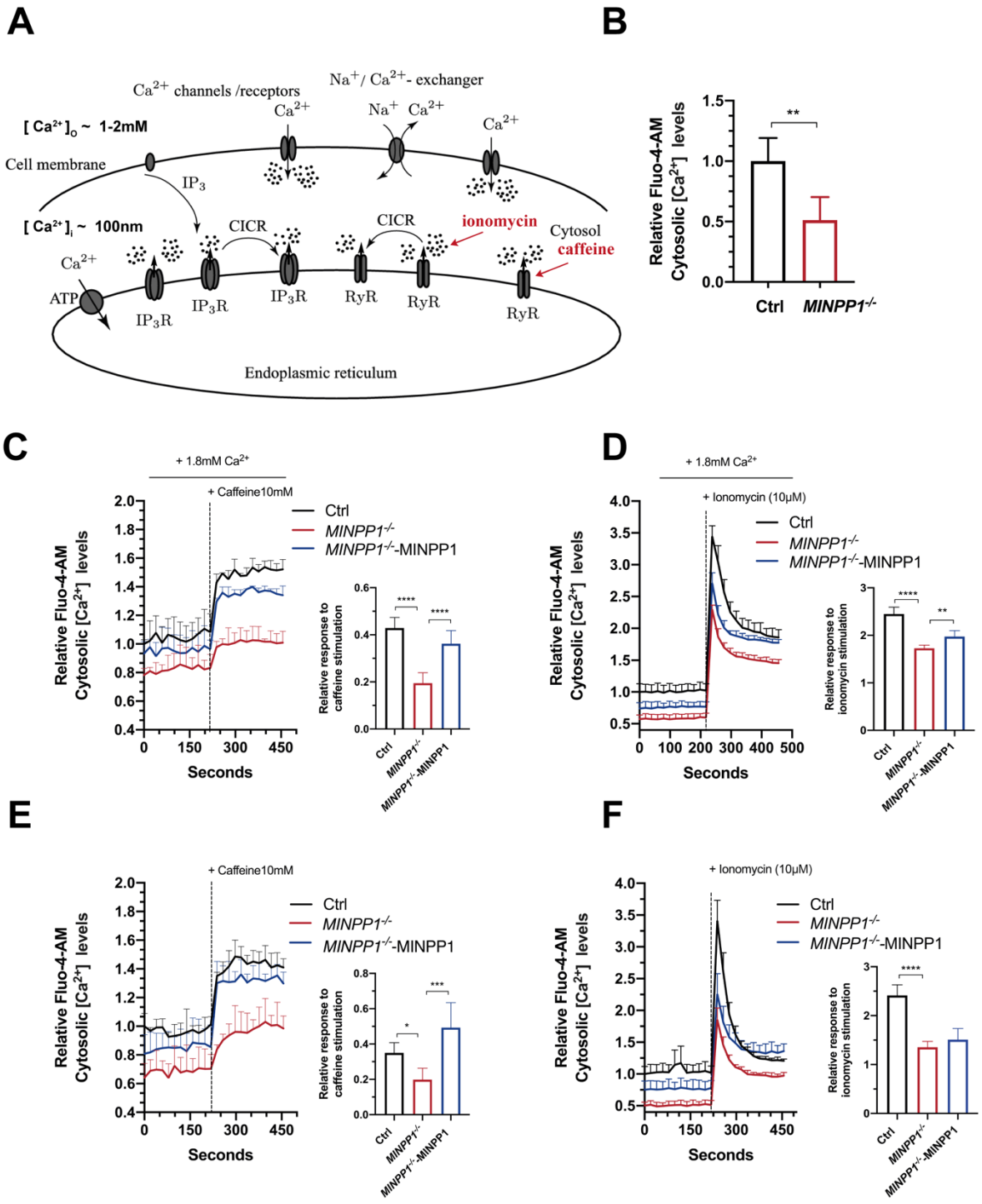


**Figure 32. MINPP1 loss alters intracellular $Ca^{2+}$ homeostasis by depleting cytosolic calcium levels in HEK293 cells. (A)** Diagrammatic representation depicting the calcium-induced calcium release (CICR) mechanism and mode of action of ionomycin and caffeine on $Ca^{2+}$ signalling. CICR is a ubiquitous process by which $Ca^{2+}$ enhances its own release from the endoplasmic reticulum via inositol trisphosphate (IP3Rs) and ryanodine receptors (RyRs), hence resulting in the amplification of the $Ca^{2+}$ signals. Caffeine, as a $Ca^{2+}$ mobilizer, induces $Ca^{2+}$ release from the endoplasmic reticulum by activating mainly the ryanodine receptors (RyRs). On the one hand, ionomycin, as a membrane permeable $Ca^{2+}$ ionophore, increase massively the cytosolic $Ca^{2+}$ levels by activating CICR mechanism, mainly via the RyRs. (adapted from Timofeeva, 2019). **(B)** Relative Fluo-4-AM cytosolic $Ca^{2+}$ levels in control and

*MINPP1*$^{-/-}$ HEK293 cells. **(C-F)** Relative Fluo-4-AM cytosolic $Ca^{2+}$ levels in control, *MINPP1*$^{-/-}$ and overexpression line of MINPP1 in *MINPP1*$^{-/-}$ HEK293 cells (*MINPP1*$^{-/-}$-MINPP1) loaded either with 10 mM caffeine (**C, E**) or 10 µM ionomycin (**D, F**) in the presence (1.8mM) or absence of extracellular calcium**.** The dotted line indicates the addition of either caffeine (**C, E**) or ionomycin (**D, F**). Relative response after caffeine or ionomycin stimulation (peak) is represented graphically (inset). For all of the calcium assay experiments, the data are normalized to the cell number with MTT colorimetric assay and presented as mean values relative to the control baseline fluorescence intensity ± s.d. (**B**) n=5 (**C-F**) n=6, Two-tailed student's t-test (E-F) and one-way ANOVA, Tukey's post hoc test, *, **,*** and **** indicate p values $p<0.05$, $p<0.01$, $p<0.001$, $p<0.0001$, respectively).

### 1.2.9 Summary of the findings obtained from our HEK293 cell models

Altogether, our HEK293 cell models with PCH-associated *MINPP1* mutations allowed us to draw the following main conclusions: First, we identified that MINPP1 loss impairs cell proliferation in HEK293 cells and hence impedes cellular physiology. Then, we demonstrated that PCH-associated *MINPP1* mutations are deleterious for the protein function. Additionally, we have shown that MINPP1 loss leads to defects in inositol phosphate metabolism, with a marked accumulation of intracellular $IP_{6.}$ Finally, we found that MINPP1 loss has a major impact on cation homeostasis.

## 1.3 Insights into the function of *MINPP1* on mammalian brain development

The identification of *MINPP1* as a PCH-causing gene prompted us to question whether the initial characterization study of a previously generated *Minpp1*$^{-/-}$ mouse model had overlooked a brain phenotype. To assess that, we generated a CRISPR/Cas9-mediated *Minpp1*$^{-/-}$ mouse model on a C57BLKS/J background, which indeed allowed us to reveal initial insights into the impact of Minpp1 absence on mammalian brain development (Figure 33).

### 1.3.1 Minpp1 loss leads to a reduction in brain weight and cerebral cortical thickness in P21 mouse.

To identify a mouse brain developmental defect, we first determined the brain weight of wild type and *Minpp1*$^{-/-}$ mice. Interestingly, *Minpp1*$^{-/-}$ mice showed a mild but significant reduction (~13%) in the brain weight at P21, a time point when the brain reached its final organization (Figure 33C, Altman and Bayer, 1979; Miale and Sidman, 1961). To assess whether this brain phenotype is progressive, we further determined the brain weight of *Minpp1*$^{-/-}$ mice at 11-months-old. The decrease of the average brain weight of 11-month-old *Minpp1*$^{-/-}$ mice was comparable to that of P21 (Figure 33C). Hence, these observations suggested that reduction in brain weight is likely to result from an early defect occurring during development, rather than from a progressive neurodegeneration or delayed maturation. In an attempt to better characterize this brain phenotype, we next histologically analysed the cerebellum and cerebral cortex of wild type and *Minpp1*$^{-/-}$ mice at P21. The histological analyses with haematoxylin and eosin staining did not reveal major differences in cerebellar and cerebral cortex architecture between the wild type and *Minpp1*$^{-/-}$ mice (Figure 33D, E). However, interestingly, we detected a mild but significant ~10% decrease in the cortical thickness in *Minpp1*$^{-/-}$ mice at P21 (Figure 33E, F). Hence, although our *Minpp1*$^{-/-}$ mice model awaits more thorough characterization, these initial observations suggested that Minpp1 loss impacts mouse brain, including cerebral cortex development.

### 1.3.2 Minpp1 loss reduces intracellular free $Ca^{2+}$ levels in E14.5 mouse cortical neural progenitors.

Next, we sought to identify a potential cause for the cortical phenotype observed in our *Minpp1*$^{-/-}$ mouse model. For that, we have taken into account the $IP_6$ accumulation phenotype identified in the previously generated *Minpp1*$^{-/-}$ mice and the cation depletion phenotypes that we detected in our MINPP1$^{-/-}$ HEK293 cell model. Hence, based on these two observations, we hypothesized that Minpp1 loss could have an impact on cation physiology in the mouse brain, impairing the proper development of the cerebral cortex. To assess this hypothesis, we explored the effect of Minpp1 absence on $Ca^{2+}$ homeostasis in E14.5 cortical neural progenitors, a developmental time point when there is a neurogenesis peak in the telencephalon with a major increment in the cortical thickness (Altman and Bayer, 1979; Grove and Tole, 1999; Molyneaux et al., 2007; Takahashi et al., 1993). Intriguingly, in line with our *MINPP1*$^{-/-}$ HEK293 cell model, we observed a 34% decrease in intracellular free $Ca^{2+}$ levels in the *Minpp1*$^{-/-}$ mouse neural progenitor cells when compared to the wild type cells (Figure 33G). Hence these initial attempts, showed that Minpp1 loss also has a major impact on free $Ca^{2+}$ availability in mouse cortical neural progenitors. This finding further revealed the presence of a common *MINPP1*-related pathological mechanism between species, suggesting an abnormal cation homeostasis due to the defective regulation of MINPP1-mediated $IP_6$ homeostasis.

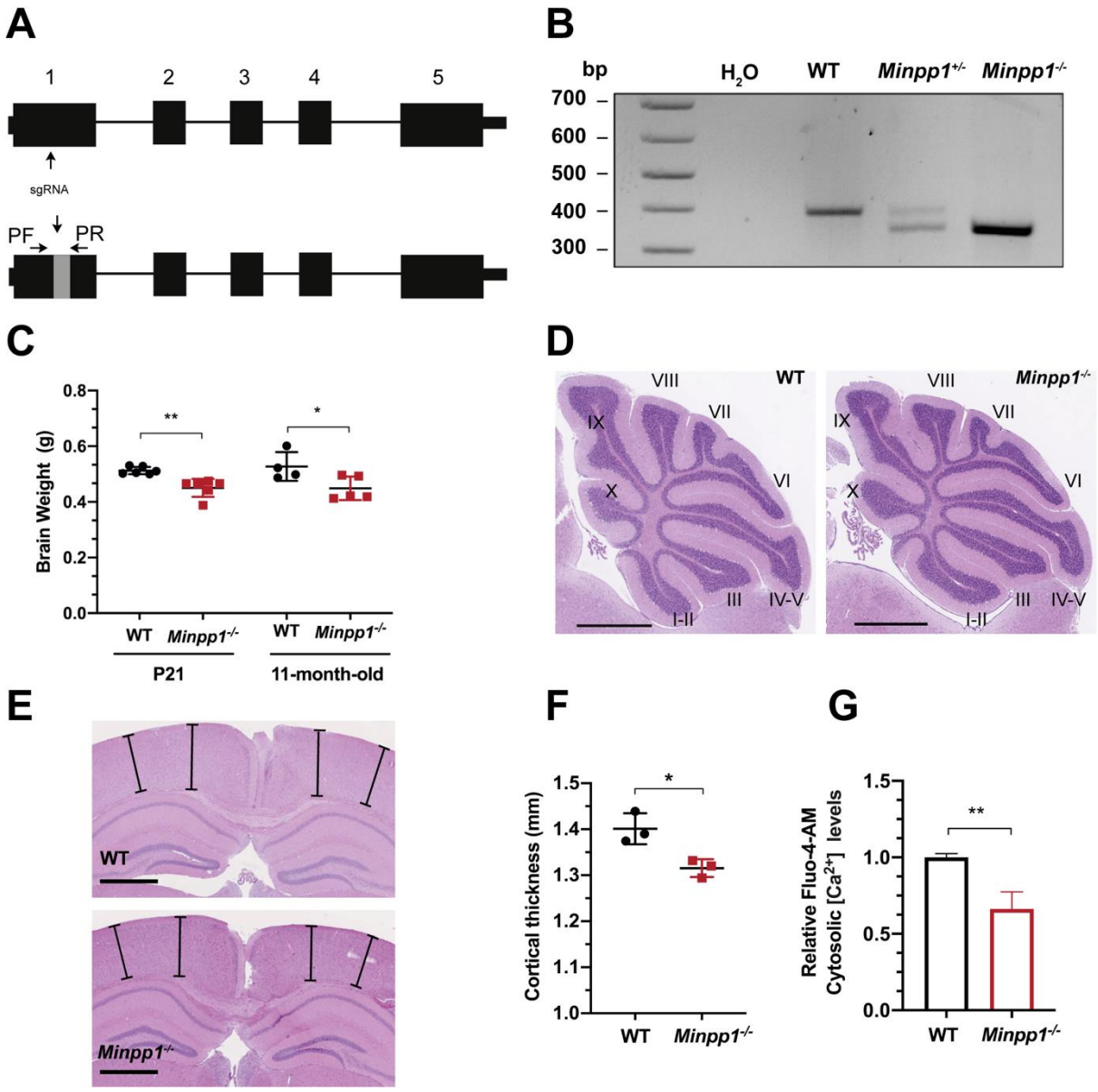


**Figure 33. Generation and characterization of CRISPR-Cas9 *Minpp1*$^{-/-}$ mouse. (A)** Schematic representation of the sgRNA targeting site and the location of PCR primers. Abbreviations used: Primer Forward (PF) and Primer Reverse (PR). (**B**) PCR based genotyping of *Minpp1*$^{-/-}$ mice indicated successful knockout alleles showing a 31 bp deletion and a smaller PCR product. (**C**) Quantification of total brain weight in grams (g) from P21 and 11-month old WT and *Minpp1*$^{-/-}$ mice. (N>4 mice, Two-tailed student's t-test, * and ** indicate p values $p<0.05$ and $p<0.01$, respectively). **(D)** Representative images of haematoxylin-eosin (HE) staining on P21 sagittal slices of wild type (WT) and *Minpp1*$^{-/-}$ mutant cerebellum, scale bar 1 mm. (**E**) Representative images of haematoxylin-eosin (HE) staining on P21 coronal slices of WT and *Minpp1*$^{-/-}$ mutant cortex **(F)** Quantification of the cortical thickness for the WT and *Minpp1*$^{-/-}$ cortex at P21 (N=3 mice, 30 sections per each mouse; Two-tailed Student's t-test, * indicates p value $p<0.05$). **(G)** Relative Fluo-4-AM cytosolic $Ca^{2+}$ levels in WT and *Minpp1*$^{-/-}$ E14 mouse neural progenitors. The data are normalized to cell number with MTT colorimetric assay and presented as mean values relative to control baseline fluorescence intensity control ± s.d.(N=3, Two-tailed student's t-test, ** indicates the p value $p<0.01$).

### 1.3.3 The summary of the findings obtained from our *Minpp1*$^{-/-}$ mouse model

To sum up this section, our initial characterization studies in *Minpp1*$^{-/-}$ mouse model allowed us to deduce the following conclusions. We identified that Minpp1 plays a role during mouse cortical cortex development. It is possible that this role is played through the regulation of cation physiology as Minpp1 absence impairs $Ca^{2+}$ physiology in mouse cortical neural progenitors.

## 1.4 Unravelling *MINPP1*-PCH disease mechanisms using iPSCs

Next, we wanted to investigate how loss-of-function mutations in *MINPP1* could cause the neurological dysfunctions observed in PCH patients. To explore this point, we took an iPSC-based disease modelling approach and hence derived iPSCs from patient CerID-30-2, harbouring a homozygous early-truncating mutation in *MINPP1* (Figure 34A, Figure 35). To study the patient-mutation in an isogenic cellular setting, we also generated *MINPP1*$^{-/-}$ iPSCs derived from a non-disease affected individual, which indeed allowed us to establish direct causality between loss of function of *MINPP1* and its PCH-causing phenotypic effects (Figure 34B, Figure 35).

We designed our study by considering the fact that both of our *MINPP1*-PCH iPSC models were generated using different non-integrative reprogramming methods (Figure 34). Indeed, while patient-derived iPSC line was derived via RNA-based reprogramming approach, the unedited isogenic control of *MINPP*$^{-/-}$ iPSC line (Ctrl-I004) was generated using Sendai virus-mediated reprogramming technique. Hence, in an attempt to minimize reprogramming-based variability between our *MINPP1*-PCH iPSC models, we used a matched pair design in which patient-derived iPSC line was matched with a control iPSC line (Ctrl-D10) generated using RNA-based reprogramming approach (Figure 34A). Likewise, we paired *MINPP1*$^{-/-}$ iPSCs with its isogenic control iPSC line (Ctrl-I004) (Figure 34B). Hence, all the phenotypic comparisons are assessed based on this matched pairs design.

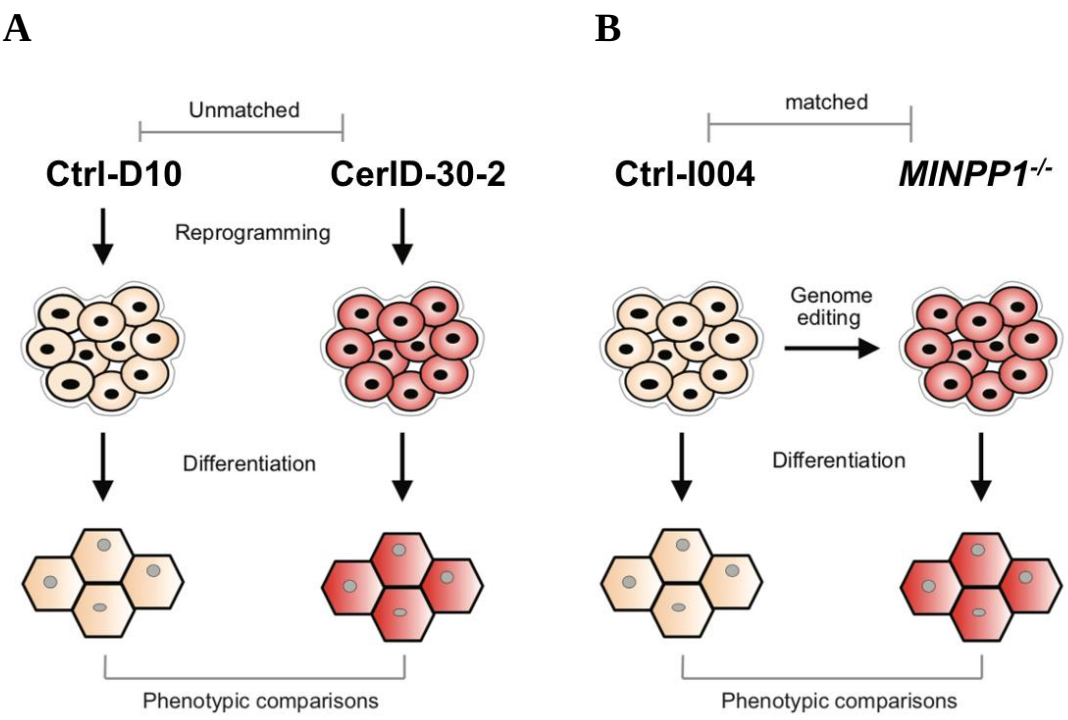


**Figure 34. Schematic illustration of our study design for modelling *MINPP1*-PCH using iPSCs (adapted from Musunuru, 2013)**. To establish direct causality between genotype and phenotype, we generated a patient-derived iPSC line (CerID-30-2) harbouring early-truncating mutation in *MINPP1* and a CRISPR-Cas9 *MINPP1* knock-out iPSC line (*MINPP1*$^{-/-}$) derived from a non-disease affected individual. Control (Ctrl-D-10 and Ctrl-I004) and *MINPP1* mutant (CerID-30-2 and *MINPP1*$^{-/-}$) iPSC lines were matched based on the reprogramming strategy.

We next assessed the quality of our iPSC lines to ensure their usability for modelling *MINPP1*-PCH (Figure 35). Indeed, we confirmed the pluripotency in all of our iPSC models by performing first immunofluorescence and flow cytometry for the embryonic and pluripotency markers OCT4, SOX2, SSEA-4 and TRA-1-81 (Figure 35A, B). Additionally, we assessed embryoid body formation and showed their differentiation potential into three germ layers (Figure 35C, the ectoderm marker is not shown). Furthermore, we assessed the genomic integrity in all of the iPSC lines by performing 60K CGH array analysis, containing 60K probes that covers up the whole genome with a space of 40kb between the probes (Malan and Romana, 2012). This analysis did not reveal obvious chromosomal abnormalities in our iPSC lines (data not shown). Overall, this characterization study allowed us to confirm the quality of our iPSC models, ensuring valid disease modelling.

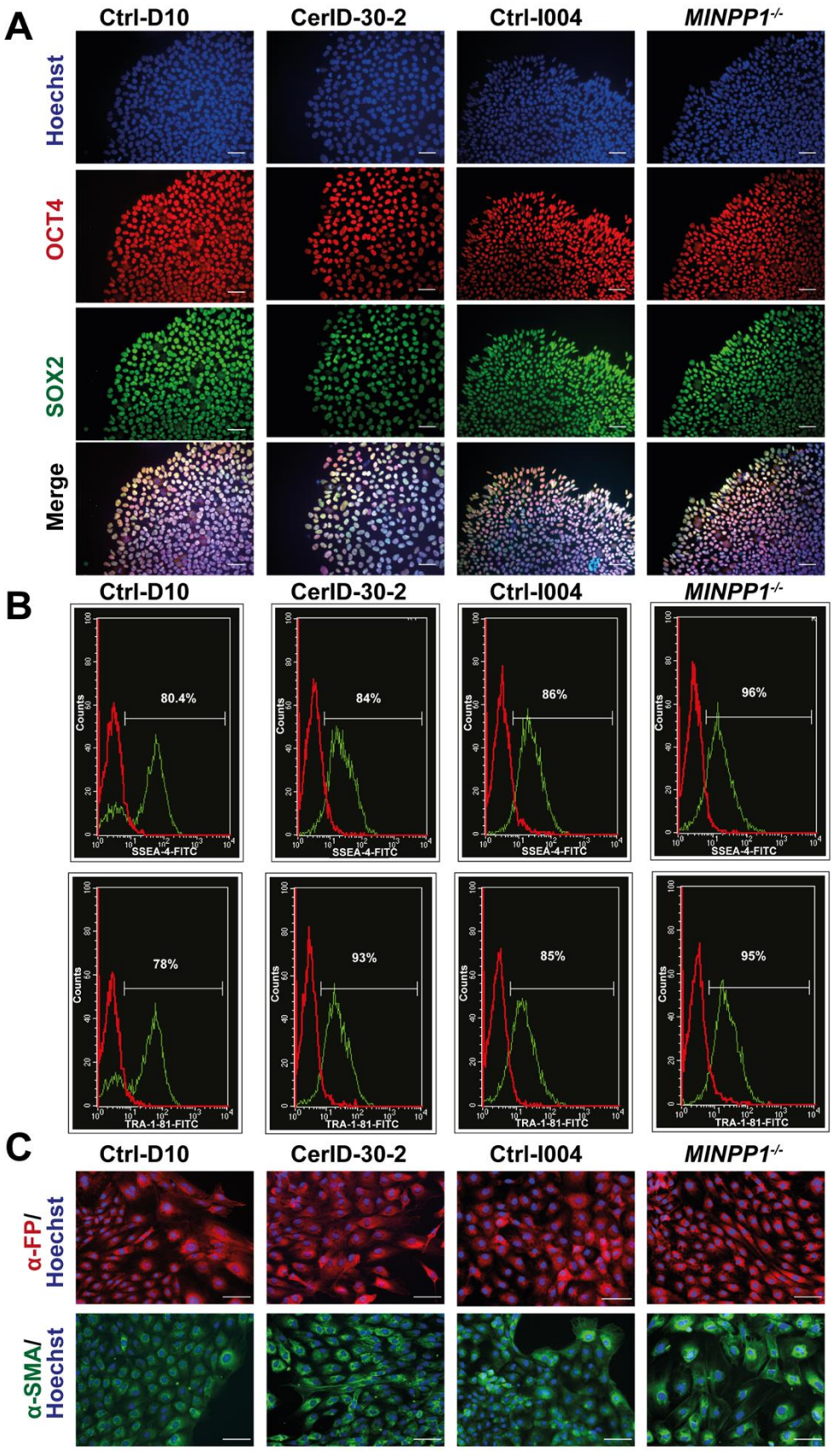
A
Ctrl-D10
CerID-30-2
Ctrl-I004
MINPP1-/-
Hoechst
OCT4
SOX2
Merge
B
Ctrl-D10
CerID-30-2
Ctrl-I004
MINPP1-/-
80.4%
84%
86%
96%
SSEA-4-FITC
78%
93%
85%
95%
TRA-1-81-FITC
Counts
C
Ctrl-D10
CerID-30-2
Ctrl-I004
MINPP1-/-
α-FP/ Hoechst
α-SMA/ Hoechst

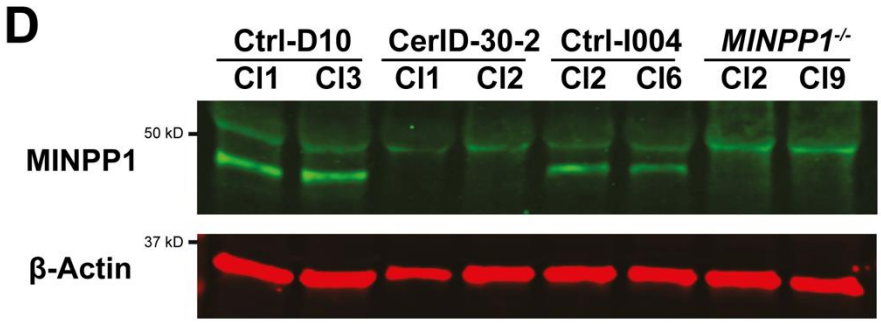


**Figure 35. Characterization of patient-derived (CerID-30-2) and *MINPP1*$^{-/-}$ iPSCs. (A)** Immunofluorescence staining of embryonic stem cell markers OCT4 and SOX2 and **(B)** flow cytometer analysis of pluripotency markers SSEA-4 and TRA-1-81 in control (Ctrl-D10 and Ctrl-I004), patient-derived (CerID-30-2), and *MINPP1*$^{-/-}$ iPSCs. **(C)** Immunofluorescence staining of endoderm (alpha-Fetoprotein/AFP) and mesoderm (smooth muscle actin (α-SMA)) markers following embryoid formation from control (Ctrl-D10 and Ctrl-I004), patient-derived (CerID-30-2), and *MINPP1*$^{-/-}$ iPSCs. **(D)** Western blot data showing the absence of MINPP1 in patient-derived CerID-30-2 and *MINPP1*$^{-/-}$ iPSCs. MINPP1 (48 kDa) is present in controls (Ctrl-D10 and Ctrl-I004) iPSC lines (lower band). β-actin is shown as loading control. All scale bars correspond to 50 μm.

### 1.4.1 MINPP1 loss does not affect proliferation and apoptosis in iPSCs.

Prior to differentiating our iPSC lines into disease relevant cell types, we assessed whether our *MINPP1* mutant iPSCs lines display an impaired proliferation, considering the proliferation phenotype we observed in *MINPP1*$^{-/-}$ HEK293 cells. Thus, we labelled both *MINPP1* mutant iPSCs and their corresponding controls with bromodeoxyuridine (BrdU), an analogue of the nucleoside thymidine, in order to detect proliferating cells undergoing DNA synthesis (Limoli and Ward, 1993). After six hours of labelling, we fixed the cells, proceeded with DNA hydrolysis and performed immunofluorescence with Anti-BrdU. Interestingly, the percentage of BrdU$^{+}$ cells were comparable among iPSC lines, suggesting that MINPP1 loss does not affect proliferation in iPSCs (Figure 36A).

Next, we also wanted to assess the apoptosis level in *MINPP1* mutant iPSC lines using a TUNEL assay, a widely used method to detect double strand DNA breaks during apoptosis via deoxynucleotide transferase that adds fluoro-labelled deoxynucleotides to the 3'-hydroxyl terminus of DNA breaks (Gavrieli et al., 1992; Huerta et al., 2007). In line with the *MINPP1*$^{-/-}$ HEK293 cell phenotype, these analysis revealed no major differences in apoptosis levels

among iPSC lines, showing that MINPP1 loss also does not affect apoptosis in iPSCs (Figure 36B).

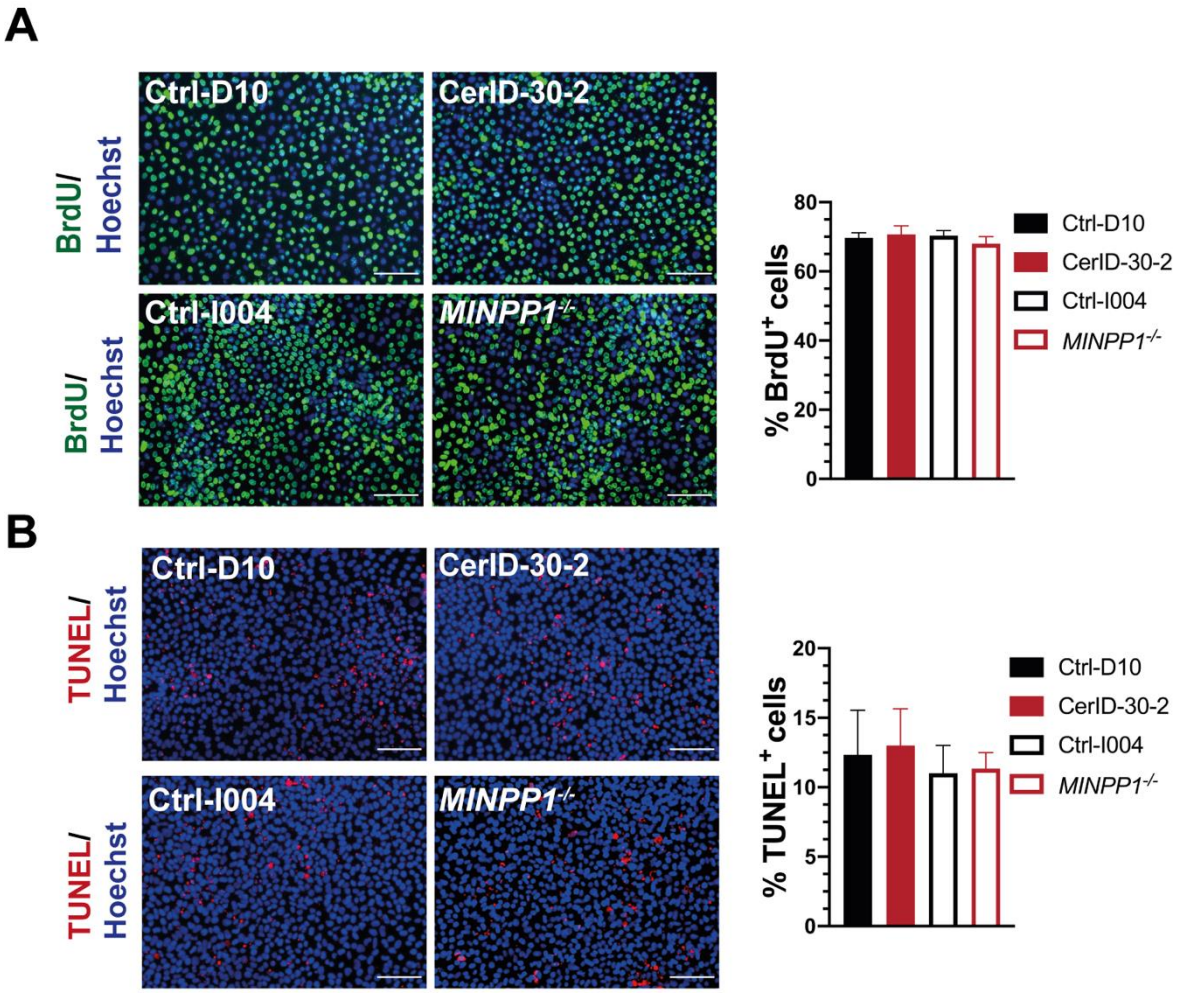


**Figure 36. MINPP1 loss does not affect proliferation and apoptosis in iPSCs.** Representative images and quantification data of $BrdU^+$ staining **(A)** and TUNEL assay **(B)** in control (Ctrl-D10 and Ctrl-I004), patient-derived (CerID-30-2), and *MINPP1*$^{-/-}$ iPSCs. All scale bars correspond to 50 µm. (n=3, one-way ANOVA, Tukey's post hoc, no significance). One clone per line was used in both experiments.

### 1.4.2 MINPP1 loss leads to a delayed neuronal differentiation in iPSCs associated with an increased rate of early-onset apoptosis.

In an attempt to model *MINPP1*-PCH with iPSCs, we next differentiated both control and *MINPP1* mutant iPSC lines towards neuronal lineage by following the dual-SMAD inhibition-based neural induction method, given its high reproducibility and efficiency

(Boissart et al., 2013; Chambers et al., 2009). However, unexpectedly, this protocol did not allow the generation of viable neural progenitor cells from both *MINPP1* mutant iPSC lines. Indeed, following mechanical isolation of the neural rosettes, patient-derived iPSCs systematically generated a mixed cell population of $HNK1^+$ neural progenitors (62%) and undefined HNK1 negative cells (32%) (Figure 37). To purify $HNK1^+$ neural progenitors from this undefined cell population, we performed FACS sorting for HNK1. However, the isolated $HNK1^+$ patient-derived neural progenitors did not survive for further study. Interestingly, we observed a comparable phenomenon during the neural differentiation of *MINPP1*$^{-/-}$ iPSCs. For these cells, the dual-SMAD inhibition neural induction protocol allowed the efficient generation of $HNK1^+$ neural progenitors from *MINPP1*$^{-/-}$ iPSCs (Figure 37). However, we could not obtain viable *MINPP1*$^{-/-}$ $HNK1^+$ neural progenitors in later passages. Hence, these observations point to a specific sensitivity for these cells in the absence of MINPP1 and suggest a role for this enzyme during neural differentiation of iPSCs.

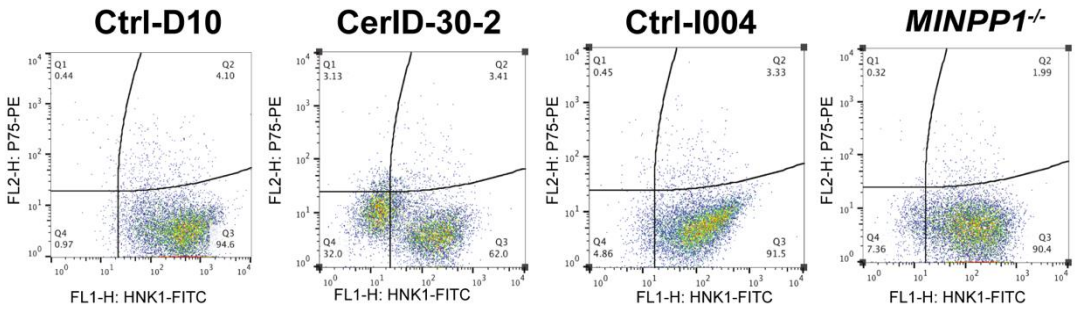


**Figure 37. Flow cytometry analysis of patient-derived (CerID-30-2) and *MINPP1*$^{-/-}$ iPSCs following dual SMAD inhibition-based neural induction.** Analysis of P75 and HNK1 in control (Ctrl-D10 and Ctrl-I004), patient-derived (CerID-30-2) and *MINPP1*$^{-/-}$ cells that are mechanically isolated from neural rosette cultures. While HNK1 single positive defines the neural progenitors, P75/HNK1 double positive marks neural crest progenitor cells. Three clones per line were used in the experiment and analysis of one clone per line was represented in the figure.

In an attempt to generate *MINPP1* neural progenitor cell lines, we used a different neural induction protocol that preserved the neural rosette environment and slowed down the neural induction process by solely relying on a single-neural inducing molecule, noggin (Gerrard et al., 2005). To assess the effect of MINPP1 loss on iPSC neuronal differentiation, we performed immunofluorescence staining for neuronal progenitor marker PAX6 and early neuronal marker TUJ1. The immunofluorescence staining at neural differentiation day 10 did not reveal major differences in PAX6/TUJ1 cell populations among iPSC lines (Figure 38A, quantification not shown). However, at day 14, patient-derived cells and *MINPP1*$^{-/-}$ cells showed 65% and 42% decreases in TUJ1$^{+}$ neurons, when compared to their respective controls, respectively (Figure 38B, C). Interestingly, these phenotypes were mirrored by 3.1 and 2.6 fold increases in PAX6$^{+}$ neuronal progenitors, respectively. Hence, these data showed that MINPP1 absence causes a delayed neuronal differentiation in iPSCs.

The observed neuronal differentiation phenotype led us to question whether *MINPP1* mutant PAX6$^{+}$ neuronal progenitors are not fully differentiating into neurons or they differentiate properly but then degenerate post day 10. In order to provide potential clues to this question, we assessed the apoptosis level in *MINPP1* mutant cells at neural differentiation day 10 and day 14, using TUNEL assay. Interestingly, at day 10, we detected an increase in apoptosis in both *MINPP1* mutant cells (Figure 38A, D). Intriguingly, this apoptotic phenotype became more significant at day 14, displaying 2.4 and 1.6 fold increases in patient-derived and *MINPP1*$^{-/-}$ cells, when compared to their respective controls, respectively (Figure 38B, D). Thus, these results showed that MINPP1 absence leads to an increased cell death during early stage of neural differentiation of iPSCs.

Overall, these characterization studies revealed two major phenotypes during neural differentiation of *MINPP1* mutant cells: a delayed neuronal differentiation phenotype and an early-onset cell survival defect. Although the exact link between the two defects and the nature

of the apoptosis are not known, it was interesting for us to observe the involvement of both of these defects in our *MINPP1*-PCH-iPSC models. Indeed, as PCH is recognized as a disorder where neurodevelopmental and early-onset neurodegenerative mechanisms intersect, iPSCs can be especially relevant for this class of disorder.

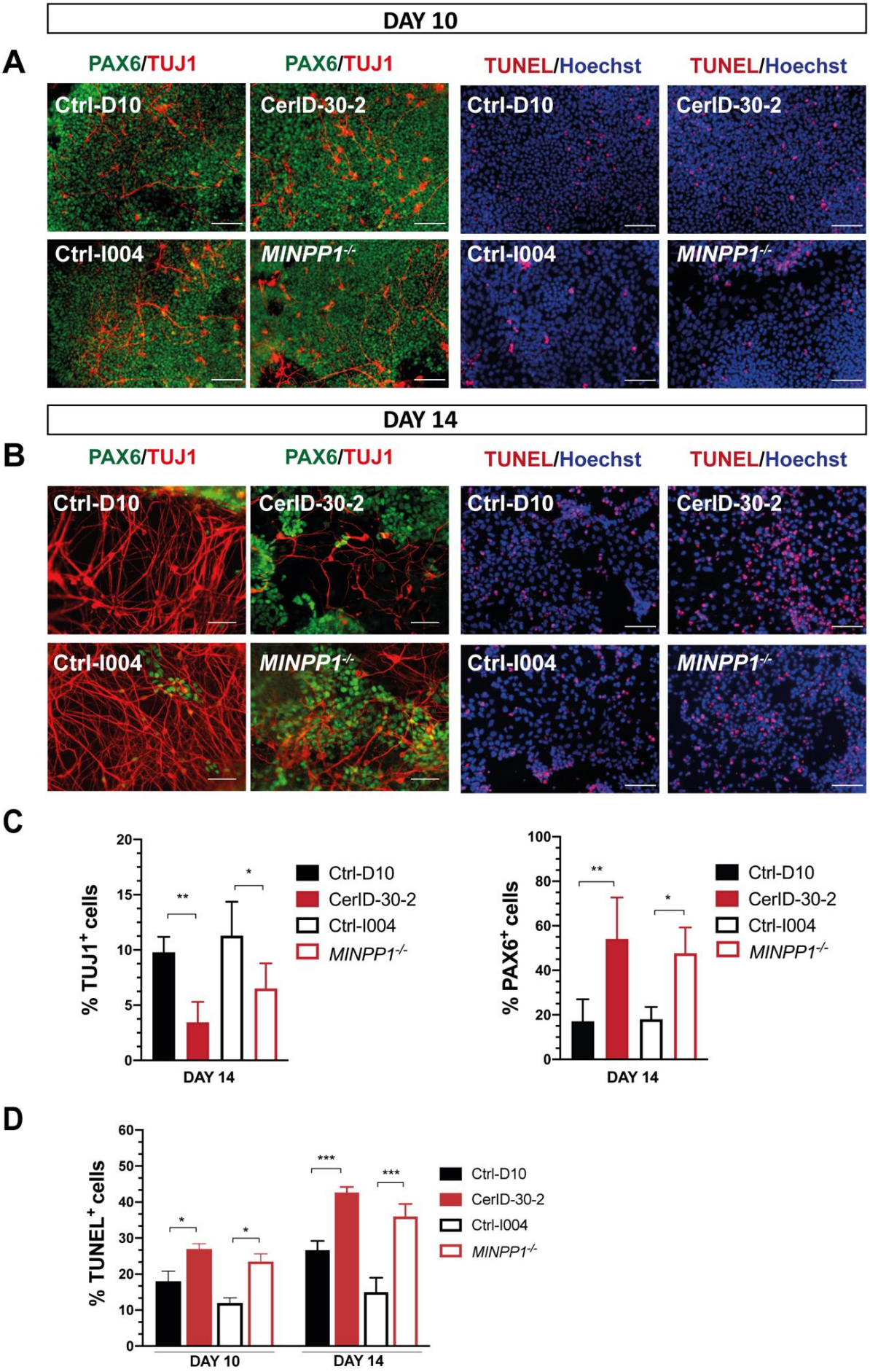
DAY 10
A
PAX6/TUJ1
PAX6/TUJ1
TUNEL/Hoechst
TUNEL/Hoechst
Ctrl-D10
CerID-30-2
Ctrl-D10
CerID-30-2
Ctrl-I004
MINPP1-/-
Ctrl-I004
MINPP1-/-
DAY 14
B
PAX6/TUJ1
PAX6/TUJ1
TUNEL/Hoechst
TUNEL/Hoechst
Ctrl-D10
CerID-30-2
Ctrl-D10
CerID-30-2
Ctrl-I004
MINPP1-/-
Ctrl-I004
MINPP1-/-
C
% TUJ1+ cells
20
15
10
5
0
**
*
DAY 14
Ctrl-D10
CerID-30-2
Ctrl-I004
MINPP1-/-
% PAX6+ cells
100
80
60
40
20
0
**
*
DAY 14
Ctrl-D10
CerID-30-2
Ctrl-I004
MINPP1-/-
D
% TUNEL+ cells
60
50
40
30
20
10
0
*
*
***
***
DAY 10
DAY 14
Ctrl-D10
CerID-30-2
Ctrl-I004
MINPP1-/-

**Figure 38. MINPP1 loss leads to a delayed neuronal differentiation in iPSCs associated with an increased rate of apoptosis. (A-B)** Representative immunofluorescence images of PAX6 /TUJ1 and TUNEL assay during neural differentiation of control (Ctrl-D10 and Ctrl-I004), patient-derived (CerID-30-2) and *MINPP1*$^{-/-}$ iPSCs at day 10 **(A)** and day 14 **(B)**. **(C)** Quantification of the PAX6 /TUJ1 immunostaining at day 14 of neural differentiation. **(D)** Quantification of the TUNEL assay during neural differentiation (Day 10 and Day 14). All scale bars correspond to 50 μm. (Duplicate/triplicate analysis of two independent experiments, one-way ANOVA, Tukey's post hoc test, * and **, *** indicate p values: $p<0.05$, $p<0.01$ and $p\leq0.001$, respectively). The data are presented as mean percentage values ± s.d. One clone per line was used in both experiments.

### 1.4.3 MINPP1 loss leads to an abnormal cellular inositol phosphate metabolism with an accumulation of $IP_6$ during early stages of neural differentiation of iPSCs.

Next, we wanted to explore whether disruption of the MINPP1 enzyme activity can be the underlying cause of the differentiation and cell survival defects observed in *MINPP1* mutant cells. To assess this hypothesis, we quantified inositol phosphate levels during early stage of neural differentiation. Hence, we performed three days of inositol metabolic radiolabelling of *MINPP1* mutant cell lines at the iPSC stage and at day 7 of neuronal differentiation. Then, we analysed the inositol derivatives by SAX-HPLC analysis (as previously explained in the section 1.2.4-5, Figure 39A). The time point day 7 was chosen in order to analyse the inositol phosphate levels at a time prior the detection of a differentiation phenotype and a severe cell survival defect (i.e. day 10 of neural differentiation stage) (Figure 38A, D). Along with the study of these two cell types, we also applied this method to patient fibroblasts (CerID-30-1 and CerID-30-2) in an attempt to further explore the cell-type-specific differences. Indeed, the investigation of patient fibroblasts did not reveal a significant differences in the level of inositol derivatives when compared to the control fibroblasts, although a tendency towards increased $IP_6$ and $IP_5$ levels were detected (Figure 39B). However, in iPSCs, $IP_6$ levels showed a significant 1.6-fold increase in both patient-derived and *MINPP1*$^{-/-}$ iPSCs, associated with a trend or significant increase in $IP_5$ levels (Fig 39C, D). Interestingly, the $IP_6$ accumulation phenotype became more significant in day 10-differentiated *MINPP1*

mutant cells, with a 1.9 and 1.6-fold increases in $IP_6$ levels in patient-derived and *MINPP1*$^{-/-}$ cells, respectively (Figure 39E, F). In addition to this $IP_6$ accumulation phenotype, we also observed a trend or significant decrease in $IP_2$ levels in both of the differentiated *MINPP1* mutant cells. Hence, these findings clearly showed that MINPP1 loss leads to an abnormal inositol phosphate metabolism with an accumulation of $IP_6$ during early stage of neural differentiation of iPSCs. Thus, this conclusion suggested the involvement of MINPP1-mediated $IP_6$ deregulation as the cause of the neuronal differentiation and apoptotic phenotypes observed in our *MINPP1* mutant iPSCs models, revealing insights into the pathological mechanism underlying *MINPP1*-PCH.

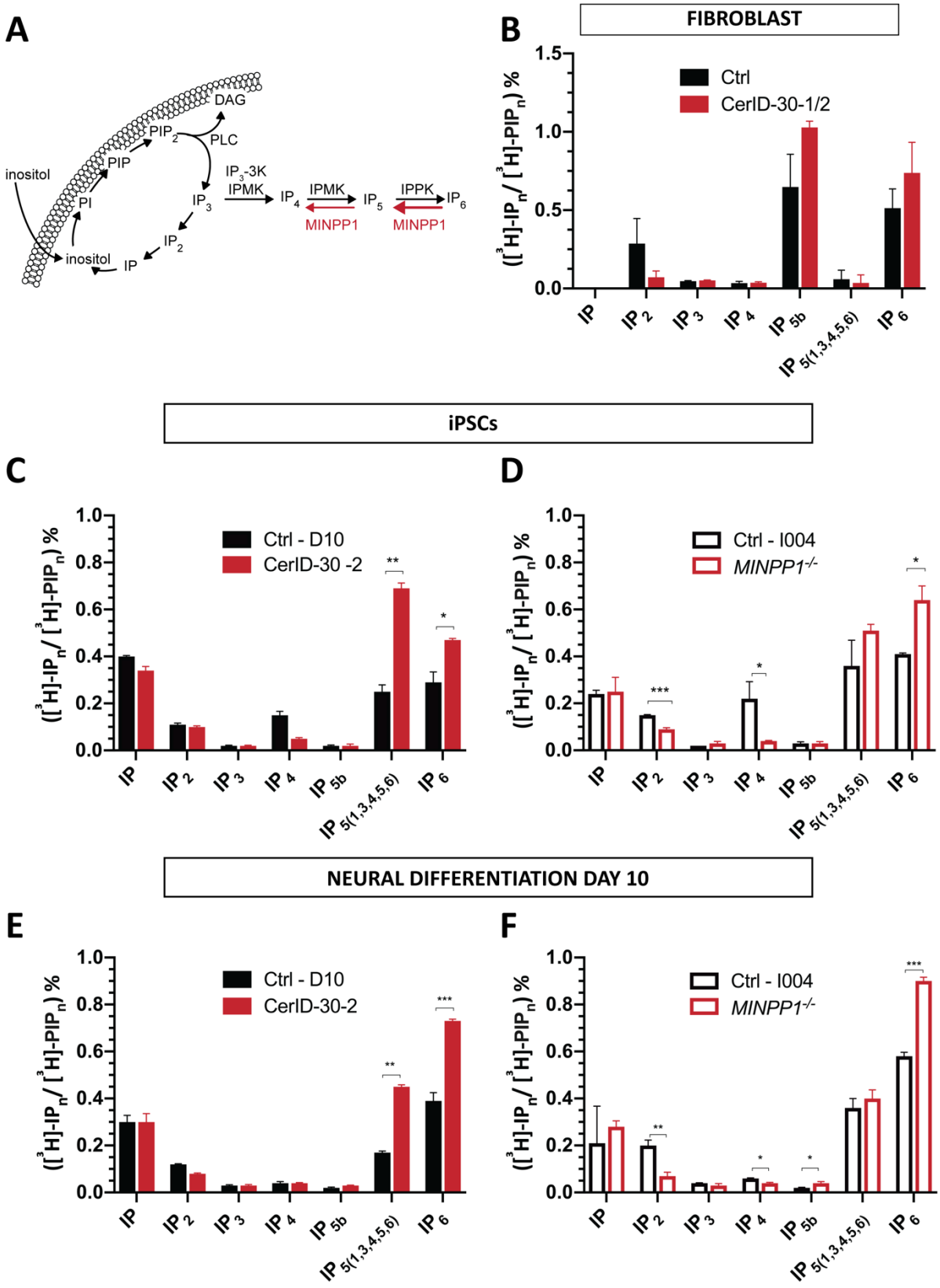


**Figure 39. MINPP1 loss disrupts cellular inositol phosphate metabolism with an accumulation of $IP_6$ during neural differentiation of iPSCs. (A)** Schematic representation of the inositol cycle. **(B-F)** SAX-HPLC analysis of inositol phosphate levels in patient fibroblasts (CerID-30-1 and CerID-30-2) **(B),** patient-derived (CerID-30-2) **(C)** and *MINPP1*$^{-/-}$ iPSCs **(D)**, and their day-10 neural differentiating counterparts **(E-F)**. The peaks ([$^3$H]-$IP_n$)

were identified based on comparison to standards. [$^3$H]-$IP_n$ levels are presented as percentage of total radioactivity in the inositol-lipid fraction ([$^3$H]-$PIP_n$). All error bars represent standard deviation (s.d.). (n=2, Two-tailed student's t-test for fibroblast data; One-way ANOVA for iPSCs and their differentiated counterparts data, Tukey's post hoc test, *, **, ***, **** indicate p values $p<0.05$, $p<0.01$, $p<0.001$, $p \leq 0.0001$, respectively). Abbreviations used: IPn, inositol phosphates; $PIP_n$, phosphatidyl inositol phosphates. One clone per line was used in the experiment.

### 1.4.4 The summary of the findings obtained from our *MINPP1*-PCH iPSC models

To sum up this last section, our *MINPP1*-PCH iPSC models allowed us to identify the following cellular and biochemical consequences associated with the loss of function of *MINPP1*. In the absence of MINPP1, iPSCs present a delayed neuronal differentiation combined with an increased rate of early-onset apoptosis. The mechanism underlying this phenotype is likely to be related to an abnormal inositol phosphate metabolism causing an accumulation of $IP_6$ during early stages of neural differentiation.

# CONCLUSION

In this study, we identified *MINPP1* as causative of a distinct PCH subtype, with typical basal ganglia involvement on neuroimaging. MINPP1 deficiency results in an intracellular imbalance of the inositol polyphosphate metabolism. This metabolic defect is characterized by an accumulation of highly phosphorylated inositol phosphates, mostly $IP_6$. As a potential cellular consequence of $IP_6$ accumulation and its enhanced cation-chelating activity, we found that MINPP1 deficiency impacts cellular cation physiology, by depleting intracellular iron as well as calcium in the cytosolic and the ER pools. Our disease modelling study with iPSCs, showed that MINPP1 deficiency leads to a delayed neuronal differentiation combined with an increased rate of early-onset apoptosis. Furthermore, we found that Minpp1 loss impacts mouse brain, including cerebral cortex development. Hence, our study shows the critical role of MINPP1 in the regulation of inositol phosphate metabolism, cation physiology and human brain development.

# DISCUSSION

## 1.1 PCH14: the first brain disorder caused by an altered inositol phosphate metabolism

PCH is a severe neurodevelopmental and early-onset neurodegenerative brain disorder that includes a broad phenotypic and genetic spectrum, involving 13 subtypes (Uwineza et al., 2019; van Dijk et al., 2018a; Van Dijk et al., 2018). However, many PCH patients still remain without a genetic diagnosis, highlighting the great need for the identification of new PCH disease mechanisms. Herein, we discovered a new PCH subtype with specific involvement of basal ganglia/thalami, caused by loss of function mutations of *MINPP1*: a novel-disease causing gene encoding an inositol polyphosphate phosphatase with a previously unknown function in the human cellular physiology and the brain. Hence, this study set out to develop cellular and mouse models to gain initial insights into the disease mechanism of *MINPP1*-PCH, which we propose as PCH type 14.

To our knowledge, our study represents the first study that investigates the loss of function of *MINPP1* in human cellular models, including HEK293 cells, patient-derived fibroblasts and iPSCs and their neural differentiated counterparts. Cumulatively, in all of our models, we identified an imbalance in the intracellular inositol phosphate metabolism, where increase in the amounts of higher inositol polyphosphate derivatives $IP_5$ and $IP_6$ were associated with a decrease in lower-phosphorylated $IP_2$ and IP species. However, interestingly, $IP_6$ accumulation phenotype appeared to be the most consistent result from this imbalance. Hence, here we propose altered cellular $IP_6$ levels as central to the *MINPP1* pathogenesis, although, at this point, we do not totally exclude the possible contribution of the abnormal levels of cellular $IP_2$ as well as the extracellular inositol phosphates to the disease pathogenesis. Altogether, this study reveals for the first time the abnormal intracellular inositol phosphate metabolism as the cause of a brain disorder.

## 1.2 The consequences of $IP_6$ accumulation on cellular physiology

### 1.2.1 Hypothesis on the subcellular localization of the accumulated $IP_6$

The impact of $IP_6$ accumulation on cellular physiology has been difficult to address, mainly due to the uncertainties concerning the subcellular localization of $IP_6$ and MINPP1. Indeed, the predominant localization of MINPP1 in the ER has favoured the presence of some of its substrate, $IP_6$, also in the ER lumen (Ali et al., 1993; Craxton et al., 1995). However, so far the available data did not localize $IP_6$ in any of the subcellular compartment, except the cytosol (Michell et al., 1992; Stuart et al., 1993; Stuart et al., 1994).This is mainly due to the technical challenges associated with its measurement in the intracellular organelles. In addition to this discrepancy, a relatively recent study proposed that MINPP1 is also localized, although to a lower extent, in the Golgi, lysosome and endosome (Windhorst et al., 2013). Thereby, these findings further suggest the presence of $IP_6$ in additional subcellular pools. Hence, although, at this point, a more thorough study is needed to localize cellular $IP_6$ and MINPP1, here we hypothetically assume that, in our *MINPP1*-cellular models, $IP_6$ accumulates in the subcellular compartments in which MINPP1 activity is lost. Furthermore, among these compartments, we propose the ER to be primarily affected by this accumulation and that this localized defect is at the basis of the pathology mechanism. Support for this proposal comes from the following observations: (1) the identification of the CerID-09 family harbouring a missense variant in the ER retention domain of MINPP1 (2) the very similar clinical phenotype of the CerID-09 patient versus the others (3) the clear inability of this *MINPP1* missense mutant (i.e. E486K) to rescue the proliferation phenotype in *MINPP1*$^{-/-}$ HEK293 cells despite its fully active enzyme activity, (4) the potential reduced stability and mislocalization associated with this mutant. Although the latter point needs to be further studied (e.g. via a functional, tagged version of E486K mutant, without altered ER targeting and ER retention), these observations

led us to deduce that the loss of MINPP1 activity and thereby $IP_6$ accumulation within the ER lumen is likely to be the major contributor to the *MINPP1* pathogenesis.

### 1.2.2 The impact of $IP_6$ accumulation on cellular cation homeostasis: revealing a previously unappreciated phenotype

$IP_6$ differs from other inositol phosphates by its ability to form high-affinity complexes with polyvalent cations, including $Ca^{2+}$, $Mg^{2+}$, $Fe^{3+}$ and $Zn^{2+}$ (Hawkins et al., 1993; Mali et al., 2006; Poyner et al., 1993; Torres et al., 2005; Veiga et al., 2006). However, such chelating activity of $IP_6$ is often ignored in most of the studies investigating the role of $IP_6$ in cellular physiology. For instance, high concentrations of extracellular $IP_6$ have been systematically shown to inhibit cancer cell growth *in vitro* and *in vivo* (Vucenik and Shamsuddin, 2006; Brehm and Windhorst, 2019; Shamsuddin and Bose, 2012). By virtue of its anti-cancer effect, most of the studies have recognized $IP_6$ per se as an anti-tumour agent, without considering the fact that such effect more likely reflects the secondary effects resulting from the increased chelation activity of $IP_6$ (e.g. the depletion of the essential cations in the cell culture media and the gut). Hence, conversely to such studies, here we based our hypothesis by primarily considering the chelating activity of $IP_6$ as a potential pathological basis of MINPP1 deficiency.

Based on the above rationality and the strong impact of MINPP1 loss on cellular $IP_6$ levels, we hypothesize that the accumulation of $IP_6$ in a given subcellular compartment leads to an increase in $IP_6$-cation complexes, causing the depletion of the available free ions and thus impairing the local cation physiology in MINPP1 deficient cells. Indeed, in support of this hypothesis, we identified an altered iron and calcium homeostasis in *MINPP1*$^{-/-}$ HEK293 cells, with a marked depletion of the intracellular free iron and cytosolic $Ca^{2+}$. In line with the latter result, we also found a similar cytosolic $Ca^{2+}$ depletion phenotype in *Minpp1*$^{-/-}$ E14.5 cortical mouse progenitors, suggesting a common pathological mechanism between species. Moreover, the absence of MINPP1 also severely impaired $Ca^{2+}$ mobilization in HEK293 cells by reducing

the intracellular calcium pools in the ER. This observation was particularly interesting for us as it further supported our previous hypothesis proposing the ER as the place of the primary defect. Altogether, our initial studies provide initial insights into the previously unappreciated chelating activity of $IP_6$ and further suggest the involvement of $IP_6$-mediated cation-chelation as the cellular consequence of loss of function of *MINPP1*.

## 1.3 The brain-specific effects of the loss of function of *MINPP1*

Understanding how loss of function of *MINPP1* can lead to a PCH disease pathology has been initially challenging for us, due to the unknown role of MINPP1 in brain physiology. Hence, herein, we sought new information by developing both mouse and iPSC-based models for loss of function of *MINPP1*.

### 1.3.1 Insights from *Minpp1*$^{-/-}$ mice

Intriguingly, our initial characterization of *Minpp1*$^{-/-}$ mice revealed a previously overlooked brain phenotype, showing a slight decrease in the brain weight and cortical thickness (Chi et al., 2000). Hence, these initial observations suggested that Minpp1 loss impacts mouse brain, including cerebral cortex, development. Interestingly, a comparable difference was also observed in the mouse model for another PCH gene, *CLP1* (Karaca et al., 2014). Further characterization studies of this mouse model showed reduction in the number of neurons and potential increased number of apoptotic cells in the neocortex, thus suggesting for a neurodegenerative brain phenotype. To this extent, in the future, it will be important to explore whether *Minpp1*$^{-/-}$ mouse model show a comparable phenotype. Nevertheless, our initial characterization study allowed us to reveal initial insights into the previously missed effect of Minpp1 loss on mammalian brain development.

### 1.3.2 Insights from *MINPP1*-iPSCs models

Our *MINPP1*-iPSCs models have provided insights into the neuronal-specific effect of loss of function of *MINPP1*. Indeed, in this study, we found that MINPP1 loss does not affect the potential of iPSCs to differentiate into meso-endodermal lineages, but rather impacts iPSCs to differentiate into neural cells. Intriguingly, this differentiation phenotype was sensitive to the neural induction method used. For instance, while *MINPP1* mutant neural progenitors derived from dual SMAD inhibition protocol were not viable, the ones obtained by using noggin as the sole SMAD inhibitor, were not able to differentiate efficiently into neurons. Interestingly, this neuronal differentiation defect was proceeded with an increase in cell death. Although the exact mechanisms underlying these two aspects remain to be identified, the sensitivity of the human neural progenitors to the abnormal cellular inositol phosphate metabolism is likely to be involved. To this extent, it was interesting to notice the absence of a cell survival phenotype in other *MINPP1* mutant human cells (i.e. *MINPP1*$^{-/-}$ HEK293, patient-derived and *MINPP1*$^{-/-}$ iPSCs), despite their defective cellular inositol phosphate profile. Thus, this observation further suggests that neural progenitors might be specifically vulnerable to MINPP1-mediated inositol phosphate metabolic defects.

Interestingly, defects in neural progenitors were also suggested to be central to the disease pathogenesis in studies modelling PCH via iPSCs. For instance neural progenitors-derived from PCH patients with loss of function mutation in *AMPD2*, displayed a dramatic reduction in cell survival (Akizu et al., 2013). Likewise, iPSCs knock-out for *CHMP1A*, PCH8 causing-gene, resulted in a defective cerebral-organoid formation due to impaired neural progenitor maintenance (Coulter et al., 2018). Hence, these findings, including ours, suggest that neural progenitor cells might indeed be selectively vulnerable in PCH pathogenesis.

### 1.3.3 *MINPP1*-iPSCs models: suitable for the study of *MINNP1-PCH*

As often in PCH, early-onset neurodegeneration intersects with neurodevelopment, in this study we found very interesting to observe the occurrence of both neuronal differentiation and early-onset neural cell survival defects in *MINPP1* mutant iPSCs. In a broader frame, this observation suggests that our *MINPP1*-iPSCs models provide relevant insights into human disease phenotypes and hence are suitable model to study the mechanisms of *MINPP1*-PCH. However, at this point we cannot exclude the fact that it is difficult to compare the *in vivo* outcome with *in vitro* cultured cells. Hence, it is likely that *MINPP1* mutant neural progenitors out of their physiological environment show exacerbated phenotypes *in vitro*.

Nevertheless altogether, based on our *MINPP1*-PCH iPSC models, here we suggest that both neuronal differentiation and early-onset neurodegeneration mechanisms contribute to *MINPP1*-PCH pathogenesis, likely due to the defects in intracellular inositol phosphate metabolism. Indeed, in support to our hypothesis, it was interesting to notice that Saiardi and his colleagues have also observed a neurodegenerative phenotype in primary culture of superior cervical ganglion (SCG) neurons overexpressed with IPPK, a gene involved in the synthesis of $IP_6$. Hence, these data further suggested a role for disrupted inositol phosphate metabolism in neuronal defects (Loss et al., 2013a).

## 1.4 The impact of defective MINPP1-mediated inositol phosphate metabolism on neuronal differentiation and survival

Beside the role of $IP_3$ as a $Ca^{2+}$ mobilizer, there is almost nothing known about the role of inositol phosphates in the brain physiology and development (reviewed in (Berridge, 2016)). Hence, in an attempt to provide a link between this metabolic defect and the neuronal differentiation and cell survival phenotype, we have developed hypothesis based on the following two points. In the first point, we will elaborate on how neuronal cells could be specifically affected by this metabolic defect. In the second point, we will discuss how neuronal

differentiation and survival can be affected from $IP_6$-mediated-cation chelation, a mechanism identified in this study as responsible for the *MINPP1* pathogenesis.

### 1.4.1 Specificities in the inositol phosphate metabolism of neural cells

**Metabolic changes during transition from neural progenitors to neural cells**

Interestingly, the inositol phosphate metabolism seems to be differently regulated between neural progenitor cells and their differentiated counterparts. Intriguingly, in neurons and astrocytes, the inositol is supplied solely from the extracellular fluid, as these neural cells cannot synthesize inositol, due to their lack of expression of *ISYNA1*, a gene encoding the enzyme involved in the conversion of glucose-6-phosphate to inositol-3-monophosphate (Di Daniel et al., 2006; Fu et al., 2012; Wong et al., 1987). In contrast, neural progenitors are shown to express *ISYNA1*, suggesting that they are capable of synthesizing inositol *de novo* (Ring et al., 2012). Hence, these observations suggest that as neural progenitors undergo differentiation, they gradually lose their *de novo* inositol synthesis capacity, eventually becoming dependent on the supply of inositol from the extracellular environment. Thereby, hypothetically, as MINPP1 deficient neural progenitors differentiate into neurons, such restriction in inositol supply can further aggravate the imbalance between higher and lower ordered inositol phosphates, which can eventually impact the following cascade of events that are essential in various aspects of neuronal differentiation, function and survival : (1) the recycle of inositol, (2) the synthesis of inositol lipids, and (3) $IP_3$-based $Ca^{2+}$ signalling pathway (Frere et al., 2015; Kruse et al., 2016; Raghu et al., 2019; Zurashvili et al., 2013).

**Differences in the expression and regulation of inositol transporters between neural cells**

Interestingly, inositol uptake mechanism also seems to differ between neural cells. Indeed, in the adult brain, inositol is up taken mainly via three main inositol transporters. These include the two high capacity sodium-dependent-myo-inositol transporters (SMITs-1 and 2) and $H^+$-dependent *myo*-inositol transporter (HMIT). While astrocytes uptake inositol by

plasma-membrane-inositol-transporter SMIT1 and HMIT, neurons acquire inositol only via HMIT (SMIT-2 is only found in meninges) (Di Daniel et al., 2006; Guo et al., 1997; Maallem et al., 2006; Uldry et al., 2004). Interestingly, unlike SMITs but like MINPP1, HMIT transporters are shown to be localized in different subcellular compartments, including ER, Golgi and intracellular vesicles (Di Daniel et al., 2006; Uldry et al., 2004). Although the exact mechanisms underlying HMIT-mediated inositol uptake remains unclear, studies showed that the activation of HMIT is sensitive to the $Ca^{2+}$ levels (Uldry et al., 2004). Hence, it can be hypothesized that MINPP1-dependant disrupted cation homeostasis (e.g. $Ca^{2+}$) can affect HMIT regulation. Thus, within this context, MINPP1 absence can indirectly impair the regulation of inositol uptake in neurons. Such deregulation may have particular consequences on specialized neuronal structures (e.g. synapses and growth cones) where rapid inositol-lipid synthesis is required to regulate the activity of ion channels and vesicle recycling for synaptic plasticity (Hee and Thayer, 2009; Lykidis et al., 1997; McPhee et al., 1991). Indeed, to this extent, Saiardi's group recently showed that the cortical neurons preferentially use newly-imported inositol for rapid inositol-lipid synthesis, hence further highlighting the critical role of inositol transport for proper neuronal activity and survival (Saiardi and Mudge, 2018).

Hence, while unravelling the impact of *MINPP1*-related metabolic defects on neuronal phenotypes, it seems important to consider these brain-cell specific differences, which might need further investigation.

### 1.4.2 The impact of $IP_6$-mediation cation chelation

As a potential new pathological mechanism, herein we suggest that $IP_6$-mediated-cation chelation plays a key role in the *MINPPP1* pathogenesis. Support for this proposal comes from the findings showing the strong impact of loss of function of *MINPP1* on cellular $IP_6$ levels and cation homeostasis (for more in depth discussion see the previous section 1.2.2). Indeed, as divalent cations (e.g. $Ca^{2+}$, $Fe^{2+}$, $Fe^{3+}$, $Mg^{2+}$, $Zn^{2+}$) are known to play critical roles in various

aspects of neuronal development, maturation, physiology and activity, it seems likely that $IP_6$-mediated-disrupted cation homeostasis is responsible for the neuronal differentiation and survival defects observed in our *MINPP1*-iPSCs models (Castro et al., 2014; Gleichmann and Mattson, 2011; Hare et al., 2013; Szewczyk, 2013; Toth et al., 2016; White et al., 2015; Yamanaka et al., 2019). Although, at this point, how much and which metal ions bind to $IP_6$ *in vivo* remains elusive, here we will briefly discuss how (1) accumulation of cation-$IP_6$ complexes as well as (2) depletion of available metal-cations (due to high $IP_6$ chelating activity) can lead to neurodevelopmental and neurodegenerative defects, and thereby to a *MINPP1*-PCH disease pathology.

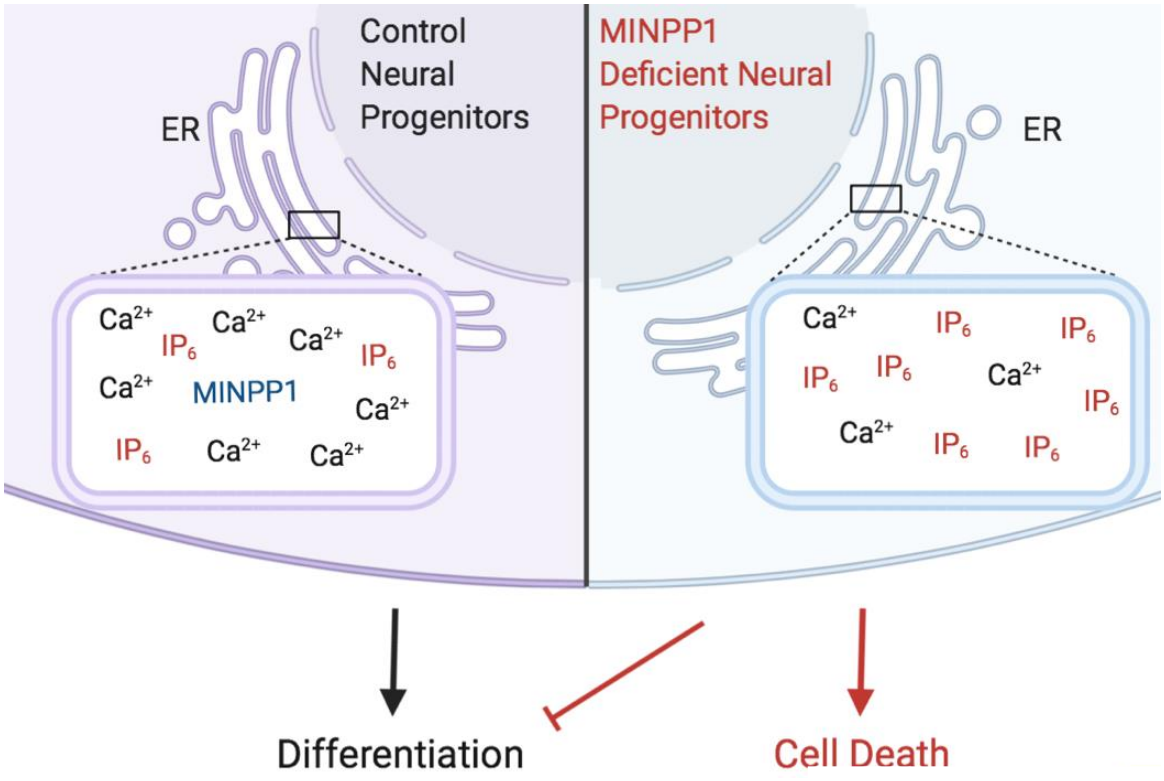


**Figure 40. Schematic illustration showing the study model.** In this study, we propose the involvement of $IP_6$-mediated cation-chelation as mechanistic basis of the *MINPP1*-PCH disease pathology. Indeed, we hypothesize that in the absence of MINPP1, higher $IP_6$ level is expected to be associated with an increased chelation of intracellular cations (e.g. $Ca^{2+}$ in the ER), resulting in decreased levels of available ions. Such $IP_6$-mediated deregulation in cation physiology is likely to be causative of early-onset neuronal survival and differentiation defects observed in MINPP1 deficient neural progenitor cells, hence leading to a PCH-disease pathology. $Ca^{2+}$ represent free $Ca^{2+}$ ions (i.e. non-chelated).

**The impact of metal ion accumulation**

Metal accumulation in brain (e.g. iron, zinc, copper) is known to induce neurotoxicity and neuronal cell death, mainly by enhancing the generation of reactive oxygen species, inducing oxidative stress pathways and increasing protein aggregation and misfolding (reviewed in (Hare et al., 2013; Skjørringe et al., 2012; White et al., 2015). Interestingly, although metal accumulation is not an obvious mechanism for other PCH subtypes, it is central to multiple neurodegenerative disorders, including Parkinson's disease (iron and manganese accumulation), Alzheimer's disease (iron accumulation), Fahr's disease (accumulation of calcium deposits), childhood disorders including Wilson's disease (Copper accumulation) and neurodegeneration with brain iron accumulation (NBIA) (Bandmann et al., 2015; Di Meo and Tiranti, 2018; Juneja et al., 2018; Levi and Finazzi, 2014; Parmalee and Aschner, 2016; Saleem et al., 2013; Skjørringe et al., 2012; White et al., 2015). Intriguingly, in most of these disorders, metal accumulation occurs mostly in the basal ganglia. Indeed, this observation was really interesting for us, given the fact that all of our PCH patients with *MINPP1* mutations differ from other PCH cases by a severe neurodegeneration in the basal ganglia. Hence, it seems likely that accumulation of $IP_6$-cation-complex is responsible for the early-onset neurodegenerative phenotypes in *MINPP1*-PCH.

**The impact of depletion of intracellular free metal cations**

Depletion of intracellular free cations have been associated with both neurodevelopmental and neurodegenerative defects, owing to their critical role in neuronal development and cell physiology. For instance, depletion of cellular iron is shown to impair proper neuronal development by deregulating expression of genes involved in the regulation of synaptic activity and dendritic growth (Jorgenson et al., 2005). Furthermore, depletion of $Ca^{2+}$ in the ER, has been shown to induce apoptosis, by enhancing protein misfolding and mitochondrial $Ca^{2+}$ overload in motor neurons in Amyotrophic lateral sclerosis (Grosskreutz

et al., 2010; Lautenschläger et al., 2013). Moreover, reduced cytosolic $Ca^{2+}$ levels are also shown to cause neurodegenerative phenotypes particularly by enhancing the accumulation of protein aggregates in the cellular models of Parkinson's disease (Betzer and Jensen, 2018). Indeed, as MINPP1 absence alters both intracellular iron and calcium homeostasis by depleting free intracellular iron and calcium pools in the cytosol and in the ER, it seems likely that these intracellular free metal cation depletion phenotypes contribute to the neurodevelopmental and neurodegenerative mechanisms in *MINPP1*-PCH.

## 1.5 Conclusion and Perspectives

The goal of this study was to make noteworthy contributions to the understanding of the neurodevelopmental brain disorders. First, it provides novel insights into the genetic, molecular and phenotypic spectrum of PCH by demonstrating for the first time the involvement of an abnormal inositol phosphate metabolism as a cause of PCH and a human developmental brain disorder. Second, this study shows the critical role of MINPP1 in the regulation of human brain development. Third, it reveals an unappreciated basic role for $IP_6$ in cellular homeostasis, which is critical during neurodevelopment. Fourth, it provides an example of how iPSC-based approach can provide relevant insights to better understand the neurodevelopmental and early-onset neurodegenerative disorders like PCH. Fifth, this study encourages future studies to consider MINPP1-related inositol phosphate metabolism as a neurodevelopmental and early-onset neurodegenerative brain disorder mechanism.

In the meanwhile, this study has thrown up several questions in need of further investigation. One of them involves the concern regarding the subcellular localization of $IP_6$ and MINPP1. Interestingly, Raman spectroscopy has been useful to detect $IP_6$ in plant seeds (Kolozsvari et al., 2015). This promising observation suggests that further development of this microscopy technique can help localize $IP_6$ subcellularly (Kolozsvari et al., 2015). Moreover, a recently developed method that uses high-throughput cellular fractionation and proteomic

profiling, opens an investigative path to follow for better assessing the subcellular localization of MINPP1 (Geladaki et al., 2019). Indeed, such strategies could provide us to identify the subcellular organelles in which $IP_6$-cation complexes accumulates in MINPP1 deficient cells.

Another question raised by this study is how MINPP1 absence can affect neuronal differentiation and survival. Although our study suggests the involvement of $IP_6$-mediated-cation-chelation on *MINPP1* pathogenesis, in this study we have not tested this hypothesis in our MINPP1 deficient neural models. Hence, further research should be undertaken to explore the intracellular cation homeostasis and signalling (e.g. iron and calcium) during differentiation of MINPP1 deficient neural progenitors. From another angle, it would be also interesting to assess whether *Minpp1*$^{-/-}$ neural progenitors with cytosolic $Ca^{2+}$ depletion phenotype, manifest phenotypic characteristics of our *in vitro* MINPP1 iPSCs models, including neuronal differentiation and survival phenotypes.

In a long term-goal, although no curative treatment exists for any of the PCH subtypes, it would be important to explore the development of a potential therapeutic strategy for *MINPP1*-PCH. For instance, if we consider iron brain accumulation phenotype as central to the MINPP1-PCH disease mechanism, brain permeable iron chelators, such as clioquinol, could be a potential therapeutic agent for *MINPP1*-PCH. Indeed, interestingly, in pre-clinical trials, clioquinol has been shown to reduce iron levels in the basal ganglia of the mouse models of Parkinson's disease (Kaur et al., 2003; Lei et al., 2012). Hence, to this extent, developing a *Minpp1*$^{-/-}$ mouse model with a brain iron accumulation phenotype might be an essential next step for the development of a potential treatment strategy for this PCH subtype involving a unique neurodegeneration in the basal ganglia, the brain structure that is primarily affected by metal accumulation.

In summary, the accumulation of $IP_6$ is a completely unexpected finding in the context of this neurological disorder. Further studies of this mechanism could provide a better understanding of the regulation of cations homeostasis during neuronal differentiation and potentially also demonstrate its role in metal ion-related neurodegeneration.

# REFERENCES


**Ábrahám, H., Tornóczky, T., Kosztolányi, G. and Seress, L.** (2001). Cell formation in the cortical layers of the developing human cerebellum. *Int. J. Dev. Neurosci.*

**Accogli, A., Iacomino, M., Pinto, F., Orsini, A., Vari, M. S., Selmi, R., Torella, A., Nigro, V., Minetti, C., Severino, M., et al.** (2017). Clinical/Scientific Notes: Novel AMPD2 mutation in pontocerebellar hypoplasia, dysmorphisms, and teeth abnormalities. *Neurol. Genet.*

**Adams, R. L., Mason, A. C., Glass, L., Aditi and Wente, S. R.** (2017). Nup42 and IP6 coordinate Gle1 stimulation of Dbp5/DDX19B for mRNA export in yeast and human cells. *Traffic*.

**Agamy, O., Ben Zeev, B., Lev, D., Marcus, B., Fine, D., Su, D., Narkis, G., Ofir, R., Hoffmann, C., Leshinsky-Silver, E., et al.** (2010). Mutations disrupting selenocysteine formation cause progressive cerebello-cerebral atrophy. *Am. J. Hum. Genet.*

**Agarwal, R., Mumtaz, H. and Ali, N.** (2009). Role of inositol polyphosphates in programmed cell death. *Mol. Cell. Biochem.*

**Ahmed, M. Y., Chioza, B. A., Rajab, A., Schmitz-Abe, K., Al-Khayat, A., Al-Turki, S., Baple, E. L., Patton, M. A., Al-Memar, A. Y., Hurles, M. E., et al.** (2015). Loss of PCLO function underlies pontocerebellar hypoplasia type III. *Neurology*.

**Akiyama, H., Matsu-ura, T., Mikoshiba, K. and Kamiguchi, H.** (2009). Control of neuronal growth cone navigation by asymmetric inositol 1,4,5-trisphosphate signals. *Sci. Signal.* **2**, ra34.

**Akizu, N., Cantagrel, V., Schroth, J., Cai, N., Vaux, K., McCloskey, D., Naviaux, R. K., Van Vleet, J., Fenstermaker, A. G., Silhavy, J. L., et al.** (2013). AMPD2 regulates GTP synthesis and is mutated in a potentially treatable neurodegenerative brainstem disorder. *Cell* **154**, 505–517.

**Alcázar-Román, A. R., Tran, E. J., Guo, S. and Wente, S. R.** (2006). Inositol hexakisphosphate and Gle1 activate the DEAD-box protein Dbp5 for nuclear mRNA export. *Nat. Cell Biol.*

**Aldinger, K. A. and Doherty, D.** (2016). The genetics of cerebellar malformations. *Semin. Fetal Neonatal Med.*

**Ali, N., Craxton, A. and Shears, S. B.** (1993). Hepatic ins(1,3,4,5)P4 3-phosphatase is compartmentalized inside endoplasmic reticulum. *J. Biol. Chem.* **268**, 6161–6167.

**Altman, J. and Bayer, S. A.** (1979). Development of the diencephalon in the rat. V. Thymidine- radiographic observations on internuclear and intranuclear gradients in the thalmus. *J. Comp. Neurol.*

**Altman, J. and Bayer, S. A.** (1985). Embryonic development of the rat cerebellum. I. Delineation of the cerebellar primordium and early cell movements. *J. Comp. Neurol.*

**Amaral, M. D. and Pozzo-Miller, L.** (2007). TRPC3 channels are necessary for brain-derived neurotrophic factor to activate a nonselective cationic current and to induce dendritic spine formation. *J. Neurosci.*

**Anderson, J. S., Nielsen, J. A., Ferguson, M. A., Burback, M. C., Cox, E. T., Dai, L., Gerig, G. and Korenberg, J. R.** (2013). Abnormal brain synchrony in Down Syndrome. *NeuroImage Clin.*

**Anekonda, T. S., Wadsworth, T. L., Sabin, R., Frahler, K., Harris, C., Petriko, B., Ralle, M., Woltjer, R. and Quinn, J. F.** (2011). Phytic acid as a potential treatment for Alzheimer's pathology: Evidence from animal and in vitro models. *J. Alzheimer's Dis.*

**Antonsson, B.** (1997). Phosphatidylinositol synthase from mammalian tissues. *Biochim. Biophys. Acta - Lipids Lipid Metab.*

**Appelhof, B., Barth, P. G. and Baas, F.** (2019). Classification of Pontocerebellar

Hypoplasia: Where does it End? 52–61.

**Ardhanareeswaran, K., Mariani, J., Coppola, G., Abyzov, A. and Vaccarino, F. M.** (2017). Human induced pluripotent stem cells for modelling neurodevelopmental disorders. *Nat. Rev. Neurol.*

**Atasoy, D., Schoch, S., Ho, A., Nadasy, K. A., Liu, X., Zhang, W., Mukherjee, K., Nosyreva, E. D., Fernandez-Chacon, R., Missler, M., et al.** (2007). Deletion of CASK in mice is lethal and impairs synaptic function. *Proc. Natl. Acad. Sci. U. S. A.*

**Azevedo, C. and Saiardi, A.** (2006). Extraction and analysis of soluble inositol polyphosphates from yeast. *Nat. Protoc.*

**Azevedo, F. A. C., Carvalho, L. R. B., Grinberg, L. T., Farfel, J. M., Ferretti, R. E. L., Leite, R. E. P., Filho, W. J., Lent, R. and Herculano-Houzel, S.** (2009). Equal numbers of neuronal and nonneuronal cells make the human brain an isometrically scaled-up primate brain. *J. Comp. Neurol.* **513**, 532–541.

**Bakker, S. P. and Bouman, K. H.** (1924). Atrophia olivo-pontocerebellaris. *Zeitschrift für die gesamte Neurol. und Psychiatr.*

**Bandmann, O., Weiss, K. H. and Kaler, S. G.** (2015). Wilson's disease and other neurological copper disorders. *Lancet Neurol.*

**Bardy, C., Van Den Hurk, M., Eames, T., Marchand, C., Hernandez, R. V., Kellogg, M., Gorris, M., Galet, B., Palomares, V., Brown, J., et al.** (2015). Neuronal medium that supports basic synaptic functions and activity of human neurons in vitro. *Proc. Natl. Acad. Sci. U. S. A.*

**Barone, R., Fiumara, A. and Jaeken, J.** (2014). Congenital disorders of glycosylation with emphasis on cerebellar involvement. *Semin. Neurol.*

**Barth, P. G.** Pontocerebellar hypoplasias. An overview of a group of inherited neurodegenerative disorders with fetal onset. *Brain Dev.* **15**, 411–22.

**Barth, P. G., Vrensen, G. F. J. M., Uylings, H. B. M., Oorthuys, J. W. E. and Stam, F. C.** (1990). Inherited syndrome of microcephaly, dyskinesia and pontocerebellar hypoplasia: A systemic atrophy with early onset. *J. Neurol. Sci.*

**Barth, P. G., Aronica, E., Vries, L., Nikkels, P. G. J., Scheper, W., Hoozemans, J. J., Poll-The, B. T. and Troost, D.** (2007). Pontocerebellar hypoplasia type 2: A neuropathological update. *Acta Neuropathol.*

**Bashir, Z. I., Bortolotto, Z. A., Davies, C. H., Berretta, N., Irving, A. J., Seal, A. J., Henley, J. M., Jane, D. E., Watkins, J. C. and Collingridge, G. L.** (1993). Induction of LTP in the hippocampus needs synaptic activation of glutamate metabotropic receptors. *Nature.*

**Basson, M. A. and Wingate, R. J.** (2013). Congenital hypoplasia of the cerebellum: developmental causes and behavioral consequences. *Front. Neuroanat.* **7**, 29.

**Batty, I. R., Nahorski, S. R. and Irvine, R. F.** (1985). Rapid formation of inositol 1,3,4,5-tetrakisphosphate following muscarinic receptor stimulation of rat cerebral cortical slices. *Biochem. J.*

**Bauer, P. O., Hudec, R., Ozaki, S., Okuno, M., Ebisui, E., Mikoshiba, K. and Nukina, N.** (2011). Genetic ablation and chemical inhibition of IP3R1 reduce mutant huntingtin aggregation. *Biochem. Biophys. Res. Commun.*

**Berninger, B., García, D. E., Inagaki, N., Hahnel, C. and Lindholm, D.** (1993). BDNF and NT-3 induce intracellular Ca2+ elevation in hippocampal neurones. *Neuroreport.*

**Berridge, M. J.** (1990). Calcium oscillations. *J. Biol. Chem.*

**Berridge, M. J.** (1993). Inositol trisphosphate and calcium signalling. *Nature*.

**Berridge, M. J.** (2007). Inositol trisphosphate and calcium oscillations. *Biochem. Soc. Symp.*

**Berridge, M. J.** (2014). Calcium regulation of neural rhythms, memory and alzheimer's disease. *J. Physiol.*

**Berridge, M. J.** (2016). The inositol trisphosphate/calcium signaling pathway in health and disease. *Physiol. Rev.*

**Berridge, M. J. and Irvine, R. F.** (1989). Inositol phosphates and cell signalling. *Nature*.

**Berridge, M. J., Lipp, P. and Bootman, M. D.** (2000). The versatility and universality of calcium signalling. *Nat. Rev. Mol. Cell Biol.*

**Berry, G. T., Mallee, J. J., Kwon, H. M., Rim, J. S., Mulla, W. R., Muenke, M. and Spinner, N. B.** (1995). The human osmoregulatory Na+/myo-inositol cotransporter gene (SLC5A3): Molecular cloning and localization to chromosome 21. *Genomics*.

**Bershteyn, M., Nowakowski, T. J., Pollen, A. A., Di Lullo, E., Nene, A., Wynshaw-Boris, A. and Kriegstein, A. R.** (2017). Human iPSC-Derived Cerebral Organoids Model Cellular Features of Lissencephaly and Reveal Prolonged Mitosis of Outer Radial Glia. *Cell Stem Cell*.

**Betzer, C. and Jensen, P. H.** (2018). Reduced cytosolic calcium as an early decisive cellular state in Parkinson⇔s disease and synucleinopathies. *Front. Neurosci.*

**Bezprozvanny, I.** (2011). Role of inositol 1,4,5-trishosphate receptors in pathogenesis of Huntington's disease and spinocerebellar ataxias. *Neurochem. Res.*

**Bhowmik, A., Ojha, D., Goswami, D., Das, R., Chandra, N. S., Chatterjee, T. K., Chakravarty, A., Chakravarty, S. and Chattopadhyay, D.** (2017). Inositol hexa phosphoric acid (phytic acid), a nutraceuticals, attenuates iron-induced oxidative stress and alleviates liver injury in iron overloaded mice. *Biomed. Pharmacother.*

**Biederer, T., Sara, Y., Mozhayeva, M., Atasoy, D., Liu, X., Kavalali, E. T. and Südhof, T. C.** (2002). SynCAM, a synaptic adhesion molecule that drives synapse assembly. *Science (80-. ).*

**Bierhals, T., Korenke, G. C., Uyanik, G. and Kutsche, K.** (2013). Pontocerebellar hypoplasia type 2 and TSEN2: Review of the literature and two novel mutations. *Eur. J. Med. Genet.* **56**, 325–330.

**Boczonadi, V., Müller, J. S., Pyle, A., Munkley, J., Dor, T., Quartararo, J., Ferrero, I., Karcagi, V., Giunta, M., Polvikoski, T., et al.** (2014). EXOSC8 mutations alter mRNA metabolism and cause hypomyelination with spinal muscular atrophy and cerebellar hypoplasia. *Nat. Commun.*

**Bohne, P., Schwarz, M. K., Herlitze, S. and Mark, M. D.** (2019). A New Projection From the Deep Cerebellar Nuclei to the Hippocampus via the Ventrolateral and Laterodorsal Thalamus in Mice. *Front. Neural Circuits*.

**Boissart, C., Poulet, A., Georges, P., Darville, H., Julita, E., Delorme, R., Bourgeron, T., Peschanski, M. and Benchoua, A.** (2013). Differentiation from human pluripotent stem cells of cortical neurons of the superficial layers amenable to psychiatric disease modeling and high-throughput drug screening. *Transl. Psychiatry*.

**Bostan, A. C. and Strick, P. L.** (2018). The basal ganglia and the cerebellum: Nodes in an integrated network. *Nat. Rev. Neurosci.*

**Boycott, K. M., Flavelle, S., Bureau, A., Glass, H. C., Fujiwara, T. M., Wirrell, E., Davey, K., Chudley, A. E., Scott, J. N., McLeod, D. R., et al.** (2005). Homozygous deletion of the very low density lipoprotein receptor gene causes autosomal recessive cerebellar hypoplasia with cerebral gyral simplification. *Am. J. Hum. Genet.*

**Brehm, M. A. and Windhorst, S.** (2019). New options of cancer treatment employing InsP 6. *Biochem. Pharmacol.*

**Brennan, A. R., Dolinsky, B., Vu, M. A. T., Stanley, M., Yeckel, M. F. and Arnsten, A. F. T.** (2008). Blockade of IP3-mediated SK channel signaling in the rat medial prefrontal cortex improves spatial working memory. *Learn. Mem.*

**Breuss, M. W., Sultan, T., James, K. N., Rosti, R. O., Scott, E., Musaev, D., Furia, B., Reis, A., Sticht, H., Al-Owain, M., et al.** (2016). Autosomal-Recessive Mutations in

the tRNA Splicing Endonuclease Subunit TSEN15 Cause Pontocerebellar Hypoplasia and Progressive Microcephaly. *Am. J. Hum. Genet.* **99**, 228–235.

**Brown, S. A. and Loew, L. M.** (2015). Integration of modeling with experimental and clinical findings synthesizes and refines the central role of inositol 1,4,5-trisphosphate receptor 1 in spinocerebellar ataxia. *Front. Neurosci.*

**Bruggeman, S. W. M., Valk-Lingbeek, M. E., Van Der Stoop, P. P. M., Jacobs, J. J. L., Kieboom, K., Tanger, E., Hulsman, D., Leung, C., Arsenijevic, Y., Marino, S., et al.** (2005). Ink4a and Arf differentially affect cell proliferation and neural stem cell self-renewal in Bmi1-deficient mice. *Genes Dev.*

**Brun, R. and Psychiatrie., S. A. fur N. und** (1917). *Zur Kenntnis der Bildungsfehler des Kleinhirns*. Zurich: Art. Institut Orell Fussli.

**Budde, B. S., Namavar, Y., Barth, P. G., Poll-The, B. T., Nürnberg, G., Becker, C., Van Ruissen, F., Weterman, M. A. J., Fluiter, K., Te Beek, E. T., et al.** (2008). tRNA splicing endonuclease mutations cause pontocerebellar hypoplasia. *Nat. Genet.*

**Buganim, Y., Faddah, D. A. and Jaenisch, R.** (2013). Mechanisms and models of somatic cell reprogramming. *Nat. Rev. Genet.*

**Bunce, C. M., French, P. J., Allen, P., Mountford, J. C., Moor, B., Greaves, M. F., Michell, R. H. and Brown, G.** (1993). Comparison of the levels of inositol metabolites in transformed haemopoietic cells and their normal counterparts. *Biochem. J.*

**Burglen, L., Chantot-Bastaraud, S., Garel, C., Milh, M., Touraine, R., Zanni, G., Petit, F., Afenjar, A., Goizet, C., Barresi, S., et al.** (2012). Spectrum of pontocerebellar hypoplasia in 13 girls and boys with CASK mutations: Confirmation of a recognizable phenotype and first description of a male mosaic patient. *Orphanet J. Rare Dis.*

**Burns, D. T., Donkervoort, S., Müller, J. S., Knierim, E., Bharucha-Goebel, D., Faqeih, E. A., Bell, S. K., AlFaifi, A. Y., Monies, D., Millan, F., et al.** (2018). Variants in EXOSC9 Disrupt the RNA Exosome and Result in Cerebellar Atrophy with Spinal Motor Neuronopathy. *Am. J. Hum. Genet.*

**Byrne, S. M., Mali, P. and Church, G. M.** (2014). Genome editing in human stem cells. *Methods Enzymol.* **546**, 119–138.

**Cabantchik, Z. I.** (2014). Labile iron in cells and body fluids: Physiology, pathology, and pharmacology. *Front. Pharmacol.*

**Caffrey, J. J., Hidaka, K., Matsuda, M., Hirata, M. and Shears, S. B.** (1999). The human and rat forms of multiple inositol polyphosphate phosphatase: Functional homology with a histidine acid phosphatase up-regulated during endochondral ossification. *FEBS Lett.* **442**, 99–104.

**Carey, B. W., Markoulaki, S., Hanna, J. H., Faddah, D. A., Buganim, Y., Kim, J., Ganz, K., Steine, E. J., Cassady, J. P., Creyghton, M. P., et al.** (2011). Reprogramming factor stoichiometry influences the epigenetic state and biological properties of induced pluripotent stem cells. *Cell Stem Cell*.

**Carta, I., Chen, C. H., Schott, A. L., Dorizan, S. and Khodakhah, K.** (2019). Cerebellar modulation of the reward circuitry and social behavior. *Science (80-. ).*

**Cassandrini, D., Cilio, M. R., Bianchi, M., Doimo, M., Balestri, M., Tessa, A., Rizza, T., Sartori, G., Meschini, M. C., Nesti, C., et al.** (2013). Pontocerebellar hypoplasia type 6 caused by mutations in RARS2: Definition of the clinical spectrum and molecular findings in five patients. *J. Inherit. Metab. Dis.*

**Castro, P. A., Ramirez, A., Sepúlveda, F. J., Peters, C., Fierro, H., Waldron, J., Luza, S., Fuentealba, J., Muñoz, F. J., De Ferrari, G. V., et al.** (2014). Copper-uptake is critical for the down regulation of synapsin and dynamin induced by neocuproine: Modulation of synaptic activity in hippocampal neurons. *Front. Aging Neurosci.*

**Chambers, S. M., Fasano, C. A., Papapetrou, E. P., Tomishima, M., Sadelain, M. and**

**Studer, L.** (2009). Highly efficient neural conversion of human ES and iPS cells by dual inhibition of SMAD signaling. *Nat. Biotechnol.*

**Chemin, J., Siquier-Pernet, K., Nicouleau, M., Barcia, G., Ahmad, A., Medina-Cano, D., Hanein, S., Altin, N., Hubert, L., Bole-Feysot, C., et al.** (2018). De novo mutation screening in childhood-onset cerebellar atrophy identifies gain-of-function mutations in the CACNA1G calcium channel gene. *Brain*.

**Chen, Y. and Brandizzi, F.** (2013). IRE1: ER stress sensor and cell fate executor. *Trends Cell Biol.* **23**, 547–555.

**Chen, F., Pruett-Miller, S. M., Huang, Y., Gjoka, M., Duda, K., Taunton, J., Collingwood, T. N., Frodin, M. and Davis, G. D.** (2011). High-frequency genome editing using ssDNA oligonucleotides with zinc-finger nucleases. *Nat. Methods*.

**Chen, Y., Cao, J., Xiong, M., Petersen, A. J., Dong, Y., Tao, Y., Huang, C. T. L., Du, Z. and Zhang, S. C.** (2015). Engineering Human Stem Cell Lines with Inducible Gene Knockout using CRISPR/Cas9. *Cell Stem Cell*.

**Chen, I. Y., Matsa, E. and Wu, J. C.** (2016). Induced pluripotent stem cells: At the heart of cardiovascular precision medicine. *Nat. Rev. Cardiol.*

**Cheng, Y. L. and Andrew, D. J.** (2015). Extracellular Mipp1 Activity Confers Migratory Advantage to Epithelial Cells during Collective Migration. *Cell Rep.* **13**, 2174–2188.

**Cheung, J. C. Y., Salerno, B. and Hanakahi, L. A.** (2008). Evidence for an inositol hexakisphosphate-dependent role for Ku in mammalian nonhomologous end joining that is independent of its role in the DNA-dependent protein kinase. *Nucleic Acids Res.*

**Chi, H., Tiller, G. E., Dasouki, M. J., Romano, P. R., Wang, J., O'keefe, R. J., Puzas, J. E., Rosier, R. N. and Reynolds, P. R.** (1999). Multiple inositol polyphosphate phosphatase: evolution as a distinct group within the histidine phosphatase family and chromosomal localization of the human and mouse genes to chromosomes 10q23 and 19. *Genomics* **56**, 324–336.

**Chi, H., Yang, X., Kingsley, P. D., O'Keefe, R. J., Puzas, J. E., Rosier, R. N., Shears, S. B. and Reynolds, P. R.** (2000). Targeted Deletion of Minpp1 Provides New Insight into the Activity of Multiple Inositol Polyphosphate Phosphatase In Vivo. *Mol. Cell. Biol.* **20**, 6496–507.

**Cho, J., King, J. S., Qian, X., Harwood, A. J. and Shears, S. B.** (2008). Dephosphorylation of 2,3-bisphosphoglycerate by MIPP expands the regulatory capacity of the Rapoport-Luebering glycolytic shunt. *Proc. Natl. Acad. Sci. U. S. A.*

**Choi, J., Lee, S., Mallard, W., Clement, K., Tagliazucchi, G. M., Lim, H., Choi, I. Y., Ferrari, F., Tsankov, A. M., Pop, R., et al.** (2015). A comparison of genetically matched cell lines reveals the equivalence of human iPSCs and ESCs. *Nat. Biotechnol.*

**Chou, S. M., Gilbert, E. F., Chun, R. W. M., Laxova, R., Tuffli, G. A., Sufit, R. L. and Krassikot, N.** (1990). Infantile olivopontocerebellar atrophy with spinal muscular atrophy (infantile OPCA + SMA). *Clin. Neuropathol.*

**Clement, E., Mercuri, E., Godfrey, C., Smith, J., Robb, S., Kinali, M., Straub, V., Bushby, K., Manzur, A., Talim, B., et al.** (2008). Brain involvement in muscular dystrophies with defective dystroglycan glycosylation. *Ann. Neurol.*

**Cocco, L., Martelli, A. M., Gilmour, R. S., Rhee, S. G. and Manzoli, F. A.** (2001). Nuclear phospholipase C and signaling. *Biochim. Biophys. Acta - Mol. Cell Biol. Lipids*.

**Cocco, L., Follo, M. Y., Manzoli, L. and Suh, P. G.** (2015). Phosphoinositide-specific phospholipase C in health and disease. *J. Lipid Res.*

**Cockroft, D. L.** (1988). Changes with gestational age in the nutritional requirements of postimplantation rat embryos in culture. *Teratology*.

**Cockroft, D. L., Brook, F. A. and Copp, A. J.** (1992). Inositol deficiency increases the susceptibility to neural tube defects of genetically predisposed (curly tail) mouse

embryos in vitro. *Teratology*.

**Connolly, T. M., Bansal, V. S., Bross, T. E., Irvine, R. F. and Majerus, P. W.** (1987). The metabolism of tris- and tetraphosphates of inositol by 5-phosphomonoesterase and 3-kinase enzymes. *J. Biol. Chem.*

**Coughney, C., McPherson, M. A. and Dormer, R. L.** (1988). Metabolism of inositol 1,3,4,5-tetrakisphosphate by human erythrocyte membranes. A new mechanism for the formation of inositol 1,4,5-trisphosphate. *Biochem. J.*

**Coulter, M. E., Dorobantu, C. M., Lodewijk, G. A., Delalande, F., Cianferani, S., Ganesh, V. S., Smith, R. S., Lim, E. T., Xu, C. S., Pang, S., et al.** (2018). The ESCRT-III Protein CHMP1A Mediates Secretion of Sonic Hedgehog on a Distinctive Subtype of Extracellular Vesicles. *Cell Rep.*

**Cowan, C. A., Atienza, J., Melton, D. A. and Eggan, K.** (2005). Developmental Biology: Nuclear reprogramming of somatic cells after fusion with human embryonic stem cells. *Science (80-. ).*

**Craxton, a, Ali, N. and Shears, S. B.** (1995). Comparison of the activities of a multiple inositol polyphosphate phosphatase obtained from several sources: a search for heterogeneity in this enzyme. *Biochem. J.* **305 ( Pt 2**, 491–498.

**Craxton, a, Caffrey, J. J., Burkhart, W., Safrany, S. T. and Shears, S. B.** (1997). Molecular cloning and expression of a rat hepatic multiple inositol polyphosphate phosphatase. *Biochem. J.* **328 ( Pt 1**, 75–81.

**Crichton, R.** (2001). *of Iron Metabolism Inorganic Biochemistry of Iron Metabolism From Molecular Mechanisms*.

**Crossley, P. H., Martinez, S. and Martin, G. R.** (1996). Midbrain development induced by FGF8 in the chick embryo. *Nature*.

**Cullen, P. J., Irvine, R. F., Drobak, B. K. and Daswon, A. P.** (1989). Inositol 1,3,4,5-tetrakisphosphate causes release of Ca2+ from permeabilized mouse lymphoma L1210 cells by its conversion into inositol 1,4,5-trisphosphate. *Biochem. J.*

**Cullen PJ, Hsuan JJ, Truong O, Letcher AJ, Jackson TR, Dawson AP, Irvine RF.** (1995). Identification of a specific Ins(1,3,4,5)P4-binding protein as a member of the GAP1 family. *Nature.*

**Cunha-Melo, J. R., Dean, N. M., Ali, H. and Beaven, M. A.** (1988). Formation of inositol 1,4,5-trisphosphate and inositol 1,3,4-trisphosphate from inositol 1,3,4,5-tetrakisphosphate and their pathways of degradation in RBL-2H3 cells. *J. Biol. Chem.*

**Dahmane, N. and Ruiz I Altaba, A.** (1999). Sonic hedgehog regulates the growth and patterning of the cerebellum. *Development*.

**Das, S. K., Wang, W., Zhabyeyev, P., Basu, R., Mclean, B., Fan, D., Parajuli, N., Desaulniers, J., Patel, V. B., Hajjar, R. J., et al.** (2015). Iron-overload injury and cardiomyopathy in acquired and genetic models is attenuated by resveratrol therapy. *Sci. Rep.*

**Davanzo, P., Thomas, M. A., Yue, K., Oshiro, T., Belin, T., Strober, M. and McCracken, J.** (2001). Decreased anterior cingulate myo-inositol/creatine spectroscopy resonance with lithium treatment in children with bipolar disorder. *Neuropsychopharmacology*.

**Davis, R. L., Weintraub, H. and Lassar, A. B.** (1987). Expression of a single transfected cDNA converts fibroblasts to myoblasts. *Cell*.

**De Lonlay, P., Seta, N., Barrot, S., Chabrol, B., Drouin, V., Gabriel, B. M., Journel, H., Kretz, M., Laurent, J., Le Merrer, M., et al.** (2001). A broad spectrum of clinical presentations in congenital disorders of glycosylation I: A series of 26 cases. *J. Med. Genet.*

**De Waard, M., Seagar, M., Feltz, A. and Couraud, F.** (1992). Inositol phosphate regulation of voltage-dependent calcium channels in cerebellar granule neurons. *Neuron*

**9**, 497–503.

**Dean, N. M. and Moyer, J. D.** (1988). Metabolism of inositol bis-, tris-, tetrakis- and pentakis-phosphates in GH3 cells. *Biochem. J.*

**DeLorenzo, R. J., Sun, D. A., Blair, R. E. and Sombati, S.** (2007). An in vitro model of Stroke-Induced Epilepsy: Elucidation of The roles of Glutamate and Calcium in The induction and Maintenance of Stroke-Induced Epileptogenesis. *Int. Rev. Neurobiol.*

**Demuro, A. and Parker, I.** (2013). Cytotoxicity of intracellular Aβ42 amyloid oligomers involves Ca2+ release from the endoplasmic reticulum by stimulated production of inositol trisphosphate. *J. Neurosci.*

**Desfougères, Y., Wilson, M. S. C., Laha, D., Miller, G. J. and Saiardi, A.** (2019). ITPK1 mediates the lipid-independent synthesis of inositol phosphates controlled by metabolism. *Proc. Natl. Acad. Sci. U. S. A.*

**Di Daniel, E., Cheng, L., Maycox, P. R. and Mudge, A. W.** (2006). The common inositol-reversible effect of mood stabilizers on neurons does not involve GSK3 inhibition, myo-inositol-1-phosphate synthase or the sodium-dependent myo-inositol transporters. *Mol. Cell. Neurosci.*

**Di Meo, I. and Tiranti, V.** (2018). Classification and molecular pathogenesis of NBIA syndromes. *Eur. J. Paediatr. Neurol.*

**Diedrichsen, J., King, M., Hernandez-Castillo, C., Sereno, M. and Ivry, R. B.** (2019). Universal Transform or Multiple Functionality? Understanding the Contribution of the Human Cerebellum across Task Domains. *Neuron*.

**Donahue, T. F. and Henry, S. A.** (1981). myo-Inositol-1-phosphate synthase. Characteristics of the enzyme and identification of its structural gene in yeast. *J. Biol. Chem.*

**Donis, K. C., Mattos, E. P., Silva, A. A., Furtado, G. V., Saraiva-Pereira, M. L., Jardim, L. B. and Saute, J. A.** (2015). Infantile spinocerebellar ataxia type 7: Case report and a review of the literature. *J. Neurol. Sci.*

**Drecourt, A., Babdor, J., Dussiot, M., Petit, F., Goudin, N., Garfa-Traoré, M., Habarou, F., Bole-Feysot, C., Nitschké, P., Ottolenghi, C., et al.** (2018). Impaired Transferrin Receptor Palmitoylation and Recycling in Neurodegeneration with Brain Iron Accumulation. *Am. J. Hum. Genet.*

**Durmaz, B., Wollnik, B., Cogulu, O., Li, Y., Tekgul, H., Hazan, F. and Ozkinay, F.** (2009). Pontocerebellar hypoplasia type III (CLAM): Extended phenotype and novel molecular findings. *J. Neurol.*

**Edvardson, S., Shaag, A., Kolesnikova, O., Gomori, J. M., Tarassov, I., Einbinder, T., Saada, A. and Elpeleg, O.** (2007). Deleterious mutation in the mitochondrial arginyl-transfer RNA synthetase gene is associated with pontocerebellar hypoplasia. *Am. J. Hum. Genet.*

**Eggens, V. R. C., Barth, P. G., Niermeijer, J. M. F., Berg, J. N., Darin, N., Dixit, A., Fluss, J., Foulds, N., Fowler, D., Hortobágyi, T., et al.** (2014). EXOSC3 mutations in pontocerebellar hypoplasia type 1: Novel mutations and genotype-phenotype correlations. *Orphanet J. Rare Dis.*

**Eiraku, M., Watanabe, K., Matsuo-Takasaki, M., Kawada, M., Yonemura, S., Matsumura, M., Wataya, T., Nishiyama, A., Muguruma, K. and Sasai, Y.** (2008). Self-Organized Formation of Polarized Cortical Tissues from ESCs and Its Active Manipulation by Extrinsic Signals. *Cell Stem Cell*.

**Eiseman, J., Lan, J., Guo, J., Joseph, E. and Vucenik, I.** (2011). Pharmacokinetics and tissue distribution of inositol hexaphosphate in C.B17 SCID mice bearing human breast cancer xenografts. *Metabolism.*

**Englund, C., Kowalczyk, T., Daza, R. A. M., Dagan, A., Lau, C., Rose, M. F. and**

**Hevner, R. F.** (2006). Unipolar brush cells of the cerebellum are produced in the rhombic lip and migrate through developing white matter. *J. Neurosci.*

**Erceg, S., Ronaghi, M., Zipancic, I., Lainez, S., Roselló, M. G., Xiong, C., Moreno-Manzano, V., Rodríguez-Jiménez, F. J., Planells, R., Alvarez-Dolado, M., et al.** (2010). Efficient differentiation of human embryonic stem Cells into Functional Cerebellar-Like Cells. *Stem Cells Dev.*

**Espuny-Camacho, I., Michelsen, K. A., Gall, D., Linaro, D., Hasche, A., Bonnefont, J., Bali, C., Orduz, D., Bilheu, A., Herpoel, A., et al.** (2013). Pyramidal Neurons Derived from Human Pluripotent Stem Cells Integrate Efficiently into Mouse Brain Circuits In Vivo. *Neuron*.

**Estrada-Garcia, T., Craxton, A., Kirk, C. J. and Michell, R. H.** (1991). A salt-activated inositol 1,3,4,5-tetrakisphosphate 3-phosphatase at the inner surface of the human erythrocyte membrane. *Proc. R. Soc. B Biol. Sci.*

**Fainsod, A., Deißler, K., Yelin, R., Marom, K., Epstein, M., Pillemer, G., Steinbeisser, H. and Blum, M.** (1997). The dorsalizing and neural inducing gene follistatin is an antagonist of BMP-4. *Mech. Dev.*

**Fedorenko, O. A., Popugaeva, E., Enomoto, M., Stathopulos, P. B., Ikura, M. and Bezprozvanny, I.** (2014). Intracellular calcium channels: Inositol-1,4,5-trisphosphate receptors. *Eur. J. Pharmacol.*

**Feinstein, M., Flusser, H., Tally, L. S., Ben-Zeev, B., Lev, D., Agamy, O., Cohen, I., Kadir, R., Sivan, S., Leshinsky-Silver, E., et al.** (2014). VPS53 mutations cause progressive cerebello-cerebral atrophy type 2 (PCCA2). *J. Med. Genet.*

**Feraco, P., Mirabelli-Badenier, M., Severino, M., Alpigiani, M. G., Di Rocco, M., Biancheri, R. and Rossi, A.** (2012). The shrunken, bright cerebellum: A characteristic MRI finding in congenital disorders of glycosylation type 1a. *Am. J. Neuroradiol.*

**Ferreiro, E., Oliveira, C. R. and Pereira, C. M. F.** (2004). Involvement of endoplasmic reticulum Ca2+ release through ryanodine and inositol 1,4,5-triphosphate receptors in the neurotoxic effects induced by the amyloid-β peptide. *J. Neurosci. Res.*

**Frederick, J. P., Mattiske, D., Wofford, J. A., Megosh, L. C., Drake, L. Y., Chiou, S. T., Hogan, B. L. M. and York, J. D.** (2005). An essential role for an inositol polyphosphate multikinase, Ipk2, in mouse embryogenesis and second messenger production. *Proc. Natl. Acad. Sci. U. S. A.*

**Frere, S. G., Chang-Ileto, B. and Di Paolo, G.** (2015). Role of phosphoinositides at the neuronal synapse. *Subcell. Biochem.*

**Frey, R., Metzler, D., Fischer, P., Heiden, A., Scharfetter, J., Moser, E. and Kasper, S.** (1998). Myo-inositol in depressive and healthy subjects determined by frontal 1H-magnetic resonance spectroscopy at 1.5 tesla. *J. Psychiatr. Res.*

**Friedman, S. D., Shaw, D. W., Artru, A. A., Richards, T. L., Gardner, J., Dawson, G., Posse, S. and Dager, S. R.** (2003). Regional brain chemical alterations in young children with autism spectrum disorder. *Neurology*.

**Frischmeyer, P. A. and Dietz, H. C.** (1999). Nonsense-mediated mRNA decay in health and disease. *Hum. Mol. Genet.*

**Fry, A. E., Cushion, T. D. and Pilz, D. T.** (2014). The genetics of lissencephaly. *Am. J. Med. Genet. Part C Semin. Med. Genet.*

**Fu, H., Li, B., Hertz, L. and Peng, L.** (2012). Contributions in astrocytes of SMIT1/2 and HMIT to myo-inositol uptake at different concentrations and pH. *Neurochem. Int.*

**Fu, M., Song, Y., Wen, Z., Lu, X. and Cui, L.** (2016). Inositol hexaphosphate and inositol inhibit colorectal cancer metastasis to the liver in BALB/c mice. *Nutrients*.

**Gavrieli, Y., Sherman, Y. and Ben-Sasson, S. A.** (1992). Identification of programmed cell death in situ via specific labeling of nuclear DNA fragmentation. *J. Cell Biol.*

**Geladaki, A., Kočevar Britovšek, N., Breckels, L. M., Smith, T. S., Vennard, O. L., Mulvey, C. M., Crook, O. M., Gatto, L. and Lilley, K. S.** (2019). Combining LOPIT with differential ultracentrifugation for high-resolution spatial proteomics. *NatCommun.*

**Gerrard, L., Rodgers, L. and Cui, W.** (2005). Differentiation of Human Embryonic Stem Cells to Neural Lineages in Adherent Culture by Blocking Bone Morphogenetic Protein Signaling. *Stem Cells*.

**Gilman, S. R., Iossifov, I., Levy, D., Ronemus, M., Wigler, M. and Vitkup, D.** (2011). Rare De Novo Variants Associated with Autism Implicate a Large Functional Network of Genes Involved in Formation and Function of Synapses. *Neuron*.

**Gleichmann, M. and Mattson, M. P.** (2011). Neuronal calcium homeostasis and dysregulation. *Antioxidants Redox Signal.*

**Gonzaga-Jauregui, C., Lotze, T., Jamal, L., Penney, S., Campbell, I. M., Pehlivan, D., Hunter, J. V., Woodbury, S. L., Raymond, G., Adesina, A. M., et al.** (2013). Mutations in VRK1 associated with complex motor and sensory axonal neuropathy plus microcephaly. *JAMA Neurol.*

**Goutieres, F., Aicardi, J. and Farkas, E.** (1977). Anterior horn cell disease associated with pontocerebellar hypoplasia in infants. *J. Neurol. Neurosurg. Psychiatry*.

**Graf, E. and Eaton, J. W.** (1985). Dietary suppression of colonic cancer fiber or phytate? *Cancer*.

**Griffith, H. R., den Hollander, J. A., Okonkwo, O. C., O'Brien, T., Watts, R. L. and Marson, D. C.** (2008). Brain metabolism differs in Alzheimer's disease and Parkinson's disease dementia. *Alzheimer's Dement.*

**Grosskreutz, J., Van Den Bosch, L. and Keller, B. U.** (2010). Calcium dysregulation in amyotrophic lateral sclerosis. *Cell Calcium*.

**Grove, E. A. and Tole, S.** (1999). Patterning events and specification signals in the developing hippocampus. *Cereb. Cortex*.

**Guo, W., Shimada, S., Tajiri, H., Yamauchi, A., Yamashita, T., Okada, S. and Tohyama, M.** (1997). Developmental regulation of Na+/myo-inositol cotransporter gene expression. *Mol. Brain Res.*

**Guo, C., Qiu, H. Y., Huang, Y., Chen, H., Yang, R. Q., Chen, S. Di, Johnson, R. L., Chen, Z. F. and Ding, Y. Q.** (2007). Lmx1b is essential for Fgf8 and Wnt1 expression in the isthmic organizer during tectum and cerebellum development in mice. *Development*.

**Gurdon, J. B.** (1963). Nuclear Transplantation in Amphibia and the Importance of Stable Nuclear Changes in Promoting Cellular Differentiation. *Q. Rev. Biol.*

**GURDON, J. B.** (1962). The developmental capacity of nuclei taken from intestinal epithelium cells of feeding tadpoles. *J. Embryol. Exp. Morphol.*

**Guse, A. H., Greiner, E., Emmrich, F. and Brand, K.** (1993). Mass changes of inositol 1,3,4,5,6-pentakisphosphate and inositol hexakisphosphate during cell cycle progression in rat thymocytes. *J. Biol. Chem.* **268**, 7129–7133.

**Hackett, A., Tarpey, P. S., Licata, A., Cox, J., Whibley, A., Boyle, J., Rogers, C., Grigg, J., Partington, M., Stevenson, R. E., et al.** (2010). CASK mutations are frequent in males and cause X-linked nystagmus and variable XLMR phenotypes. *Eur. J. Hum. Genet.*

**Haldipur, P. and Millen, K. J.** (2019). What cerebellar malformations tell us about cerebellar development. *Neurosci. Lett.*

**Hambidge, K. M.** (2010). Micronutrient bioavailability: Dietary reference intakes and a future perspective. *Am. J. Clin. Nutr.*

**Hanada, T., Weitzer, S., Mair, B., Bernreuther, C., Wainger, B. J., Ichida, J., Hanada, R., Orthofer, M., Cronin, S. J., Komnenovic, V., et al.** (2013). CLP1 links tRNA

metabolism to progressive motor-neuron loss. *Nature*.

**Hanakahi, L. A., Bartlet-jones, M., Chappell, C., Pappin, D. and West, S. C.** (2000). Binding of inositol phosphate to DNA-PK and stimulation of double-strand break repair. *Cell* **102**, 721–9.

**Handel, A. E., Chintawar, S., Lalic, T., Whiteley, E., Vowles, J., Giustacchini, A., Argoud, K., Sopp, P., Nakanishi, M., Bowden, R., et al.** (2016). Assessing similarity to primary tissue and cortical layer identity in induced pluripotent stem cell-derived cortical neurons through single-cell transcriptomics. *Hum. Mol. Genet.*

**Hare, D., Ayton, S., Bush, A. and Lei, P.** (2013). A delicate balance: Iron metabolism and diseases of the brain. *Front. Aging Neurosci.*

**Harland, B. F. and Oberleas, D.** (1987). Phytate in foods. *World Rev. Nutr. Diet.*

**Harvey, J. and Collingridge, G. L.** (1992). Thapsigargin blocks the induction of long-term potentiation in rat hippocampal slices. *Neurosci. Lett.*

**Hata, Y., Butz, S. and Südhof, T. C.** (1996). CASK: A novel dlg/PSD95 homolog with an N-terminal calmodulin-dependent protein kinase domain identified by interaction with neurexins. *J. Neurosci.*

**Hawkins, P. T., Poyner, D. R., Jackson, T. R., Letcher, A. J., Lander, D. A. and Irvine, R. F.** (1993). Inhibition of iron-catalysed hydroxyl radical formation by inositol polyphosphates: A possible physiological function for myo-inositol hexakisphosphate. *Biochem. J.*

**Hayashi, S., Okamoto, N., Chinen, Y., Takanashi, J. I., Makita, Y., Hata, A., Imoto, I. and Inazawa, J.** (2012). Novel intragenic duplications and mutations of CASK in patients with mental retardation and microcephaly with pontine and cerebellar hypoplasia (MICPCH). *Hum. Genet.*

**Hee, J. K. and Thayer, S. A.** (2009). Lithium increases synapse formation between hippocampal neurons by depleting phosphoinositides. *Mol. Pharmacol.*

**Helmis, C., Blechner, C., Lin, H., Schweizer, M., Mayr, G. W., Nielsen, P. and Windhorst, S.** (2013). Malignant H1299 tumour cells preferentially internalize iron-bound inositol hexakisphosphate. *Biosci. Rep.* **33**, 815–822.

**Hermosura, M. C., Takeuchi, H., Fleig, A., Riley, A. M., Potter, B. V. L., Hirata, M. and Penner, R.** (2000). InsP4 facilitates store-operated calcium influx by inhibition of InsP3 5-phosphatase. *Nature*.

**Hernádez-López, S., Tkatch, T., Perez-Garci, E., Galarraga, E., Bargas, J., Hamm, H. and Surmeier, D. J.** (2000). D2 dopamine receptors in striatal medium spiny neurons reduce L-type Ca2+ currents and excitability via a novel PLCβ1-IP3-Calcineurin-signaling cascade. *J. Neurosci.*

**Hernjak, N., Slepchenko, B. M., Fernald, K., Fink, C. C., Fortin, D., Moraru, I. I., Watras, J. and Loew, L. M.** (2005). Modeling and analysis of calcium signaling events leading to long-term depression in cerebellar Purkinje cells. *Biophys. J.*

**Ho, M. W. Y., Yang, X., Carew, M. A., Zhang, T., Hua, L., Kwon, Y. U., Chung, S. K., Adelt, S., Vogel, G., Riley, A. M., et al.** (2002). Regulation of Ins(3, 4, 5, 6)P4signaling by a reversible kinase/phosphatase. *Curr. Biol.*

**Hockemeyer, D. and Jaenisch, R.** (2016a). Induced pluripotent stem cells meet genome editing. *Cell Stem Cell* **18**, 573–586.

**Hockemeyer, D. and Jaenisch, R.** (2016b). Induced pluripotent stem cells meet genome editing. *Cell Stem Cell*.

**Hodgson, M. E. and Shears, S. B.** (1990). Rat liver contains a potent endogenous inhibitor of inositol 1,3,4,5-tetrakisphopshate 3-phosphatase. *Biochem. J.*

**Höer, D., Kwiatkowski, A., Seib, C., Rosenthal, W., Schultz, G. and Oberdisse, E.** (1988). Degradation of inositol 1,3,4,5-tetrakisphosphates by porcine brain cytosol

yields inositol 1,3,4-trisphosphate and inositol 1,4,5-trisphosphate. *Biochem. Biophys. Res. Commun.*

**Höer, A., Höer, D. and Oberdisse, E.** (1990). Properties of a soluble inositol 1,3,4,5-tetrakisphosphate 3-phosphatase from porcine brain. *Biochem. J.*

**Hokin, L. E.** (1985). Receptors and phosphoinositide-generated second messengers. *Annu. Rev. Biochem.*

**Holmes, G.** (1939). The cerebellum of man. *Brain*.

**Hong, S. E., Shugart, Y. Y., Huang, D. T., Al Shahwan, S., Grant, P. E., Hourihane, J. O. B., Martin, N. D. T. and Walsh, C. A.** (2000). Autosomal recessive lissencephaly with cerebellar hypoplasia is associated with human RELN mutations. *Nat. Genet.*

**Hongo, I., Kengaku, M. and Okamoto, H.** (1999). FGF signaling and the anterior neural induction in Xenopus. *Dev. Biol.*

**Howarth, C., Peppiatt-Wildman, C. M. and Attwell, D.** (2010). The energy use associated with neural computation in the cerebellum. *J. Cereb. Blood Flow Metab.*

**Høy, M., Efanov, A. M., Bertorello, A. M., Zaitsev, S. V., Olsen, H. L., Bokvist, K., Leibiger, B., Leibiger, I. B., Zwiller, J., Berggren, P. O., et al.** (2002). Inositol hexakisphosphate promotes dynamin I-mediated endocytosis. *Proc. Natl. Acad. Sci. U. S. A.*

**Høy, M., Berggren, P. O. and Gromada, J.** (2003). Involvement of protein kinase C-ε in inositol hexakisphosphate-induced exocytosis in mouse pancreatic β-cells. *J. Biol. Chem.*

**Hsueh, Y. P., Wang, T. F., Yang, F. C. and Sheng, M.** (2000). Nuclear translocation and transcription regulation by the membrane- associated guanylate kinase CASK/LIN-2. *Nature*.

**Huerta, S., Goulet, E. J., Huerta-Yepez, S. and Livingston, E. H.** (2007). Screening and Detection of Apoptosis. *J. Surg. Res.*

**Hughes, P. J. and Shears, S. B.** (1990). Inositol 1,3,4,5,6-pentakisphosphate and inositol hexakisphosphate inhibit inositol-1,3,4,5-tetrakisphosphate 3-phosphatase in rat parotid glands. *J. Biol. Chem.*

**Il, H. K., Soon, K. P., Soon, T. H., Sang Jo, Y., Eun, J. K., Eun, H. P., Seung, B. H., Shin, H. S., Sun, W., Hyun, T. K., et al.** (2009). Inositol 1,4,5-trisphosphate 3-kinase A functions as a scaffold for synaptic rac signaling. *J. Neurosci.*

**Inoue, T., Kato, K., Kohda, K. and Mikoshiba, K.** (1998). Type 1 inositol 1,4,5-trisphosphate receptor is required for induction of long-term depression in cerebellar Purkinje neurons. *J. Neurosci.*

**Irvine, R. F. and Schell, M. J.** (2001). Back in the water: The return of the inositol phosphates. *Nat. Rev. Mol. Cell Biol.*

**Irvine, R. F., Letcher, A. J., Heslop, J. P. and Berridge, M. J.** (1986). The inositol tris/tetrakisphosphate pathway - Demonstration of Ins(l,4,5)P3 3-kinase activity in animal tissues. *Nature*.

**Ishida, Y., Kawakami, H., Kitajima, H., Nishiyama, A., Sasai, Y., Inoue, H. and Muguruma, K.** (2016a). Vulnerability of Purkinje Cells Generated from Spinocerebellar Ataxia Type 6 Patient-Derived iPSCs. *Cell Rep.* **17**, 1482–1490.

**Ishida, Y., Kawakami, H., Kitajima, H., Nishiyama, A., Sasai, Y., Inoue, H. and Muguruma, K.** (2016b). Vulnerability of Purkinje Cells Generated from Spinocerebellar Ataxia Type 6 Patient-Derived iPSCs. *Cell Rep.*

**Ito, M.** (1984). *The cerebellum and neural control*. New York: Raven Press.

**Ivanova, E. L., Mau-Them, F. T., Riazuddin, S., Kahrizi, K., Laugel, V., Schaefer, E., de Saint Martin, A., Runge, K., Iqbal, Z., Spitz, M. A., et al.** (2017). Homozygous Truncating Variants in TBC1D23 Cause Pontocerebellar Hypoplasia and Alter Cortical

Development. *Am. J. Hum. Genet.*

**Ives, E. B., Nichols, J., Wente, S. R. and York, J. D.** (2000). Biochemical and functional characterization of inositol 1,3,4,5,6-pentakisphosphate 2-kinases. *J. Biol. Chem.*

**Iwama, K., Sasaki, M., Hirabayashi, S., Ohba, C., Iwabuchi, E., Miyatake, S., Nakashima, M., Miyake, N., Ito, S., Saitsu, H., et al.** (2016). Milder progressive cerebellar atrophy caused by biallelic SEPSECS mutations. *J. Hum. Genet.*

**Jacobs, H. I. L., Hopkins, D. A., Mayrhofer, H. C., Bruner, E., Van Leeuwen, F. W., Raaijmakers, W. and Schmahmann, J. D.** (2018). The cerebellum in Alzheimer's disease: Evaluating its role in cognitive decline. *Brain*.

**Jaglin, X. H. and Chelly, J.** (2009). Tubulin-related cortical dysgeneses: microtubule dysfunction underlying neuronal migration defects. *Trends Genet.*

**Jensen, L. E., Bultynck, G., Luyten, T., Amijee, H., Bootman, M. D. and Roderick, H. L.** (2013). Alzheimer's disease-associated peptide Aβ42 mobilizes ER Ca2+ via InsP3R-dependent and -independent mechanisms. *Front. Mol. Neurosci.*

**Jia Y, Subramanian KK, Erneux C, Pouillon V, Hattori H, Jo H, You J, Zhu D, Schurmans S, Luo HR.** (2007). Inositol 1,3,4,5-tetrakisphosphate negatively regulates phosphatidylinositol-3,4,5- trisphosphate signaling in neutrophils. *Immunity.*

**Jinek, M., Chylinski, K., Fonfara, I., Hauer, M., Doudna, J. A. and Charpentier, E.** (2012a). A Programmable Dual-RNA – Guided. **337**, 816–822.

**Jinek, M., Chylinski, K., Fonfara, I., Hauer, M., Doudna, J. A. and Charpentier, E.** (2012b). A programmable dual-RNA-guided DNA endonuclease in adaptive bacterial immunity. *Science (80-. ).*

**Johnson, M. A., Weick, J. P., Pearce, R. A. and Zhang, S. C.** (2007). Functional neural development from human embryonic stem cells: Accelerated synaptic activity via astrocyte coculture. *J. Neurosci.*

**Jorgenson, L. A., Sun, M., O'Connor, M. and Georgieff, M. K.** (2005). Fetal iron deficiency disrupts the maturation of synaptic function and efficacy in area CA1 of the developing rat hippocampus. *Hippocampus.*

**Joyner, A. L., Herrup, K., Auerbach, B. A., Davis, C. A. and Rossant, J.** (1991). Subtle cerebellar phenotype in mice homozygous for a targeted deletion of the En-2 homeobox. *Science (80-. ).*

**Jun, K., Choi, G., Yang, S. G., Choi, K. Y., Kim, H., Chan, G. C. K., Storm, D. R., Albert, C., Mayr, G. W., Lee, C. J., et al.** (1998). Enhanced hippocampal CA1 LTP but normal spatial learning in inositol 1,4,5-trisphosphate 3-kinase(A)-deficient mice. *Learn. Mem.*

**Juneja, M., Shamim, U., Joshi, A., Mathur, A., Uppili, B., Sairam, S., Ambawat, S., Dixit, R. and Faruq, M.** (2018). A novel mutation in SLC39A14 causing hypermanganesemia associated with infantile onset dystonia. *J. Gene Med.*

**Kamoshita, S., Takei, Y., Miyao, M., Yanagisawa, M., Kobayashi, S. and Saito, K.** (1990). Pontocerebellar hypoplasia associated with infantile motor neuron disease (norman's disease). *Fetal Pediatr. Pathol.*

**Karaca, E., Weitzer, S., Pehlivan, D., Shiraishi, H., Gogakos, T., Hanada, T., Jhangiani, S. N., Wiszniewski, W., Withers, M., Campbell, I. M., et al.** (2014). Human CLP1 mutations alter tRNA biogenesis, Affecting both peripheral and central nervous system function. *Cell*.

**Kato, T., Shioiri, T., Takahashi, S. and Inubushi, T.** (1991). Measurement of brain phosphoinositide metabolism in bipolar patients using in vivo 31P-MRS. *J. Affect. Disord.*

**Kato, T., Shioiri, T., Murashita, J., Hamakawa, H., Inubushi, T. and Takahashi, S.** (1994). Phosphorus-31 magnetic resonance spectroscopy and ventricular enlargement in

bipolar disorder. *Psychiatry Res. Neuroimaging*.
**KAUFMANN, P.** (2000). The Anatomical Basis of Mouse Development. By MATTHEW H. KAUFMAN and JONATHAN B. L. BARD. (Pp. xii+291; fully illustrated; $99.95; ISBN 0 12 402060 7.) San Diego: Academic Press. 1999. *J. Anat.*
**Kaur, D., Yantiri, F., Rajagopalan, S., Kumar, J., Mo, J. Q., Boonplueang, R., Viswanath, V., Jacobs, R., Yang, L., Beal, M. F., et al.** (2003). Genetic or pharmacological iron chelation prevents MPTP-induced neurotoxicity in vivo: A novel therapy for Parkinson's disease. *Neuron*.
**Kelava, I. and Lancaster, M. a.** (2016). Stem Cell Models of Human Brain Development. *Cell Stem Cell* **18**, 736–748.
**Kelly, P. T., MacKinnon, R. L., Dietz, R. V., Maher, B. J. and Wang, J.** (2005). Postsynaptic IP3 receptor-mediated Ca2+ release modulates synaptic transmission in hippocampal neurons. *Mol. Brain Res.*
**Kiecker, C. and Lumsden, A.** (2012). The role of organizers in patterning the nervous system. *Annu. Rev. Neurosci.*
**Kiessling, M. C., Büttner, A., Butti, C., Müller-Starck, J., Milz, S., Hof, P. R., Frank, H. G. and Schmitz, C.** (2014). Cerebellar granule cells are generated postnatally in humans. *Brain Struct. Funct.*
**Kilaparty, S. P., Singh, A., Baltosser, W. H. and Ali, N.** (2014). Computational analysis reveals a successive adaptation of multiple inositol polyphosphate phosphatase 1 in higher organisms through evolution. *Evol. Bioinforma.*
**Kilaparty, S. P., Agarwal, R., Singh, P., Kannan, K. and Ali, N.** (2016). Endoplasmic reticulum stress-induced apoptosis accompanies enhanced expression of multiple inositol polyphosphate phosphatase 1 (Minpp1): a possible role for Minpp1 in cellular stress response. *Cell Stress Chaperones* **21**, 593–608.
**King, M., Hernandez-Castillo, C. R., Poldrack, R. A., Ivry, R. B. and Diedrichsen, J.** (2019). Functional boundaries in the human cerebellum revealed by a multi-domain task battery. *Nat. Neurosci.*
**Kim JH, Lee HK, Takamiya K, Huganir RL**. (2003). The role of synaptic GTPase-activating protein in neuronal development and synaptic plasticity. *J Neurosci.*
**Knight, S. W., Heiss, N. S., Vulliamy, T. J., Aalfs, C. M., McMahon, C., Richmond, P., Jones, A., Hennekam, R. C. M., Poustka, A., Mason, P. J., et al.** (1999). Unexplained aplastic anaemia, immunodeficiency, and cerebellar hypoplasia (Hoyeraal-Hreidarsson syndrome) due to mutations in the dyskeratosis congenita gene, DKC1. *Br. J. Haematol.*
**Koizumi, S., Bootman, M. D., Bobanović, L. K., Schell, M. J., Berridge, M. J. and Lipp, P.** (1999). Characterization of elementary Ca2+ release signals in NGF- differentiated PC12 cells and hippocampal neurons. *Neuron.*
**Kolozsvari, B., Firth, S. and Saiardi, A.** (2015). Raman spectroscopy detection of phytic acid in plant seeds reveals the absence of inorganic polyphosphate. *Mol. Plant*.
**Kong, H., Jones, P. P., Koop, A., Zhang, L., Duff, H. J. and Chen, S. R. W.** (2008). Caffeine induces Ca2+ release by reducing the threshold for luminal Ca2+ activation of the ryanodine receptor. *Biochem. J.*
**KOSTER, S.** (1926). TWO CASES OF HYPOPLASIA PONTONEOCEREBELLARIS. *Acta Psychiatr. Scand.*
**Krause, F.** (1929). Über einen Bildungsfehler des Kleinhirns und einige faseranatomische Beziehungen des Organs. *Zeitschrift für die gesamte Neurol. und Psychiatr.*
**Kreitzer, A. C., Gee, K. R., Archer, E. A. and Regehr, W. G.** (2000). Monitoring presynaptic calcium dynamics in projection fibers by in vivo loading of a novel calcium indicator. *Neuron*.
**Kruse, M., Vivas, O., Traynor-Kaplan, A. and Hille, B.** (2016). Dynamics of

phosphoinositide-dependent signaling in sympathetic neurons. *J. Neurosci.*

**Kulessa, H., Frampton, J. and Graf, T.** (1995). GATA-1 reprograms avian myelomonocytic cell lines into eosinophils, thromboblasts, and erythroblasts. *Genes Dev.*

**Kumar, R. A., Pilz, D. T., Babatz, T. D., Cushion, T. D., Harvey, K., Topf, M., Yates, L., Robb, S., Uyanik, G., Mancini, G. M. S., et al.** (2010). TUBA1A mutations cause wide spectrum lissencephaly (smooth brain) and suggest that multiple neuronal migration pathways converge on alpha tubulins. *Hum. Mol. Genet.*

**Kurosaki, T. and Maquat, L. E.** (2016). Nonsense-mediated mRNA decay in humans at a glance. *J. Cell Sci.*

**Lardelli, R. M., Schaffer, A. E., Eggens, V. R. C., Zaki, M. S., Grainger, S., Sathe, S., Van Nostrand, E. L., Schlachetzki, Z., Rosti, B., Akizu, N., et al.** (2017). Biallelic mutations in the 3' exonuclease TOE1 cause pontocerebellar hypoplasia and uncover a role in snRNA processing. *Nat. Genet.*

**Larsson, O., Barker, C. J., Sjöholm, Å., Carlqvist, H., Michell, R. H., Bertorello, A., Nilsson, T., Honkanen, R. E., Mayr, G. W., Zwiller, J., et al.** (1997). Inhibition of phosphatases and increased Ca2+ channel activity by inositol hexakisphosphate. *Science (80-. ).*

**Lautenschläger, J., Prell, T., Ruhmer, J., Weidemann, L., Witte, O. W. and Grosskreutz, J.** (2013). Overexpression of human mutated G93A SOD1 changes dynamics of the ER mitochondria calcium cycle specifically in mouse embryonic motor neurons. *Exp. Neurol.*

**Le Dréau, G. and Martí, E.** (2012). Dorsal-ventral patterning of the neural tube: A tale of three signals. *Dev. Neurobiol.*

**Lee, S. H., Park, H. J., Chun, H. K., Cho, S. Y., Cho, S. M. and Lillehoj, H. S.** (2006). Dietary phytic acid lowers the blood glucose level in diabetic KK mice. *Nutr. Res.*

**Lee, H. S., Qi, Y. and Im, W.** (2015). Effects of N-glycosylation on protein conformation and dynamics: Protein Data Bank analysis and molecular dynamics simulation study. *Sci. Rep.*

**Lei, P., Ayton, S., Finkelstein, D. I., Spoerri, L., Ciccotosto, G. D., Wright, D. K., Wong, B. X. W., Adlard, P. A., Cherny, R. A., Lam, L. Q., et al.** (2012). Tau deficiency induces parkinsonism with dementia by impairing APP-mediated iron export. *Nat. Med.*

**Letcher, A. J., Schell, M. J. and Irvine, R. F.** (2008). Do mammals make all their own inositol hexakisphosphate? *Biochem. J.* **416**, 263–270.

**Leto, K., Carletti, B., Williams, I. M., Magrassi, L. and Rossi, F.** (2006). Different types of cerebellar GABAergic interneurons originate from a common pool of multipotent progenitor cells. *J. Neurosci.*

**Leto, K., Arancillo, M., Becker, E. B. E., Buffo, A., Chiang, C., Ding, B., Dobyns, W. B., Dusart, I., Haldipur, P., Hatten, M. E., et al.** (2015). Consensus Paper: Cerebellar Development. *Cerebellum*.

**Levi, S. and Finazzi, D.** (2014). Neurodegeneration with brain iron accumulation: Update on pathogenic mechanisms. *Front. Pharmacol.*

**Li, M. and Belmonte, J. C. I.** (2016). Looking to the future following 10 years of induced pluripotent stem cell technologies. *Nat. Protoc.* **11**, 1579–1585.

**Li, H. S., Xu, X. Z. S. and Montell, C.** (1999). Activation of a trpc3-dependent cation current through the neurotrophin bdnf. *Neuron*.

**Li, Y., Jin, Y. C., Cul, K., Li, N., Zheng, Z. Y., Wang, Y. Z. and Yuan, X. B.** (2005). Essential role of TRPC channels in the guidance of nerve growth cones by brain-derived neurotrophic factor. *Nature*.

**Li, X. J., Zhang, X., Johnson, M. A., Wang, Z. B., LaVaute, T. and Zhang, S. C.** (2009).

Coordination of sonic hedgehog and Wnt signaling determines ventral and dorsal telencephalic neuron types from human embryonic stem cells. *Development*.

**Limoli, C. L. and Ward, J. F.** (1993). A new method for introducing double-strand breaks into cellular DNA. *Radiat. Res.*

**Limperopoulos, C., Soul, J. S., Gauvreau, K., Huppi, P. S., Warfield, S. K., Bassan, H., Robertson, R. L., Volpe, J. J. and Du Plessis, A. J.** (2005). Late gestation cerebellar growth is rapid and impeded by premature birth. *Pediatrics*.

**Liu Q, Huang S, Yin P, Yang S, Zhang J, Jing L, Cheng S, Tang B, Li XJ, Pan Y, Li S.** (2020). Cerebellum-enriched protein INPP5A contributes to selective neuropathology in mouse model of spinocerebellar ataxias type 17. *Nat Commun.*

**Loss, O., Wu, C. T., Riccio, A. and Saiardi, A.** (2013). Modulation of inositol polyphosphate levels regulates neuronal differentiation. *Mol. Biol. Cell*.

**Luo, D., Sun, H., Xiao, R. P. and Han, Q.** (2005). Caffeine induced Ca2+ release and capacitative Ca2+ entry in human embryonic kidney (HEK293) cells. *Eur. J. Pharmacol.*

**Lykidis, A., Jackson, P. D., Rock, C. O. and Jackowski, S.** (1997). The role of CDP-diacylglycerol synthetase and phosphatidylinositol synthase activity levels in the regulation of cellular phosphatidylinositol content. *J. Biol. Chem.*

**Ma, W. J., Hashii, M., Munesue, T., Hayashi, K., Yagi, K., Yamagishi, M., Higashida, H. and Yokoyama, S.** (2013). Non-synonymous single-nucleotide variations of the human oxytocin receptor gene and autism spectrum disorders: A case-control study in a Japanese population and functional analysis. *Mol. Autism*.

**Maallem, S., Berod, A., Mutin, M., Kwon, H. M. and Tappaz, M. L.** (2006). Large discrepancies in cellular distribution of the tonicity-induced expression of osmoprotective genes and their regulatory transcription factor TonEBP in rat brain. *Neuroscience*.

**Macbeth, M. R., Schubert, H. L., VanDemark, A. F., Lingam, A. T., Hill, C. P. and Bass, B. L.** (2005). Structural biology: Inositol hexakisphosphate is bound in the ADAR2 core and required for RNA editing. *Science (80-. ).*

**MacHold, R. and Fishell, G.** (2005). Math1 is expressed in temporally discrete pools of cerebellar rhombic-lip neural progenitors. *Neuron*.

**Maherali, N. and Hochedlinger, K.** (2008). Guidelines and Techniques for the Generation of Induced Pluripotent Stem Cells. *Cell Stem Cell* **3**, 595–605.

**Mailleux P, Takazawa K, Erneux C, Vanderhaeghen JJ.** (1991). Inositol 1,4,5-trisphosphate 3-kinase mRNA: high levels in the rat hippocampal CA1 pyramidal and dentate gyrus granule cells and in cerebellar Purkinje cells. *J Neurochem.*

**Majerus, P. W.** (1992). Inositol phosphate biochemistry. *Annu. Rev. Biochem.*

**Majerus, P. W., Kisseleva, M. V. and Anderson Norris, F.** (1999). The role of phosphatases in inositol signaling reactions. *J. Biol. Chem.*

**Malabanan MM, Blind RD.** (2016). Inositol polyphosphate multikinase (IPMK) in transcriptional regulation and nuclear inositide metabolism. *Biochem Soc Trans*.

**Malan, V. and Romana, S.** (2012). Diagnosis of chromosomal abnormalities by array CGH in constitutional pathology: The end of the first-line karyotype. *Arch. Pediatr.*

**Mali, G., Šala, M., Arčon, I., Kaučič, V. and Kolar, J.** (2006). Insight into the short-range structure of amorphous iron inositol hexaphosphate as provided by31P NMR and Fe X-ray absorption spectroscopy. *J. Phys. Chem. B.*

**Manto, M., Bower, J. M., Conforto, A. B., Delgado-García, J. M., Da Guarda, S. N. F., Gerwig, M., Habas, C., Hagura, N., Ivry, R. B., Marien, P., et al.** (2012). Consensus paper: Roles of the cerebellum in motor control-the diversity of ideas on cerebellar involvement in movement. In *Cerebellum*, .

**Marek, S., Siegel, J. S., Gordon, E. M., Raut, R. V., Gratton, C., Newbold, D. J., Ortega, M., Laumann, T. O., Adeyemo, B., Miller, D. B., et al.** (2018). Spatial and Temporal Organization of the Individual Human Cerebellum. *Neuron*.

**Marin-Valencia, I., Gerondopoulos, A., Zaki, M. S., Ben-Omran, T., Almureikhi, M., Demir, E., Guemez-Gamboa, A., Gregor, A., Issa, M. Y., Appelhof, B., et al.** (2017). Homozygous Mutations in TBC1D23 Lead to a Non-degenerative Form of Pontocerebellar Hypoplasia. *Am. J. Hum. Genet.*

**Mariño, G. and Kroemer, G.** (2013). Mechanisms of apoptotic phosphatidylserine exposure. *Cell Res.*

**Marsh, A. P. L., Lukic, V., Pope, K., Bromhead, C., Tankard, R., Ryan, M. M., Yiu, E. M., Sim, J. C. H., Delatycki, M. B., Amor, D. J., et al.** (2015). Complete callosal agenesis, pontocerebellar hypoplasia, and axonal neuropathy due to AMPD2 loss. *Neurol. Genet.*

**Marsh, A. P. L., Yap, P., Tan, T., Pope, K., White, S. M., Chong, B., Mcgillivray, G., Boys, A., Stephenson, S. E. M., Leventer, R. J., et al.** (2017). A novel AMPD2 mutation outside the AMP deaminase domain causes pontocerebellar hypoplasia type 9. *Am. J. Med. Genet. Part A.*

**Martinez, S., Wassef, M. and Alvarado-Mallart, R. M.** (1991). Induction of a mesencephalic phenotype in the 2-day-old chick prosencephalon is preceded by the early expression of the homeobox gene en. *Neuron*.

**Martinez, S., Andreu, A., Mecklenburg, N. and Echevarria, D.** (2013). Cellular and molecular basis of cerebellar development. *Front. Neuroanat.*

**Marzban, H., Del Bigio, M. R., Alizadeh, J., Ghavami, S., Zachariah, R. M. and Rastegar, M.** (2015). Cellular commitment in the developing cerebellum. *Front. Cell. Neurosci.*

**McLaurin, J., Franklin, T., Chakrabartty, A. and Fraser, P. E.** (1998). Phosphatidylinositol and inositol involvement in Alzheimer amyloid-β fibril growth and arrest. *J. Mol. Biol.*

**McPhee, F., Lowe, G., Vaziri, C. and Downes, C. P.** (1991). Phosphatidylinositol synthase and phosphatidylinositol/inositol exchange reactions in turkey erythrocyte membranes. *Biochem. J.*

**Medina-Cano, D., Ucuncu, E., Nguyen, L. S., Nicouleau, M., Lipecka, J., Bizot, J. C., Thiel, C., Foulquier, F., Lefort, N., Faivre-Sarrailh, C., et al.** (2018). High N-glycan multiplicity is critical for neuronal adhesion and sensitizes the developing cerebellum to N-glycosylation defect. *Elife*.

**Megahed, H., Nicouleau, M., Barcia, G., Medina-Cano, D., Siquier-Pernet, K., Bole-Feysot, C., Parisot, M., Masson, C., Nitschké, P. and Rio, M.** (2016). Utility of whole exome sequencing for the early diagnosis of pediatric-onset cerebellar atrophy associated with developmental delay in an inbred population. *Orphanet J. Rare Dis.* **11**, 1.

**Menara, G., Lefort, N., Antignac, C. and Mollet, G.** (2020). Generation of an induced pluripotent stem cell (iPSC) line (IMAGINi007) from a patient with steroid-resistant nephrotic syndrome carrying the homozygous p.R138Q mutation in the podocin-encoding NPHS2 gene. *Stem Cell Res.*

**Miale, I. L. and Sidman, R. L.** (1961). An autoradiographic analysis of histogenesis in the mouse cerebellum. *Exp. Neurol.*

**Michaelis, T., Helms, G., Merboldt, K. - D, Hänicke, W., Bruhn, H. and Frahm, J.** (1993). Identification of scyllo- inositol in proton NMR spectra of human brain in vivo. *NMR Biomed.*

**Michell, R. H., Conroy, L. A., Finney, M., French, P. J., Bunce, C. M., Anderson, K.,**

**Baxter, M. A., Brown, G., Gordon, J. and Jenkinson, E. J.** (1992). Inositol lipids and phosphates in the proliferation and differentiation of lymphocytes and myeloid cells. *Ciba Found. Symp.*

**Mikoshiba, K., Furuichi, T., Miyawaki, A., Yoshikawa, S., Nakagawa, T., Yamada, N., Hamanaka, Y., Fujino, I., Michikawa, T. and Ryo, Y.** (1993). Inositol trisphosphate receptor and Ca2+ signalling. *Philos. Trans. R. Soc. Lond. B. Biol. Sci.*

**Millet, S., Campbell, K., Epstein, D. J., Losos, K., Harris, E. and Joyner, A. L.** (1999). A role for Gbx2 in repression of Otx2 and positioning the mid/hindbrain organizer. *Nature*.

**Mitchell, J., Wang, X., Zhang, G., Gentzsch, M., Nelson, D. J. and Shears, S. B.** (2008). An Expanded Biological Repertoire for Ins(3,4,5,6)P4 through its Modulation of ClC-3 Function. *Curr. Biol.*

**Mitsunori Fukuda and Katsuhiko Mikoshiba** (1997). The function of inositol high polyphosphate binding proteins. **2**,.

**Mochida, G. H., Ganesh, V. S., De Michelena, M. I., Dias, H., Atabay, K. D., Kathrein, K. L., Huang, H. T., Sean Hill, R., Felie, J. M., Rakiec, D., et al.** (2012). CHMP1A encodes an essential regulator of BMI1-INK4A in cerebellar development. *Nat. Genet.*

**Molyneaux, B. J., Arlotta, P., Menezes, J. R. L. and Macklis, J. D.** (2007). Neuronal subtype specification in the cerebral cortex. *Nat. Rev. Neurosci.*

**Monserrate, J. P. and York, J. D.** (2010). Inositol phosphate synthesis and the nuclear processes they affect. *Curr. Opin. Cell Biol.* **22**, 365–373.

**Moog, U., Bierhals, T., Brand, K., Bautsch, J., Biskup, S., Brune, T., Denecke, J., De Die-Smulders, C. E., Evers, C., Hempel, M., et al.** (2015). Phenotypic and molecular insights into CASK-related disorders in males. *Orphanet J. Rare Dis.*

**Moore, G. J., Bebchuk, J. M., Parrish, J. K., Faulk, M. W., Arfken, C. L., Strahl-Bevacqua, J. and Manji, H. K.** (1999). Temporal dissociation between lithium-induced changes in frontal lobe myo-inositol and clinical response in manic-depressive illness. *Am. J. Psychiatry*.

**Mori, T., Kasem, E. A., Suzuki-Kouyama, E., Cao, X., Li, X., Kurihara, T., Uemura, T., Yanagawa, T. and Tabuchi, K.** (2019). Deficiency of calcium/calmodulin-dependent serine protein kinase disrupts the excitatory-inhibitory balance of synapses by down-regulating GluN2B. *Mol. Psychiatry*.

**Morrison, R. S., Shi, E., Kan, M., Yamaguchi, F., McKeehan, W., Rudnicka-Nawrot, M. and Palczewski, K.** (1994). Inositolhexakisphosphate (InsP6): An antagonist of fibroblast growth factor receptor binding and activity. *Vitr. Cell. Dev. Biol. - Anim.*

**Mosmann, T.** (1983). Rapid colorimetric assay for cellular growth and survival: Application to proliferation and cytotoxicity assays. *J. Immunol. Methods*.

**Muguruma, K.** (2018). Self-Organized Cerebellar Tissue from Human Pluripotent Stem Cells and Disease Modeling with Patient-Derived iPSCs. *Cerebellum*.

**Muguruma, K., Nishiyama, A., Ono, Y., Miyawaki, H., Mizuhara, E., Hori, S., Kakizuka, A., Obata, K., Yanagawa, Y., Hirano, T., et al.** (2010). Ontogeny-recapitulating generation and tissue integration of ES cell-derived Purkinje cells. *Nat. Neurosci.* **13**, 1171–80.

**Muguruma, K., Nishiyama, A., Kawakami, H., Hashimoto, K. and Sasai, Y.** (2015). Self-organization of polarized cerebellar tissue in 3D culture of human pluripotent stem cells. *Cell Rep.* **10**, 537–550.

**Müller, M. S., Obel, L. F., Waagepetersen, H. S., Schousboe, A. and Bak, L. K.** (2013). Complex actions of ionomycin in cultured cerebellar astrocytes affecting both calcium-induced calcium release and store-operated calcium entry. *Neurochem. Res.*

**Musunuru, K.** (2013). Genome editing of human pluripotent stem cells to generate human cellular disease models. *Dis. Model. Mech.* **6**, 896–904.

**Nagarkatti, N., Deshpande, L. S. and DeLorenzo, R. J.** (2008). Levetiracetam Inhibits both ryanodine and IP3 receptor activated calcium induced calcium release in hippocampal neurons in culture. *Neurosci. Lett.*

**Najm, J., Horn, D., Wimplinger, I., Golden, J. A., Chizhikov, V. V., Sudi, J., Christian, S. L., Ullmann, R., Kuechler, A., Haas, C. A., et al.** (2008). Mutations of CASK cause an X-linked brain malformation phenotype with microcephaly and hypoplasia of the brainstem and cerebellum. *Nat. Genet.*

**Nakamura, H., Katahira, T., Matsunaga, E. and Sato, T.** (2005). Isthmus organizer for midbrain and hindbrain development. *Brain Res. Rev.*

**Nalaskowski, M. M., Deschermeier, C., Fanick, W. and Mayr, G. W.** (2002). The human homologue of yeast ArgRIII protein is an inositol phosphate multikinase with predominantly nuclear localization. *Biochem. J.*

**Namavar, Y., Eggens, V. R., Barth, P. G. and Baas, F.** (1993). *TSEN54-Related Pontocerebellar Hypoplasia*.

**Namavar, Y., Barth, P. G., Tien Poll-The, B. and Baas, F.** (2011a). Classification, diagnosis and potential mechanisms in Pontocerebellar Hypoplasia. *Orphanet J. Rare Dis.* **6**, 50.

**Namavar, Y., Chitayat, D., Barth, P. G., Van Ruissen, F., De Wissel, M. B., Poll-The, B. T., Silver, R. and Baas, F.** (2011b). TSEN54 mutations cause pontocerebellar hypoplasia type 5. *Eur. J. Hum. Genet.*

**Nayler, S. P., Powell, J. E., Vanichkina, D. P., Korn, O., Wells, C. A., Kanjhan, R., Sun, J., Taft, R. J., Lavin, M. F. and Wolvetang, E. J.** (2017). Human iPSC-derived cerebellar neurons from a patient with ataxia-telangiectasia reveal disrupted gene regulatory networks. *Front. Cell. Neurosci.*

**Nishizuka, Y.** (1986). Studies and perspectives of protein kinase C. *Science (80-. ).*

**Nogimori, K., Hughes, P. J., Glennon, M. C., Hodgson, M. E., Putney, J. W. and Shears, S. B.** (1991). Purification of an Inositol (1,3,4,5)-tetrakisphosphate 3-phosphatase activity from rat liver and the evaluation of its substrate specificity. *J. Biol. Chem.* **266**, 16499–16506.

**Norman, R. M.** (1961). Cerebellar hypoplasia in Werdnig-Hoffmann disease. *Arch. Dis. Child.*

**Oberdisse, E., Nolan, R. D. and Lapetina, E. G.** (1990). Thrombin and phorbol ester stimulate inositol 1,3,4,5-tetrakisphosphate 3-phosphomonoesterase in human platelets. *J. Biol. Chem.*

**Odom, A. R., Stahlberg, A., Wente, S. R. and York, J. D.** (2000). A role for nuclear inositol 1,4,5-trisphosphate kinase in transcriptional control. *Science (80-. ).*

**Otis, T. S., Mathews, P. J., Lee, K. H. and Maiz, J.** (2012). How do climbing fibers teach? *Front. Neural Circuits*.

**Otto, J. C., Mulugu, S., Fridy, P. C., Chiou, S. T., Armbruster, B. N., Ribeiro, A. A. and York, J. D.** (2007). Biochemical Analysis of Inositol Phosphate Kinases. *Methods Enzymol.* **434**, 171–185.

**Pal, S., Sun, D., Limbrick, D., Rafiq, A. and DeLorenzo, R. J.** (2001). Epileptogenesis induces long-term alterations in intracellular calcium release and sequestration mechanisms in the hippocampal neuronal culture model of epilepsy. *Cell Calcium*.

**Pankratz, M. T., Li, X.-J., LaVaute, T. M., Lyons, E. A., Chen, X. and Zhang, S.-C.** (2007). Directed Neural Differentiation of Human Embryonic Stem Cells via an Obligated Primitive Anterior Stage. *Stem Cells*.

**Park, C. Y., Kim, D. H., Son, J. S., Sung, J. J., Lee, J., Bae, S., Kim, J. H., Kim, D. W. and Kim, J. S.** (2015). Functional Correction of Large Factor VIII Gene Chromosomal Inversions in Hemophilia A Patient-Derived iPSCs Using CRISPR-Cas9. *Cell Stem Cell*

**17**, 213–220.
**Parmalee, N. L. and Aschner, M.** (2016). Manganese and aging. *Neurotoxicology*.
**Partridge, L. D. and Valenzuela, C. F.** (1999). Ca2+ store-dependent potentiation of Ca2+-activated non-selective cation channels in rat hippocampal neurones in vitro. *J. Physiol.*
**Patel, M. S., Becker, L. E., Toi, A., Armstrong, D. L. and Chitayat, D.** (2006). Severe, fetal-onset form of olivopontocerebellar hypoplasia in three sibs: PCH type 5? *Am. J. Med. Genet.*
**Pavlidou, E., Salpietro, V., Phadke, R., Hargreaves, I. P., Batten, L., McElreavy, K., Pitt, M., Mankad, K., Wilson, C., Cutrupi, M. C., et al.** (2016). Pontocerebellar hypoplasia type 2D and optic nerve atrophy further expand the spectrum associated with selenoprotein biosynthesis deficiency. *Eur. J. Paediatr. Neurol.*
**Perez, E. E., Wang, J., Miller, J. C., Jouvenot, Y., Kim, K. A., Liu, O., Wang, N., Lee, G., Bartsevich, V. V., Lee, Y. L., et al.** (2008). Establishment of HIV-1 resistance in CD4+ T cells by genome editing using zinc-finger nucleases. *Nat. Biotechnol.*
**Piccolo, S., Sasai, Y., Lu, B. and De Robertis, E. M.** (1996). Dorsoventral patterning in Xenopus: Inhibition of ventral signals by direct binding of chordin to BMP-4. *Cell*.
**Pisani, F., Livermore, T., Rose, G., Chubb, J. R., Gaspari, M. and Saiardi, A.** (2014). Analysis of Dictyostelium discoideum inositol pyrophosphate metabolism by gel electrophoresis. *PLoS One*.
**Plummer, T. H. and Tarentino, A. L.** (1991). Purification of the oligosaccharide-cleaving enzymes of Flavobacterium meningosepticum. *Glycobiology*.
**Poretti, A., Wolf, N. I. and Boltshauser, E.** (2015). Differential Diagnosis of Cerebellar Atrophy in Childhood: An Update. *Neuropediatrics*.
**Poyner, D. R., Cooke, F., Hanley, M. R., Reynolds, D. J. M. and Hawkins, P. T.** (1993). Characterization of metal ion-induced [3H]inositol hexakisphosphate binding to rat cerebellar membranes. *J. Biol. Chem.* **268**, 1032–1038.
**Pradhan, J., Noakes, P. G. and Bellingham, M. C.** (2019). The Role of Altered BDNF/TrkB Signaling in Amyotrophic Lateral Sclerosis. *Front. Cell. Neurosci.*
**Raghu, P., Joseph, A., Krishnan, H., Singh, P. and Saha, S.** (2019). Phosphoinositides: Regulators of Nervous System Function in Health and Disease. *Front. Mol. Neurosci.*
**Rajab, A., Mochida, G. H., Hill, A., Ganesh, V., Bodell, A., Riaz, A., Grant, P. E., Shugart, Y. Y. and Walsh, C. A.** (2003). A novel form of pontocerebellar hypoplasia maps to chromosome 7q11-21. *Neurology*.
**Rakic, P. and Sidman, R. L.** (1970). Histogenesis of cortical layers in human cerebellum, particularly the lamina dissecans. *J. Comp. Neurol.*
**Rameh, L. E., Tolias, K. F., Duckworth, B. C. and Cantley, L. C.** (1997). A new pathway for synthesis of phosphatidylinositol-4,5-bisphosphate. *Nature*.
**Ramos AR, Ghosh S, Erneux C.** (2019).The impact of PI 5-phosphatases on phosphoinositides in cell function and human disease. *J Lipid Res.*
**Ran, F. A., Hsu, P. D., Wright, J., Agarwala, V., Scott, D. A. and Zhang, F.** (2013). Genome engineering using the CRISPR-Cas9 system. *Nat Protoc* **8**, 2281–2308.
**Reddy, N. R., Sathe, S. K. and Salunkhe, D. K.** (1982). Phytates in legumes and cereals. *Adv. Food Res.*
**Renbaum, P., Kellerman, E., Jaron, R., Geiger, D., Segel, R., Lee, M., King, M. C. and Levy-Lahad, E.** (2009). Spinal Muscular Atrophy with Pontocerebellar Hypoplasia Is Caused by a Mutation in the VRK1 Gene. *Am. J. Hum. Genet.*
**Resnick, A. C., Snowman, A. M., Kang, B. M., Hurt, K. J., Snyder, S. H. and Saiardi, A.** (2005). Inositol polyphosphate multikinase is a nuclear PI3-kinase with transcriptional regulatory activity. *Proc. Natl. Acad. Sci. U. S. A.*
**Reynolds, S. D., Johnston, C., Leboy, P. S., O'Keefe, R. J., Puzas, J. E., Rosier, R. N.**

**and Reynolds, P. R.** (1996). Identification and characterization of a unique chondrocyte gene involved in transition to hypertrophy. *Exp. Cell Res.*

**Riemer, J., Hoepken, H. H., Czerwinska, H., Robinson, S. R. and Dringen, R.** (2004). Colorimetric ferrozine-based assay for the quantitation of iron in cultured cells. *Anal. Biochem.*

**Rigden, D. J.** (2008). The histidine phosphatase superfamily: structure and function. *Biochem. J.* **409**, 333–48.

**Ring, K. L., Tong, L. M., Balestra, M. E., Javier, R., Andrews-Zwilling, Y., Li, G., Walker, D., Zhang, W. R., Kreitzer, A. C. and Huang, Y.** (2012). Direct reprogramming of mouse and human fibroblasts into multipotent neural stem cells with a single factor. *Cell Stem Cell*.

**Rogers, C. D., Moody, S. A. and Casey, E. S.** (2009). Neural induction and factors that stabilize a neural fate. *Birth Defects Res. Part C - Embryo Today Rev.*

**Rogers, T. D., McKimm, E., Dickson, P. E., Goldowitz, D., Blaha, C. D. and Mittleman, G.** (2013). Is autism a disease of the cerebellum? An integration of clinical and pre-clinical research. *Front. Syst. Neurosci.* **7**, 15.

**Romano, P. R., Wang, J., O'Keefe, R. J., Puzas, J. E., Rosier, R. N. and Reynolds, P. R.** (1998). HiPER1, a phosphatase of the endoplasmic reticulum with a role in chondrocyte maturation. *J. Cell Sci.* **111 ( Pt 6**, 803–813.

**Roth, M. G.** (2004). Phosphoinositides in constitutive membrane traffic. *Physiol. Rev.*

**Rudaks, L. I., Moore, L., Shand, K. L., Wilkinson, C. and Barnett, C. P.** (2011). Novel TSEN54 mutation causing pontocerebellar hypoplasia type 4. *Pediatr. Neurol.*

**Rudnik-Schöneborn, S., Senderek, J., Jen, J. C., Houge, G., Seeman, P., Puchmajerová, A., Graul-Neumann, L., Seidel, U., Korinthenberg, R., Kirschner, J., et al.** (2013). Pontocerebellar hypoplasia type 1: Clinical spectrum and relevance of EXOSC3 mutations. *Neurology*.

**Rumpel, H., Lim, W. E. H., Chang, H. M., Chan, L. L., Ho, G. L., Wong, M. C. and Tan, K. P.** (2003). Is myo-inositol a measure of glial swelling after stroke? A magnetic resonance study. *J. Magn. Reson. Imaging*.

**Saiardi, A.** (2017). Has Inositol Played Any Role in the Origin of Life? *Life*.

**Saiardi, A. and Cockcroft, S.** (2008). Human ITPK1: A reversible inositol phosphate kinase/phosphatase that links receptor-dependent phospholipase C to Ca2+-activated chloride channels. *Sci. Signal.*

**Saiardi, A. and Mudge, A. W.** (2018). Lithium and fluoxetine regulate the rate of phosphoinositide synthesis in neurons: a new view of their mechanisms of action in bipolar disorder. *Transl. Psychiatry*.

**Saiardi, A., Erdjument-Bromage, H., Snowman, A. M., Tempst, P. and Snyder, S. H.** (1999). Synthesis of diphosphoinositol pentakisphosphate by a newly identified family of higher inositol polyphosphate kinases. *Curr. Biol.*

**Saiardi, A., Nagata, E., Luo, H. R., Snowman, A. M. and Snyder, S. H.** (2001). Identification and Characterization of a Novel Inositol Hexakisphosphate Kinase. *J. Biol. Chem.*

**Saiardi, A., Azevedo, C., Desfougères, Y., Portela-Torres, P. and Wilson, M. S. C.** (2018). Microbial inositol polyphosphate metabolic pathway as drug development target. *Adv. Biol. Regul.*

**Sakamoto, K., Vucenik, I. and Shamsuddin, A. M.** (1993). [3H]phytic acid (inositol hexaphosphate) is absorbed and distributed to various tissues in rats. *J. Nutr.*

**Saleem, S., Aslam, H. M., Anwar, M., Anwar, S., Saleem, M., Saleem, A. and Rehmani, M. A. K.** (2013). Fahr's syndrome: Literature review of current evidence. *Orphanet J. Rare Dis.*

**Sánchez-Albisua, I., Frölich, S., Barth, P. G., Steinlin, M. and Krägeloh-Mann, I.** (2014). Natural course of pontocerebellar hypoplasia type 2A. *Orphanet J. Rare Dis.*

**Sasakawa, N., Nakaki, T., Kakinuma, E. and Kato, R.** (1993). Increase in inositol tris-, pentakis- and hexakisphosphates by high K+ stimulation in cultured rat cerebellar granule cells. *Brain Res.* **623**, 155–160.

**Sathyanesan, A., Zhou, J., Scafidi, J., Heck, D. H., Sillitoe, R. V. and Gallo, V.** (2019). Emerging connections between cerebellar development, behaviour and complex brain disorders. *Nat. Rev. Neurosci.*

**Sato, T. and Joyner, A. L.** (2009). The duration of Fgf8 isthmic organizer expression is key to patterning different tectal-isthmo-cerebellum structures. *Development*.

**Schaffer, A. E., Eggens, V. R. C., Caglayan, A. O., Reuter, M. S., Scott, E., Coufal, N. G., Silhavy, J. L., Xue, Y., Kayserili, H., Yasuno, K., et al.** (2014). CLP1 founder mutation links tRNA splicing and maturation to cerebellar development and neurodegeneration. *Cell* **157**, 651–663.

**Scherer, P. C., Ding, Y., Liu, Z., Xu, J., Mao, H., Barrow, J. C., Wei, N., Zheng, N., Snyder, S. H. and Rao, F.** (2016). Inositol hexakisphosphate (IP6) generated by IP5K mediates cullin-COP9 signalosome interactions and CRL function. *Proc. Natl. Acad. Sci. U. S. A.*

**Schmahmann, J. D.** (1997). Rediscovery of an early concept. *Int. Rev. Neurobiol.*

**Schmahmann, J. D.** (2019). The cerebellum and cognition. *Neurosci. Lett.*

**Schmahmann, J. D. and Pandya, D. N.** (1991). Projections to the basis pontis from the superior temporal sulcus and superior temporal region in the rhesus monkey. *J. Comp. Neurol.*

**Schmahmann, J. D. and Pandya, D. N.** (1993). Prelunate, occipitotemporal, and parahippocampal projections to the basis pontis in rhesus monkey. *J. Comp. Neurol.*

**Schmahmann, J. D. and Pandya, D. N.** (1997). Anatomic organization of the basilar pontine projections from prefrontal cortices in rhesus monkey. *J. Neurosci.*

**Schmunk, G., Boubion, B. J., Smith, I. F., Parker, I. and Gargus, J. J.** (2015). Shared functional defect in IP3R-mediated calcium signaling in diverse monogenic autism syndromes. *Transl. Psychiatry*.

**Schorge, S., van de Leemput, J., Singleton, A., Houlden, H. and Hardy, J.** (2010). Human ataxias: a genetic dissection of inositol triphosphate receptor (ITPR1)-dependent signaling. *Trends Neurosci.*

**Schuh, K., Uldrijan, S., Gambaryan, S., Roethlein, N. and Neyses, L.** (2003). Interaction of the plasma membrane Ca2+ pump 4b/CI with the Ca2+/calmodulin-dependent membrane-associated kinase CASK. *J. Biol. Chem.*

**Shamsuddin, A. K. and Bose, S.** (2012). IP6 (Inositol Hexaphosphate) as a Signaling Molecule. *Curr. Signal Transduct. Ther.* **7**, 289–304.

**Shears, S. B.** (1990). Kinetic consequences of the inhibition by ATP of the metabolism of inositol (1,4,5) trisphosphate and inositol (1,3,4,5) tetrakisphosphate in liver. Different effects upon the 3- and 5-phosphatases. *Cell. Signal.*

**Shears, S. B.** (2001). Assessing the omnipotence of inositol hexakisphosphate. *Cell. Signal.*

**Shears, S. B.** (2009). Molecular basis for the integration of inositol phosphate signaling pathways via human ITPK1. *Adv. Enzyme Regul.*

**Shi, Y., Inoue, H., Wu, J. C. and Yamanaka, S.** (2017). Induced pluripotent stem cell technology: A decade of progress. *Nat. Rev. Drug Discov.*

**Shimohama, S., Tanino, H., Sumida, Y., Tsuda, J. and Fujimoto, S.** (1998). Alteration of myo-inositol monophosphatase in Alzheimer's disease brains. *Neurosci. Lett.*

**Shimon, H., Agam, G., Belmaker, R. H., Hyde, T. M. and Kleinman, J. E.** (1997). Reduced frontal cortex inositol levels in postmortem brain of suicide victims and

patients with bipolar disorder. *Am. J. Psychiatry*.

**Shimon, H., Sobolev, Y., Davidson, M., Haroutunian, V., Belmaker, R. H. and Agam, G.** (1998). Inositol levels are decreased in postmortem brain of schizophrenic patients. *Biol. Psychiatry*.

**Silva, T. P., Bekman, E. P., Fernandes, T. G., Vaz, S. H., Rodrigues, C. A. V., Diogo, M. M., Cabral, J. M. S. and Carmo-Fonseca, M.** (2020). Maturation of Human Pluripotent Stem Cell-Derived Cerebellar Neurons in the Absence of Co-culture. *Front. Bioeng. Biotechnol.*

**Singh, R. P., Agarwal, C. and Agarwal, R.** (2003). Inositol hexaphosphate inhibits growth, and induces G1 arrest and apoptotic death of prostate carcinoma DU145 cells: Modulation of CDKI-CDK-cyclin and pRb-related protein-E2F complexes. *Carcinogenesis*.

**Singh, A., Faruq, M., Mukerji, M., Dwivedi, M. K., Pruthi, S. and Kapoor, S.** (2014). Infantile onset spinocerebellar ataxia 2 (SCA2): A clinical report with review of previous cases. *J. Child Neurol.*

**Skjørringe, T., Møller, L. B. and Moos, T.** (2012). Impairment of interrelated ironand copper homeostatic mechanisms in brain contributes to the pathogenesis of neurodegenerative disorders. *Front. Pharmacol.*

**Smith, J. R., Vallier, L., Lupo, G., Alexander, M., Harris, W. A. and Pedersen, R. A.** (2008). Inhibition of Activin/Nodal signaling promotes specification of human embryonic stem cells into neuroectoderm. *Dev. Biol.*

**Sokolov, A. A., Miall, R. C. and Ivry, R. B.** (2017). The Cerebellum: Adaptive Prediction for Movement and Cognition. *Trends Cogn. Sci.*

**Soldner, F., Laganière, J., Cheng, A. W., Hockemeyer, D., Gao, Q., Alagappan, R., Khurana, V., Golbe, L. I., Myers, R. H., Lindquist, S., et al.** (2011). Generation of isogenic pluripotent stem cells differing exclusively at two early onset parkinson point mutations. *Cell*.

**Stephens, L., Radenberg, T., Thiel, U., Vogel, G., Khoo, K. H., Dell, A., Jackson, T. R., Hawkins, P. T. and Mayr, G. W.** (1993). The detection, purification, structural characterization, and metabolism of diphosphoinositol pentakisphosphate(s) and bisdiphosphoinositol tetrakisphosphate(s). *J. Biol. Chem.*

**Stevenson-Paulik, J., Chiou, S. T., Frederick, J. P., Cruz, J. dela, Seeds, A. M., Otto, J. C. and York, J. D.** (2006). Inositol phosphate metabolomics: Merging genetic perturbation with modernized radiolabeling methods. *Methods* **39**, 112–121.

**Stoll, M., Teoh, H., Lee, J., Reddel, S., Zhu, Y., Buckley, M., Sampaio, H., Roscioli, T., Farrar, M. and Nicholson, G.** (2016). Novel motor phenotypes in patients with VRK1 mutations without pontocerebellar hypoplasia. *Neurology*.

**Storey, E.** (2014). Genetic cerebellar ataxias. *Semin. Neurol.*

**Streb, H., Irvine, R. F., Berridge, M. J. and Schulz, I.** (1983). Release of Ca2+ from a nonmitochondrial intracellular store in pancreatic acinar cells by inositol-1,4,5-trisphosphate. *Nature*.

**Strick, P. L., Dum, R. P. and Fiez, J. A.** (2009). Cerebellum and nonmotor function. *Annu. Rev. Neurosci.*

**Stuart, J. A., Anderson, K. L., Kirk, C. J. and Michell, R. H.** (1993). The intracellular distribution of inositol polyphosphates. In *Biochemical Society Transactions*, .

**Stuart, J. a, Anderson, K. L., French, P. J., Kirk, C. J. and Michell, R. H.** (1994). The intracellular distribution of inositol polyphosphates in HL60 promyeloid cells. *Biochem. J.* **303 (Pt 2)**, 517–525.

**Studer, L., Vera, E. and Cornacchia, D.** (2015). Programming and Reprogramming Cellular Age in the Era of Induced Pluripotency. *Cell Stem Cell*.

**Sundberg, M., Tochitsky, I., Buchholz, D. E., Winden, K., Kujala, V., Kapur, K., Cataltepe, D., Turner, D., Han, M. J., Woolf, C. J., et al.** (2018). Purkinje cells derived from TSC patients display hypoexcitability and synaptic deficits associated with reduced FMRP levels and reversed by rapamycin. *Mol. Psychiatry*.

**Sussman, D., Leung, R. C., Chakravarty, M. M., Lerch, J. P. and Taylor, M. J.** (2016). Developing human brain: Age-related changes in cortical, subcortical, and cerebellar anatomy. *Brain Behav.*

**Szewczyk, B.** (2013). Zinc homeostasis and neurodegenerative disorders. *Front. Aging Neurosci.*

**Szinyei, C., Behnisch, T., Reiser, G. and Reymann, K. G.** (1999). Inositol 1,3,4,5-tetrakisphosphate enhances long-term potentiation by regulating Ca2+ entry in rat hippocampus. *J. Physiol.*

**Sznajer, Y., Baumann, C., David, A., Journel, H., Lacombe, D., Perel, Y., Blouin, P., Segura, J. F., Cezard, J. P., Peuchmaur, M., et al.** (2003). Further delineation of the congenital form of X-linked dyskeratosis congenita (Hoyeraal-Hreidarsson syndrome). *Eur. J. Pediatr.*

**Szwergold, B. S., Graham, R. A. and Brown, T. R.** (1987). Observation of inositol pentakis- and hexakis-phosphates in mammalian tissues by 31P NMR. *Biochem. Biophys. Res. Commun.*

**Tada, M., Takahama, Y., Abe, K., Nakatsuji, N. and Tada, T.** (2001). Nuclear reprogramming of somatic cells by in vitro hybridization with ES cells. *Curr. Biol.*

**Takahashi, K. and Yamanaka, S.** (2006). Induction of Pluripotent Stem Cells from Mouse Embryonic and Adult Fibroblast Cultures by Defined Factors. *Cell*.

**Takahashi, K. and Yamanaka, S.** (2016). A decade of transcription factor-mediated reprogramming to pluripotency. *Nat. Rev. Mol. Cell Biol.* **17**, 183–93.

**Takahashi, T., Nowakowski, R. S. and Caviness, V. S.** (1993). Cell cycle parameters and patterns of nuclear movement in the neocortical proliferative zone of the fetal mouse. *J. Neurosci.*

**Takahashi, K., Tanabe, K., Ohnuki, M., Narita, M., Ichisaka, T., Tomoda, K. and Yamanaka, S.** (2007). Induction of Pluripotent Stem Cells from Adult Human Fibroblasts by Defined Factors. *Cell* **131**, 861–872.

**Takazawa K, Vandekerckhove J, Dumont JE, Erneux C.** (1990). Cloning and expression in Escherichia coli of a rat brain cDNA encoding a Ca2+/calmodulin-sensitive inositol 1,4,5-trisphosphate 3-kinase. *Biochem J*.

**Takeo, Y., Kurabayashi, N., Nguyen, M. D. and Sanada, K.** (2016). The G protein-coupled receptor GPR157 regulates neuronal differentiation of radial glial progenitors through the Gq-IP3 pathway. *Sci. Rep.*

**Tang, T. S., Tu, H., Chan, E. Y. W., Maximov, A., Wang, Z., Wellington, C. L., Hayden, M. R. and Bezprozvanny, I.** (2003). Huntingtin and huntingtin-associated protein 1 influence neuronal calcium signaling mediated by inositol-(1,4,5) triphosphate receptor type 1. *Neuron*.

**Tao, Y. and Zhang, S. C.** (2016). Neural Subtype Specification from Human Pluripotent Stem Cells. *Cell Stem Cell* **19**, 573–586.

**Taylor, E. N., Stampfer, M. J. and Curhan, G. C.** (2004). Dietary factors and the risk of incident kidney stones in men: New insights after 14 years of follow-up. *J. Am. Soc. Nephrol.*

**Thompson, E. J.** (1980). Advances in neurochemistry. By B. W. Agranoff and M. H. Aprison, 304 pp, Plenum Press, New York, NY, 1978. $32.50. *Muscle Nerve*.

**Tiemeier, H., Lenroot, R. K., Greenstein, D. K., Tran, L., Pierson, R. and Giedd, J. N.** (2010). Cerebellum development during childhood and adolescence: A longitudinal

morphometric MRI study. *Neuroimage.*

**Timofeeva, Y.** (2019). Intracellular Calcium Dynamics: Biophysical and Simplified Models.

**Tomasch, J.** (1969). The numerical capacity of the human cortico-pontocerebellar system. *Brain Res.*

**Torres, J., Domínguez, S., Cerdá, M. F., Obal, G., Mederos, A., Irvine, R. F., Díaz, A. and Kremer, C.** (2005). Solution behaviour of myo-inositol hexakisphosphate in the presence of multivalent cations. Prediction of a neutral pentamagnesium species under cytosolic/nuclear conditions. *J. Inorg. Biochem.*

**Toth, A. B., Shum, A. K. and Prakriya, M.** (2016). Regulation of neurogenesis by calcium signaling. *Cell Calcium.*

**Tschopp O, Yang ZZ, Brodbeck D, Dummler BA, Hemmings-Mieszczak M, Watanabe T, Michaelis T, Frahm J, Hemmings BA**. (2005). Essential role of protein kinase B gamma (PKB gamma/Akt3) in postnatal brain development but not in glucose homeostasis. *Development.*

**Tsubokawa, H., Oguro, K., Robinson, H. P. C., Masuzawa, T. and Kawai, N.** (1996). Intracellular inositol 1,3,4,5-tetrakisphosphate enhances the calcium current in hippocampal CA1 neurones of the gerbil after ischaemia. *J. Physiol.*

**Tsui, M. M. and York, J. D.** (2010). Roles of inositol phosphates and inositol pyrophosphates in development, cell signaling and nuclear processes. *Adv. Enzyme Regul.* **50**, 324–337.

**Uldry, M., Steiner, P., Zurich, M. G., Béguin, P., Hirling, H., Dolci, W. and Thorens, B.** (2004). Regulated exocytosis of an H+ /myo-inositol symporter at synapses and growth cones. *EMBO J.*

**Uwineza, A., Caberg, J. H., Hitayezu, J., Wenric, S., Mutesa, L., Vial, Y., Drunat, S., Passemard, S., Verloes, A., El Ghouzzi, V., et al.** (2019). VPS51 biallelic variants cause microcephaly with brain malformations: A confirmatory report. *Eur. J. Med. Genet.*

**Valence, S., Garel, C., Barth, M., Toutain, A., Paris, C., Amsallem, D., Barthez, M. A., Mayer, M., Rodriguez, D. and Burglen, L.** (2016). RELN and VLDLR mutations underlie two distinguishable clinico-radiological phenotypes. *Clin. Genet.*

**van Dijk, T., Barth, P., Reneman, L., Appelhof, B., Baas, F. and Poll-The, B. T.** (2017). A de novo missense mutation in the inositol 1,4,5-triphosphate receptor type 1 gene causing severe pontine and cerebellar hypoplasia: Expanding the phenotype of *ITPR1* -related spinocerebellar ataxia's. *Am. J. Med. Genet. Part A* **173**, 207–212.

**van Dijk, T., Ferdinandusse, S., Ruiter, J. P. N., Alders, M., Mathijssen, I. B., Parboosingh, J. S., Innes, A. M., Meijers-Heijboer, H., Poll-The, B. T., Bernier, F. P., et al.** (2018a). Biallelic loss of function variants in COASY cause prenatal onset pontocerebellar hypoplasia, microcephaly, and arthrogryposis. *Eur. J. Hum. Genet.*

**van Dijk, T., Baas, F., Barth, P. G. and Poll-The, B. T.** (2018b). What's new in pontocerebellar hypoplasia? An update on genes and subtypes. *Orphanet J. Rare Dis.* **13**, 92.

**Van Dijk, T., Rudnik-Schöneborn, S., Senderek, J., Hajmousa, G., Mei, H., Dusl, M., Aronica, E., Barth, P. and Baas, F.** (2017). Pontocerebellar hypoplasia with spinal muscular atrophy (PCH1): Identification of SLC25A46 mutations in the original Dutch PCH1 family. *Brain*.

**Van Dijk, T., Baas, F., Barth, P. G. and Poll-The, B. T.** (2018). What's new in pontocerebellar hypoplasia? An update on genes and subtypes. *Orphanet J. Rare Dis.*

**Vasconcelos, M. M., Brito, A. R., Domingues, R. C., Da Cruz, L. C. H., Gasparetto, E. L., Werner, J. and Gonçalves, J. P. S.** (2008). Proton magnetic resonance spectroscopy in school-aged autistic children. *J. Neuroimaging*.

**Veiga, N., Torres, J., Domínguez, S., Mederos, A., Irvine, R. F., Díaz, A. and Kremer, C.** (2006). The behaviour of myo-inositol hexakisphosphate in the presence of magnesium(II) and calcium(II): Protein-free soluble InsP6 is limited to 49 μM under cytosolic/nuclear conditions. *J. Inorg. Biochem.*

**Veiga, N., Torres, J., Godage, H. Y., Riley, A. M., Domínguez, S., Potter, B. V. L., Díaz, A. and Kremer, C.** (2009). The behaviour of inositol 1,3,4,5,6-pentakisphosphate in the presence of the major biological metal cations. *J. Biol. Inorg. Chem.*

**Verjans, B., De Smedt, F., Lecocq, R., Vanweyenberg, V., Moreau, C. and Erneux, C.** (1994). Cloning and expression in Escherichia coli of a dog thyroid cDNA encoding a novel inositol 1,4,5-trisphosphate 5-phosphatase. *Biochem. J.*

**Vermes, I., Haanen, C., Steffens-Nakken, H. and Reutellingsperger, C.** (1995). A novel assay for apoptosis Flow cytometric detection of phosphatidylserine expression on early apoptotic cells using fluorescein labelled Annexin V. *J. Immunol. Methods*.

**Vieira, B. S., Caramori Junior, J. G., Oliveira, C. F. S. and Correa, G. S. S.** (2018). Combination of phytase and organic acid for broilers: Role in mineral digestibility and phytic acid degradation. *Worlds. Poult. Sci. J.*

**Volpato, V. and Webber, C.** (2020). Addressing variability in iPSC-derived models of human disease: Guidelines to promote reproducibility. *DMM Dis. Model. Mech.*

**Volpe, J. J.** (2009). Cerebellum of the premature infant: Rapidly developing, vulnerable, clinically important. *J. Child Neurol.*

**Vucenik, I. and Shamsuddin, A. M.** (2006). Protection against cancer by dietary IP6 and inositol. *Nutr. Cancer*.

**Vucenik, I., Yang, G. yu and Shamsuddin, A. M.** (1995). Inositol hexaphosphate and inositol inhibit DMBA-induced rat mammary cancer. *Carcinogenesis*.

**Wakayama, T., Perry, A. C. F., Zuccotti, M., Johnson, K. R. and Yanagimachi, R.** (1998). Full-term development of mice from enucleated oocytes injected with cumulus cell nuclei. *Nature*.

**Wan, J., Yourshaw, M., Mamsa, H., Rudnik-Schöneborn, S., Menezes, M. P., Hong, J. E., Leong, D. W., Senderek, J., Salman, M. S., Chitayat, D., et al.** (2012). Mutations in the RNA exosome component gene EXOSC3 cause pontocerebellar hypoplasia and spinal motor neuron degeneration. *Nat. Genet.*

**Wan, J., Steffen, J., Yourshaw, M., Mamsa, H., Andersen, E., Rudnik-Schöneborn, S., Pope, K., Howell, K. B., Mclean, C. A., Kornberg, A. J., et al.** (2016). Loss of function of SLC25A46 causes lethal congenital pontocerebellar hypoplasia. *Brain*.

**Wang, V. Y. and Zoghbi, H. Y.** (2001). Genetic regulation of cerebellar development. *Nat. Rev. Neurosci.* **2**, 484–491.

**Wang, G. S., Hong, C. J., Yen, T. Y., Huang, H. Y., Ou, Y., Huang, T. N., Jung, W. G., Kuo, T. Y., Sheng, M., Wang, T. F., et al.** (2004). Transcriptional modification by a CASK-interacting nucleosome assembly protein. *Neuron*.

**Wang, S., Wang, B., Pan, N., Fu, L., Wang, C., Song, G., An, J., Liu, Z., Zhu, W., Guan, Y., et al.** (2015). Differentiation of human induced pluripotent stem cells to mature functional Purkinje neurons. *Sci. Rep.*

**Watson, L. M., Wong, M. M. K., Vowles, J., Cowley, S. A. and Becker, E. B. E.** (2018). A Simplified Method for Generating Purkinje Cells from Human-Induced Pluripotent Stem Cells. *Cerebellum*.

**Weirich, C. S., Erzberger, J. P., Flick, J. S., Berger, J. M., Thorner, J. and Weis, K.** (2006). Activation of the DExD/H-box protein Dbp5 by the nuclear-pore protein Gle1 and its coactivator InsP6 is required for mRNA export. *Nat. Cell Biol.*

**Weissman, T. A., Riquelme, P. A., Ivic, L., Flint, A. C. and Kriegstein, A. R.** (2004). Calcium waves propagate through radial glial cells and modulate proliferation in the

developing neocortex. *Neuron*.

**Wellard, R. M., Briellmann, R. S., Prichard, J. W., Syngeniotis, A. and Jackson, G. D.** (2003). Myoinositol abnormalities in temporal lobe epilepsy. *Epilepsia*.

**White, A. R., Kanninen, K. M. and Crouch, P. J.** (2015). Editorial: Metals and neurodegeneration: Restoring the balance. *Front. Aging Neurosci.*

**Wiethoff, S., Arber, C., Li, A., Wray, S., Houlden, H. and Patani, R.** (2015). Using human induced pluripotent stem cells to model cerebellar disease: Hope and hype. *J. Neurogenet.*

**Wilmut, I., Schnieke, A. E., McWhir, J., Kind, A. J. and Campbell, K. H. S.** (1997). Viable offspring derived from fetal and adult mammalian cells. *Nature*.

**Wilson, M. and Saiardi, A.** (2018). Inositol Phosphates Purification Using Titanium Dioxide Beads. *BIO-PROTOCOL*.

**Wilson, M. S. C., Livermore, T. M. and Saiardi, A.** (2013). Inositol pyrophosphates: between signalling and metabolism. *Biochem. J.* **452**,.

**Wilson, M. S. C., Bulley, S. J., Pisani, F., Irvine, R. F. and Saiardi, A.** (2015). A novel method for the purification of inositol phosphates from biological samples reveals that no phytate is present in human plasma or urine. *Open Biol.* **5**, 150014.

**Windhorst, S., Lin, H., Blechner, C., Fanick, W., Brandt, L., Brehm, M. A. and Mayr, G. W.** (2013). Tumour cells can employ extracellular Ins(1,2,3,4,5,6)P6 and multiple inositol-polyphosphate phosphatase 1 (MINPP1) dephosphorylation to improve their proliferation. *Biochem. J.*

**Wise, A. and Gilburt, D. J.** (1982). Phytate hydrolysis by germfree and conventional rats. *Appl. Environ. Microbiol.*

**Wittmann, D. M., Blöchl, F., Trümbach, D., Wurst, W., Prakash, N. and Theis, F. J.** (2009). Spatial analysis of expression patterns predicts genetic interactions at the mid-hindbrain boundary. *PLoS Comput. Biol.*

**Wong, Y. H., Kalmbach, S. J., Hartman, B. K. and Sherman, W. R.** (1987). Immunohistochemical Staining and Enzyme Activity Measurements Show myo-Inositol- 1- Phosphate Synthase to Be Localized in the Vasculature of Brain. *J. Neurochem.*

**Wundenberg, T., Grabinski, N., Lin, H. and Mayr, G. W.** (2014). Discovery of InsP6-kinases as InsP6-dephosphorylating enzymes provides a new mechanism of cytosolic InsP6 degradation driven by the cellular ATP/ADP ratio. *Biochem. J.* **462**, 173–84.

**Xie, H., Ye, M., Feng, R. and Graf, T.** (2004). Stepwise reprogramming of B cells into macrophages. *Cell*.

**Yamamoto, K., Sakagami, Y., Sugiura, S., Inokuchi, K., Shimohama, S. and Kato, N.** (2005). Homer 1a enhances spike-induced calcium influx via L-type calcium channels in neocortex pyramidal cells. *Eur. J. Neurosci.*

**Yamanaka, R., Shindo, Y. and Oka, K.** (2019). Magnesium is a key player in neuronal maturation and neuropathology. *Int. J. Mol. Sci.*

**Yamazaki, Y., Sugihara, T., Goto, J. I., Chida, K., Fujiwara, H., Kaneko, K., Fujii, S. and Mikoshiba, K.** (2011). Role of inositol 1, 4, 5-trisphosphate receptors in the postsynaptic expression of guinea pig hippocampal mossy fiber depotentiation. *Brain Res.*

**Yang, X., Rudolf, M., Carew, M. A., Yoshida, M., Nerreter, V., Riley, A. M., Chung, S. K., Bruzik, K. S., Potter, B. V. L., Schultz, C., et al.** (1999). Inositol 1,3,4-trisphosphate acts in vivo as a specific regulator of cellular signaling by inositol 3,4,5,6-tetrakisphosphate. *J. Biol. Chem.*

**Yang, S. N., Yu, J., Mayr, G. W., Hofmann, F., Larsson, O. and Berggren, P. O.** (2001). Inositol hexakisphosphate increases L-type Ca2+ channel activity by stimulation of

adenylyl cyclase. *FASEB J.* **15**, 1753–63.

**Yang, S. N., Shi, Y., Yang, G., Li, Y., Yu, L., Shin, O. H., Bacaj, T., Sudhof, T. C., Yu, J. and Berggren, P. O.** (2012). Inositol hexakisphosphate suppresses excitatory neurotransmission via synaptotagmin-1 C2B domain in the hippocampal neuron. *Proc Natl Acad Sci U S A* **109**, 12183–12188.

**Yildiz, A., Sachs, G. S., Dorer, D. J. and Renshaw, P. F.** (2001). 31P nuclear magnetic resonance spectroscopy findings in bipolar illness: A meta-analysis. *Psychiatry Res. - Neuroimaging*.

**York, J. D.** (2006a). Regulation of nuclear processes by inositol polyphosphates. *Biochim. Biophys. Acta - Mol. Cell Biol. Lipids* **1761**, 552–559.

**York, J. D.** (2006b). Regulation of nuclear processes by inositol polyphosphates. *Biochim. Biophys. Acta - Mol. Cell Biol. Lipids*.

**Yu, J., Vodyanik, M. A., Smuga-Otto, K., Antosiewicz-Bourget, J., Frane, J. L., Tian, S., Nie, J., Jonsdottir, G. A., Ruotti, V., Stewart, R., et al.** (2007). Induced pluripotent stem cell lines derived from human somatic cells. *Science (80-. ).*

**Zetsche, B., Gootenberg, J. S., Abudayyeh, O. O., Slaymaker, I. M., Makarova, K. S., Essletzbichler, P., Volz, S. E., Joung, J., Van Der Oost, J., Regev, A., et al.** (2015). Cpf1 Is a Single RNA-Guided Endonuclease of a Class 2 CRISPR-Cas System. *Cell*.

**Zhang, S. C., Wernig, M., Duncan, I. D., Brüstle, O. and Thomson, J. A.** (2001). In vitro differentiation of transplantable neural precursors from human embryonic stem cells. *Nat. Biotechnol.*

**Zheng, Q., Zhao, Y., Guo, J., Zhao, S., Fei, C., Xiao, C., Wu, D., Wu, L., Li, X. and Chang, C.** (2018). Iron overload promotes mitochondrial fragmentation in mesenchymal stromal cells from myelodysplastic syndrome patients through activation of the AMPK/MFF/Drp1 pathway article. *Cell Death Dis.*

**Zimmerman, L. B., De Jesús-Escobar, J. M. and Harland, R. M.** (1996). The Spemann organizer signal noggin binds and inactivates bone morphogenetic protein 4. *Cell*.

**Zurashvili, T., Cordon-Barris, L., Ruiz-Babot, G., Zhou, X., Lizcano, J. M., Gomez, N., Gimenez-Llort, L. and Bayascas, J. R.** (2013). Interaction of PDK1 with Phosphoinositides Is Essential for Neuronal Differentiation but Dispensable for Neuronal Survival. *Mol. Cell. Biol.*

# APPENDIX-PUBLICATIONS

Publications related to this PhD thesis were listed below. The first publication refers to the study mentioned in this manuscript. The study related to the second publication is not included here, as most of the work was conducted by the previous PhD student Daniel-Medina Cano. Briefly, within the second study, my work consists of developing an iPSC-based disease modelling strategy for another developmental brain disorder, called Congenital Disorders of Glycosylation (CDG). To achieve that, I was involved in the generation of iPSC lines KO for *SRD5A3*, a CDG-causing gene, and their subsequent differentiation into cortical neuronal progenitors.

Ucuncu, E., Rajamani, K., Wilson, M.S.C. *et al. MINPP1* prevents intracellular accumulation of the chelator inositol hexakisphosphate and is mutated in Pontocerebellar Hypoplasia. *Nat Commun* 11**,** 6087 (2020). (in bioRxiv *doi: https://doi.org/10.1101/2020.05.17.100248*)

Medina-Cano D, Ucuncu E, Nguyen LS, et al. High N-glycan multiplicity is critical for neuronal adhesion and sensitizes the developing cerebellum to N-glycosylation defect. Elife, Oct 12. (2018) (2nd author, not included within this manuscript)

eLIFE elifesciences.org

RESEARCH ARTICLE

# High N-glycan multiplicity is critical for neuronal adhesion and sensitizes the developing cerebellum to N-glycosylation defect

**Daniel Medina-Cano[1,2,3], Ekin Ucuncu[1,2,3], Lam Son Nguyen[1,2,3], Michael Nicouleau[1,2,3], Joanna Lipecka[4], Jean-Charles Bizot[5], Christian Thiel[6], Francois Foulquier[7,8], Nathalie Lefort[9], Catherine Faivre-Sarrailh[10], Laurence Colleaux[1,2,3], Chiara Guerrera[4], Vincent Cantagrel[1,2,3]***

[1]Paris Descartes-Sorbonne Paris Cite´ University, Paris, France; [2]Developmental brain disorders Laboratory, INSERM UMR, Paris, France; [3]Imagine Institute, Paris, France; [4]Proteomics Platform 3P5-Necker, Université Paris Descartes-Structure Fédérative de Recherche Necker, Inserm, Paris, France; [5]Key-Obs SAS, Orléans, France; [6]Center for Child and Adolescent Medicine, Kinderheilkunde I, University of Heidelberg, Heidelberg, Germany; [7]Unité de Glycobiologie Structurale et Fonctionnelle, Université Lille, Lille, France; [8]Centre National de la Recherche Française, Paris, France; [9]iPS Core Facility, Imagine Institute, Paris, France; [10]Aix Marseille Université, Marseille, France

**Abstract** Proper brain development relies highly on protein N-glycosylation to sustain neuronal migration, axon guidance and synaptic physiology. Impairing the N-glycosylation pathway at early steps produces broad neurological symptoms identified in congenital disorders of glycosylation. However, little is known about the molecular mechanisms underlying these defects. We generated a cerebellum specific knockout mouse for *Srd5a3*, a gene involved in the initiation of N-glycosylation. In addition to motor coordination defects and abnormal granule cell development, *Srd5a3* deletion causes mild N-glycosylation impairment without significantly altering ER homeostasis. Using proteomic approaches, we identified that *Srd5a3* loss affects a subset of glycoproteins with high N-glycans multiplicity per protein and decreased protein abundance or N-glycosylation level. As IgSF-CAM adhesion proteins are critical for neuron adhesion and highly N-glycosylated, we observed impaired IgSF-CAM-mediated neurite outgrowth and axon guidance in *Srd5a3* mutant cerebellum. Our results link high N-glycan multiplicity to fine-tuned neural cell adhesion during mammalian brain development.
DOI: https://doi.org/10.7554/eLife.38309.001

***For correspondence:** vincent.cantagrel@inserm.fr

**Competing interests:** The authors declare that no competing interests exist.

**Funding:** See page 21

**Received:** 11 May 2018
**Accepted:** 01 October 2018

**Reviewing editor:** David D Ginty, Harvard Medical School, United States

© Copyright Medina-Cano et al. This article is distributed under the terms of the Creative Commons Attribution License, which permits unrestricted use and redistribution provided that the original author and source are credited.

## Introduction

Protein N-glycosylation, one of the most abundant post-translational modification, helps direct various cellular functions, such as protein folding, stability, trafficking and localization(***Cherepanova and Gilmore, 2016***) (***Freeze et al., 2014***). Nearly all proteins transported through the secretory pathway undergo N-glycosylation, particularly to regulate cell surface abundance and cellular interactions (***Dennis et al., 2009***). This template-independent process shows distinct glycosylation patterns that vary by protein and physiological context(***Dennis et al., 2009***). Protein N-glycosylation begins in the endoplasmic reticulum (ER), where a tightly controlled and conserved biosynthetic pathway

synthesizes a precursor named the lipid-linked oligosaccharide (LLO). This LLO comprises a sequential assembly of 14 monosaccharides ($Glc_3Man_9GlcNAc_2$) on top of the phosphorylated lipid carrier dolichol. Then, the oligosaccharyltransferase (OST) complex transfers *en bloc* the oligosaccharide part of the LLO to Asn residues on specific sites (Asn-X-Ser/Thr, X≠Pro) in nascent glycoproteins (**Chavan and Lennarz, 2006**). N-linked glycan undergoes final modifications in the ER and Golgi compartments.

Disrupting the N-glycosylation process in humans causes congenital disorders of glycosylation (CDG), a wide and highly heterogeneous group of inherited metabolic disorders (**Ng and Freeze, 2018**) (**Freeze et al., 2014**) (**Jaeken and Péanne, 2017**). The analysis of the clinical and metabolic consequences of each defect is challenging as the underlying mutated enzymes or transporters are often involved in multiple and intricate pathways(**Freeze et al., 2014**). Among them, disrupted synthesis or transfer of LLO underlies the most prevalent disorder, CDG type I (CDG-I)(**Jaeken and Péanne, 2017**). CDG-I diagnosis is based on the detection of hypoglycosylation of the patients' serum transferrin that exhibits unoccupied N-glycosylation site(s). Clinically, CDG-I disorders present psychomotor retardation (the most common feature) associated with cerebellar ataxia, seizures, retinopathy, liver fibrosis, coagulopathies, abnormal fat distribution and failure to thrive. Cerebellar ataxia is the primary diagnostic indicator in patients with *PMM2* mutations (PMM2-CDG, also known as CDG-Ia disorder), which is the most frequent CDG (**Schiff et al., 2017**). These phenotypic defects may arise from unoccupied glycosylation sites (i.e. protein hypoglycosylation) in numerous and mostly unidentified proteins.

The efficacy of protein glycosylation relies on the primary sequence at the glycosylation site (i.e. the sequon), the neighboring amino acids and the local structure (**Poljak et al., 2018**) (**Murray et al., 2015**). In CDG, the limited amount of LLO, the OST complex substrate, can also impact glycosylation site occupancy to cause hypoglycosylation (**Burda and Aebi, 1999**) (**Freeze et al., 2015b**). Initial studies investigated the consequences of this metabolic defect mainly in serum (**Hülsmeier et al., 2007**) (**Richard et al., 2009**). However, tissue accessibility and technical limitations precluded examining defects in organs, specifically the developing brain (**Freeze et al., 2015b**). The lack of data related to the consequence of the defect at the proteomic level contrasts with the well-known importance of N-glycans in specific phases of neural development (**Scott and Panin, 2014b**).

While several CDG models showing neural developmental defects exist, the mis-glycosylated targets remain unidentified (**Chan et al., 2016**; **Cline et al., 2012**; **Scott and Panin, 2014a**). We still do not know whether some specific proteins show a predisposition for these alterations, which contribute to disease pathogenesis. We predict that some glycoproteins possess a proclivity for hypoglycosylation based on their intrinsic properties (**Poljak et al., 2018**) (**Hülsmeier et al., 2007**). Previous studies identified SRD5A3, an enzyme involved in LLO synthesis, as mutated in CDG type I patients (SRD5A3-CDG) (**Cantagrel et al., 2010**) (**Morava et al., 2010**). SRD5A3 is a steroid-reductase-like enzyme involved in the last step of de novo synthesis of dolichol, the lipid used to build the LLO precursor. The broad clinical spectrum observed in patients with *SRD5A3* mutations shows many similarities with other ER-related glycosylation defects including psychomotor retardation and cerebellar ataxia. These symptoms result from likely null *SRD5A3* alleles (**Kara et al., 2014**; **Tuysuz et al., 2016**) (**Wheeler et al., 2016**) (**Cantagrel et al., 2010**) (**Gründahl et al., 2012**) and reflect impaired protein N-glycosylation, as previously described in yeast and mouse embryos mutated for the corresponding *SRD5A3* ortholog (**Cantagrel et al., 2010**). Here, we sought to gain mechanistic and functional insight into protein N-glycosylation during neural development, so we used conditional disruption of the *Srd5a3* gene in the mouse cerebellum, a tissue often affected in CDG.

# Results

## Conditional deletion of Srd5a3 in the whole developing cerebellum

Since we sought to examine the function of *SRD5A3* in brain disease pathogenesis, we generated targeted conditional and null alleles of mouse *Srd5a3*, flanking exons 2 – 4 with loxP sequences (**Figure 1—figure supplement 1A,B**). Homozygous germline mutants ($Srd5a3^{-/-}$) are embryonic lethal (data not shown) consistent with results from the *Srd5a3* gene-trap mutant (**Cantagrel et al., 2010**). So, we used the Engrailed1-cre (En1-Cre) transgenic line to produce conditional knockouts En1-Cre;

*Srd5a3*$^{fl/-}$ in the developing hindbrain (***Sgaier et al., 2007***) and confirmed the gene deletion at the transcript level (***Figure 1—figure supplement 1C–E***). En1-Cre; *Srd5a3*$^{fl/-}$ mice were fertile and showed nearly Mendelian ratios at weaning age (data not shown). We used far-western blotting (far-WB) with biotinylated Sambucus Nigra lectin (SNA) to investigate the abundance of complex sialylated N-glycans (***Cao et al., 2013***). Total protein extracts from mutant cerebellums showed a non-significant 12% decrease in normalized signal intensity (***Figure 1A,B***). We obtained similar results with Concanavalin A (ConA) lectin that binds to core and immature mannosylated N-glycans (***Figure 1—figure supplement 1F,G***). These results indicate that cerebellar *Srd5a3* deletion does not cause a severe general glycosylation defect. However, Lamp1, a broadly used marker for N-glycosylation defects (***Rujano et al., 2017***) (***Kretzer et al., 2016***), indicated a severe decrease in protein levels across different tissues (***Figure 1C–E***). The remaining Lamp1 showed a shift toward a lower molecular weight before PNGase treatment, which indicated impaired glycosylation (***Figure 1D,F***).

Next, we investigated the functional consequences of this cerebellar glycosylation defect on learning ability and motor behavior (***Koziol et al., 2014***) in a cohort of control and mutant mice (n = 30). In the Morris Water Maze (MWM), we exposed mice twice to the same hidden platform to test working memory. We found no significant difference on swimming speed between En1-Cre;

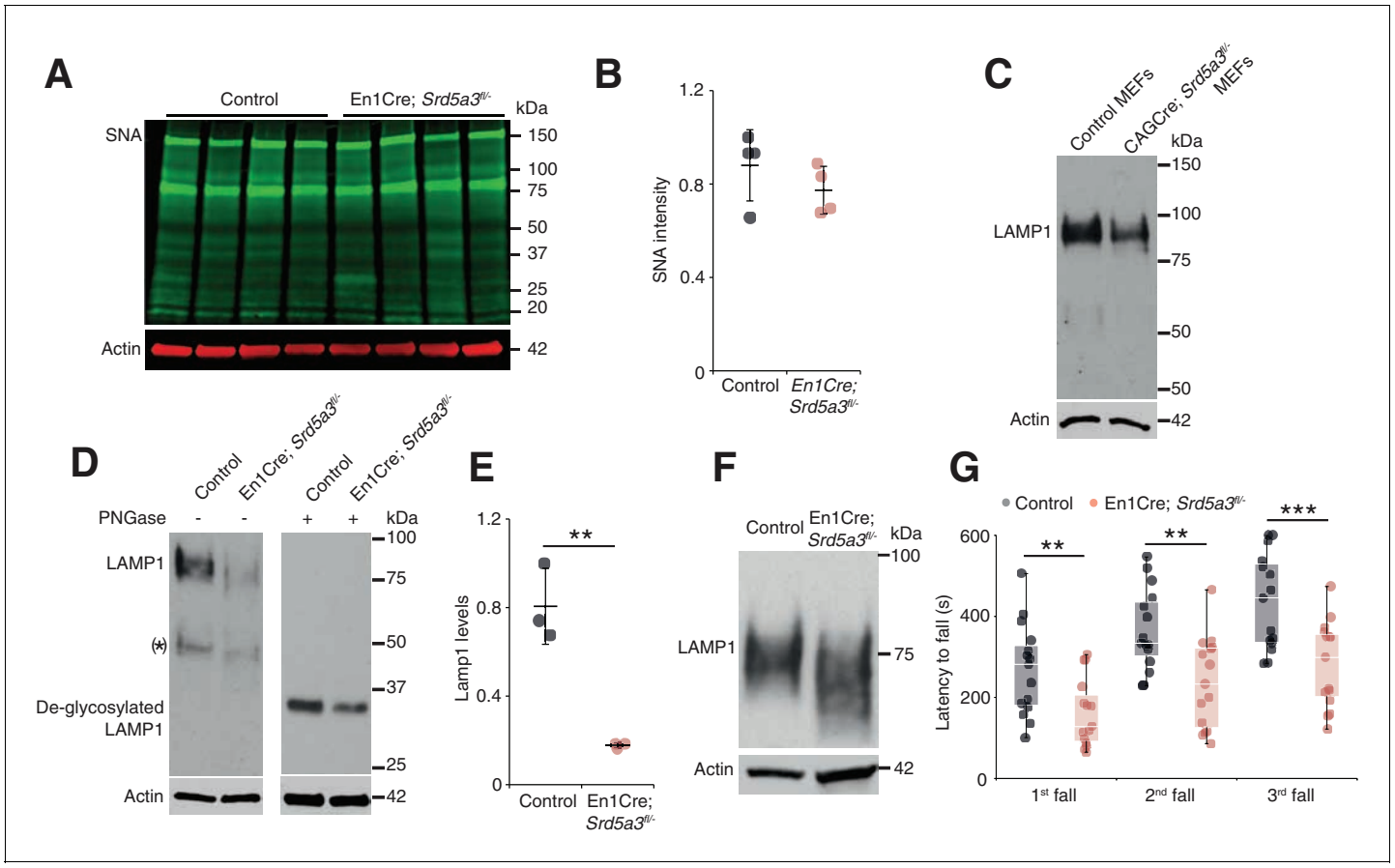


**Figure 1.** Deletion of *Srd5a3* in the cerebellum impairs protein N-glycosylation and motor function. (**A**) Far-WB with SNA lectin in P7 cerebellum and (**B**) quantification (n = 4 per genotype), p-value=0.29 (**C**) WB analysis of LAMP1 expression in mouse embryonic fibroblasts (MEFs). (**D**) WB analysis of LAMP1 level from P7 cerebellum and quantification (**E**). * indicates a PNGase sensitive LAMP1 isoform; **p-value=0.0032. (**F**) WB analysis as described in (**D**) but with increased electrophoretic migration and adjusted protein amounts to highlight LAMP1 hypoglycosylation in the mutant sample. (**G**) Box plot of the latency to fall during rotarod testing (n = 15 for each condition). One-way ANOVA was used for rotarod statistics. For all others, two-tailed student t-test was used. **p<0.01; ***p<0.001. Results are presented as mean ±s.d.

DOI: https://doi.org/10.7554/eLife.38309.002

The following figure supplement is available for figure 1:

**Figure supplement 1.** Generation of conditional *Srd5a3* knockout mice and extended biochemical and behavioral analyses.

DOI: https://doi.org/10.7554/eLife.38309.003

*Srd5a3*$^{fl/-}$ and control mice (***Figure 1—figure supplement 1H***). The latency to reach the platform was significantly lower on the second trial than on the first one for control mice, but not for En1-Cre; *Srd5a3*$^{fl/-}$ mice (***Figure 1—figure supplement 1I***). This result suggests a mild impairment of working memory in the mutant mice. In contrast, En1-Cre; *Srd5a3*$^{fl/-}$ mice showed a severe and highly significant (p=0.0007) motor coordination defect assessed with the rotarod test (***Figure 1G***). These results suggest that in the absence of *Srd5a3,* the impaired cerebellum function arises from a mild and potentially selective hypoglycosylation of glycoproteins.

## Conditional deletion of Srd5a3 disrupts cerebellum granule cell development

Then, we wanted to examine cerebellar development after deletion of *Srd5a*3 by conducting a morphological and histological survey at P14, P21, 2 and 6 months. We observed a significant hypoplasia in the En1-Cre; *Srd5a3*$^{fl/-}$ mice (***Figure 2A–D***). Examining the mutant cerebellum cytoarchitecture revealed an accumulation of scattered ectopic cell clusters in the external part of the molecular layer (ML; ***Figure 2E***). These clusters were NeuN-positive, post-mitotic granule cells (GCs) (***Figure 2F***) that failed to migrate to the internal granule cell layer (IGL). These cells remained in the external granule cell layer (EGL), a transient germinal zone. We observed this pattern at all our investigated latter timepoints with a higher incidence of ectopic clusters in the posterior lobules (***Figure 2—figure supplement 1***). Our examination of the two other major cerebellar cell populations, Purkinje cells (PCs) and Bergman glia (BG), did not reveal major cellular defects (***Figure 2—figure supplement 2A–C***). Cerebellar development relies on key glycosylated proteins expressed and secreted by PC or BG cells, such as Shh (***Dahmane and Ruiz i Altaba, 1999***) or dystroglycan (***Nguyen et al., 2013***). So, we investigated the origin of the identified GCs ectopia. We deleted *Srd5a3* using a GC-specific Cre line (Atoh1-Cre)(***Matei et al., 2005***) (***Figure 2—figure supplement 2D***). Atoh1-Cre; *Srd5a3*$^{fl/-}$ mice exhibit similar GC ectopias although in a lesser extent compared to the En1-Cre; *Srd5a3*$^{fl/-}$ mice (***Figure 2G***, ***Figure 2—figure supplement 1C,D***). This observation indicates a partial GC-autonomous defect and could be explained by the involvement of GC glycoproteins and non-GC interactors that interplay to allow GCs to initiate their migration and prevent the formation of these ectopic clusters.

Taken together, our results support a critical role for *Srd5a3* during cerebellar granule cells development likely through a GC-autonomous mechanism involving the glycosylation of specific, but undetermined, proteins.

## Cerebellum-specific Srd5a3 deletion decreases the levels of highly glycosylated proteins

Next, we evaluated the molecular mechanisms underlying our observed cerebellar defect by conducting a total proteomic analysis on the developing P7 mouse cerebellum (***Lipecka et al., 2016***; ***Wiśniewski et al., 2009***). This approach quantified 1982 proteins, whose abundance profiles can cluster each sample by genotype (***Figure 3—figure supplement 1A***, ***Supplementary file 1***). Our statistical analysis identified 97 differentially abundant proteins (DAP) (≈ 5% of the total; q-value <0,05) in the En1-Cre; *Srd5a3*$^{fl/-}$ mice (***Figure 3A***). To determine the deregulated pathways among the highly active, neural development pathways at this stage, we performed an over-representation analysis of the 97 DAP using ConsensusPathDB. Our analysis indicated that different pathways involved in ion and amino acid transport, synapse function, cell adhesion-related signaling and cholesterol biosynthesis interplay to generate the mouse phenotype (***Figure 3B***). Aside from changes in cholesterol metabolism, all enriched pathways contained at least one deregulated N-glycoprotein. Protein N-glycosylation is critical for ER-protein folding, however we did not find any enrichment in the ER stress pathway. Manual inspection of the 97 DAP revealed increased levels of only two ER-stress-related proteins, SDF2L1 (***Fujimori et al., 2017***) and HYOU1 (***Zhao et al., 2010***), while BiP, the classical ER-stress marker(***Ron and Walter, 2007***), showed a 1.3 fold non-significant (q = 0.08) increase (***Supplementary file 1***). We then performed a transcriptomic study on additional samples at the same stage, which confirmed the absence of any significant deregulation of the most widely used UPR markers (***Figure 3—figure supplement 1B***). In addition, we did not observe any change in BIP levels restricted to ectopic GC clusters (***Figure 3—figure supplement 1C,D***). Surprisingly, our results exclude a main effect of deregulated N-glycosylation processes on ER stress.

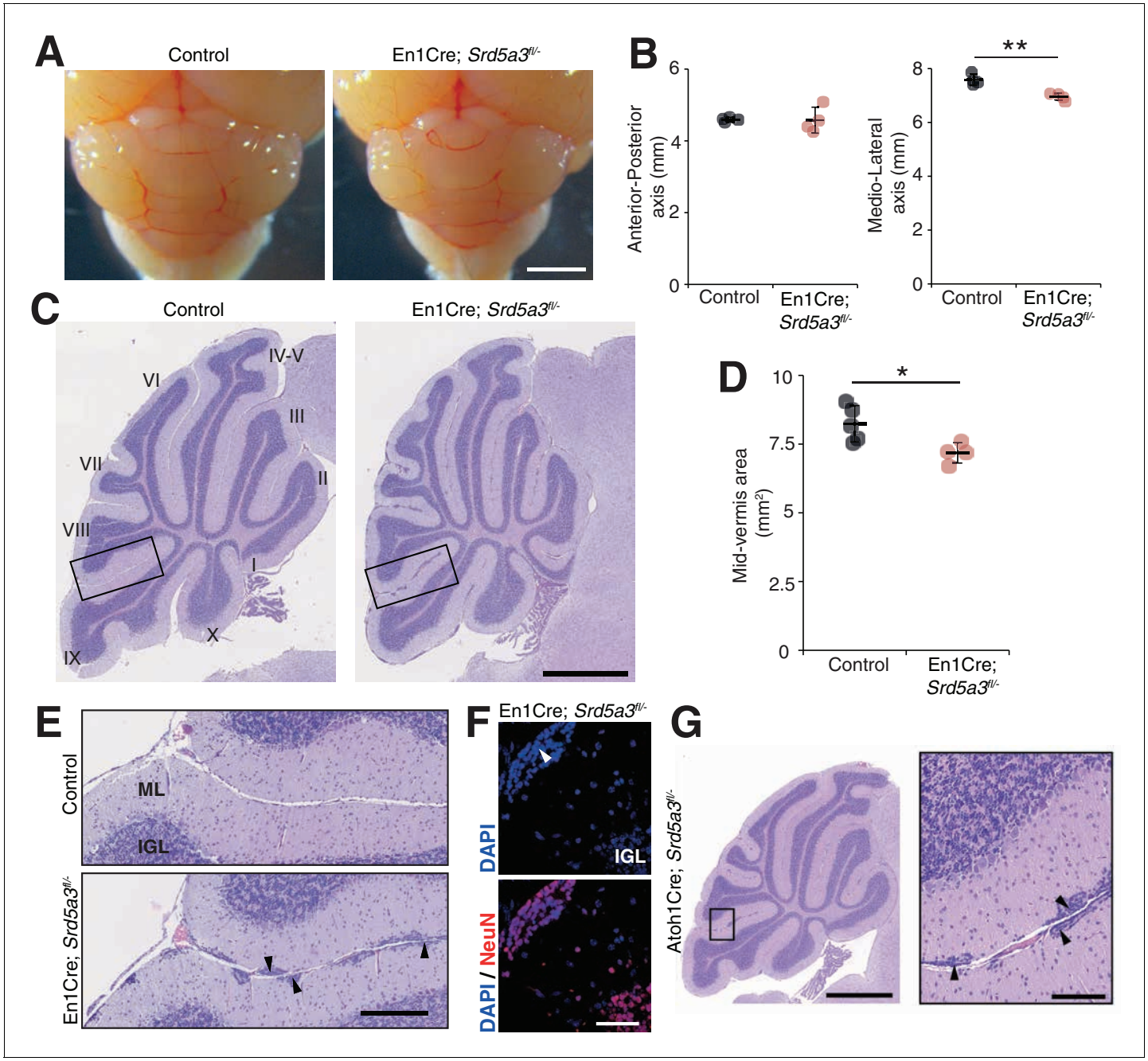


**Figure 2.** Reduced cerebellum size and ectopic granule neurons in the *Srd5a3* mutant. (**A**) Dorsal view of P21 posterior brains, scale bar 2 mm. (**B**) Quantification of the cerebellar anterior-posterior and medio-lateral axes (n = 4 for each genotype), **p-value=0.0018. (**C**) Representative images of hematoxylin-eosin (HE) stained P21 sagittal slices of control and mutant cerebella, scale bar 1 mm. Lobule numbers are indicated. (**D**) Quantification of the midline sagittal cerebellar area (Control, n = 5; En1-Cre; *Srd5a3*$^{fl/-}$, n = 4); *p-value=0.0245. (**E**) Magnification of HE-stained cerebellar cortex, scale bar 200 µm. All examined mutants show ectopic cell clusters (arrow-head) in the outer part of the molecular layer (ML). (**F**) DAPI (blue) and NeuN (red) staining of P21 En1-Cre; *Srd5a3*$^{fl/-}$ cerebellum. Ectopic cells (arrow-head) are positive for the post-mitotic GCs marker NeuN, scale bar 50 µm. (**G**) Representative image of an HE-stained sagittal slice of Atoh1-Cre; *Srd5a3*$^{fl/-}$ cerebellum showing similar ectopic cells in the outer ML under GC-specific *Srd5a3* deletion, scale bar 1 mm and 100 µm, respectively (n = 4). Two-tailed Student t-test was used for statistics. *p<0.05; **p<0.01. Results are presented as mean ± s.d.

DOI: https://doi.org/10.7554/eLife.38309.004

The following figure supplements are available for figure 2:

**Figure supplement 1.** Cerebellar granule cell ectopias quantification.

DOI: https://doi.org/10.7554/eLife.38309.005

*Figure 2 continued on next page*

*Figure 2 continued*

**Figure supplement 2.** Histological analysis of Purkinje cells (PCs) and Bergmann glia (BG).
DOI: https://doi.org/10.7554/eLife.38309.006

One possible consequence of defective protein N-glycosylation is decreased stability of hypoglycosylated proteins. We observed a significant, 4-fold enrichment of N-glycoproteins among the DAP with decreased levels (simplified as decreased N-glycoproteins; p=0.0012, ***Figure 3A***). Examining this group of decreased N-glycoproteins revealed that they have more N-glycosylation sites (i.e. higher site multiplicity) with an average of 5.57 sites versus 3.24 in unchanged N-glycoproteins

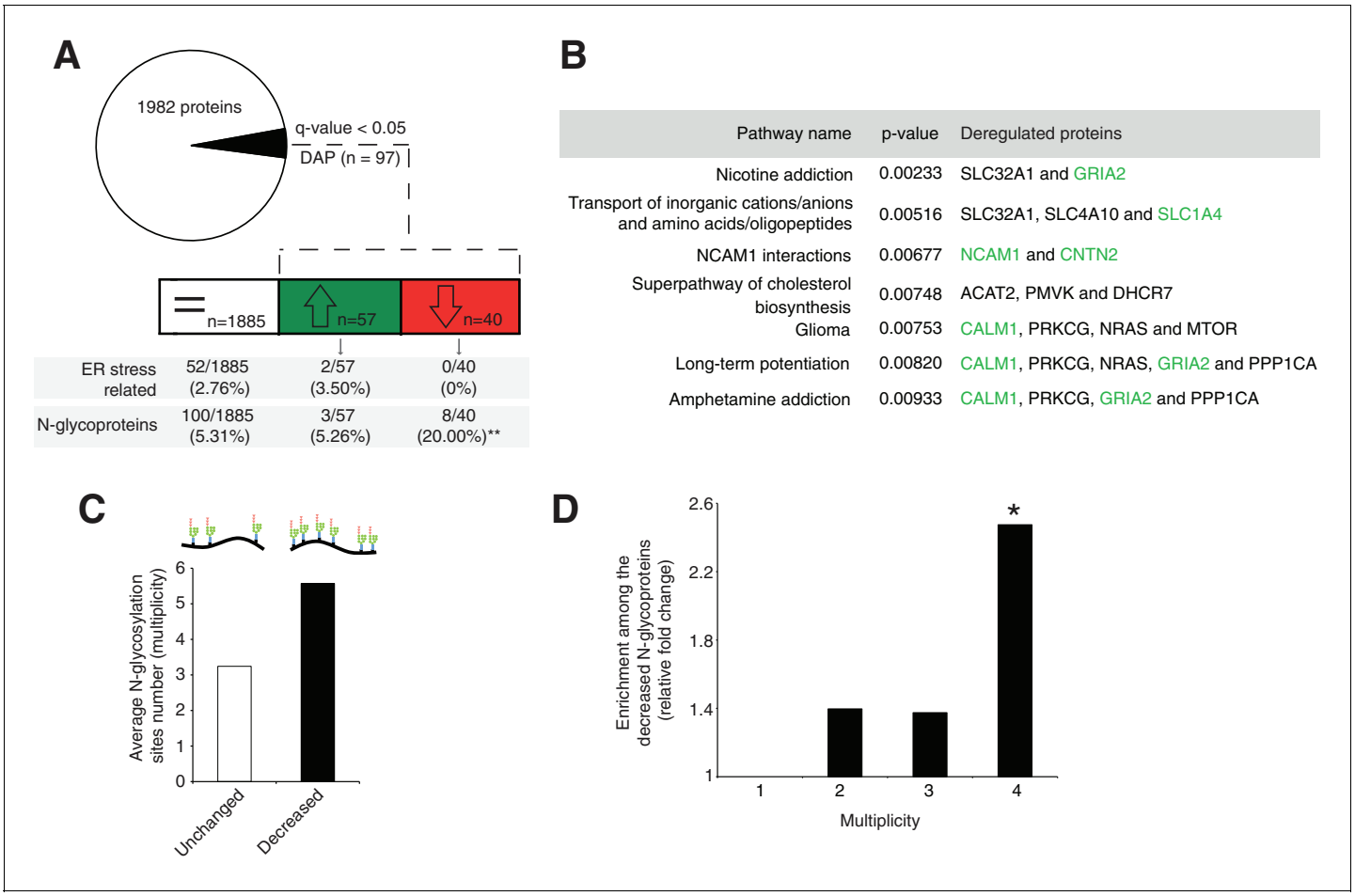


**Figure 3.** Disrupted neural pathways in the *Srd5a3* mutant developing cerebellum. (**A**, upper panel) Pie chart representing the total proteomics analysis in P7 cerebellum (n = 4 for each genotype). 97 proteins were detected as differentially abundant proteins (DAP) in the mutant samples (q-value <0.05). (**A**, lower panel) Distribution of unchanged proteins (white box), increased DAP (green box) and decreased DAP (red box) into ER stress-related (GO:0034976) or N-glycoproteins (Reference glycoproteomic database, see Materials andmethod) categories. A significant enrichment was detected within the decreased DAP for N-glycoproteins (n = 8, Fisher exact test, p-value=0.0012). (**B**) Over-representation analysis on DAP performed with ConsensusPathDB using the 1982 detected proteins as background. All pathways with p-value<0.01 are represented. N-glycoproteins are indicated in green. (**C**) Average multiplicity in the unchanged and the decreased N-glycoproteins groups. (**D**) Enrichment for different glycoprotein categories among the decreased N-glycoproteins. Multiplicity represents groups of proteins with more than one (≥2), two (≥3) or three (≥4) N-glycosylation sites. Multiplicity of ≥1 represents all of the decreased N-glycoproteins and is set to one (no enrichment). There is a significant 2.4 fold-change enrichment for glycoproteins with four or more N-glycans among the decreased N-glycoproteins (Fischer exact test, p-value=0.0378).
DOI: https://doi.org/10.7554/eLife.38309.007

The following figure supplement is available for figure 3:

**Figure supplement 1.** Extended total proteomic analysis of the unfolded protein response (UPR).
DOI: https://doi.org/10.7554/eLife.38309.008

(*Figure 3C*). Indeed, N-glycoproteins with four or more N-glycosylation sites are significantly enriched within the decreased N-glycoproteins (*Figure 3D*).

These data demonstrate that the mild glycosylation defect detected in the *Srd5a3* mutant cerebellum disrupts the levels of highly glycosylated proteins, but does not disrupt ER homeostasis.

## N-glycosylation site multiplicity and primary sequence underlies the selective protein glycosylation defect

To further elucidate the N-glycosylation deficiency, we included a lectin-affinity based (ConA, WGA, $RCA_{120}$) enrichment step at the peptide level, followed by deglycosylation (*Zielinska et al., 2010*), prior proteomic analysis (*Figure 4—figure supplement 1A*, data are available via ProteomeXchange with identifier PXD009906). This enrichment can identify N-glycosylation sites and quantify the abundance of each site when they are glycosylated. Using this dataset, we identified 140 likely new glycosylation sites (≈8% of the total, see Materials and method, *Supplementary file 2*) with high recurrence of non-canonical sequons (≈40% of the new sites, *Supplementary file 2*). Most proteins carrying these sites are intrinsic to membrane as observed for proteins with previously identified glycosylation sites (Gene Ontology analysis in *Supplementary file 2*). In total, we identified 1404 glycopeptides detected in at least 3 out of 4 control samples (*Figure 4A*, *Supplementary file 2*). As we observed for the total proteome, we could cluster the samples according to the genotype based on the expression levels of all the glycopeptides (see Materials and method, *Figure 4—figure supplement 1B*). Total proteomics and glycoproteomic analysis yielded complementary information. Total proteomics provides information of the protein abundance level but can only detect peptides containing an unoccupied N-glycosylation site. Glycoproteomics only allows detection of glycopeptides if the site is occupied. For 15% of the N-glycopeptides detected in glycoproteomics (n = 206), we found decreased levels in the mutant samples. Of these, we only detected 24 N-glycopeptides in the previous total proteomic experimental settings, consistent with the high enrichment observed with the glycoproteomics analysis (*Figure 4—figure supplement 1C*, *Supplementary file 3*). Among these peptides, 13 were never detected in control but only in mutant samples in total proteomics. These data indicate that these 13 peptides were not glycosylated in the mutant. We conclude that most differences we detected in the glycoproteomic experiment reflect reduced glycosylation site occupancy.

We also detected an extremely significant correlation between N-glycan multiplicity and N-glycopeptide levels (*Figure 4B*, Mann-Whitney test, p-value<0.0001). This result is consistent with our larger glycoprotein dataset. To delineate the origin of reduced occupancy of individual N-glycosylation sites, we analyzed their primary sequences (*Figure 4C*). We identified a mild effect of the presence of a non-aromatic amino-acid (other than Phe, Tyr, His or Trp) at position −2 and a more significant effect of the Serine at position +2 (*Figure 4D*), as previously described(*Gavel and Heijne, 1990*; *Murray et al., 2015*), with an increased impact in highly glycosylated proteins (*Figure 4E*). These findings demonstrate that N-glycan multiplicity combined with sequon efficiency is a major parameter driving protein sensitivity to N-glycosylation defects.

## Impaired protein N-glycosylation targets IgSF-CAMs

We next wanted to delineate the affected pathways based on our glycoproteomic results. We performed an over-representation analysis using proteins carrying at least one N-glycopeptide significantly decreased in mutant samples (145 N-glycoproteins, 206 N-glycopeptides). This analysis revealed that the most significantly affected proteins (4 out of the top 10 deregulated pathways) derive directly from cell adhesion and axon guidance-related pathways involving adhesion proteins from the L1CAM family (*Figure 5A*, red circles). L1CAMs and the previously identified NCAM1 and CNTN2 (*Figure 3B*) belong to the immunoglobulin superfamily of cell adhesion molecules (IgSF-CAMs) with critical roles in brain development (*Maness and Schachner, 2007*; *Pollerberg et al., 2013*; *Stoeckli, 2010*). We speculate that this particular sensitivity of IgSF-CAMs to a N-glycosylation defect arises from their higher N-glycosylation site multiplicity with an average of 3.3 sites versus 2.3 in non IgSF-CAM proteins (Calculated based on the reference glycoproteomic dataset, *Supplementary file 2*, Mann Whitney test, p-value<0.0001).

So, we next hypothesized that impaired IgSF-CAMs function derived from sub-optimal N-glycosylation and that defective IgSF-CAMs contributed to our observed histological defect.

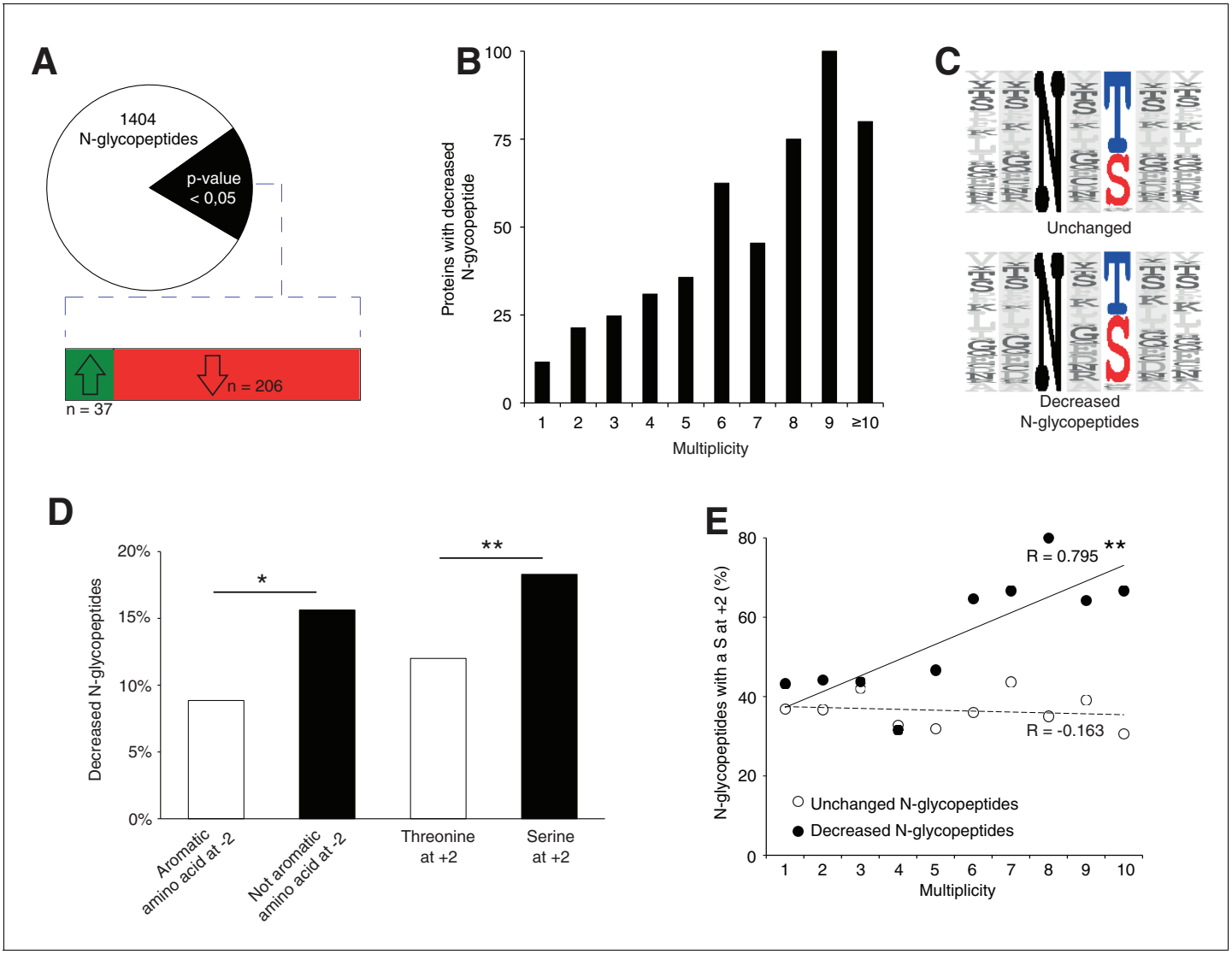


**Figure 4.** *Srd5a3* deletion impairs protein N-glycosylation in a sequon and multiplicity-dependent manner. (**A**) Pie chart representation of the glycoproteomic analysis in P7 cerebellum (n = 4 for each genotype). The vast majority of the differentially abundant N-glycopeptides was decreased in the mutant samples (206/241, 85%). (**B**) Percentage of proteins with decreased N-glycopeptide according to their multiplicity (Mann-Whitney test, p-value<0.0001). Proteins with higher multiplicity are more likely to have decreased N-glycopeptide levels. (**C**) Motif analyses of the N-glycopeptides unchanged or decreased in the mutant. (**D**) Significant enrichment within the decreased N-glycopeptides for a non-aromatic amino acid (other than Phe, Tyr, His or Trp) in position −2 and a Ser in position +2 (NxS motif). (**E**) Correlation between protein multiplicity and their percentages of decreased (black) or unchanged (dashed line) glycopeptides with NxS sequon in the mutant samples. A significant positive correlation was found between the percentage of NxS-containing glycopeptides with decreased occupancy in the mutant and the N-glycoprotein multiplicity (Pearson's coefficient, p-value=0.0062). NxS-containing N-glycopeptides are more likely to have decreased level when located in a highly glycosylated protein. Unless indicated, two-tailed Student t-test was used for statistics. *p<0.05; **p<0.01.

DOI: https://doi.org/10.7554/eLife.38309.009

The following figure supplement is available for figure 4:

**Figure supplement 1.** Extended glycoproteomic analysis results and validation.

DOI: https://doi.org/10.7554/eLife.38309.010

We confirmed our observed enrichment for IgSF-CAMs found in our over-representation analysis at the N-glycopeptide level (18.4% of the decreased N-glycopeptides belong to an IgSF-CAM protein, Fisher exact test, p-value=0.0058, ***Figure 5B***).

We selected two highly N-glycosylated IgSF-CAMs relevant for the granule cell histological phenotype for validation by WB. We did observe a clear hypoglycosylation defect for L1CAM and

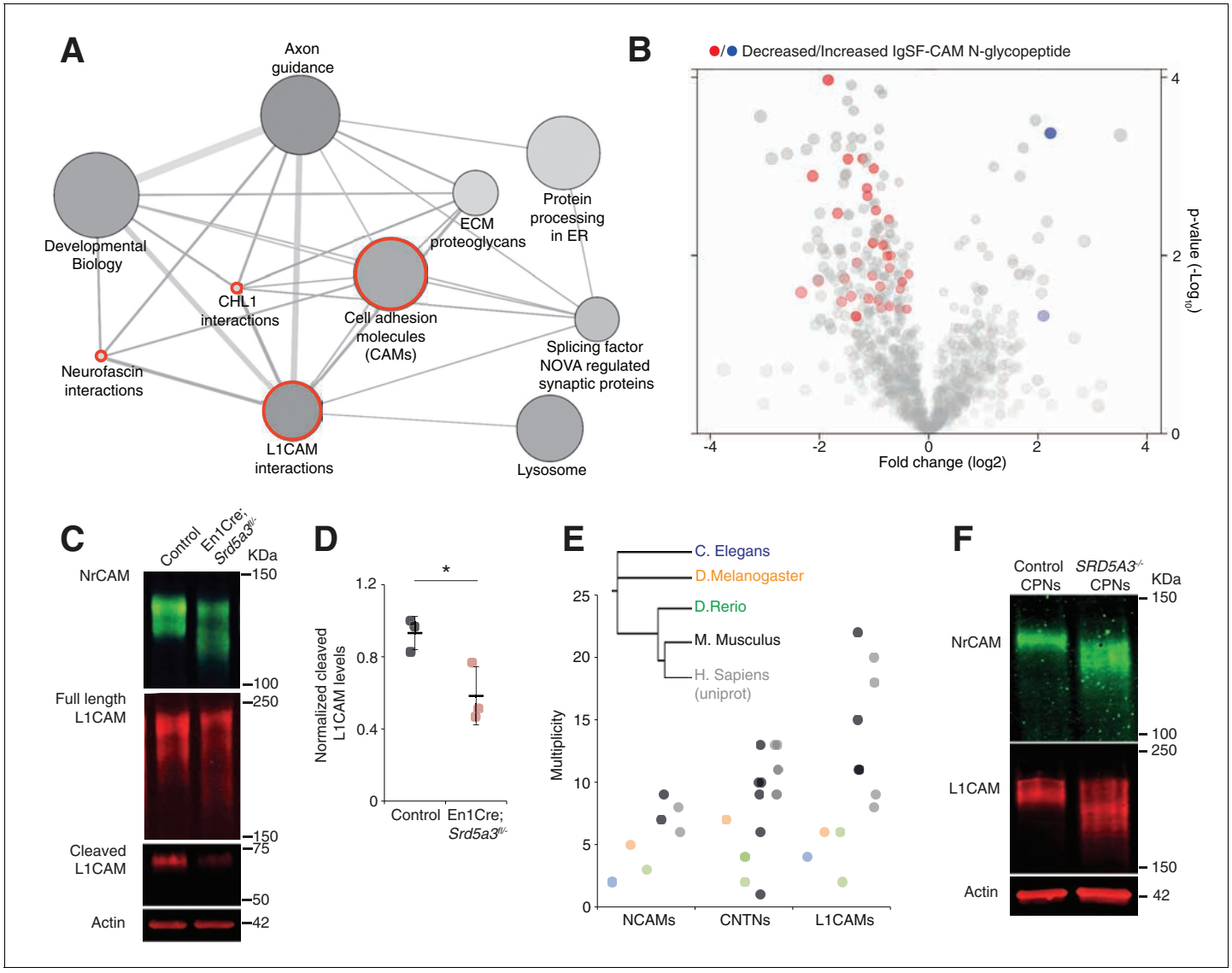


**Figure 5.** IgSF-CAMs are especially sensitive to a mild N-glycosylation impairment. (**A**) Graphical representation of enriched pathways and their interactions within proteins with reduced N-glycopeptide in the mutant (ConsensusPathDB). The nodes size indicates the number of proteins within the pathway, and their shade notes the significance (the darkest, the more significantly enriched). Red circles enclose the L1CAM family-related pathways. (**B**) Volcano plot against all N-glycopeptides. The decreased (red) or increased (blue) N-glycopeptides belonging to an IgSF-CAM protein are highlighted. There is enrichment for IgSF-CAMs glycopeptides within the decreased ones (Fisher exact test, p-value=0.0058). (**C**) WB against L1CAM and NrCAM in the P7 mouse cerebellum and (**D**) quantification of the 70 kDa cleaved isoform of L1CAM (n = 3 for each genotype, p-value=0.0312). (**E**) Multiplicity per protein of three IgSF-CAMs subfamilies (L1CAMs, CNTNs and NCAMs) in different species. Multiplicity information was collected from experimental datasets (***Zielinska et al., 2010***) and Zielinska et al, 2012) except for human information extracted from uniprot database. (**F**) WB analysis of L1CAM and NrCAM levels in CPNs (n = 2 per genotype, repeated twice). Unless indicated, two-tailed Student t-test was used for statistics. Results are presented as mean ±s.d. *p<0.05.

DOI: https://doi.org/10.7554/eLife.38309.011

The following figure supplements are available for figure 5:

**Figure supplement 1.** Schematic representation of the mouse L1CAM and NrCAM with their hypoglycosylated sites.

DOI: https://doi.org/10.7554/eLife.38309.012

**Figure supplement 2.** hiPSCs differentiation towards human cortical projection neurons (CPNs).

DOI: https://doi.org/10.7554/eLife.38309.013

NrCAM with a detected shift to lower molecular weights and a significant decrease in the glycosylation-dependent cleavage of L1CAM (**Lutz et al., 2014**) (**Figure 5C,D**, **Figure 5—figure supplement 1**).

A major role for IgSF-CAMs in mammalian development is illustrated by the increased number of their encoding genes across evolution (**Hortsch, 2000**). We also observed an increased in the N-glycan multiplicity for three IgSF-CAM families with critical roles in brain development (**Figure 5E**). The multiplicity of these glycoproteins is almost systematically much higher in mammals compared to the other species. To test if the IgSF-CAM sensitivity for glycosylation impairment is conserved, we generated *SRD5A3* knockout (KO) human induced pluripotent stem cells (hiPSCs). We then differentiated them toward cortical projection neurons (CPNs, **Figure 5—figure supplement 2**). As previously observed in mouse, human L1CAM and NrCAM immuno-blotting profiles exhibit clear shifts in *SRD5A3*$^{-/-}$ CPNs (**Figure 5F**). These data demonstrated a similar exacerbated sensitivity of IgSF-CAMs to SRD5A3 loss in human neurons. Our data suggest that the sensitivity of highly glycosylated IgSF-CAMs to N-glycosylation defect is conserved across mammalian species and that the increase in multiplicity during evolution parallels the acquisition of a more complex neural cell organization.

## Hypoglycosylation of L1CAM and NrCAM alters their expression level at the plasma membrane

In order to evaluate the consequences of IgSF-CAM hypoglycosylation at the cellular level, we studied the cell surface expression of L1CAM and NrCAM using antibodies directed against their ectodomain in non-permeabilized cells (see Materials and methods). We detected the expression of these IgSF-CAMs along the axons and at the growth cone but with 30.8% and 39.6% decrease for L1CAM and NrCAM, respectively, in *Srd5a3* cKO neurons (**Figure 6A,B**). We recapitulated a similar defect using Tunicamycin suggesting that the disruption of other steps of the N-glycosylation pathway as well as specific drugs can efficiently alter the cell-surface expression of these glycoproteins. Such differences in the membrane expression levels are expected to have consequences on the ability of neurons to bind their substrates. Both L1CAM and NrCAM are known to interact homophilically and heterophilically with multiple IgSF-CAM, e. g. CNTN1 and CNTN2 (**Falk et al., 2002**; **Sonderegger, 1997**). We decided to test for the homophilic binding activity, by incubating cultured GCs with chimeras made of the extracellular part of L1CAM or NrCAM fused with the IgG Fc region (L1CAM-Fc and NrCAM-Fc, respectively). Indeed, a 38.5% and 56.0% decrease in the binding of L1CAM and NrCAM chimeras, respectively, was observed in mutant cells (**Figure 6C,D**). This result validates the functional impact of IgSF-CAMs hypoglycosylation and suggests that the glycosylation level of IgSF-CAMs plays a critical role in the regulation of their cell-surface expression.

## Srd5a3 is necessary for IgSF-CAM-dependent cerebellar granule cells adhesion and axon guidance

IgSF-CAMs rely on their glycan charge to interact with each other (**Wei and Ryu, 2012**) (**Horstkorte et al., 1993**). Proper IgSF-CAMs trans-interaction is essential for adequate nervous system connectivity for fasciculation and axonal guidance(**Pollerberg et al., 2013**). To demonstrate that IgSF-CAMs hypoglycosylation is directly involved in En1-Cre; *Srd5a3*$^{fl/-}$ mouse phenotype, we examined the neurite dynamics by live cell imaging of isolated GCs cultured under different surface coating conditions. *En1-Cre; Srd5a3*$^{fl/-}$ GCs did not show any significant alterations that suggested differences in proliferation or cell death onto any substrates (**Figure 7—figure supplement 1A**). In contrast, GCs showed defective neurite sprouting with a 20% decrease when using a coating with laminin and poly-D-lysine (**Figure 7A,B**). This phenotype was exacerbated in the presence of coatings made of human recombinant L1CAM or NrCAM proteins that enhance homophilic interactions (**Dequidt et al., 2007**). We observed a 37% and 52% reduction in neurite number for mutant GCs compared to control, on L1CAM and NrCAM substrates, respectively (**Figure 7C**). A significant decrease was also observed in neurite length (**Figure 7—figure supplement 1B**) but less specifically associated with IgSF-CAM coating (**Figure 7—figure supplement 1B–D**). To further link the IgSF-CAM-dependent neurite development in the mutant GCs to the defective initiation of cell migration, we used GC re-aggregates to evaluate cellular migration in vitro under different coating conditions (**Bizzoca et al., 2003**) (**Katic et al., 2014**; **Kerjan et al., 2005**). Using laminin and poly-D-lysine coating, the mutant re-aggregates showed no significant difference in neurite number and only a mild

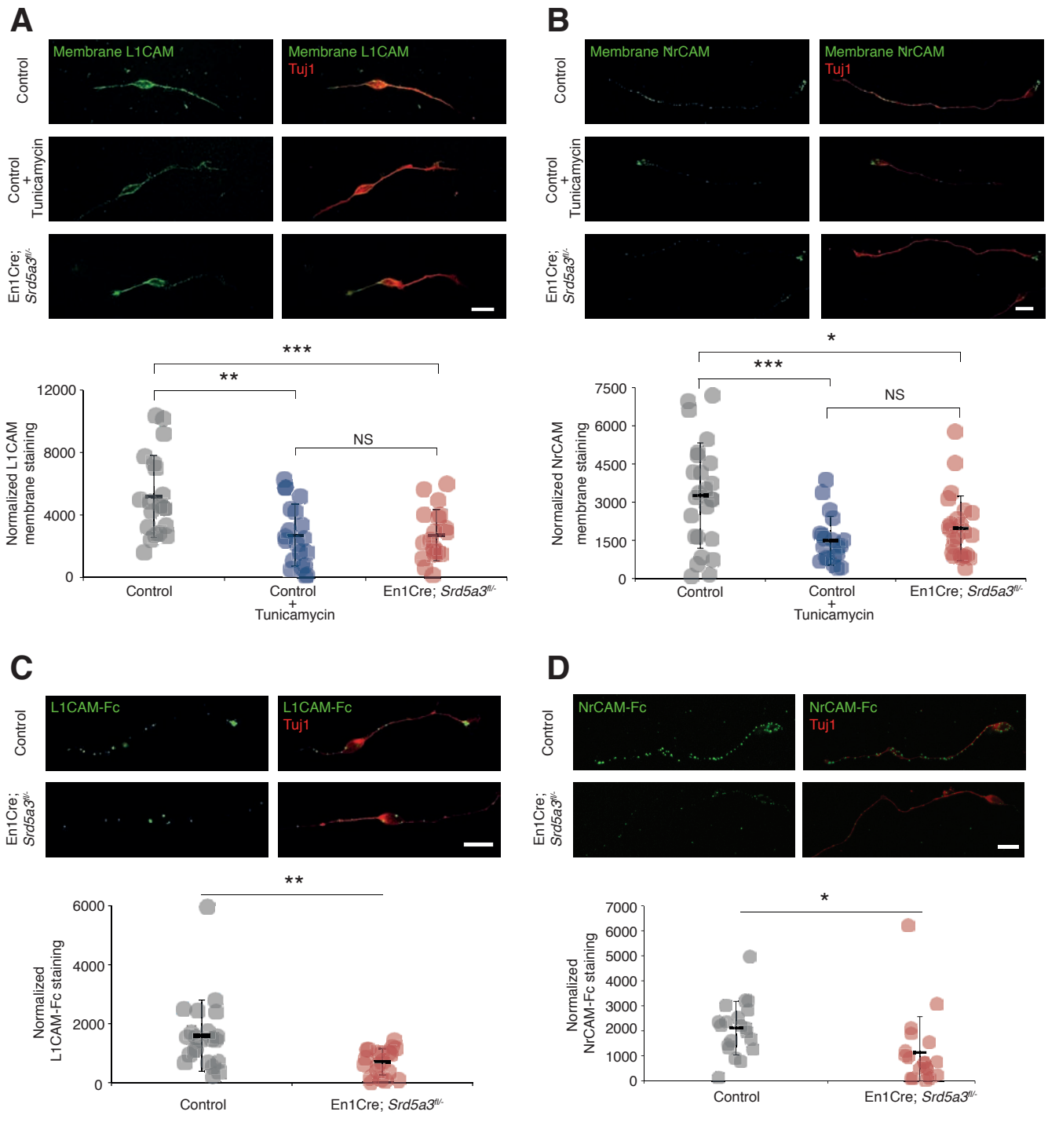


**Figure 6.** L1CAM and NrCAM hypoglycosylation affects their cell surface expression and binding activity. (**A**) L1CAM and (**B**) NrCAM surface immunostaining of cultured GCs and quantification. (**C**) L1CAM-Fc and (**D**) NrCAM-Fc binding assay on cultured GCs. The cells were incubated with the recombinant proteins and bound L1CAM-Fc or NrCAM-Fc were visualized with anti-Fc antibody. All of the staining and quantifications were performed with at least three biological replicates from different litters. Each dot represents a single neuron. Scale bar 10 μm. Results are presented as mean (black line)±s.d.

DOI: https://doi.org/10.7554/eLife.38309.014

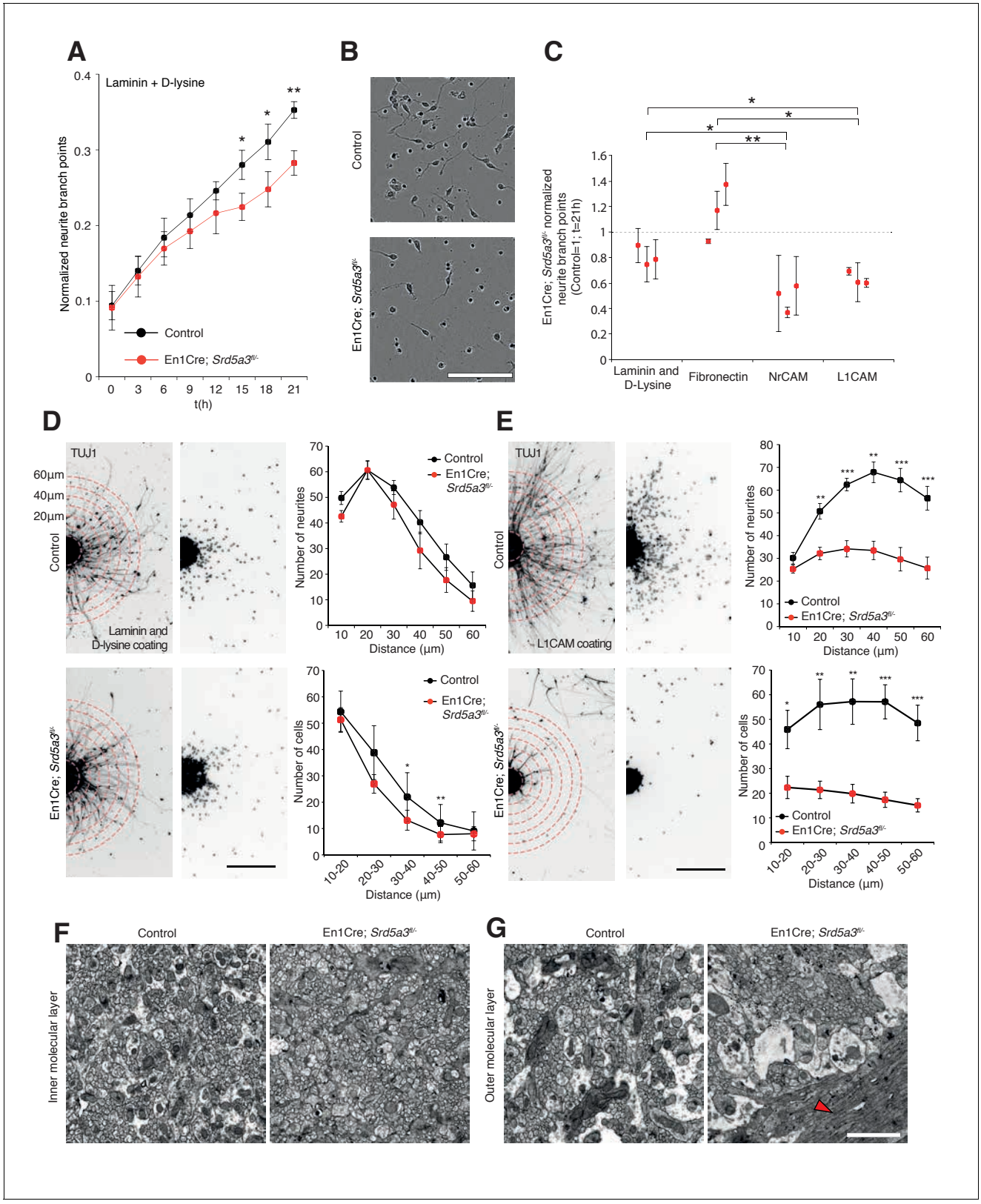


**Figure 7.** IgSF-CAM-dependent neurite dynamic and axon orientation defects in *Srd5a3* mutant cerebellum. (**A**) Neurite number per GC body cluster across 21 hr in laminin and poly-D-lysine-coated wells as measured with Incucyte live cell imaging system (Control, n = 3; En1-Cre; *Srd5a3*$^{fl/-}$, n = 3). (**B**) Representative image of control and En1-Cre; *Srd5a3*$^{fl/-}$ GCs after 21 hr in laminin and poly-D-lysine-coated wells. Scale bar 100 µm. (**C**) Neurite number normalized to GC body clusters after 21 hr with laminin/poly-D-lysine coatings, fibronectin or IgSF-CAMs-coated wells (NrCAM and L1CAM). Each dot

*Figure 7 continued on next page*

*Figure 7 continued*

per coating represents results from a single mutant mouse. All GC cultures were performed in technical triplicates (Control, n = 3; En1-Cre; *Srd5a3*$^{fl/-}$, n = 3). (**D**) Neurite number and number of migrating neurons in GC re-aggregates plated for 24 hr on laminin and poly-D-lysine and (**E**) L1CAM coated surfaces. Five aggregates were quantified per mouse and coating condition (Control n = 5, En1Cre; *Srd5a3*$^{fl/-}$, n = 7). (**F**) Representative electron microscopy images of cerebellar ML sagittal view at P21 taken from control (n = 3) and *Srd5a3* mutant (En1-Cre; *Srd5a3*$^{fl/-}$ n = 1; Atoh1-Cre; *Srd5a3*$^{fl/-}$ n = 2) mice. Scale bar 2 μm. Parallel fibers show a single orientation in control ML, whereas some exhibit an abnormal perpendicular orientation in the most outer ML in the mutant mice (G, red arrowhead). Two-tailed Student t-test was used for statistics. *p<0.05; **p<0.01. Results are presented as mean ± s.d.

DOI: https://doi.org/10.7554/eLife.38309.015

The following figure supplement is available for figure 7:

**Figure supplement 1.** Changes in granule cell (GC) number and neurite length under different coating conditions.

DOI: https://doi.org/10.7554/eLife.38309.016

defect in migration (***Figure 7D***). However, when the aggregates were plated on L1CAM-coated surfaces, a major defect in both neurite number and subsequent cell migration was observed (***Figure 7E***). This result highlights the substrate specificity of the adhesion phenotype and overall these data show that the correct glycosylation of IgSF-CAM is critical for neurite outgrowth, especially in the initiation step. Interestingly, GCs axons development is a process CNTN2 dependent that precedes the initiation of GCs migration towards the IGL (***Xenaki et al., 2011***).

Given the prominent role of many IgSF-CAMs in axon guidance and the granule cells adhesion defect, we examined axon orientation in GCs. We analyzed the parallel fibers (PFs) organization in the cerebellar ML using electronic microscopy. In control samples, PFs are consistently oriented perpendicular to PCs branches. However, *Srd5a3* mutant mice exhibit an aberrant orientation of groups of PFs in the outer ML, likely due to defective axonal guidance (***Figure 7F,G***). Taken together, our data suggest that IgSF-CAMs hypoglycosylation may underlie many neurological defects in CDG.

## Discussion

We sought to delineate the impact of *Srd5a3*-driven hypoglycosylation of N-glycoproteins during development, a biochemical defect likely shared between multiple CDG. Here, we generated a conditional KO mouse that recapitulates some neurological symptoms induced by this ER glycosylation defect. We hypothesized that patients with *SRD5A3*-related and other types of CDG exhibit protein hypoglycosylation leading to cerebellar dysfunction. From a physiological perspective, we hypothesized that the characterization of the affected glycoproteins and glycosylation sites would identify new roles for protein N-glycosylation during central nervous system development. So, we combined total proteomic and glycoproteomic approaches to identify the molecular mechanisms underlying the observed cerebellar dysfunction and GC histological defects. Our strategy assessed the relative occupancy at each N-glycosylation site regardless of the N-glycan nature. The pleiotropic roles of glycans on development and synaptic transmission suggest that genetic defects in the synthesis of the N-glycan core structure would have multiple distinct and integrated consequences. We unexpectedly found that partial inhibition in N-glycosylation during cerebellar development has persistent consequences on a specific set of glycoproteins and pathways. Among them, we found that IgSF-CAMs-mediated cell adhesion is the most consistently affected. Our further investigations revealed impaired GC adhesion and axon growth, which support IgSF-CAM hypoglycosylation as the primary underlying defect. Our glycoproteomic and total proteomic analyses strongly suggest an intuitive mechanism where N-glycan multiplicity is a critical factor driving the molecular defects.

SRD5A3 acts at the last step of dolichol synthesis and facilitates also the synthesis of O-mannose-linked glycans, C-mannosylation, and glycophosphatidylinositol (GPI) anchored proteins. However, N-glycosylation is the most demanding cellular process with eight dolichol molecules needed for each N-linked glycan(***Cantagrel and Lefeber, 2011***). Defects in SRD5A3 alter lipid membrane composition that subsequently impairs protein N-glycosylation. Consistently with previous results using *Srd5a3* gene-trapped embryos(***Cantagrel et al., 2010***), several enzymes from the cholesterol/mevalonate pathway were found deregulated (***Figure 3B***). These observations indicate a regulatory mechanism that could alleviate these glycosylation defects by stimulating the mevalonate pathway (***Haeuptle et al., 2011***) (***Welti, 2013***). While we cannot exclude defects in other glycosylation

pathways, our results demonstrate that changes in N-glycosylated proteins and correlations between the N-glycan number and peptides abundance in both proteomic and glycoproteomic analyses strongly implicate the N-glycosylation pathway as the major metabolic target underlying the phenotype and neurological symptoms in SRD5A3-CDG. Surprisingly, we did not observe a signature of the UPR pathway as seen in other CDG models. This result does not exclude a minimal glycoprotein folding impairment that does not significantly alter the ER homeostasis. A potential mechanism of adaptation to this mild impairment is detected with the over-expression of the HYOU1 and SDF2L1 chaperones.

Our work shows that proteins with high N-glycan multiplicity, estimated to average four or more sites, show an increased risk for hypoglycosylation to induce protein degradation or dysfunction. Moreover, differences in the sequon can have an additive effect to this increased risk. Although several highly-glycosylated proteins are frequently used as sensitive biomarker for N-glycosylation defects(**He et al., 2012**) (**Park et al., 2014**), we provide initial evidence that the total number of glycosites per protein is a major parameter that influences N-glycoproteins sensitivity. Our total proteomic analysis clearly indicates that decreased glycoprotein abundance is a direct consequence of incomplete glycosylation of highly glycosylated proteins. Yet, examining individual proteins, such as the IgSF-CAM member L1CAM, did not reveal significant differences in full-length isoform abundance by western blot but showed altered cleavage as well as reduced cell surface expression as a consequence of its hypoglycosylation. The cleaved L1CAM isoform (70 kDa) enhances cerebellar GC neurite outgrowth(**Lutz et al., 2014**), which indicates that hypoglycosylation of some proteins can impair their processing, trafficking and/or functioning without necessarily causing significant changes in their cellular abundance.

The number of N-glycans, in conjunction with their degree of branching, regulates cell proliferation and differentiation. Highly glycosylated growth factor receptors show increased cell-surface expression by forming galectin-mediated molecular lattices(**Lau et al., 2007**). We cannot exclude that some cell adhesion proteins utilizing a similar mechanism also show alterations in the *Srd5a3* mutant cerebellum. To our knowledge, neuronal galectin-IgSF-CAM interactions remain unreported. The pivotal role of IgSF-CAMs in cell migration, axonal guidance and synaptogenesis has been widely studied in mouse (**Sakurai et al., 2001**) (**Fransen et al., 1998**) (**Berglund et al., 1999**) (**Çolakoğlu et al., 2014**) (**Sytnyk et al., 2017**). However, we still understand very poorly how N-glycans contribute to these functions with few exceptions such as the established role for the polysialic acid modification of NCAM1 N-glycan chains(**Weinhold et al., 2005**). Interestingly, specific N-glycosylated residues, alpha2,3-linked sialic acid and Lewis(x) of L1CAM, CNTN1 and CNTN2 have been reported to mediate interaction with the glycopeptide CD24 modulating cell adhesion and neurite outgrowth of cerebellar neurons (**Lieberoth et al., 2009**).

Among proteins identified in our proteomic approaches, NrCAM and L1CAM show redundant functions in cerebellar GC development, in addition to their roles in axonal growth (**Sakurai et al., 2001**) (**Demyanenko et al., 1999**) (**Demyanenko et al., 2011**). CNTN2/TAG-1 contributes to neuronal polarization and axonal organization. Interestingly, the corresponding KO mouse shows ectopic GC clusters at the pial surface of the cerebellum (**Xenaki et al., 2011**), as observed in the *Srd5a3* mutant cerebellum. Mice lacking *Cntn1* show aberrant parallel fibers distribution and motor coordination defects (**Berglund et al., 1999**). Since neural IgSF-CAMs largely bind to each other homophilically and heterophilically (**Pollerberg et al., 2013**), we suspect that the observed neuronal adhesion defects arise from a cumulative effect of partial hypoglycosylation of multiple interacting partners (**Schwarz et al., 2009**) (**Stoeckli et al., 1997**). IgSF-CAMs show increased complexity and members in vertebrates (**Vogel and Chothia, 2006**). The increased diversity in some IgSF-CAM proteins correlates with the presence of homologs with higher multiplicity in mammals (**Figure 5E**). We speculate that a positive selection of adhesion proteins with high N-glycosylation site multiplicity can support the increased complexity of mammalian neuronal organization and connectivity.

In addition to the central nervous system, highly glycosylated IgSF-CAM members also play critical roles in other systems affected in CDG patients, such as the developing eyes (**Morava et al., 2009**) and immune system with ICAM1 (**Blank et al., 2006**; **He et al., 2014**), or in other diseases like cancer, where L1CAM plays a critical role in tumor metastasis (**Kiefel et al., 2012**) (**Agrawal et al., 2017**). Further investigations will determine how IgSF-CAM hypoglycosylation regulates or alters the clinical outcomes and responsivity to therapeutic strategies. In conclusion, our study demonstrates that suboptimal functioning of the ER-glycosylation machinery impairs primarily highly glycosylated

N-glycoproteins with mild or no effect on ER homeostasis. We propose that the prevalent neurological symptoms observed in SRD5A3-CDG patients and likely other types of CDG type I result from defective neural cell adhesion, caused by IgSF-CAM hypoglycosylation. Deciphering how multiple N-glycans can influence differential IgSF-CAM adhesion properties will address important unresolved neurobiological questions regarding neuronal migration, axonal outgrowth and synaptogenesis.

# Materials and methods

### Key resources table

| Reagent type (species) or resource | Designation | Source or reference | Identifiers | Additional information |
|---|---|---|---|---|
| Genetic reagent (M. musculus) | *ACTB:FLPe B6J* | JAX stock #005703 | ACTB:FLPe B6J | |
| Genetic reagent (M. musculus) | *Atoh1-Cre* | JAX stock #011104 | Tg(Atoh1-cre)1Bfri | |
| Genetic reagent (M. musculus) | CAG-Cre | JAX stock #004682 | B6.Cg-Tg (CAG-cre/Esr1*)5Amc/J | |
| Genetic reagent (M. musculus) | *CMV-Cre* | PMID: 7624356 | En1tm2(cre)Wrst | |
| Genetic reagent (M. musculus) | *En1-Cre* | JAX stock #007916 | En1tm2(cre)Wrst | |
| Genetic reagent (M. musculus) | R26RLacZ | PMID: 25594525 | | |
| Genetic reagent (M. musculus) | *Srd5a3Floxed* | IMPC - ES cell clone EPD0575_2_F01 carrying the Srd5a3tm1a (EUCOMM)Wtsi allele | Srd5a3tm1a (EUCOMM)Wtsi | |
| Antibody | BiP | Enzo | ADI-SPA-826 | 1:50 |
| Antibody | Calbindin | Swant | CB-38A | 1:10.000 |
| Antibody | GFAP | Millipore | AB5804; RRID:AB_2109645 | 1:1.000 |
| Antibody | L1CAM | Abcam | AB24345; RRID:AB_448025 | 1:2.000 |
| Antibody | L1CAM | ***Appel et al. (1995)*** | 557.B6 | Membrane staining |
| Antibody | Laminin | Sigma | L9393; RRID:AB_477163 | 1:33 |
| Antibody | LAMP1 | Abcam | AB24170; RRID:AB_775978 | 1:2.000 |
| Antibody | NeuN | Millipore | MAB377; RRID:AB_2298772 | 1:200 |
| Antibody | NrCAM | Abcam | AB24344; RRID:AB_448024 | 1:2.000/Also used for membrane staining |
| Antibody | Tuj1 | Sigma | T2200 | 1:2.000 |
| Antibody | β-actin | Thermo Fisher | AM4302; RRID:AB_2536382 | 1:20.000 |
| Chemical compound, drug | D-Lysine | Sigma | P6407 | |
| Chemical compound, drug | Fibronectin | Sigma | F2006 | |
| Chemical compound, drug | Laminin | Sigma | 11243217001 | Coating reagent |
| Chemical compound, drug | Lectin ConA | Sigma | C2272 | 1:2.000 |

*Continued on next page*

*Continued*

| Reagent type (species) or resource | Designation | Source or reference | Identifiers | Additional information |
|---|---|---|---|---|
| Chemical compound, drug | Lectin ConA | Sigma | C2010 | Glycoproteomics reagent |
| Chemical compound, drug | Lectin RCA120 | CliniSciences | L-1080 | Glycoproteomics reagent |
| Chemical compound, drug | Lectin SNA | Vector laboratories | B-1305 | 1:2.000 |
| Chemical compound, drug | Lectin WGA | Sigma | L9640 | Glycoproteomics reagent |
| Chemical compound, drug | PNGase | New England BioLabs | P0704L | |
| Chemical compound, drug | Tamoxifen | Sigma | H6278 | 1 µM |
| Chemical compound, drug | Tunicamycin | BioTechne | 3516/10 | 0.01 µg/mL |
| Chemical compound, drug | WATER-18O, 97 ATOM % 18O | Sigma | 329878 | Glycoproteomics reagent |
| Commercial assay or kit | GeneChip Mouse Transcriptome Array 1.0 | Affimetrix | MTA1.0 | |
| Peptide, recombinant protein | L1CAM-Fc | R and D | 777-NC | |
| Peptide, recombinant protein | NrCAM-Fc | R and D | 2034-NR | |
| Software, algorithm | ParTek Genomics Suite | ParTek | | |
| Other | IncuCyte | Essen Bioscience | IncuCyte S2 with NeuroTrack module | |

## Animal care

Animals were used in compliance with the French Animal Care and Use Committee from the Paris Descartes University (APAFIS#961 – 201506231137361). All behavioural analysis were performed in compliance with the guidelines of the French Ministry of Agriculture for experiments with laboratory animals. The experimental protocol and euthanasia have been approved by the Ethical Committee 27, registered at the French ministry of research.

## Generation of the *Srd5a3* conditional KO mouse

Embryonic stem (ES) cell clone EPD0575_2_F01 carrying the *Srd5a3*$^{tm1a(EUCOMM)Wtsi}$ allele was acquired from the International Mouse Phenotyping Consortium (IMPC; http://www.mousephenotype.org/). After additional QC validation based on Southern-blot, ES cells were injected into C57BL/6 at the University of California, San Diego Transgenic and Gene targeting Core yielding chimeric mice. Chimera were bred to C57Bl/6 until germline transmission was successful to produce knockout first allele. Then, the *Srd5a3*tm1a mice were bred with ACTB:FLPe B6J (JAX stock #005703) Flp recombinase expressing transgenic mice to produce mice expressing a functional *Srd5a3* allele that retained flox sites surrounding exon 2 to 4 (out of the six exons) and including part of the enzymatic domain (PFAM, *Steroid_dh*). After outbreeding the Flp recombinase transgene, *Srd5a3* floxed mice were crossed with hemizygous CMV-Cre line transgenic mice (**Metzger et al., 1995**) to generate *Srd5a3* KO allele. *Srd5a3* floxed mice were bred with hemizygous *En1*$^{tm2(cre)Wrst}$ transgenic mice (JAX stock #007916) expressing Engrailed1 promoter driven Cre to produce cerebellum-specific deletion (En1Cre; *Srd5a3*$^{fl/-}$) or with hemizygous Tg(Atoh1-cre)1Bfri (JAX stock #011104) expressing Atoh1 promoter driven Cre to produce cerebellum granule cell-specific deletion (Atoh1Cre; *Srd5a3*$^{fl/-}$). Specific Cre expression was confirmed by breeding with a LacZ

reporter-carrier mouse line (R26R$^{LacZ}$ mouse). Efficient *Srd5a3* recombination was assessed by RT-PCR and RT-qPCR in the absence of any specific antibody.

## Mouse embryonic fibroblasts (MEFs) generation

For MEFs generation, *Srd5a3$^{fl/-}$* mice were bred with CAGCre mice (B6.Cg-Tg(CAG-cre/Esr1*)5Amc/J; CAGCre; *Srd5a3$^{fl/-}$*). *CAGCre;Srd5a3$^{fl/-}$* embryonic fibroblasts were isolated at E14.5 and immortalized by serial passaging as described by **Xu, 2005**. For *Srd5a3* recombination primary MEFs were treated for 4 days with tamoxifen (1 µM, H6278, Sigma) prior to immortalization. Efficient *Srd5a3* recombination was assessed by RT-qPCR after immortalization.

## Behavioral studies

For behavioral analysis, 15 *En1Cre; Srd5a3$^{fl/-}$* and 15 control littermates, gender-matched, 2 – 3 months old were used. The number of animals per group was chosen as the optimal number likely required for conclusion of statistical significance, established from prior experience using the same behavioral tests (**Pereira et al., 2009**). Morris water maze (MWM) test was used to assess working memory. Prior to the test, the mouse swimming speed was analyzed. No differences in the swimming speed were detected. For MWM, mice were exposed twice to the same hidden platform for a total of eight sessions. The average latency for each mouse is represented. The improvement to find the platform on the second trial was evaluated. For motor coordination, classic accelerating rotarod testing was done for 10 min and for a total of three sessions, 24 hr apart. The first three falls from the rod during each session were annotated. A statistical Grubbs test was performed to verify the absence of significant outliers in each group.

## Histological analysis

Gross anatomical analyses and HE staining were performed as previously described (**Akizu et al., 2013**). The resulting slices were scanned with NanoZoomer-XR (Hamamatsu Photonics, Japan). We evaluated the cerebellum size difference by measuring the vermis area from mid-sagittal sections (**Pogoriler et al., 2006**). We identified the midline by the absence of fastigial nucleus and cerebellar peduncles. A single midline section was used to calculate the area with ImageJ. For quantification of the surface occupied by the clusters and their distribution, two mice and one slice per region were quantified per genotype. For IHC, the cerebellum was embedded in OCT. 12µm-thick slices were generated with cryostat. The following antibodies were used for IHC: NeuN (1:200, MAB377; Millipore), Calbindin (1:10.000; CB-38A, Swant), GFAP (1:1.000; AB5804, Millipore), laminin (1:33, L9393, Sigma) and BiP (1:50, ADI-SPA-826, Enzo). All samples were mounted with ProLong Gold Antifade Mountant with DAPI (Life Tech). Images were taken with confocal Leica SP8 STED and analyzed with ImageJ.

## Protein extraction and western blotting

P7 mouse cerebellum samples and MEFs were isolated in RIPA buffer (1% SDS; 0,1% for cell extracts) supplemented with EDTA-free protease inhibitor (11836170001, Sigma) and phosphatase inhibitor cocktail (4906845001, Sigma), homogenized by sonication (Bioruptor Pico sonication device – 8 cycles 30''ON/30''OFF) and centrifuged at 12.000 g at 4°C for 20 min. The supernatant was recovered and quantified with BCA (Life technologies). For cell extracts, RIPA was added directly to the flask and the cells were recovered with a cell scrapper followed by the same protocol. Equal amounts of protein were loaded from each sample in polyacrylamide gels. Gel transfer to nitrocellulose membranes was performed with the Trans-Blot Turbo Transfer System for 10 min at 1.3A and 25V. Membranes were blocked with 5% dry milk and incubated O/N at 4°C with the following antibodies: LAMP1 (1:2.000; AB24170, Abcam), L1CAM (1:2.000; AB24345, Abcam), NrCAM (1:2.000; AB24344, Abcam) and β-actin (1:20.000; AM4302, Thermo Fisher). Depending on the antibody suitability, the membrane was developed by HRP system (LAMP1, ChemiDoc XRS + System) or with fluorescent secondary antibodies (Odyssey CLx imaging system). All secondary antibodies were used at 1:10000. For far-western blotting, no blocking step was performed, and the membrane was directly incubated for 1 hr with biotinylated SNA (1:2.000; B-1305, Vector laboratories) or ConA (1:2000; C2272, Sigma) and posteriorly with IRDye 800CW-streptavidin for 1 extra hour (1:10.000;

926 – 32,230, LI-COR). All mouse WB results were replicated at least three times with several litters. Far-western blots were repeated at least twice with several litters.

## RNA extraction, RT-PCR, RT-qPCR and transcriptomic analysis

RNA was extracted with Trizol reagent (15,596–026, Thermo Fisher) according to manufacturer's instructions. For transcriptomic studies, *En1Cre;Srda5a3$^{fl/-}$* P7 mice (n = 4) and control littermates (n = 4) were used. RNA quality was validated with Bioanalyzer 2100 (using Agilent RNA6000 nano chip kit) and 180 ng of total RNA were reverse transcribed using the GeneChip WT Plus Reagent Kit (Affymetrix). The resulting double strand cDNA was used for in vitro transcription with T7 RNA polymerase (WT cDNA synthesis and amplification kit, Affymetrix). After purification according to Affymetrix protocol, 5.5 ug of the cDNA obtained were fragmented and biotin-labelled using Terminal Transferase (WT terminal labelling kit, Affymetrix). cDNA was then hybridized to GeneChip Mouse Transcriptome Array 1.0 (MTA 1.0., Affymetrix) at 45°C for 17 hr. After O/N hybridization, chips were washed on the fluidic station FS450 following specific protocols (Affymetrix) and scanned using the GCS3000 7G. The scanned images were then analyzed with Expression Console software (Affymetrix) to obtain raw data (cel files) and metrics for Quality Controls. The observations of these metrics and the study of the distribution of raw data showed no outlier experiment. Robust multi-array average (RMA) normalization was obtained using R, and normalized data were subjected to statistical tests. For RT-PCR/RT-qPCR 1 µg of RNA was retrotranscribed into cDNA with SuperScript II reverse transcriptase (18064014, Thermo Fisher). qPCR was performed with PowerUp SYBR Green Master Mix (A25777, Thermo Fisher). The following primers were used: m*βActin* (F 5'-TACAGC TTCACCACCACAGC-3'; R 5'-AAGGAAGGCTGGAAAAGAGC-3') and m*Srd5a3* (F 5'-CCGGGCTA TGGCTGGGTGG-3' and R 5'-CTGTCTCAGTGCCTCTAGGAATGG-3').

## Total proteomics and glycoproteomics

P7 *En1Cre;Srd5a3$^{fl/-}$* (n = 4) and control (n = 4) littermates were used for total proteomics and the same number, but distinct mice, were used for glycoproteomics. The cerebellar protein extraction was performed as described above. For total proteomics, 100 µg of protein were processed by filter-aided sample preparation (FASP) protocol, as described previously (***Lipecka et al., 2016***). Briefly, samples were applied to 30 KDa MWCO centrifugal filter units (UFC503024, Amicon Ultra, Millipore) mixed with 200 uL of urea (UA) buffer (8M urea, 100 mM Tris-HCl pH 8.8) and centrifuged twice. The samples were incubated for 20 min in the dark with UA buffer containing 50 mM iodocetamide for alkylation. The filter units were subsequently washed twice with UA buffer and twice more with ABC buffer (50 mM ammonium bicarbonate). Peptide digestion was carried by incubation with trypsin (1:50) O/N at 37°C. The resulting peptides were collected by two washes with ABC buffer, vacuum dried and dissolved in 0.1% (v/v) trifluoroacetic acid with 10% acetonitrile.

Glycoproteome analysis was performed by FASP with an additional step of enrichment in N-glycopeptides by lectins, as described by M. Mann and colleagues (***Zielinska et al., 2010***). Briefly, 100 µg of trypsinized peptides were recovered in binding buffer (20 mM Tris/HCl pH 7.6, 1 mM $MnCl_2$, 1 mM $CaCl_2$, 0.5; NaCl) and incubated with a lectin mixture (90 µg ConA, 90 µg WGA and 71.5 µg $RCA_{120}$) for 1 hr. To elute the non-glycosylated peptides, not attached to the lectins, the filter units were washed four times with binding buffer and after with ABC solution in $H_2O_{18}$ (O188P, Eurositop). To release the N-glycopeptides from the lectins, the samples were incubated with PNGase diluted in $H_2O_{18}$ (P0704L, New England BioLabs) for 3 hr at 37°C. The N-glycopeptides were recovered by washing twice with ABC. All centrifugation steps were performed at 14.000 g at RT.

## LC-MS/MS analysis

For each run, estimated 0.5 µg were injected in a nanoRSLC-Q Exactive PLUS (Dionex RSLC Ultimate 3000, Thermo Scientific, Waltham, MA, USA). Peptides were separated on a 50 cm reversed-phase liquid chromatographic column (Pepmap C18, Dionex). Chromatography solvents were (A) 0.1% formic acid in water and (B) 80% acetonitrile, 0.08% formic acid. Peptides were eluted from the column with a linear gradient of 120 min from 5% A to 80% B followed by 27 min of column re-equilibration in 5% A. Two blanks, each with two 25 min-linear gradient, were run between samples to prevent carryover. Peptides eluting from the column were analyzed by data dependent MS/MS, using top-10 acquisition method. Briefly, the instrument settings were as follows: resolution was set to 70,000 for

MS scans and 17,500 for the data dependent MS/MS scans in order to increase speed. The MS AGC target was set to $3.10^6$counts with 200 ms for the injection time, while MS/MS AGC target was set to $1.10^5$ with 120 ms for the injection time. The MS scan range was from 400 to 2000 m/z. Dynamic exclusion was set to 30 s. All analyses were performed in technical triplicate for each biological replicate.

## Total proteomics and glycoproteomics data analysis

The MS files were processed with MaxQuant software version 1.5.8.3 and searched with Andromeda search engine against the mouse subset from the UniProtKB/Swiss-Prot complete proteome database (release 2016_06). Statistical analysis and logo extractions were performed using Perseus version 1.5.5.3. Different thresholds were applied to total proteomics and glycoproteomics analysis given that the intensity of several peptides in total proteomics is used for determining protein intensity, while a single peptide in glycoproteomics is analysed at the time. For total proteomics, only proteins detected in all eight samples (4 controls and four mutants) were retained for statistical analysis, avoiding all data imputation. For comparative glycoproteomics, we retained glycosites detected in at least 3 out of 4 control samples. Additionally, we selected proteins that were specifically detected in control or mutant samples by retaining proteins detected solely in at least 3 samples of one group. Both FDR and p-value (q-value <0,05, paired student t-test) was used for total proteomics, whereas the p-value (<0,05, unpaired student t-test) was used for N-glycopeptides. As a database for N-glycoproteins and number of N-glycosylation sites per protein (qualitative dataset, reference glycoproteomic dataset), the data obtained by glycoproteomics was used: any glycopeptide detected in at least two control samples was considered as potentially N-glycosylated (***Supplementary File 2***). Sites that were not previously described in Zielinska et al. or not predicted by uniprot were classified as likely novel N-glycosylation sites. Volcano plots were generated using the VolcanoShiny app (https://hardingnj.shinyapps.io/volcanoshiny/). PCA and variance analysis were done with the Partek Genomics Suite software. For homologous IgSF-CAM proteins (CNTNs, L1CAMs and NCAMs), HomoloGene and the study from Chen et al. (***Chen and Zhou, 2010***) were used.

## Granule cell culture

Cerebellar granule cells were isolated from P7 cerebellum following the Manzini and colleagues protocol(***Lee et al., 2009***). Cells were kept at 37°C in 24 or 48-well plates for at least 24 hr. To detect expression of proteins at the plasma membrane, the protocol published by Carrodus et al. was followed(***Carrodus et al., 2014***). The rat monoclonal anti-L1CAM antibody (557.B6; 1:100) has been described (***Appel et al., 1995***). The anti-NrCAM antibody was purchased from Abcam (AB24344, 1:400). For binding with L1CAM-Fc (10 µg/mL; 777-NC, R and D) and NrCAM-Fc chimeras (10 µg/mL; 2034-NR, R and D), the cells were incubated at 37°C with the chimeras for 4 hr and 10 min, respectively, in granule cell culture media. Both the cell surface protein expression and binding assays were repeated three times with biological replicates. For each experiment, at least 20 neurons per mice were analyzed. The differences measured between control and mutant cells and expressed as a percentage in the main text represent the average of all the repeated experiments. Quantification and normalization were performed using imageJ and Tuj1 staining. For tunicamycin treatment, the cells were incubated for 16 hr with 0.01 µg /mL tunicamycin in culture media prior ICC. For surface coating, 48 or 24-well plates were incubated at 4°C overnight with the coating solution, followed by 3 PBS washes, blocking for 30 min with BSA to inhibit non-specific binding (10 mg/mL) and three more PBS washes. The coatings used were: human recombinant L1CAM (10 µg/mL; 777-NC, R and D), human recombinant NrCAM (5 µg/mL; 2034-NR, R and D), fibronectin (50 µg/mL; F2006, Sigma) and Laminin and poly-D-Lysine (2 µg/mL and 30 µg/mL; 11243217001 and P6407, respectively, Sigma). Cell and neurite dynamics were measured every 3 hr by live cell imaging (Incucyte ZOOM with Neurotracker module, Essen Bioscience). Neurite branching points and neurite length were normalized to the total number of cell body clusters. As long as GCs do not arborize, the neurite branching points parameter provided by the Incucyte software was translated as neurite number. For GCs re-aggregates, cells were isolated and plated for 24 hr in un-coated surfaces ($2 \times 10^6$ cells/$cm^2$) to promote aggregation. The aggregates were then collected and seeded on the coated surface for 24 hr. Sholl analysis (using the ImageJ plugin) was performed to quantify the

aggregates' neurite number as the number of neurites crossing each circle. For migration analyses, the cells within the same circles used in Sholl analyses but the first circle, were counted (**Tanaka et al., 2004**). Five different aggregates were quantified per mouse and coating condition.

## Human-induced pluripotent stem cells (hiPSCs) *SRD5A3*$^{-/-}$ generation and culture

iPSCs were derived from hPBMCs from a control male donor via Cyto-Tune Sendai virus reprogramming. Cells were cultured at 37°C on vitronectin-coated (10 µg/mL; 07180, Stem Cell) dishes with mTeSR media (Stem Cell). *SRD5A3* KO hiPSCs clones were generated by CRISPR/Cas9. sgRNA (inserted into a GFP-containing PX458 plasmid, Addgene) targeting the first exon of the gene were generated via the CRISPOR website and validated in T293 HEK cells by Sanger sequencing combined with tides analysis (https://tide-calculator.nki.nl/; data not shown). hiPSCs were transfected by nucleofection (Amaxa 4D, Lonza) and transfected cells (GFP+) were isolated by FACs (BD FACSAria II SORP, BD Biosciences) to generate single-cell-of-origin colonies. DNA was extracted from a piece of each colony by ZR-Duet DNA MiniPrep (D7003, Zymo) and sequenced. After selection, SOX2 (1:2000; AB5603, Millipore) and OCT4 (1:100; SC5279, Santa Cruz) immunostaining was used to confirm pluripotency (***Figure 5—figure supplement 2***). No major chromosomal abnormalities were detected by CGH array (60K, data not shown).

## hiPSCs differentiation towards late cortical progenitors (LCPs)

Differentiation of hiPSCs towards LCPs and cortical projection neurons (CPNs) was carried as described by Benchoua and colleagues (**Boissart et al., 2013**). Briefly, iPSCs colonies were transferred to a non-coated dish with neural induction media (N2B27 with FGF2 and double SMAD inhibition by SB431542 and LDN193189, Stem Cell) for 6 hr and were afterwards transferred onto poly-ornithine and laminincoated dishes. Following neural rosette formation (12 – 15 days), the cells were passaged onto a geltrex-coated (A1413301, Life Tech) flask (LCPs P1) and were further cultured with N2B27 supplemented with FGF2, EGF and BDNF (Stem Cell). SOX2 and Nestin (1:250; N5413, Sigma) staining confirmed LCPs multipotency. Neuroectodermal origin of the emerging neural progenitor-like cells was assessed by HNK1/P75 FACs staining (data not shown). LCPs were further differentiated towards CPNs by growth factor withdrawal for 15 days. Neuronal identity was assessed with Tuj1 (1:2000; T2200, Sigma) staining (data not shown). WB results were replicated with two different clones of control and *SRD5A3* mutant hiPSCs.

## Electronic microscopy experiments

P21 *En1Cre; Srd5a3*$^{fl/-}$ (n = 1), *Atoh1Cre; Srd5a3*$^{fl/-}$ (n = 2) and control littermates (n = 3) were perfused with 4% PFA/2% glutaraldehyde. The cerebellum was kept in the same solution for at least one week. Sagittal slices, less than 1 mm thick, were post-fixed with 1% osmium tetroxide in 0.1 M phosphate buffer and then dehydrated in ethanol. After 10 min in a 1:2 mixture of epoxy propane and epoxy resin and 10 min in epon, samples were covered by upside down gelatin capsules filled with freshly prepared epoxy resin and polymerized at 60°C for 24 hr. After heat separation, ultrathin sections of 90 nm were cut with an ultra-microtome (Reichert ultracut S), stained with uranyl acetate and Reynold's lead and observed with a transmission electron microscope (JEOL 1011). Acquisition was performed with a Gatan Orius 1000 CCD camera.

## Statistics

For mouse experiments, no statistical methods were used to predetermine sample size. No animals or samples were excluded from the analysis. All mouse experiments included at least two different litters. For mouse behavioral analysis, one way ANOVA was used. Regular enrichment analyses were performed by Fisher exact test (significance 0.05). For multiplicity and NxS motif correlation, the Pearson coefficient was used. For enrichment in highly N-glycosylated proteins, two-tailed Mann-Whitney test was performed. Statistical differences between groups were assessed by two-tailed student t-test. For all statistical tests, confidence intervals were set at 95%. All results are presented in mean value and standard deviation was used to calculate the error bars.

### Data availability

Full transcriptomic data is publicly available at ArrayExpress (accession no. E-MTAB-6861). Total proteomics and glycoproteomics data are available via ProteomeXchange with identifier PXD009906.

## Acknowledgements

We thank JG Gleeson for the support to generate *Srd5a3* conditional mouse and helpful advices. We are grateful to L Goutebroze, F Francis, N Altin, K Siquier, K Radjamani for valuable discussions or technical help. The project is funded by the French National Research Agency ANR-16-CE12-0005-01 (VC), la Fondation pour la Recherche Médicale FRM-DEQ20160334938 (LC), the association Connaître les Syndromes Cérébelleux CSC (VC), the program ERA-NET 643578-EURO-CDG2 and E-Rare-3 (FF and CT), Paris Descartes University BioSPC program (DM-C), Imagine Foundation (DM-C), Imagine International PhD program with Bettencourt-Schueller-foundation (EU). We thank Cochin genomic (GENOM'IC), electron microscopy core facilities and the Imagine animal facilities (LEAT) for services and support. We also thank the Animal Histology and Morphology Core Facility of SFR Necker (Inserm US24). We also thank L. Legeai-Mallet and C Colnot for providing the CMV-Cre and the Rosa26-LacZ mouse, respectively and Nicolas Cagnard for statistical advice.

## Additional information

### Funding


| Funder | Grant reference number | Author |
|---|---|---|
| Université Paris Descartes | BioSPC program | Daniel Medina-Cano |
| European Commission | ERA-NET 643578-EURO-CDG2 | Christian Thiel<br>Francois Foulquier |
| European Commission | ERA-NET E-Rare-3 | Christian Thiel<br>Francois Foulquier |
| Fondation pour la Recherche Médicale | FRM-DEQ20160334938 | Laurence Colleaux |
| Agence Nationale de la Recherche | ANR-16-CE12- 0005-01 | Vincent Cantagrel |
| Association Connaître les Syndromes Cérébelleux | | Vincent Cantagrel |

The funders had no role in study design, data collection and interpretation, or the decision to submit the work for publication.


### Author contributions

Daniel Medina-Cano, Data curation, Formal analysis, Validation, Investigation, Visualization, Methodology, Writing—original draft; Ekin Ucuncu, Data curation, Formal analysis, Methodology; Lam Son Nguyen, Joanna Lipecka, Christian Thiel, Formal analysis, Methodology; Michael Nicouleau, Data curation, Formal analysis; Jean-Charles Bizot, Data curation, Formal analysis, Supervision; Francois Foulquier, Data curation, Investigation; Nathalie Lefort, Formal analysis; Catherine Faivre-Sarrailh, Conceptualization, Resources, Supervision, Methodology, Writing—review and editing; Laurence Colleaux, Formal analysis, Funding acquisition, Project administration, Writing—review and editing; Chiara Guerrera, Resources, Data curation, Formal analysis, Supervision, Visualization, Methodology; Vincent Cantagrel, Conceptualization, Formal analysis, Supervision, Funding acquisition, Validation, Investigation, Methodology, Writing—original draft, Writing—review and editing

### Author ORCIDs

Vincent Cantagrel https://orcid.org/0000-0002-5180-4848

### Ethics

Human subjects: Primary human mononuclear cells were isolated from peripheral blood and were obtained using Institutional Review Board-approved consent forms. Induced human pluripotent stem

cells protocols, samples collection and storage were approved by the French research ministry, identification DC 2015-2595 obtained on Sept-05 2016.
Animal experimentation: In this study, animals were used in compliance with the French Animal Care and Use Committee from the Paris Descartes University (APAFIS#961-201506231137361). All behavioural analysis were performed in compliance with the guidelines of the French Ministry of Agriculture for experiments with laboratory animals. The experimental protocol and euthanasia have been approved by the Ethical Committee 27, registered at the French ministry of research.

### Decision letter and Author response

Decision letter https://doi.org/10.7554/eLife.38309.026
Author response https://doi.org/10.7554/eLife.38309.027

## Additional files

### Supplementary files

- Supplementary file 1. Total proteomics. Normalized and log2 transformed intensities of the 1982 proteins detected by total proteomics and their relative abundance levels in the En1-Cre; *Srd5a3*$^{fl/-}$ mutant cerebellum.

DOI: https://doi.org/10.7554/eLife.38309.017

- Supplementary file 2. Glycoproteomics. All of the N-glycosylation sites detected in at least 2 out of 4 control samples are included and classified based on their presence in PMID: 20510933 or if they are predicted by uniprot (reference glycoproteomic dataset, spread sheet 1). Sequon analyses on the 1665 N-glycopeptides within the glycoproteomic dataset (spread sheet 2). Gene ontology analyses on the N-glycosylation sites within the reference glycoproteomic dataset predicted by uniprot and/or found in PMID: 20510933 and on the N-glycosylation sites not present in none of them (novel sites, spread sheet 3). 1404 N-glycopeptides detected in at least 3 out of 4 control samples and their corresponding abundance levels in the mutant samples; the intensity for each N-glycopeptide are log2 transformed (comparative glycoproteomics, spread sheet 4). Sequon analyses on the comparative glycoproteomics dataset (spread sheet 5).

DOI: https://doi.org/10.7554/eLife.38309.018

- Supplementary file 3. Total proteomics and glycoproteomics. List, normalized intensities and relative abundance of the 24 peptides detected in total proteomics and with decreased abundance in glycoproteomics in the mutant.

DOI: https://doi.org/10.7554/eLife.38309.019

- Transparent reporting form

DOI: https://doi.org/10.7554/eLife.38309.020

### Data availability

Expression microarray data are publicly available at ArrayExpress accession number E-MTAB-6861. Proteomics and Glycoproteomics data are included within supplementary files 1, 2 and 3 and full proteomics and glycoproteomics data are available via ProteomeXchange with identifier PXD009906.

The following datasets were generated:

| Author(s) | Year | Dataset title | Dataset URL | Database, license, and accessibility information |
|---|---|---|---|---|
| Medina-Cano D, Lipecka J, Guerrera IC, Cantagrel V | 2018 | GlycoProteomics in CDG (congenital disorder of glycosylation) | https://www.ebi.ac.uk/pride/archive/login | PXD009906 |
| Medina-Cano D., Cantagrel V. | 2018 | Transcriptomic analysis of the developing cerebellum in a mouse model for SRD5A3-CDG | https://www.ebi.ac.uk/arrayexpress/experiments/E-MTAB-6861/ | E-MTAB-6861 |

## References


**Agrawal P**, Fontanals-Cirera B, Sokolova E, Jacob S, Vaiana CA, Argibay D, Davalos V, McDermott M, Nayak S, Darvishian F, Castillo M, Ueberheide B, Osman I, Fenyö D, Mahal LK, Hernando E. 2017. A systems biology approach identifies FUT8 as a driver of melanoma metastasis. *Cancer Cell* **31**:804–819. DOI: https://doi.org/10.1016/j.ccell.2017.05.007, PMID: 28609658

**Akizu N**, Cantagrel V, Schroth J, Cai N, Vaux K, McCloskey D, Naviaux RK, Van Vleet J, Fenstermaker AG, Silhavy JL, Scheliga JS, Toyama K, Morisaki H, Sonmez FM, Celep F, Oraby A, Zaki MS, Al-Baradie R, Faqeih EA, Saleh MA, et al. 2013. AMPD2 regulates GTP synthesis and is mutated in a potentially treatable neurodegenerative brainstem disorder. *Cell* **154**:505–517. DOI: https://doi.org/10.1016/j.cell.2013.07.005, PMID: 23911318

**Appel F**, Holm J, Conscience JF, von Bohlen und Halbach F, Faissner A, James P, Schachner M. 1995. Identification of the border between fibronectin type III homologous repeats 2 and 3 of the neural cell adhesion molecule L1 as a neurite outgrowth promoting and signal transducing domain. *Journal of Neurobiology* **28**:297–312. DOI: https://doi.org/10.1002/neu.480280304, PMID: 8568512

**Berglund EO**, Murai KK, Fredette B, Sekerková G, Marturano B, Weber L, Mugnaini E, Ranscht B. 1999. Ataxia and abnormal cerebellar microorganization in mice with ablated contactin gene expression. *Neuron* **24**:739–750. DOI: https://doi.org/10.1016/S0896-6273(00)81126-5, PMID: 10595523

**Bizzoca A**, Virgintino D, Lorusso L, Buttiglione M, Yoshida L, Polizzi A, Tattoli M, Cagiano R, Rossi F, Kozlov S, Furley A, Gennarini G. 2003. Transgenic mice expressing F3/contactin from the TAG-1 promoter exhibit developmentally regulated changes in the differentiation of cerebellar neurons. *Development* **130**:29–43. DOI: https://doi.org/10.1242/dev.00183, PMID: 12441289

**Blank C**, Smith LA, Hammer DA, Fehrenbach M, Delisser HM, Perez E, Sullivan KE. 2006. Recurrent infections and immunological dysfunction in congenital disorder of glycosylation Ia (CDG Ia). *Journal of Inherited Metabolic Disease* **29**:592. DOI: https://doi.org/10.1007/s10545-006-0275-2, PMID: 16826448

**Boissart C**, Poulet A, Georges P, Darville H, Julita E, Delorme R, Bourgeron T, Peschanski M, Benchoua A. 2013. Differentiation from human pluripotent stem cells of cortical neurons of the superficial layers amenable to psychiatric disease modeling and high-throughput drug screening. *Translational Psychiatry* **3**:e294. DOI: https://doi.org/10.1038/tp.2013.71, PMID: 23962924

**Burda P**, Aebi M. 1999. The dolichol pathway of N-linked glycosylation. *Biochimica et Biophysica Acta (BBA) - General Subjects* **1426**:239–257. DOI: https://doi.org/10.1016/S0304-4165(98)00127-5, PMID: 9878760

**Cantagrel V**, Lefeber DJ, Ng BG, Guan Z, Silhavy JL, Bielas SL, Lehle L, Hombauer H, Adamowicz M, Swiezewska E, De Brouwer AP, Blümel P, Sykut-Cegielska J, Houliston S, Swistun D, Ali BR, Dobyns WB, Babovic-Vuksanovic D, van Bokhoven H, Wevers RA, et al. 2010. SRD5A3 is required for converting polyprenol to dolichol and is mutated in a congenital glycosylation disorder. *Cell* **142**:203–217. DOI: https://doi.org/10.1016/j.cell.2010.06.001, PMID: 20637498

**Cantagrel V**, Lefeber DJ. 2011. From glycosylation disorders to dolichol biosynthesis defects: a new class of metabolic diseases. *Journal of Inherited Metabolic Disease* **34**:859–867. DOI: https://doi.org/10.1007/s10545-011-9301-0, PMID: 21384228

**Cao J**, Guo S, Arai K, Lo EH, Ning M. 2013. Studying extracellular signaling utilizing a glycoproteomic approach: lectin blot surveys, a first and important step. *Methods in Molecular Biology* **1013**:227–233. DOI: https://doi.org/10.1007/978-1-62703-426-5_15, PMID: 23625503

**Carrodus NL**, Teng KS-L, Munro KM, Kennedy MJ, Gunnersen JM. 2014. Differential labeling of Cell-surface and internalized proteins after antibody feeding of live cultured neurons. *Journal of Visualized Experiments* **84**: e51139. DOI: https://doi.org/10.3791/51139

**Chan B**, Clasquin M, Smolen GA, Histen G, Powe J, Chen Y, Lin Z, Lu C, Liu Y, Cang Y, Yan Z, Xia Y, Thompson R, Singleton C, Dorsch M, Silverman L, Su SM, Freeze HH, Jin S. 2016. A mouse model of a human congenital disorder of glycosylation caused by loss of PMM2. *Human Molecular Genetics* **25**:2182–2193. DOI: https://doi.org/10.1093/hmg/ddw085, PMID: 27053713

**Chavan M**, Lennarz W. 2006. The molecular basis of coupling of translocation and N-glycosylation. *Trends in Biochemical Sciences* **31**:17–20. DOI: https://doi.org/10.1016/j.tibs.2005.11.010, PMID: 16356726

**Chen L**, Zhou S. 2010. "CRASH"ing with the worm: insights into L1CAM functions and mechanisms. *Developmental Dynamics : An Official Publication of the American Association of Anatomists* **239**:1490–1501. DOI: https://doi.org/10.1002/dvdy.22269, PMID: 20225255

**Cherepanova NA**, Gilmore R. 2016. Mammalian cells lacking either the cotranslational or posttranslocational oligosaccharyltransferase complex display substrate-dependent defects in asparagine linked glycosylation. *Scientific Reports* **6**:20946. DOI: https://doi.org/10.1038/srep20946, PMID: 26864433

**Cline A**, Gao N, Flanagan-Steet H, Sharma V, Rosa S, Sonon R, Azadi P, Sadler KC, Freeze HH, Lehrman MA, Steet R. 2012. A zebrafish model of PMM2-CDG reveals altered neurogenesis and a substrate-accumulation mechanism for N-linked glycosylation deficiency. *Molecular Biology of the Cell* **23**:4175–4187. DOI: https://doi.org/10.1091/mbc.e12-05-0411, PMID: 22956764

**Çolakoğlu G**, Bergstrom-Tyrberg U, Berglund EO, Ranscht B. 2014. Contactin-1 regulates myelination and nodal/paranodal domain organization in the central nervous system. *PNAS* **111**:E394–E403. DOI: https://doi.org/10.1073/pnas.1313769110, PMID: 24385581

**Dahmane N**, Ruiz i Altaba A. 1999. Sonic hedgehog regulates the growth and patterning of the cerebellum. *Development* **126**:3089–3100. PMID: 10375501

**Demyanenko GP**, Tsai AY, Maness PF. 1999. Abnormalities in neuronal process extension, hippocampal development, and the ventricular system of L1 knockout mice. *The Journal of Neuroscience* **19**:4907–4920. DOI: https://doi.org/10.1523/JNEUROSCI.19-12-04907.1999, PMID: 10366625

**Demyanenko GP**, Riday TT, Tran TS, Dalal J, Darnell EP, Brennaman LH, Sakurai T, Grumet M, Philpot BD, Maness PF. 2011. NrCAM deletion causes topographic mistargeting of thalamocortical axons to the visual cortex and disrupts visual acuity. *Journal of Neuroscience* **31**:1545–1558. DOI: https://doi.org/10.1523/JNEUROSCI.4467-10.2011, PMID: 21273439

**Dennis JW**, Nabi IR, Demetriou M. 2009. Metabolism, cell surface organization, and disease. *Cell* **139**:1229–1241. DOI: https://doi.org/10.1016/j.cell.2009.12.008, PMID: 20064370

**Dequidt C**, Danglot L, Alberts P, Galli T, Choquet D, Thoumine O. 2007. Fast turnover of L1 adhesions in neuronal growth cones involving both surface diffusion and exo/endocytosis of L1 molecules. *Molecular Biology of the Cell* **18**:3131–3143. DOI: https://doi.org/10.1091/mbc.e06-12-1101, PMID: 17538021

**Falk J**, Bonnon C, Girault JA, Faivre-Sarrailh C. 2002. F3/contactin, a neuronal cell adhesion molecule implicated in axogenesis and myelination. *Biology of the Cell* **94**:327–334. DOI: https://doi.org/10.1016/S0248-4900(02)00006-0, PMID: 12500940

**Fransen E**, D'Hooge R, Van Camp G, Verhoye M, Sijbers J, Reyniers E, Soriano P, Kamiguchi H, Willemsen R, Koekkoek SK, De Zeeuw CI, De Deyn PP, Van der Linden A, Lemmon V, Kooy RF, Willems PJ. 1998. L1 knockout mice show dilated ventricles, vermis hypoplasia and impaired exploration patterns. *Human Molecular Genetics* **7**:999–1009. DOI: https://doi.org/10.1093/hmg/7.6.999, PMID: 9580664

**Freeze HH**, Chong JX , Bamshad MJ, Ng BG . 2014. Solving glycosylation disorders: fundamental approaches reveal complicated pathways. *The American Journal of Human Genetics* **94**:161–175. DOI: https://doi.org/10.1016/j.ajhg.2013.10.024, PMID: 24507773

**Freeze HH**, Eklund EA, Ng BG, Patterson MC. 2015a. Neurological aspects of human glycosylation disorders. *Annual Review of Neuroscience* **38**:105–125. DOI: https://doi.org/10.1146/annurev-neuro-071714-034019, PMID: 25840006

**Freeze HH**, Schachter H, Kinoshita T. 2015b. Genetic Disorders of Glycosylation. In: rd A, Varki R. D, Cummings J. D, Esko P, Stanley G. W, Hart M, Aebi A. G, Darvill T, Kinoshita N. H, Packer J. H, Prestegard R. L. S. chnaar, Seeberger P. H (Eds). *Essentials of Glycobiology*. Cold Spring Harbor. p. 569–582.

**Fujimori T**, Suno R, Iemura SI, Natsume T, Wada I, Hosokawa N. 2017. Endoplasmic reticulum proteins SDF2 and SDF2L1 act as components of the BiP chaperone cycle to prevent protein aggregation. *Genes to Cells* **22**:684–698. DOI: https://doi.org/10.1111/gtc.12506, PMID: 28597544

**Gavel Y**, Heijne Gvon. 1990. Sequence differences between glycosylated and non-glycosylated Asn-X-Thr/Ser acceptor sites: implications for protein engineering. *"Protein Engineering, Design and Selection"* **3**:433–442. DOI: https://doi.org/10.1093/protein/3.5.433

**Gründahl JE**, Guan Z, Rust S, Reunert J, Müller B, Du Chesne , Zerres K, Rudnik-Schöneborn S, Ortiz-Brüchle N, Häusler MG, Siedlecka J, Swiezewska E, Raetz CR, Marquardt T. 2012. Life with too much polyprenol: polyprenol reductase deficiency. *Molecular Genetics and Metabolism* **105**:642–651. DOI: https://doi.org/10.1016/j.ymgme.2011.12.017, PMID: 22304929

**Haeuptle MA**, Welti M, Troxler H, Hülsmeier AJ, Imbach T, Hennet T. 2011. Improvement of dolichol-linked oligosaccharide biosynthesis by the squalene synthase inhibitor zaragozic acid. *Journal of Biological Chemistry* **286**:6085–6091. DOI: https://doi.org/10.1074/jbc.M110.165795, PMID: 21183681

**He P**, Ng BG, Losfeld ME, Zhu W, Freeze HH. 2012. Identification of intercellular cell adhesion molecule 1 (ICAM-1) as a hypoglycosylation marker in congenital disorders of glycosylation cells. *Journal of Biological Chemistry* **287**:18210–18217. DOI: https://doi.org/10.1074/jbc.M112.355677, PMID: 22496445

**He P**, Srikrishna G, Freeze HH. 2014. N-glycosylation deficiency reduces ICAM-1 induction and impairs inflammatory response. *Glycobiology* **24**:392–398. DOI: https://doi.org/10.1093/glycob/cwu006, PMID: 24474243

**Horstkorte R**, Schachner M, Magyar JP, Vorherr T, Schmitz B. 1993. The fourth immunoglobulin-like domain of NCAM contains a carbohydrate recognition domain for oligomannosidic glycans implicated in association with L1 and neurite outgrowth. *The Journal of Cell Biology* **121**:1409–1421. DOI: https://doi.org/10.1083/jcb.121.6.1409, PMID: 8509458

**Hortsch M**. 2000. Structural and functional evolution of the L1 family: are four adhesion molecules better than one? *Molecular and Cellular Neuroscience* **15**:1–10. DOI: https://doi.org/10.1006/mcne.1999.0809, PMID: 10662501

**Hülsmeier AJ**, Paesold-Burda P, Hennet T. 2007. N-glycosylation site occupancy in serum glycoproteins using multiple reaction monitoring liquid chromatography-mass spectrometry. *Molecular & Cellular Proteomics* **6**:2132–2138. DOI: https://doi.org/10.1074/mcp.M700361-MCP200, PMID: 17823199

**Jaeken J**, Péanne R. 2017. What is new in CDG? *Journal of Inherited Metabolic Disease* **40**:569–586. DOI: https://doi.org/10.1007/s10545-017-0050-6, PMID: 28484880

**Kara B**, Ayhan Ö, Gökçay G, Başboğaoğlu N, Tolun A. 2014. Adult phenotype and further phenotypic variability in SRD5A3-CDG. *BMC Medical Genetics* **15**:10. DOI: https://doi.org/10.1186/1471-2350-15-10, PMID: 24433453

**Katic J**, Loers G, Kleene R, Karl N, Schmidt C, Buck F, Zmijewski JW, Jakovcevski I, Preissner KT, Schachner M. 2014. Interaction of the cell adhesion molecule CHL1 with vitronectin, integrins, and the plasminogen activator inhibitor-2 promotes CHL1-induced neurite outgrowth and neuronal migration. *Journal of Neuroscience* **34**:14606–14623. DOI: https://doi.org/10.1523/JNEUROSCI.3280-13.2014, PMID: 25355214

**Kerjan G**, Dolan J, Haumaitre C, Schneider-Maunoury S, Fujisawa H, Mitchell KJ, Chédotal A. 2005. The transmembrane semaphorin Sema6A controls cerebellar granule cell migration. *Nature Neuroscience* **8**:1516–1524. DOI: https://doi.org/10.1038/nn1555, PMID: 16205717

**Kiefel H**, Bondong S, Hazin J, Ridinger J, Schirmer U, Riedle S, Altevogt P. 2012. L1CAM: a Major driver for tumor cell invasion and motility. *Cell Adhesion & Migration* **6**:374–384. DOI: https://doi.org/10.4161/cam.20832, PMID: 22796939

**Koziol LF**, Budding D, Andreasen N, D'Arrigo S, Bulgheroni S, Imamizu H, Ito M, Manto M, Marvel C, Parker K, Pezzulo G, Ramnani N, Riva D, Schmahmann J, Vandervert L, Yamazaki T. 2014. Consensus paper: the cerebellum's role in movement and cognition. *The Cerebellum* **13**:151–177. DOI: https://doi.org/10.1007/s12311-013-0511-x, PMID: 23996631

**Kretzer NM**, Theisen DJ, Tussiwand R, Briseño CG, Grajales-Reyes GE, Wu X, Durai V, Albring J, Bagadia P, Murphy TL, Murphy KM. 2016. RAB43 facilitates cross-presentation of cell-associated antigens by CD8α+ dendritic cells. *The Journal of Experimental Medicine* **213**:2871–2883. DOI: https://doi.org/10.1084/jem.20160597, PMID: 27899443

**Lau KS**, Partridge EA, Grigorian A, Silvescu CI, Reinhold VN, Demetriou M, Dennis JW. 2007. Complex N-glycan number and degree of branching cooperate to regulate cell proliferation and differentiation. *Cell* **129**:123–134. DOI: https://doi.org/10.1016/j.cell.2007.01.049, PMID: 17418791

**Lee HY**, Greene LA, Mason CA, Manzini MC. 2009. Isolation and culture of Post-Natal mouse cerebellar granule neuron progenitor cells and neurons. *Journal of Visualized Experiments* **23**. DOI: https://doi.org/10.3791/990

**Lieberoth A**, Splittstoesser F, Katagihallimath N, Jakovcevski I, Loers G, Ranscht B, Karagogeos D, Schachner M, Kleene R. 2009. Lewis(x) and alpha2,3-sialyl glycans and their receptors TAG-1, Contactin, and L1 mediate CD24-dependent neurite outgrowth. *Journal of Neuroscience* **29**:6677–6690. DOI: https://doi.org/10.1523/JNEUROSCI.4361-08.2009, PMID: 19458237

**Lipecka J**, Chhuon C, Bourderioux M, Bessard MA, van Endert P, Edelman A, Guerrera IC. 2016. Sensitivity of mass spectrometry analysis depends on the shape of the filtration unit used for filter aided sample preparation (FASP). *Proteomics* **16**:1852–1857. DOI: https://doi.org/10.1002/pmic.201600103, PMID: 27219663

**Lutz D**, Loers G, Kleene R, Oezen I, Kataria H, Katagihallimath N, Braren I, Harauz G, Schachner M. 2014. Myelin basic protein cleaves cell adhesion molecule L1 and promotes neuritogenesis and cell survival. *Journal of Biological Chemistry* **289**:13503–13518. DOI: https://doi.org/10.1074/jbc.M113.530238, PMID: 24671420

**Maness PF**, Schachner M. 2007. Neural recognition molecules of the immunoglobulin superfamily: signaling transducers of axon guidance and neuronal migration. *Nature Neuroscience* **10**:19–26. DOI: https://doi.org/10.1038/nn1827, PMID: 17189949

**Matei V**, Pauley S, Kaing S, Rowitch D, Beisel KW, Morris K, Feng F, Jones K, Lee J, Fritzsch B. 2005. Smaller inner ear sensory epithelia in Neurog 1 null mice are related to earlier hair cell cycle exit. *Developmental Dynamics* **234**:633–650. DOI: https://doi.org/10.1002/dvdy.20551, PMID: 16145671

**Metzger D**, Clifford J, Chiba H, Chambon P. 1995. Conditional site-specific recombination in mammalian cells using a ligand-dependent chimeric Cre recombinase. *PNAS* **92**:6991–6995. DOI: https://doi.org/10.1073/pnas.92.15.6991, PMID: 7624356

**Morava E**, Wosik HN, Sykut-Cegielska J, Adamowicz M, Guillard M, Wevers RA, Lefeber DJ, Cruysberg JR. 2009. Ophthalmological abnormalities in children with congenital disorders of glycosylation type I. *British Journal of Ophthalmology* **93**:350–354. DOI: https://doi.org/10.1136/bjo.2008.145359, PMID: 19019927

**Morava E**, Wevers RA, Cantagrel V, Hoefsloot LH, Al-Gazali L, Schoots J, van Rooij A, Huijben K, van Ravenswaaij-Arts CM, Jongmans MC, Sykut-Cegielska J, Hoffmann GF, Bluemel P, Adamowicz M, van Reeuwijk J, Ng BG, Bergman JE, van Bokhoven H, Körner C, Babovic-Vuksanovic D, et al. 2010. A novel cerebello-ocular syndrome with abnormal glycosylation due to abnormalities in dolichol metabolism. *Brain* **133**:3210–3220. DOI: https://doi.org/10.1093/brain/awq261, PMID: 20852264

**Murray AN**, Chen W, Antonopoulos A, Hanson SR, Wiseman RL, Dell A, Haslam SM, Powers DL, Powers ET, Kelly JW. 2015. Enhanced aromatic sequons increase oligosaccharyltransferase glycosylation efficiency and glycan homogeneity. *Chemistry & Biology* **22**:1052–1062. DOI: https://doi.org/10.1016/j.chembiol.2015.06.017, PMID: 26190824

**Ng BG**, Freeze HH. 2018. Perspectives on glycosylation and its congenital disorders. *Trends in Genetics : TIG* **34**:466–476. DOI: https://doi.org/10.1016/j.tig.2018.03.002, PMID: 29606283

**Nguyen H**, Ostendorf AP, Satz JS, Westra S, Ross-Barta SE, Campbell KP, Moore SA. 2013. Glial scaffold required for cerebellar granule cell migration is dependent on dystroglycan function as a receptor for basement membrane proteins. *Acta Neuropathologica Communications* **1**:58. DOI: https://doi.org/10.1186/2051-5960-1-58, PMID: 24252195

**Park EJ**, Grabińska KA, Guan Z, Stránecký V, Hartmannová H, Hodaňová K, Barešová V, Sovová J, Jozsef L, Ondrušková N, Hansíková H, Honzík T, Zeman J, Hůlková H, Wen R, Kmoch S, Sessa WC. 2014. Mutation of Nogo-B receptor, a subunit of cis-prenyltransferase, causes a congenital disorder of glycosylation. *Cell Metabolism* **20**:448–457. DOI: https://doi.org/10.1016/j.cmet.2014.06.016, PMID: 25066056

**Pereira PL**, Magnol L, Sahún I, Brault V, Duchon A, Prandini P, Gruart A, Bizot JC, Chadefaux-Vekemans B, Deutsch S, Trovero F, Delgado-García JM, Antonarakis SE, Dierssen M, Herault Y. 2009. A new mouse model for the trisomy of the Abcg1-U2af1 region reveals the complexity of the combinatorial genetic code of down syndrome. *Human Molecular Genetics* **18**:4756–4769. DOI: https://doi.org/10.1093/hmg/ddp438, PMID: 19783846

**Pogoriler J**, Millen K, Utset M, Du W. 2006. Loss of cyclin D1 impairs cerebellar development and suppresses medulloblastoma formation. *Development* **133**:3929–3937. DOI: https://doi.org/10.1242/dev.02556, PMID: 16943274

**Poljak K**, Selevsek N, Ngwa E, Grossmann J, Losfeld ME, Aebi M. 2018. Quantitative profiling of N-linked glycosylation machinery in yeast *Saccharomyces cerevisiae*. *Molecular & Cellular Proteomics* **17**:18–30. DOI: https://doi.org/10.1074/mcp.RA117.000096, PMID: 28993419

**Pollerberg GE**, Thelen K, Theiss MO, Hochlehnert BC. 2013. The role of cell adhesion molecules for navigating axons: density matters. *Mechanisms of Development* **130**:359–372. DOI: https://doi.org/10.1016/j.mod.2012.11.002, PMID: 23183391

**Richard E**, Vega AI, Pérez B, Roche C, Velázquez R, Ugarte M, Pérez-Cerdá C. 2009. Congenital disorder of glycosylation Ia: new differentially expressed proteins identified by 2-DE. *Biochemical and Biophysical Research Communications* **379**:267–271. DOI: https://doi.org/10.1016/j.bbrc.2008.12.036, PMID: 19101518

**Ron D**, Walter P. 2007. Signal integration in the endoplasmic reticulum unfolded protein response. *Nature Reviews Molecular Cell Biology* **8**:519–529. DOI: https://doi.org/10.1038/nrm2199, PMID: 17565364

**Rujano MA**, Cannata Serio M, Panasyuk G, Péanne R, Reunert J, Rymen D, Hauser V, Park JH, Freisinger P, Souche E, Guida MC, Maier EM, Wada Y, Jäger S, Krogan NJ, Kretz O, Nobre S, Garcia P, Quelhas D, Bird TD, et al. 2017. Mutations in the X-linked *ATP6AP2* cause a glycosylation disorder with autophagic defects. *The Journal of Experimental Medicine* **214**:3707–3729. DOI: https://doi.org/10.1084/jem.20170453, PMID: 29127204

**Sakurai T**, Lustig M, Babiarz J, Furley AJ, Tait S, Brophy PJ, Brown SA, Brown LY, Mason CA, Grumet M. 2001. Overlapping functions of the cell adhesion molecules Nr-CAM and L1 in cerebellar granule cell development. *The Journal of Cell Biology* **154**:1259–1274. DOI: https://doi.org/10.1083/jcb.200104122, PMID: 11564762

**Schiff M**, Roda C, Monin ML, Arion A, Barth M, Bednarek N, Bidet M, Bloch C, Boddaert N, Borgel D, Brassier A, Brice A, Bruneel A, Buissonnière R, Chabrol B, Chevalier MC, Cormier-Daire V, De Barace C, De Maistre E, De Saint-Martin A, et al. 2017. Clinical, laboratory and molecular findings and long-term follow-up data in 96 French patients with PMM2-CDG (phosphomannomutase 2-congenital disorder of glycosylation) and review of the literature. *Journal of Medical Genetics* **54**:843–851. DOI: https://doi.org/10.1136/jmedgenet-2017-104903, PMID: 28954837

**Schwarz V**, Pan J, Voltmer-Irsch S, Hutter H. 2009. IgCAMs redundantly control axon navigation in Caenorhabditis elegans. *Neural Development* **4**:13. DOI: https://doi.org/10.1186/1749-8104-4-13, PMID: 19341471

**Scott H**, Panin VM. 2014a. N-glycosylation in regulation of the nervous system. *Advances in Neurobiology* **9**:367–394. DOI: https://doi.org/10.1007/978-1-4939-1154-7_17, PMID: 25151388

**Scott H**, Panin VM. 2014b. The role of protein N-glycosylation in neural transmission. *Glycobiology* **24**:407–417. DOI: https://doi.org/10.1093/glycob/cwu015, PMID: 24643084

**Sgaier SK**, Lao Z, Villanueva MP, Berenshteyn F, Stephen D, Turnbull RK, Joyner AL. 2007. Genetic subdivision of the tectum and cerebellum into functionally related regions based on differential sensitivity to engrailed proteins. *Development* **134**:2325–2335. DOI: https://doi.org/10.1242/dev.000620, PMID: 17537797

**Sonderegger P**. 1997. Axonin-1 and NgCAM as "recognition" components of the pathway sensor apparatus of growth cones: a synopsis. *Cell and Tissue Research* **290**:429–439. DOI: https://doi.org/10.1007/s004410050950, PMID: 9321707

**Stoeckli ET**, Sonderegger P, Pollerberg GE, Landmesser LT. 1997. Interference with axonin-1 and NrCAM interactions unmasks a floor-plate activity inhibitory for commissural axons. *Neuron* **18**:209–221. DOI: https://doi.org/10.1016/S0896-6273(00)80262-7, PMID: 9052792

**Stoeckli ET**. 2010. Neural circuit formation in the cerebellum is controlled by cell adhesion molecules of the Contactin family. *Cell Adhesion & Migration* **4**:523–526. DOI: https://doi.org/10.4161/cam.4.4.12733, PMID: 20622526

**Sytnyk V**, Leshchyns'ka I, Schachner M. 2017. Neural cell adhesion molecules of the immunoglobulin superfamily regulate synapse formation, maintenance, and function. *Trends in Neurosciences* **40**:295–308. DOI: https://doi.org/10.1016/j.tins.2017.03.003, PMID: 28359630

**Tanaka T**, Serneo FF, Higgins C, Gambello MJ, Wynshaw-Boris A, Gleeson JG. 2004. Lis1 and doublecortin function with dynein to mediate coupling of the nucleus to the centrosome in neuronal migration. *The Journal of Cell Biology* **165**:709–721. DOI: https://doi.org/10.1083/jcb.200309025, PMID: 15173193

**Tuysuz B**, Pehlivan D, Özkök A, Jhangiani S, Yalcinkaya C, Zeybek ÇA, Muzny DM, Lupski JR, Gibbs R, Jaeken J. 2016. Phenotypic expansion of congenital disorder of glycosylation due to SRD5A3 null mutation. *JIMD Reports* **26**:7–12. DOI: https://doi.org/10.1007/8904_2015_478, PMID: 26219881

**Vogel C**, Chothia C. 2006. Protein family expansions and biological complexity. *PLoS Computational Biology* **2**:e48. DOI: https://doi.org/10.1371/journal.pcbi.0020048, PMID: 16733546

**Wei CH**, Ryu SE. 2012. Homophilic interaction of the L1 family of cell adhesion molecules. *Experimental & Molecular Medicine* **44**:413–423. DOI: https://doi.org/10.3858/emm.2012.44.7.050, PMID: 22573111

**Weinhold B**, Seidenfaden R, Röckle I, Mühlenhoff M, Schertzinger F, Conzelmann S, Marth JD, Gerardy-Schahn R, Hildebrandt H. 2005. Genetic ablation of polysialic acid causes severe neurodevelopmental defects rescued by deletion of the neural cell adhesion molecule. *Journal of Biological Chemistry* **280**:42971–42977. DOI: https://doi.org/10.1074/jbc.M511097200, PMID: 16267048

**Welti M**. 2013. Regulation of dolichol-linked glycosylation. *Glycoconjugate Journal* **30**:51–56. DOI: https://doi.org/10.1007/s10719-012-9417-y, PMID: 22717794

**Wheeler PG**, Ng BG, Sanford L, Sutton VR, Bartholomew DW, Pastore MT, Bamshad MJ, Kircher M, Buckingham KJ, Nickerson DA, Shendure J, Freeze HH. 2016. SRD5A3-CDG: Expanding the phenotype of a congenital disorder of glycosylation with emphasis on adult onset features. *American Journal of Medical Genetics Part A* **170**:3165–3171. DOI: https://doi.org/10.1002/ajmg.a.37875, PMID: 27480077

**Wiśniewski JR**, Zougman A, Nagaraj N, Mann M. 2009. Universal sample preparation method for proteome analysis. *Nature Methods* **6**:359–362. DOI: https://doi.org/10.1038/nmeth.1322, PMID: 19377485

**Xenaki D**, Martin IB, Yoshida L, Ohyama K, Gennarini G, Grumet M, Sakurai T, Furley AJ. 2011. F3/contactin and TAG1 play antagonistic roles in the regulation of sonic hedgehog-induced cerebellar granule neuron progenitor proliferation. *Development* **138**:519–529. DOI: https://doi.org/10.1242/dev.051912, PMID: 21205796

**Xu J**. 2005. Preparation, culture, and immortalization of mouse embryonic fibroblasts. *Current Protocols in Molecular Biology* **28**:21.

**Zhao L**, Rosales C, Seburn K, Ron D, Ackerman SL. 2010. Alteration of the unfolded protein response modifies neurodegeneration in a mouse model of Marinesco-Sjögren syndrome. *Human Molecular Genetics* **19**:25–35. DOI: https://doi.org/10.1093/hmg/ddp464, PMID: 19801575

**Zielinska DF**, Gnad F, Wiśniewski JR, Mann M. 2010. Precision mapping of an in vivo N-glycoproteome reveals rigid topological and sequence constraints. *Cell* **141**:897–907. DOI: https://doi.org/10.1016/j.cell.2010.04.012, PMID: 20510933

# *MINPP1* prevents intracellular accumulation of the cation chelator inositol hexakisphosphate and is mutated in Pontocerebellar Hypoplasia

Ekin Ucuncu[1]#, Karthyayani Rajamani [1]#, Miranda S.C. Wilson[2], Daniel Medina-Cano[1], Nami Altin[1], Pierre David[3], Giulia Barcia[1,4], Nathalie Lefort[5], Céline Banal[5], Marie-Thérèse Vasilache-Dangles[6], Gaële Pitelet[7], Elsa Lorino[8], Nathalie Rabasse[9], Eric Bieth[10], Maha S. Zaki[11], Meral Topcu[12], Fatma Mujgan Sonmez[13,14], Damir Musaev[15], Valentina Stanley[15], Christine Bole-Feysot[16], Patrick Nitschké[17], Arnold Munnich[18], Nadia Bahi-Buisson[19], Catherine Fossoud[20], Fabienne Giuliano[21], Laurence Colleaux[1], Lydie Burglen[1,22], Joseph G. Gleeson[15], Nathalie Boddaert[23], Adolfo Saiardi[2]*, Vincent Cantagrel[1]*

# Contributed equally

* Corresponding authors:

vincent.cantagrel@inserm.fr

a.saiardi@ucl.ac.uk

## AFFILIATIONS

1. Developmental Brain Disorders Laboratory, Université de Paris, Imagine Institute, INSERM UMR 1163, F-75015, Paris, France
2. MRC Laboratory for Molecular Cell Biology, University College London, WC1E 6BT London, UK

3. Transgenesis Platform, Laboratoire d'Expérimentation Animale et Transgenèse (LEAT), Imagine Institute, Structure Fédérative de Recherche Necker INSERM US24/CNRS UMS3633, 75015 Paris, France
4. Département de Génétique Médicale, AP-HP, Hôpital Necker-Enfants Malades, F-75015, Paris, France
5. iPSC Core Facility, Université de Paris, Imagine Institute, INSERM UMR 1163, F-75015, Paris, France
6. Département de Neurologie Pédiatrique, AP-HP, Hôpital Necker-Enfants Malades, F-75015, Paris, France
7. Service de Neuropédiatrie, CHU Nice, 06200 Nice, France
8. ESEAN, 44200 Nantes, Service de maladies chroniques de l'enfant, CHU Nantes, 44093 Nantes, France
9. Service de pédiatrie, hôpital d'Antibes-Juan-les-Pins, 06600 Antibes-Juan-les-Pins, France
10. Service de Génétique Médicale, CHU Toulouse, 31059 Toulouse, France.
11. Clinical Genetics Department, Human Genetics and Genome Research Division, National Research Centre, Cairo 12311, Egypt
12. Hacettepe University, Faculty of Medicine, Department of Child Neurology, Ankara, 06100, Turkey
13. Guven Hospital, Child Neurology Department, Ankara, Turkey
14. Karadeniz Technical University, Faculty of Medicine, Department of Child Neurology, Trabzon, 61080, Turkey.
15. Laboratory for Pediatric Brain Diseases, Rady Children's Institute for Genomic Medicine, University of California San Diego, La Jolla (CA), 92093, USA
16. Genomics Platform, Université de Paris, Imagine Institute, INSERM UMR 1163, F-75015, Paris, France
17. Bioinformatics Core Facility, Université de Paris, Imagine Institute, INSERM UMR 1163, F-75015, Paris, France

18. Translational Genetics Laboratory, Université de Paris, Imagine Institute, INSERM UMR 1163, F-75015, Paris, France
19. Genetics and Development of the Cerebral Cortex Laboratory, Université de Paris, Imagine Institute, INSERM UMR 1163, F-75015, Paris, France
20. Centre de Référence des Troubles des Apprentissages, Hôpitaux Pédiatriques de Nice CHU-Lenval, 06200 Nice, France
21. Service de Génétique Médicale, Centre Hospitalier Universitaire de Nice, 06202 Nice, France
22. Centre de Référence des Malformations et Maladies Congénitales du Cervelet, Département de Génétique, AP-HP, Sorbonne Université, Hôpital Trousseau, 75012, Paris, France.
23. Département de radiologie pédiatrique, INSERM UMR 1163 and INSERM U1000, AP-HP, Hôpital Necker-Enfants Malades, F-75015, Paris, France

## ABSTRACT

Inositol polyphosphates are vital metabolic and secondary messengers, involved in diverse cellular functions. Therefore, tight regulation of inositol polyphosphate metabolism is essential for proper cell physiology. Here, we describe an early-onset neurodegenerative syndrome caused by loss-of-function mutations in the *multiple inositol-polyphosphate phosphatase 1* gene (*MINPP1*). Patients were found to have a distinct type of Pontocerebellar Hypoplasia with typical basal ganglia involvement on neuroimaging. We found that patient-derived and genome edited *MINPP1*$^{-/-}$ induced stem cells exhibit an inefficient neuronal differentiation combined with an increased cell death. MINPP1 deficiency results in an intracellular imbalance of the inositol polyphosphate metabolism. This metabolic defect is characterized by an accumulation of highly phosphorylated inositols, mostly inositol hexakisphosphate ($IP_6$), detected in HEK293, fibroblasts, iPSCs and differentiating neurons lacking MINPP1. In mutant cells, higher $IP_6$ level is expected to be associated with an increased chelation of intracellular cations, such as iron or calcium, resulting in decreased levels of available ions. These data suggest the involvement of $IP_6$-mediated chelation on Pontocerebellar Hypoplasia disease pathology and thereby highlight the critical role of MINPP1 in the regulation of human brain development and homeostasis.

## MAIN TEXT

## INTRODUCTION

Inositol polyphosphate (IPs) comprise an ubiquitous family of small molecule messengers controlling every aspect of cell physiology [1]. The best characterized is the calcium release factor inositol trisphosphate ($I(1,4,5)P_3$ or simply $IP_3$), a classical example of second messenger [2], generated after receptor activation by the action of phospholipase C on the lipid phosphoinositide $PIP_2$. Each of the six hydroxyl groups of the inositol ring can be phosphorylated, and the combination of these phosphorylations generates multiple derivatives [3]. Among them, inositol hexakisphosphate ($IP_6$, or phytic acid) is the most abundant in nature. In plants, $IP_6$ accumulates in seeds, within storage vacuoles, where it could represent 1-2 % of their dry weight [4]. Plant seed $IP_6$ is used as the main source of phosphate and mineral nutrients (e.g. $Ca^{2+}$, $K^+$, $Fe^{2+}$) during germination. In mammalian cells, $IP_6$ is the most abundant inositol polyphosphate species, reaching cellular concentrations of ~15-100 μM [5]. $IP_6$ is synthesized from inositol monophosphate (IP) or from $IP_3$ by the action of several inositol phosphate kinases: IPMK (Inositol Polyphosphate Multikinase, also known as IPK2), $IP_3$-3K (Inositol -1,4,5-trisphophate 3-Kinase), ITPK1 (Inositol Tetrakisphosphate 1-Kinase) and IPPK (Inositol-Pentakisphosphate 2-Kinase, also known as IPK1)[1 6]. Subsequently, the fully phosphorylated ring of $IP_6$ can be further phosphorylated to generate the more polar inositol pyrophosphates such as $IP_7$ [7]. While $IP_6$ anabolism is well studied, its catabolism has been less characterized. Mammalian cells dephosphorylate $IP_6$ through the action of the MINPP1 (Multiple Inositol-Polyphosphate Phosphatase 1) enzyme [8] that is able to degrade $IP_6$ to $IP_3$ [9]. The analysis of mouse knockouts for the inositol kinases responsible for $IP_6$ synthesis have highlighted an important role for this pathway in controlling central nervous system development, since knockout of *Itpk1* or *Ipmk* is embryonically lethal due to improper neural tube development [10 11]. In mammals, $IP_6$ has been directly associated with a pleiotropy of functions, including ion channel regulation, control of mRNA export, DNA repair, and membrane dynamics [1]. Furthermore, $IP_6$ is considered as a natural antioxidant since its iron-chelating property enables it to inhibit iron-catalyzed radical formation[12]. Although not yet thoroughly studied, some of the physiological roles of $IP_6$ could be related to its high affinity for polyvalent cations [13 14].

To investigate the role of $IP_6$ in mammalian physiology, many studies use $IP_6$ exogenously added to cell lines in culture, often observing antiproliferative properties [15]. These studies give little attention to the chelating property of $IP_6$: cations-$IP_6$ precipitation depletes the medium of essential ions such as calcium or iron. Additionally, the physiological relevance of extracellular $IP_6$ in mammals is not established. Extracellular pools of $IP_6$ have only been demonstrated in a cestode intestinal parasite [16], and several studies suggest that dietary $IP_6$ cannot be absorbed as such through the digestive system and is absent from body fluids [17 18]. Instead, *de novo* synthesis of $IP_6$ occurs in all mammalian cells, including in the brain with high levels in regions such as the brainstem and striatum [17 19]. The existence of several cellular pools of $IP_6$ has been suggested [19 20 6]. However, the dynamic regulation of the endogenous intracellular pools of $IP_6$ is not fully understood, since its high cellular concentration precludes the determination of $IP_6$ pool specific fluctuations. Therefore, the exact function(s) of $IP_6$ in cell homeostasis and mammalian development remain an area of intense investigation.

Several human diseases have been genetically associated with alterations in phosphoinositide (the lipid derivatives of inositol) metabolism [21]. However, so far, no Mendelian disorder has been shown to be caused by an imbalance in the cytosolic inositol polyphosphate pathway, with the exception of two variants in a gene involved in the conversion of the pyrophosphates forms of inositol, associated with hearing or vision impairment [22 23].

Pontocerebellar hypoplasia (PCH) is a group of early-onset neurodegenerative disorders that includes at least 13 subtypes, based on neuropathological, clinical and MRI criteria [24 25]. PCH is usually associated with a combination of degeneration and lack of development of the pons and the cerebellum, suggesting a prenatal onset. The genetic basis is not known for all of the cases, and preliminary data from different PCH cohorts suggest that many subtypes remain to be identified. Based on the known molecular causes, PCH often results from a defect in apparently ubiquitous cellular processes such as RNA metabolism regulation and especially tRNA synthesis (i.e. mutations in *EXOSC3, TSEN54, TSEN2, TSEN34, CLP1* and *RARS2*). Multiple additional conditions show neurological symptoms and imaging comparable to typical PCH syndromes and are caused by defects in diverse pathways involved in mitochondrial, glycosylation or purine nucleotide metabolisms. This observation further supports the disruption of ubiquitous pathways as the unexplained basis of these neurological conditions[25].

In this study, we identify MINPP1 as necessary for the dephosphorylation of intracellular $IP_6$, and describe a new syndrome of PCH caused by a defect in this process that directly regulates cytosolic cation (e.g. $Ca^{2+}$, $Fe^{3+}$) homeostasis.

## RESULTS

### Loss of function mutations of the *MINPP1* gene are associated with a distinct subtype of Pontocerebellar Hypoplasia

To identify new etiological diagnoses of patients with PCH, we explored a group of 15 probands previously screened negative with a custom gene panel approach [26]. Whole exome sequencing (WES) was then performed through trio sequencing (i.e. both parents and the proband). Among the new candidate genes that were identified, the *MINPP1* gene was recurrent and the most obvious candidate (Table 1 and Supplementary Note). The *MINPP1* gene has not been previously associated with any Mendelian disorders. To assess how frequently *MINPP1* mutations could be involved in PCH, we explored two other cohorts of pediatric cases with neurological disorders. The presence of *MINPP1* mutations was investigated using a custom gene panel or WES (see method). Three additional families with *MINPP1* bi-allelic variants were identified, all the affected being diagnosed with PCH.

In total, bi-allelic variants in *MINPP1* were identified in eight affected children from six unrelated families (Fig.1, Table 1, Supplementary Fig.1). These variants include homozygous early-truncating mutations in the families CerID-30 and PCH-2712, compound heterozygous missense and frameshift variants in family CerID-11, a homozygous missense variant in the endoplasmic reticulum (ER) retention domain of the protein in the family CerID-09 and homozygous missense variants in the histidine phosphatase domain of the protein in the families TR-PCH-01 and PCH-2456 (Fig.1B, D). These four missense variants are predicted to be disease-causing using MutationTaster and SIFT [27], and involve amino acids fully conserved across evolution (Table 1, Fig.1C). To predict the impact of the variants on protein structure, we utilized a phytase crystal structure of D. castellii and evaluated the consequences of the missense variants involving amino-acids included in the model (Supplementary Fig.1B). Tyr53Asp variant introduces a buried charge and disrupts a hydrogen bond with the donor

amino-acid Ser299. The Phe228Leu substitution breaks a buried hydrogen bond with Lys241, both amino-acid positions are close to the $IP_6$ binding site. The Arg401Gln substitution replaces a buried charged residue with an uncharged residue and disrupts a salt bridge formed with the amino-acid Asp318. Thus, all the missense variants tested are predicted to cause structural damages with potential consequences on the enzyme activity.

The eight patients presented with almost complete absence of motor and cognitive development, progressive or congenital microcephaly, spastic tetraplegia or dystonia, and vision impairments (Table 2). For most of the patients, the first symptoms included neonatal severe axial hypotonia and epilepsy that started during the first months or years of life. Pre-natal symptoms of microcephaly associated with increased thalami echogenicity were detected for the individual CerID-11, while the seven other patients presented with progressive microcephaly. For patients from the families CerID-09 and 11, the phenotype appeared to be progressive and the affected children died in their infancy or middle-childhood. Strikingly, all the affected children harbor a unique brain MRI showing a mild to severe PCH, fluid-filled posterior fossa, with dilated lateral ventricles. Additionally, severe atrophy at the level of the basal ganglia or thalami often associated with typical T2 hypersignal were identified in all the patients MRI (Table 2, Fig.1A lower panel). This imaging is distinct from other PCH syndromes and thereby defines a new subtype that we propose as PCH type 14.

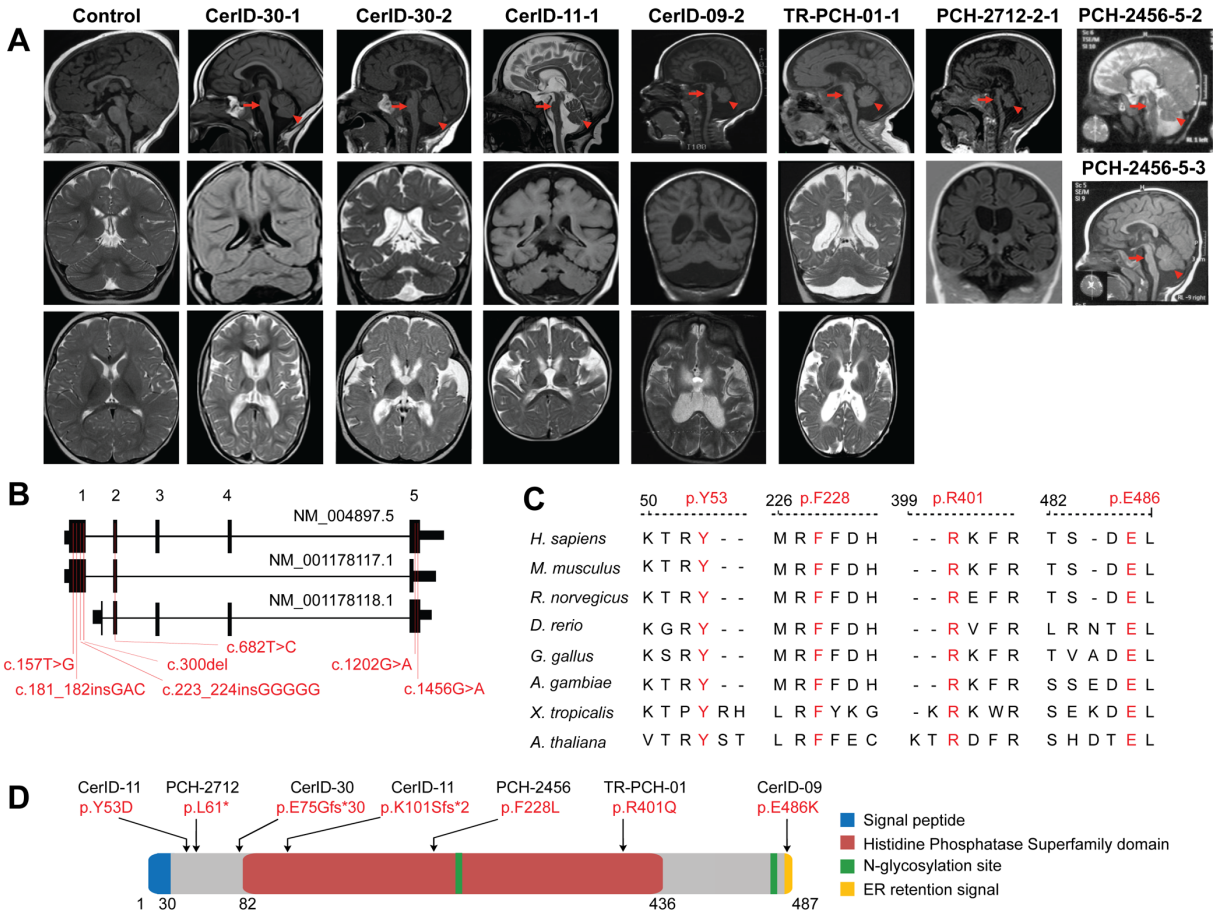


**Figure 1: Biallelic mutations in *MINPP1* cause a distinct PCH phenotype. (A)** Midline sagittal (top), coronal (middle) and axial (bottom) brain MRIs of control and patients from families CerID-30, CerID-11, CerID-09 and TR-PCH-01, respectively. Only sagittal (top) and coronal (middle) brain MRIs were available for the patient from the family PCH-2712 and sagittal brain MRI for the patients from PCH-2456 (top and middle). Sagittal MRIs show variable degree of brain stem (arrow) and cerebellar atrophy/hypoplasia (arrowhead). **(B)** Schematic representation of the *MINPP1* transcripts: NM_004897.5, NM_001178117.1 and NM_001178118.1, respectively. Exon numbers for the longest isoform NM_004897.5 are indicated above the schematic representation. Mutations are shown relative to their cDNA (NM_004897.5) position. **(C)** Multiple-sequence alignment of MINPP1 from different species. Variant amino-acid residues p.Y53, p.F228, p.R401 and p.E486 are evolutionarily conserved. **(D)** Linear schematic representation of MINPP1, showing the position of mutations with respect to predicted protein domains. Abbreviations used: Endoplasmic reticulum (ER).

## TABLE 1: *MINPP1* variants identified in the different cohorts

| Family | Genomic Coordinates (GRCh38) | Variant (transcript level) | Variant (protein level) | dbSNP | ExAC | gnomAD | SIFT | Polyphen | MutationTaster | CADD |
|---|---|---|---|---|---|---|---|---|---|---|
| **CERID-30** | Chr10:g.87505138_87505139insGGGGG | NM_004897.4(MINPP1): c.223_224insGGGGG | p.E75Gfs*30 | - | - | - | - | - | - | - |
| **CERID-11** | Chr10:g.87505072T>G | NM_004897.4(MINPP1): c.157T>G | p.Y53D | - | - | - | Deleterious (0) | Probably damaging (0.978) | Disease causing (prob: 1) | 32 |
| | Chr10:g.87505215del | NM_004897.4(MINPP1): c.300del | p.K101Sfs*2 | - | - | - | - | - | - | - |
| **CERID-09** | Chr10:g.87552470G>A | NM_004897.4(MINPP1): c.1456G>A | p.E486K | - | - | - | Deleterious (0) | Probably damaging (0.94) | Disease causing (prob: 1) | 26.6 |
| **TR-PCH-01** | Chr10:g.87552216G>A | NM_004897.4(MINPP1): c.1202G>A | p.R401Q | rs1381093602 | - | 1 allele count (freq 3.10^-6) | Deleterious (0) | Probably damaging (0.987) | Disease causing (prob: 1) | 33 |
| **PCH-2712** | Chr10:g.87505096_87505097insGAC | NM_004897.4(MINPP1): c.181_182insGAC | p.L61* | - | - | - | - | - | - | - |
| **PCH-2456** | Chr10:g.87508380T>C | NM_004897.4(MINPP1): c.682T>C | p.F228L | rs1456945513 | - | - | Deleterious (0) | Probably damaging (0.993) | Disease causing (prob: 1) | 25.8 |

CADD score ⩾ 25 indicates that the variant is among the 0.5% most deleterious substitutions in the protein-coding regions of the human genome.

## TABLE 2: Clinical information of the patients with variants in *MINPP1*

| Family | CerID-30 | | CerID-09 | CerID-11 | TR-PCH-01 | PCH-2712 | PCH-2456 | |
|---|---|---|---|---|---|---|---|---|
| **Subject** | CerID-30-1 | CerID-30-2 | CerID-09-2 | CerID-11-1 | TR-PCH-01-1 | 2712-2-1 | 2456-5-2 | 2456-5-3 |
| **Gender F/M** | F | F | M | F | M | F | M | F |
| **Origin (country)** | Tunisia | Tunisia | Tunisia | France | France | Turkey | Egypt | Egypt |
| **Documented consanguinity** | No | No | Yes | No | Yes | Yes -1st cousin parents | Yes -2nd cousin parents | Yes -2nd cousin parents |
| **Age at last follow-up** | 12 years | 9 years | 11 years | 18 months | 12 years | 2years 10 months | 4.5 years | 1.5 years |
| **Weight at birth (kg)** | 3.2 (M) | 4.2 (+2SD) | 3.2 (M) | 2.4 (-2SD) | 3.710 | 3.0 (M) | 3.4 (M) | 3 (M) |
| **Weight at last examination (kg)** | 30 (-1.5SD) | 23.4 (-0.5SD) | 16.9 (-4SD) | 10 (-1 DS) | 36 | 10.5 (-2SD) | 10.5 (-3SD) | 8.5 (-3SD) |
| **Length at birth (cm)** | 50 (M) | 51 (M) | 50.5 (M) | 43.5 (-3SD) | 50 | NA | 49.2 (M) | 47.5 (-1SD) |
| **HC at birth (cm)** | 34 (M) | 35 (+1SD) | 35 (M) | 30.6 (-3SD) | 36 | 33 (-1SD) | 34 (M) | 32 (-1SD) |
| **HC at last examination (cm, age)** | 48 cm (8 years; -2SD) | 47 cm (4 years; -2SD) | 47 cm (11 years; -5SD) | 42cm (18 months; -4SD) | -2,55 (18 mois) | 41cm (-5SD) | 44.5 (-5SD) | 42 (-3SD) |
| **Onset** | Perinatal | Perinatal | Perinatal | Prenatal | perinatal | Perinatal | Perinatal | Perinatal |
| **Progressive encephalopathy** | No | No | Yes | Yes | No | Yes | Yes | Yes |
| **Posture: bedridden (B), sitting (S), walking (W)** | B | B | B | B | B | B | B | B |
| **Development** | | | | | | | | |
| **Gross motor (normal/delayed/absent)** | Absent | Absent | Absent | Absent | Absent | Absent | Absent | Absent |
| **Fine motor (normal/delayed/absent)** | Absent | Absent | Absent | Absent | Absent | Absent | Absent | Absent |
| **Language (normal/delayed/absent)** | Absent | Absent | Absent | Absent | Absent | Absent | Absent | Absent |
| **Social (normal/delayed/absent)** | Absent | Absent | Absent | Absent | Delayed | Absent | Absent | Absent |
| **Seizures** | | | | | | | | |
| **Epileptic seizures** | + | + | + | - | + | + | + | + |
| **Onset** | 7 years | 4 years | 5 years | - | 1 day | 2 months | 3 months | 5 months |
| **Neurological Findings** | | | | | | | | |
| **Axial hypotonia** | + | + | + | + | + | + | + | + |
| **Distal hypertonia** | + | + | + | + | + | + | + | + |
| **Pyramidal signs** | Spastic tetraplegia | Spastic tetraplegia | Spastic tetraplegia | Spastic tetraplegia | Spastic tetraplegia | Spastic tetraplegia | Spastic tetraplegia | Spastic tetraplegia |
| **Extra-pyramidal signs** | + | + | + | + | - | + | + | + |
| **Ophthalmological findings** | | | | | | | | |
| **Nystagmus** | + | + | + | + | + | bilateral + | + | + |
| **Abnormal ocular movement** | + | + | + | + | + | NA | + | + |
| **Optic atrophy** | + | + | + | - | - | - | + | - |
| **VEP/ERG** | NA | ERG | VEP | ERG/VEP | NA | abnormal VEP, left eye | abnormal VEP | - |
| **Others** | Ptosis/cataract | Ptosis/cataract | Blindness | Ptosis | Cataract | Ptosis, Cataract | couldn't follow object | - |
| **Investigations** | | | | | | | | |
| **Metabolic** | Normal | Normal | Normal | Normal | Normal | Normal | Normal | Normal |
| **EEG** | Abnormal | Normal | Normal | Normal | Normal | Abnormal | Abnormal | Abnormal |
| **MRI** | | | | | | | | |
| **Age at last investigation (years(y); months (m); days(d))** | 2y7m | 8m2d | 1y11m | 8m23d | 4m | 6y8m | 2.5y | 1.5y |
| **Cerebellum (atrophy/hypoplasia/ Progressive atrophy)** | Hypoplasia | Hypoplasia | Hypoplasia | Hypoplasia | Hypoplasia | Hypoplasia | Hypoplasia | Hypoplasia |
| **Pons** | Atrophy | Atrophy | Atrophy | Atrophy | Hypoplasia | Atrophy | Atrophy | Atrophy |
| **Cerebral cortex atrophy** | Atrophy | Atrophy | Atrophy | Atrophy | - | Atrophy | Atrophy | Atrophy |
| **Ventricles** | Enlarged | Enlarged | Enlarged | Enlarged | Enlarged | Enlarged | Enlarged | Enlarged |
| **Corpus callosum** | - | - | Thin | NA | - | thin | Thin | Thin |
| **Basal Ganglia hypoplasia/atrophy** | + | + | + | + | thalamic atrophy | + | + | + |
| **Basal ganglia T2 hypersignal** | + | + | + | + | thalami | + | - | - |
| **Spectroscopy** | No lactate abnormality | NA | NA | NA | NA | No lactate abnormality | NA | NA |
| **Others (WM defect)** | WM periventricular atrophy | WM periventricular atrophy | NA | NA | NA | WM periventricular atrophy | - | - |
| **Other symptoms** | | | | | | | | |
| **Respiratory tract congestion** | No | No | Yes | No | Yes | No | Yes | No |
| **Apnea** | No | No | No | No | No | No | Yes | No |
| **Impaired swallowing** | Yes | Yes | Yes | Yes | Yes (gastrostomy) | Yes | Yes | Yes |
| **Joint stiffness** | Yes | Yes | Yes | Yes | NA | Yes | Yes | No |
| **Skeletal deformities** | Scoliosis | Scoliosis | Scoliosis | Scoliosis | Scoliosis | Scoliosis | Scoliosis | No |
| **Cardiovascular findings** | No | No | NA | NA | No | No | No | No |
| **Urine screening** | Normal | Normal | NA | Normal | Normal | recurrent urinary infection | Normal | Normal |
| **Peripheral blood smear** | NA | NA | NA | Thrombocytosis | Normal | NA | NA | NA |
| **Muscle wasting** | Yes | Yes | Yes | Yes | Yes | Yes | Yes | No |
| **Facial dysmorphism** | Yes | Yes | No | No | Yes | Micrognathia | Non specific small head, prominent nose, low set ear | Non specific small head, prominent nose, low set ears |
| **Other** | NA | NA | Mild Normochromic, normocytic anaemia | Abnormal fat distribution | NA | BAEP: no response | - | - |

Abbreviations: EEG= Electroencephalogram, ERG= abnormal electroretinography, HC= Head Circumference, M=median, NA= Not available

***MINPP1* missense PCH mutations are deleterious for protein function**

The MINPP1 enzyme is predominantly localized in the ER lumen[28]. It removes phosphate groups from inositol polyphosphate substrates starting at position 3 [29,30], with high affinity for $IP_5$ and $IP_6$ [31]. Indeed, it has been described as the main mammalian phytase, or enzyme involved in $IP_6$ degradation (Fig. 2A). Despite its name, this gene does not have any paralog in the human or mouse genome. In order to determine the effect of the patient mutations on the endogenous enzyme, we obtained skin fibroblast from patients of the CerID-30 family. MINPP1 protein was undetectable in patients' cells (Fig. 2B), supporting a complete loss of function of *MINPP1* as the cause of this PCH subtype. The *MINPP1* gene is widely expressed in the developing and adult mouse [8 31], and rat[9], as well as in human tissues (Supplementary Fig. 2A). This broad expression pattern suggests a general role for this enzyme in regulating inositol polyphosphate metabolism. To investigate this role, we generated a HEK293T cell KO model for the *MINPP1* gene (*MINPP1*$^{-/-}$ HEK293) using genome editing (Fig. 2C). *MINPP1*$^{-/-}$ HEK293 cells showed a 30% decrease in their growth rate after 48 hours of culture, likely resulting from a proliferation defect, in the absence of significant difference in the binding of the apoptosis marker Annexin-V (Fig.2D, Supplementary Fig.2B, C). This defect was partially rescued by transient over-expression of WT MINPP1 ($p<0.001$; Fig. 2E, Supplementary Fig.2D). Contrastingly, over-expression of two of the MINPP1 missense variants (i.e. Y53D and E486K) did not rescue growth, suggesting that these variants have a major impact on the protein function. MINPP1 has two predicted N-glycosylation sites (Fig.1D). In order to evaluate the glycosylation status of the endogenous and over-expressed WT MINPP1 as well as the Y53D and E486K missense variants, we treated the protein extract with the PNGase enzyme [32]. A shift in the molecular weight after treatment, in all the samples, indicated that MINPP1 is indeed glycosylated without major impact of the missense variants (Supplementary Fig.2E).

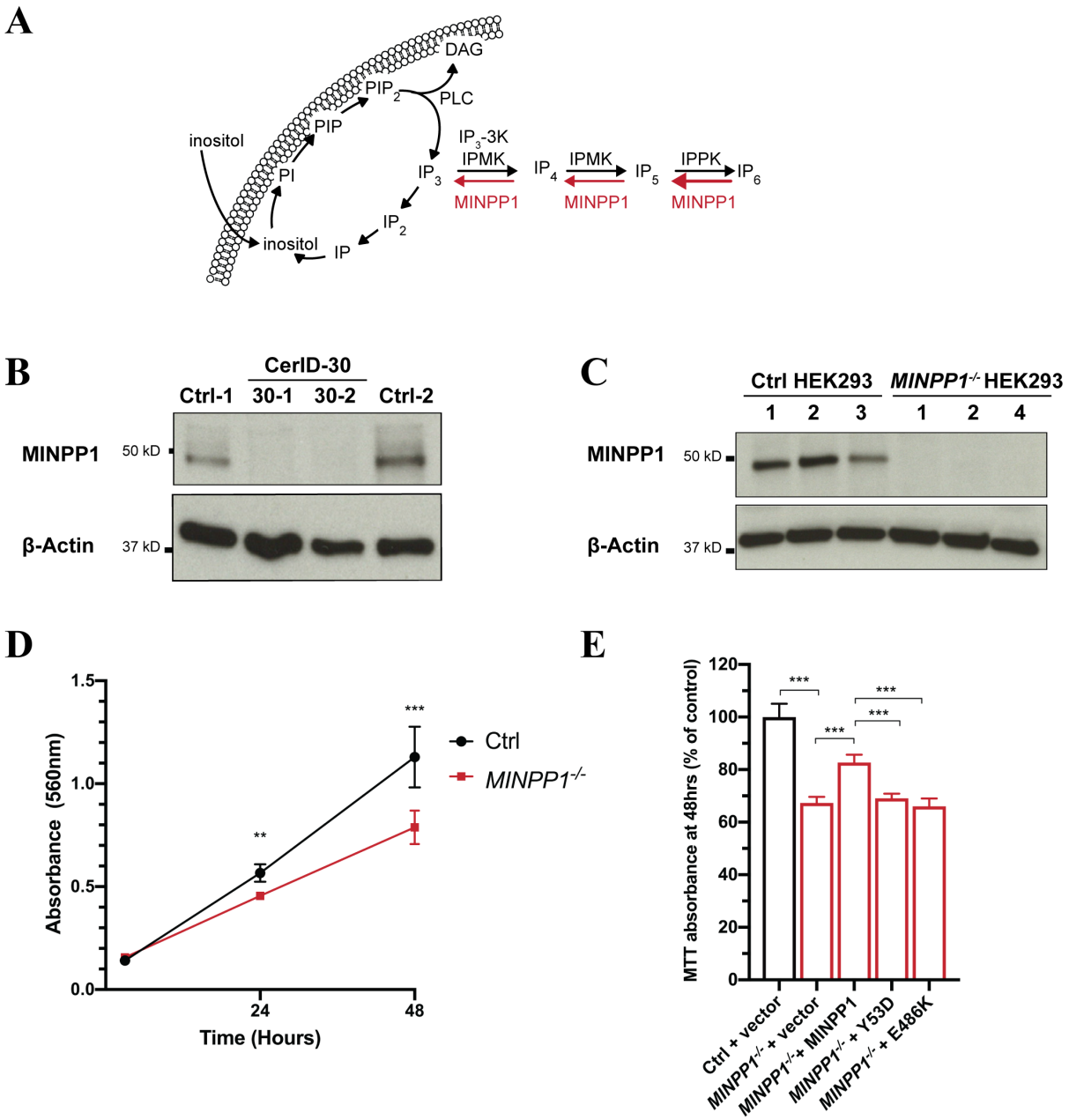


**Figure 2: PCH-associated mutations of *MINPP1* are deleterious for protein function. (A)** Schematic representation of inositol phosphate cycle. Abbreviations used: *myo*-inositol (Inositol) phosphatidylinositol (PI); phosphatidylinositol phosphate (PIP); phosphatidylinositol 4,5-bisphosphate ($PIP_2$); diacylglycerol (DAG); Phospholipase C (PLC); inositol phosphate (IP); inositol bisphosphate ($IP_2$); inositol 1,4,5-trisphosphate ($IP_3$); inositol 1,3,4,5-tetrakisphosphate ($IP_4$); inositol pentakisphosphate ($IP_5$); inositol hexakisphosphate ($IP_6$); Inositol Polyphosphate Multikinase (IPMK); $I(1,4,5)P_3$ 3-Kinase ($IP_3$-3K); Inositol-Pentakisphosphate 2-Kinase (IPPK); Multiple Inositol-Polyphosphate Phosphatase 1 (MINPP1). (**B-C**) Western blot analysis of MINPP1 level in patient

fibroblasts and HEK293 cells with β-Actin shown as loading control. Patient fibroblasts CerID-30-1 and CerID-30-2 (**B**) and *MINPP1*$^{-/-}$ HEK293 clones (**C**) show absent MINPP1. (**D)** Assessment of cell proliferation by MTT assay. For each clone, MTT absorbance was measured 3, 24 and 48 hours post-seeding. Values represent the mean ± s.d. of triplicate determinations from 4 replicates. (n=4, Two-tailed student's t-test, ** and *** indicate p values $p<0.01$ and $p\leq0.001$, respectively). **(E)** *MINPP1*$^{-/-}$ HEK293 cells were transiently transfected with plasmids encoding empty vector, wildtype, Y53D or E486K variant MINPP1. To assess the cell proliferation rate, MTT assay was performed 48 hours post-nucleofection. The data are presented as mean percentage relative to control (Ctrl) ± s.d., with triplicate determinations from four replicates. The normalization was done with 3 hours MTT assay data. (n=4, One-way ANOVA, Tukey's post hoc test, *** indicates the p value $p\leq0.001$).

**Patient and genome-edited *MINPP1* mutant neural progenitors show an impaired neuronal differentiation with increased apoptosis**

To investigate the mechanism at the origin of the neurological symptoms of *MINPP1* patients, we derived induced pluripotent stem cells (iPSCs) from patient CerID-30-2 (Supplementary Fig.3A-E, Fig. 3D). In order to assess a contribution of the genetic background or other factors to the phenotype, we also generated *MINPP1*$^{-/-}$ iPSCs in isogenic background (Supplementary Fig. 3A-E, Fig. 3D). Surprisingly, a dual SMAD inhibition-based neural induction protocol[33 34], did not allow the generation of viable neural progenitor cells for both *MINPP1* mutant lines (data not shown). Differentiation of patient-derived iPSCs systematically generated mixed cell populations with undefined HNK1 negative cells (Supplementary Fig. 3H). These observations suggest a critical role for MINPP1 during neuroectodermal induction *in vitro*, and led us to use a different protocol that preserved neural rosette environment, using only noggin as a SMAD inhibitor [35] (Supplementary Fig.3G). In these conditions, control cells efficiently differentiated toward TUJ1$^{+}$ neurons after 14 days (Fig. 3A). In contrast, both *MINPP1* mutant lines showed significant 42% and 65% decreases in TUJ1$^{+}$ post-mitotic cells mirrored by significant 2.6 and 3.1-fold increases in the number of PAX6$^{+}$ neural progenitors in *MINPP1*$^{-/-}$ and CerID-30-2 derived cells, respectively (Fig. 3A, B). To test the presence of a neurodegenerative

phenotype in our *MINPP1* mutant cells, we assessed the apoptosis level using a TUNEL assay. We observed an increase in apoptosis at day 10 of neuronal differentiation that became more significant at day 14 with 1.6-fold and 2.4-fold increases in the number of TUNEL$^{+}$ cells among the *MINPP1*$^{-/-}$ and CerID-30-2 derived differentiating neurons, respectively. (See Fig. 3 C, D). Interestingly, we observed no significant difference in apoptosis levels among the undifferentiated iPSCs lines (Fig. 3D). These results suggest that the differentiation of neural progenitors into neurons is specifically vulnerable to this inositol phosphate metabolism defect.

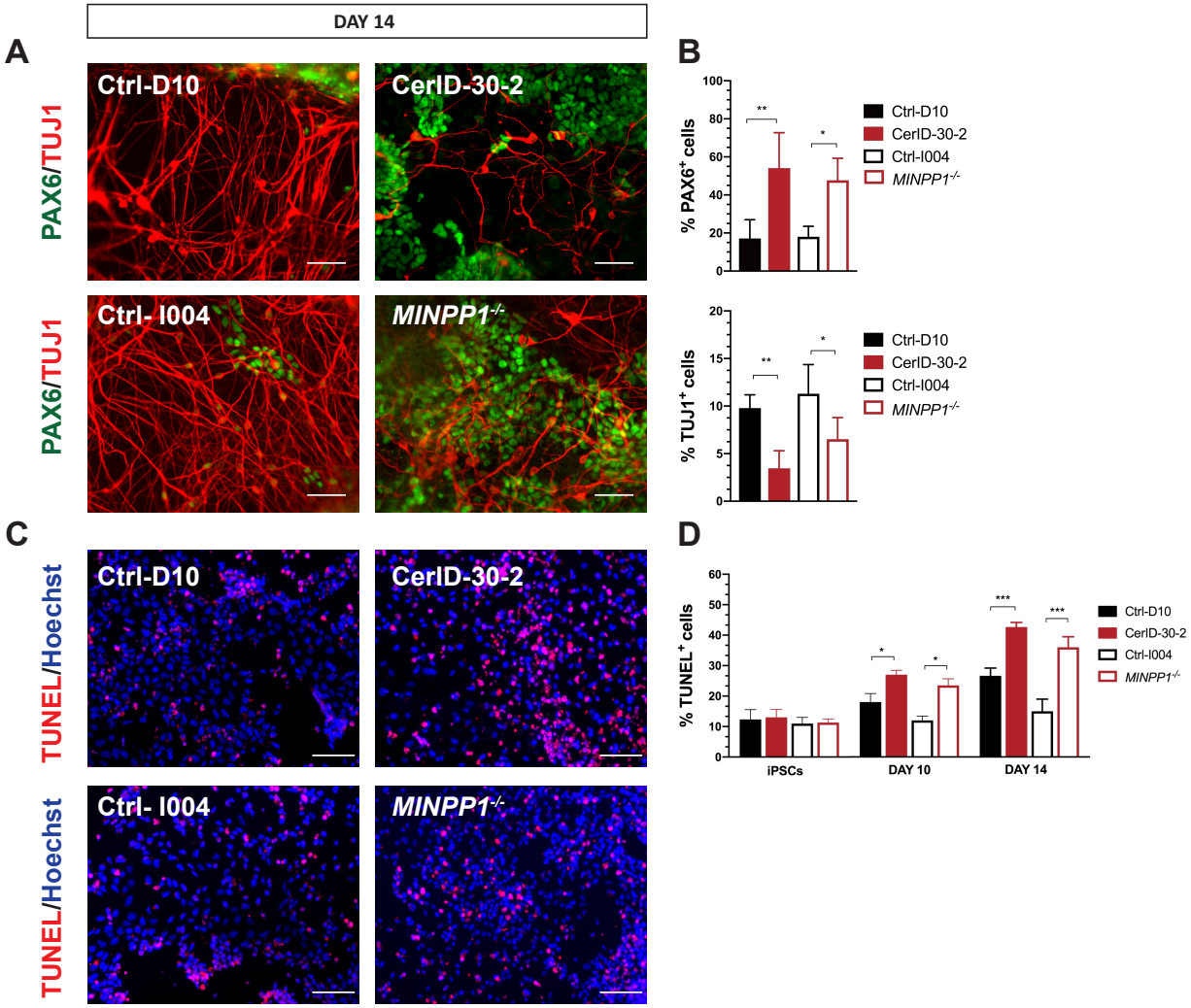


**Figure 3: MINPP1 loss causes an early neuronal differentiation defect combined with an increase in apoptosis. (A)** Control (Ctrl-D10 and Ctrl-I004), patient-derived (CerID-30-2) and *MINPP1*$^{-/-}$ iPSCs were differentiated towards neuronal lineage for 14 days. Representative images of the differentiated cells stained with early neuronal marker TUJ1 and neural progenitor marker PAX6. Hoechst was used

as a nuclear stain. **(B)** Quantitative analysis of the immunofluorescence data. **(C)** Representative images of TUNEL staining during neuronal differentiation at day 14. **(D)** Quantification of the TUNEL assay during neuronal differentiation (iPSC, Day 10 and Day 14). All scale bars correspond to 50 μm. (Duplicate/triplicate analysis of two independent experiments, one-way ANOVA, Tukey's post hoc test, * and **, *** indicate p values $p<0.05$, $p<0.01$ and $p\leq0.001$, respectively). The data are presented as mean percentage values ± s.d.

**Inositol polyphosphate metabolism is altered in HEK293, iPSCs and differentiating neurons mutated for *MINPP1***

The localization of human MINPP1 into the ER, and the demonstration that its drosophila homolog (i.e. mipp1) is anchored to the plasma membrane outside of the cell[36], prompted us to investigate the presence of phytase activity in conditioned media from control and *MINPP1* mutant HEK293 cells. In conditioned medium from control cells, exogenously added $IP_6$ was substantially processed after two hours, and completely degraded after four hours (Supplementary Fig.4A). Conversely, although partially degraded, $IP_6$ is still detectable after six hours of incubation in *MINPP1* mutant conditioned media. This result suggests that MINPP1 accounts for the main secreted phytase activity of HEK293 cells.

To explore precisely a disruption in inositol phosphate metabolism, and to better address the role of MINPP1 in this metabolic pathway, we used tritium inositol (*myo*-[$^3$H]-inositol) metabolic labeling of cultured cells, and analyzed inositol derivatives with SAX-HPLC (strong anion-exchange high-performance liquid chromatography) as previously described [37 38]. We applied this method to HEK293, skin fibroblasts, and iPSCs before or during neuronal differentiation at day 10 (referred to as Day 10 differentiating neurons) from control and *MINPP1* mutant cell lines. Exogenously added [$^3$H]-inositol is imported into the cytosol and converted into phosphoinositide lipids before processing into inositol phosphates (IPs) (Fig. 2A). As expected, after 3 days of [$^3$H]-inositol labeling, $IP_6$ was detected as the most, or the second most abundant intracellular inositol derivative in control cell lines (hollow and filled bars in Fig. 4), but was absent in the cell culture media (Fig. 4, Supplementary Fig. 4B). In all the cell models studied, the disruption of MINPP1 enzyme activity had a strong impact on intracellular IPs

profile when compared with their respective controls. The investigation of *MINPP1*$^{-/-}$ HEK293 cells revealed a 3-fold significant increase in $IP_6$ level, as well as an increase in $IP_5$ levels, and surprisingly a severe decrease in IP and $IP_2$ levels (Fig. 4A). Trends in the same direction, although not significant, were detected in patient fibroblasts (Fig. 4B) suggesting cell-type specific differences. Indeed, in iPSCs, $IP_6$ levels showed a significant 1.6-fold increase in both patient-derived and *MINPP1* KO iPSCs, also associated with an increase in $IP_5$ levels (Fig. 4C, D). Finally, we studied differentiating neurons at day 10, a time point when differences in the TUJ1/PAX6 cell populations are not detected (Supplementary Fig.3F). These data revealed significant 1.9-fold and 1.6-fold increases in $IP_6$ levels in patient-derived and *MINPP1* KO differentiating cells, respectively, with a trend or significant decrease in $IP_2$ levels (Fig.4E, F). Interestingly, the defects in $IP_6$ and $IP_2$ levels in *MINPP1*$^{-/-}$ HEK293 cells were fully rescued, considering a ~70% transfection efficiency, by the transient over-expression of WT MINPP1 (Supplementary Fig. 4C and D). We also performed radiolabeling experiments on *MINPP1*$^{-/-}$ HEK cells with Y53D and E486K MINPP1 variants. The Y53D variant had no impact on the $IP_6$ and $IP_2$ levels, indicating the clear loss of enzyme activity (Supplementary Fig.4D). However, the E486K variant did not affect the enzyme activity in this overexpression system, with apparently unchanged levels of $IP_6$ and $IP_2$. This result is in line with the previously demonstrated preserved enzyme activity in the absence of the ER retention signal [39]. Therefore, and given its inability to rescue the *MINPP*1$^{-/-}$ HEK293 proliferation, this variant could impact a critical regulation of MINPP1 protein.

In all the cell models tested, including HEK293 cells, patients' fibroblasts, and undifferentiated and differentiated iPSCs, a comparable imbalance of IPs levels were observed, where increase in the amounts of higher inositol polyphosphate derivatives $IP_5$ and $IP_6$ were associated with a decrease in lower-phosphorylated $IP_2$ and IP species (Fig. 4). Differences observed between the various cell models tested are likely to be caused by cell type differences and potentially also by the genetic background. Nevertheless, these observations clearly demonstrate the critical role played by MINPP1 in cellular inositol polyphosphate homeostasis, with the conversion of higher to lower IPs. The most robust finding was that $IP_6$ is systematically increased in *MINPP1* mutant cells compared to controls. Altogether, these observations exclude a major contribution of extracellular higher-phosphorylated IPs to this metabolic

defect, but highlight an unappreciated role for *MINPP1* in the regulation of the intracellular pool of de novo synthesized $IP_6$, the most abundant inositol derivative.

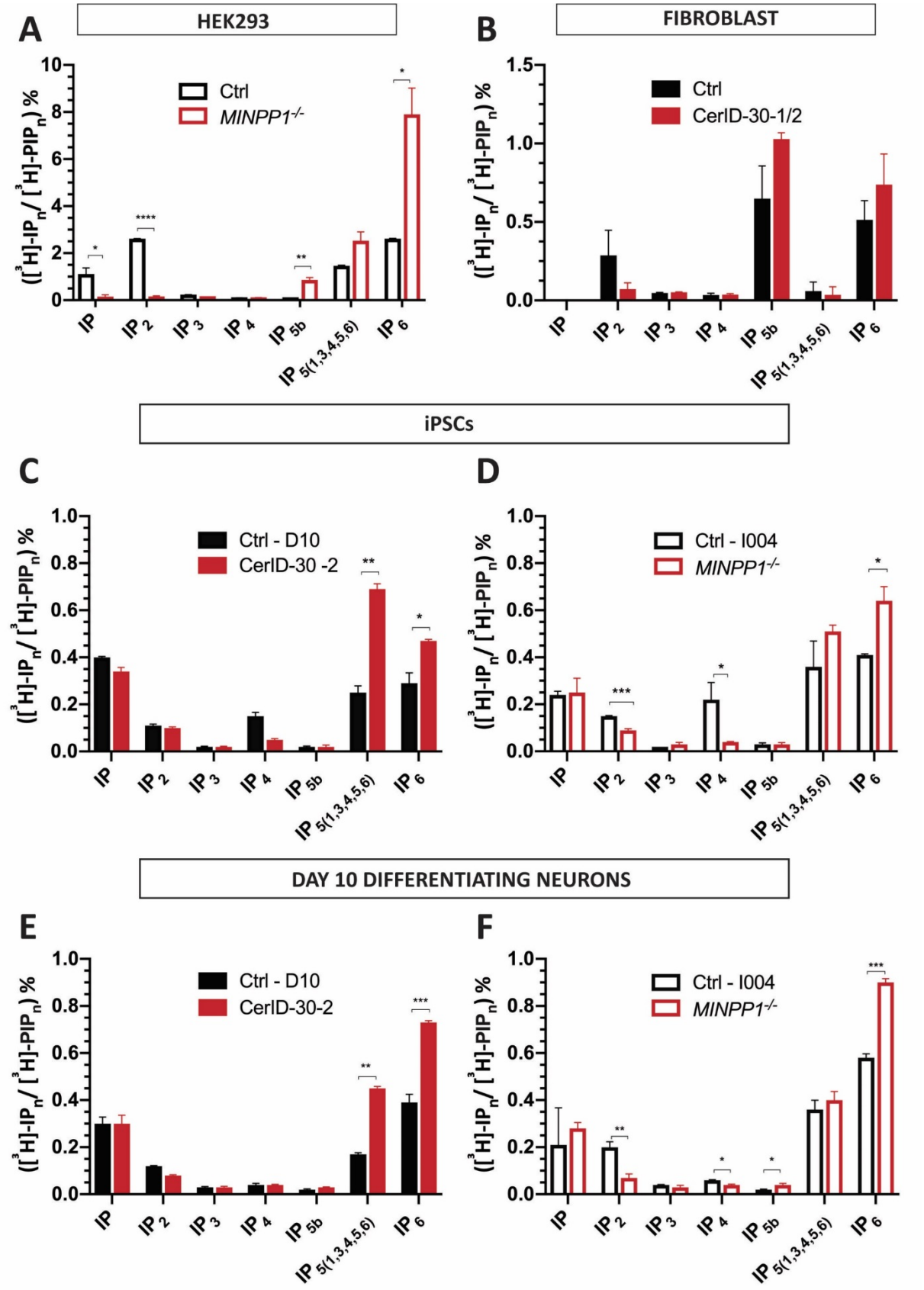

**Figure 4: MINPP1 absence leads to disruption in inositol phosphates metabolism. (A-F)** SAX-HPLC analysis of inositol phosphate levels in *MINPP1*$^{-/-}$ HEK293 cells **(A)**, patient fibroblasts (CerID-30-1 and CerID-30-2) **(B),** patient-derived (CerID-30-2) **(C)** and *MINPP1*$^{-/-}$ iPSCs **(D)**, and their day-10 differentiating neuron counterparts **(E-F)**. The peaks ([$^3$H]-IP$_n$) were identified based on comparison to standards. [$^3$H]-IP$_n$ levels are presented as percentage of total radioactivity in the inositol-lipid fraction ([$^3$H]-PIP$_n$). All error bars represent standard deviation (s.d.). (n=2, Two-tailed student's t-test for HEK293 and fibroblast data; One-way ANOVA for iPSCs and their differentiated counterparts data, Tukey's post hoc test, *, **, ***, **** indicate p values $p<0.05$, $p<0.01$, $p<0.001$, $p\leq0.0001$, respectively). Abbreviations used: IPn, inositol phosphates; PIPn, phosphatidyl inositol phosphates.

**IP$_6$ accumulation can deplete free iron in presence of high iron condition**

Considering the strong impact of *MINPP1* mutations on cellular IP$_6$ levels, and the known chelator properties of this molecule, we hypothesized that MINPP1 defects can have consequences for intracellular cations homeostasis. An intracellular accumulation of IP$_6$ could theoretically lead to the accumulation of chelated cations inside the cell, potentially reducing the pool of free cations. At physiological pH, IP$_6$ has a strong binding affinity to iron[14], therefore we evaluated the ability of HEK293 cells to store iron, in low iron (-FAC) or high iron (provided with ferric ammonium citrate; +FAC) conditions. Then, we used a colorimetric ferrozine-based assay with a HCl/KMnO$_4$ pretreatment step that separates iron from its binding molecules to measure total intracellular iron [40 41]. After two days of incubation with FAC, we observed a significant 1.5-fold increase in the total iron content in *MINPP1*$^{-/-}$ HEK293, under high iron conditions compared to control (Fig. 5A). Although based on non-physiological iron conditions, this observation suggests that IP$_6$ could play a role in the regulation of metal ion cellular storage such as iron. To investigate a potential increase of iron chelation affecting the free iron cellular pool, we measured the cellular free $Fe^{2+/3+}$ content using standard cell lysis and colorimetric assay. We detected a 58% depletion in total free iron levels in *MINPP1* mutant cells under high iron conditions (Fig.5B). Interestingly, this depletion was mainly contributed by a decrease in $Fe^{3+}$

levels (Fig.5C, D). $IP_6$, the major IPs accumulating in mutant HEK293, is known to have higher affinity for $Fe^{3+}$ versus $Fe^{2+}$ [42,43]. These data are consistent with a massive accumulation of complexed iron in the absence of the MINPP1 enzyme, in the presence of high iron, and suggest the potential involvement of $IP_6$-mediated abnormal cation homeostasis as the underlying disease mechanism.

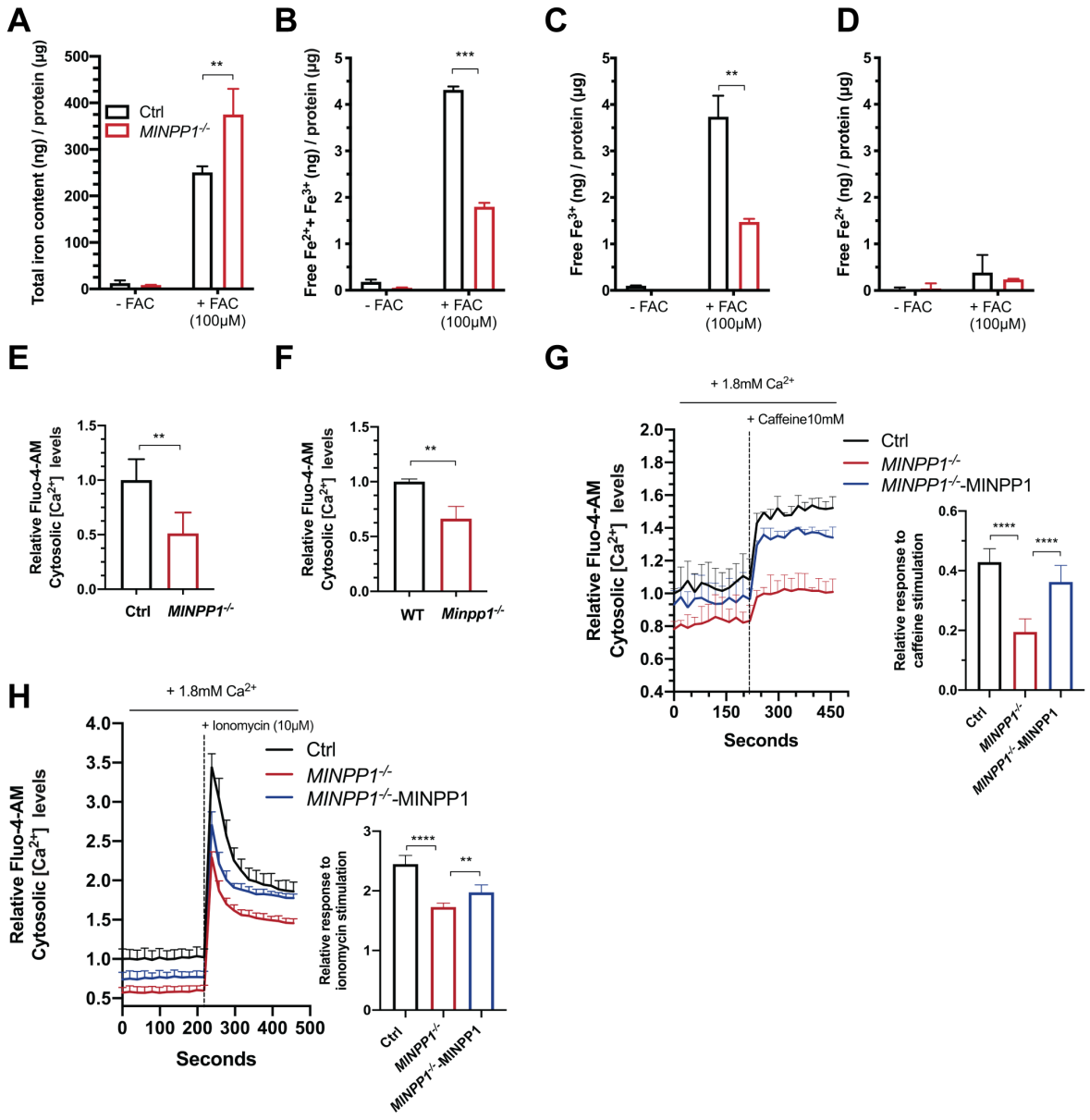


**Figure 5: Altered iron and calcium homeostasis in the absence of MINPP1 enzyme in HEK293 and *Minpp1*$^{-/-}$ mouse neural progenitor cells. (A-D)** Quantification of total iron content (**A**), free iron ($Fe^{2+}$ and $Fe^{3+}$) (**B**), $Fe^{3+}$ (**C**) and $Fe^{2+}$ (**D**) levels in extracts from control and *MINPP1*$^{-/-}$ HEK293 cells grown under low (-FAC) and high iron (+FAC, 100 µM) conditions. All values are normalized to the

total protein concentration and represent the mean ± s.d (n=3, Two-way ANOVA Sidak test, **, *** indicate p values p<0.01 and p<0.001, respectively). (**E-F**) Relative Fluo-4-AM cytosolic $Ca^{2+}$ levels in control and *MINPP1*$^{-/-}$ HEK293 cells **(E)**, wild-type (WT) and *Minpp1*$^{-/-}$ E14 mouse neural progenitors **(F). (G-H)** Relative Fluo-4-AM cytosolic $Ca^{2+}$ levels in control, *MINPP1*$^{-/-}$ and MINPP1 over-expression stable line in *MINPP1*$^{-/-}$ HEK293 cells (*MINPP1*$^{-/-}$-MINPP1) loaded either with 10 mM caffeine (**G**) or 10 µM ionomycin (**H**). The dotted line indicates the addition of either caffeine (**G**) or ionomycin (**H**). Relative response after caffeine or ionomycin stimulation (peak) is represented graphically (inset). For all of the calcium assay experiments, the data are normalized to cell number with MTT colorimetric assay and presented as mean values relative to control baseline fluorescence intensity control ± s.d. ((**E**) n=5; (**F**) N=3 mice, (**G-H**) n=6, Two-tailed student's t-test (E-F) and one-way ANOVA, Tukey's post hoc test (G-H), ** and **** indicate p values p<0.01 and p<0.0001, respectively).

**$IP_6$ accumulation causes cytosolic calcium depletion in mutant HEK293 and primary mouse neural progenitors**

To further explore the involvement of the disruption of cellular cations homeostasis in PCH, we evaluated the intracellular free $Ca^{2+}$ levels in the absence of MINPP1, using the FLUO-4-AM calcium binding indicator. Strikingly, we found a significant, close to 50% depletion of free basal $Ca^{2+}$ levels in *MINPP1*$^{-/-}$ HEK293, compared to control cell line (Fig. 5E). To further validate the involvement of such calcium depletion in the neurological phenotype, we generated a CRISPR/Cas9-mediated *Minpp1*$^{-/-}$ mouse model (Supplementary Fig. 5A-E). *Minpp1* KO mice were fertile and are born at Mendelian ratio (data not shown) as described in a previously generated *Minpp1* KO mouse model[31]. Brain histology did not identify major differences in cerebellar (Supplementary Fig.5C) or cerebral cortex architecture (not shown). However, we identified a mild but significant ~10% decrease in the brain weight associated with a reduced cortical thickness in homozygous mutant mice at P21 (Supplementary Fig.5D, E). This observation suggests the presence of an evolutionarily conserved requirement for MINPP1 activity in mammalian brain development. To identify a potential cause for this cortical phenotype, we isolated

neural progenitors at E14.5 and measured the intracellular free $Ca^{2+}$ levels. Surprisingly, we observed a significant 33.6% decrease in intracellular free $Ca^{2+}$ levels in the *Minpp1*$^{-/-}$ mouse cells when compared to wild type neural progenitors (p=0.007; Fig. 5F).

To assess the effects of $IP_6$ accumulation on calcium signaling, we studied the caffeine sensitive ER calcium release in the *MINPP1*$^{-/-}$ HEK293 cells[44]. In response to 10 mM caffeine, we observed a significant peak in the cytosolic $Ca^{2+}$ levels within a minute in the control cells. However, we could only detect a slight increase with a sustained plateau in *MINPP1*$^{-/-}$ HEK293 cells, indicating an altered response potentially caused by a decrease of $Ca^{2+}$ in intracellular ER stores (Fig.5G). To further study the $Ca^{2+}$ mobilization in *MINPP1*$^{-/-}$ HEK293 cells, we treated the cells with ionomycin as it is known to initially increase the cytoplasmic calcium levels, which in turn activates calcium induced calcium response and eventually causes $Ca^{2+}$ depletion in the ER[45]. In response to ionomycin, the control and *MINPP1*$^{-/-}$ HEK293 cells exhibited an initial $Ca^{2+}$ peak with a sustained plateau. However, the relative response to ionomycin stimulation was again significantly decreased in *MINPP1*$^{-/-}$ cells (Fig.5H). These calcium signaling defects were specifically rescued in a *MINPP1*$^{-/-}$ HEK293 line with stable expression of MINPP1 (Fig.5G and H). Interestingly, we observed similar results in the absence of extracellular calcium (Supplementary Fig. 5F and G), for both caffeine and ionomycin, indicating that the defect is not due to the inhibition of calcium entry. Therefore, these results clearly suggest that MINPP1 absence affects the calcium levels in the cytosol as well as in the intracellular stores such as the ER. Altogether, these data support the critical role played by MINPP1 in the regulation of the intracellular IPs and available cations with strong implications for neural cell signaling and homeostasis.

## DISCUSSION

The direct physiological role(s) played by $IP_6$ in mammals has been difficult to define, due to the technical challenges associated with its measurement, and its complex anabolism. Furthermore, the well described role of $IP_6$ (phytate) and phytase activity in plants and bacteria had led to the thinking that extracellular $IP_6$ degradation also supplies mammalian cells with phosphate and cations. On the contrary, we demonstrate that intracellular, not extracellular, $IP_6$ influences cation homeostasis. An imbalance of IPs derivatives has not been so far directly involved in disease, and the previously investigated *Minpp1*

KO mouse did not reveal any obvious phenotype [31]. Surprisingly, we discovered that the absence of MINPP1 in humans results in a very severe early-onset neurodegenerative disorder with specific features. Patients with loss of function mutations in the *MINPP1* gene present with PCH associated with typical basal ganglia or thalami involvement identified by MRI. The prenatal onset of the phenotype is obvious for patient CerID-11, which supports a critical and early role for MINPP1 in neuronal development and survival. In agreement with this, we observed that patient-derived and genome-edited iPSCs mutant for *MINPP1* cannot be differentiated toward neural progenitors that efficiently give rise to neurons. This defect is associated with a significant increase in apoptosis levels among the *MINPP1* mutant cells. Interestingly, this cell survival defect could recapitulate the neurodegenerative phenotype observed in the patients. Although the exact mechanisms underlying the inefficient differentiation and the apoptosis have not been identified yet, the sensitivity of human differentiating neurons to the disruption of IPs metabolism is likely to be involved [46].

While a key role for MINPP1 in the regulation of $IP_6$ cellular levels has been investigated before[31], we provide the first evidence for its critical importance on cellular physiology and human development. Our analysis of IPs profiles using metabolic labelling unambiguously identified a typical imbalance resulting from MINPP1 defect. The increase in $IP_5$ and $IP_6$ levels is consistent with a previous mouse model study[8], but our more complete assessment of the IPs metabolism imbalance also revealed alterations in lower phosphorylated IPs. Furthermore, the consequences of this metabolic block are associated with cell type-dependent differences in the IPs profile, such as the $IP_4$ depletion in mutant iPSCs and robust $IP_6$ accumulation in day-10 differentiating neurons mutated for *MINPP1*.

The discrepancy related to the supposed mostly cytosolic localization of $IP_6$ and the ER localization of MINPP1 remains an unsolved problem [19, 26, 31]. Hypothetically, the specific subcellular localization of MINPP1 prevents $IP_6$ accumulation in a specific compartment (e.g. the ER) that would have primary consequences on local cation homeostasis. We identified that MINPP1-mediated $IP_6$ regulation impacts free cations availability, as illustrated with the altered iron content of *MINPP1*$^{-/-}$ HEK293 cells as well as the severe depletion of cytosolic calcium identified in *Minpp1*$^{-/-}$ mouse primary neural progenitors

and HEK293 cells. Interestingly, the absence of MINPP1 also severely disrupts signaling based on ER calcium that could potentially be the place of the primary defect. Calcium signaling has broad functions in neural cell physiology and brain development. Basal calcium levels influence neuronal physiology and cell survival [47-49], and calcium signaling plays a role in neural induction and differentiation [50-53]. Consequently, a disruption in calcium homeostasis could be involved in PCH disease pathogenesis. A link between MINPP1 and calcium regulation has been suggested previously but it was through the synthesis of $I(1,4,5)P_3$ [54]. Hypothetically, coupling the limitation of $IP_6$-mediated chelation of calcium with the promotion of $IP_3$ synthesis could be an efficient way for MINPP1 to regulate calcium signaling dynamics and homeostasis.

A mild or absent structural brain defect was also observed in other PCH mouse models. *AMPD2* null mutations cause PCH9 but the *Ampd2* single KO mouse is not associated with any obvious histological brain defect [55]. *CLP1* is involved in tRNA processing and mutated in PCH10, however the *Clp1* mutant mouse showed only a mild decrease in the brain weight and volume, a phenotype overlooked before the identification of patients with a brain phenotype [56]. Differences in the phenotype of human and mouse with *MINPP1* loss-of-function mutations could be related to an increased sensitivity of the human brain development to metabolic defects, although the impact of the genetic background cannot be excluded at this point.

Disrupted cation homeostasis, including metal accumulation, is central to multiple degenerative disorders[57] such as neurodegeneration with brain iron accumulation[58,59], Parkinson's disease (Manganese accumulation)[60,61], Wilson's disease (Copper accumulation)[62,63]. Basal ganglia dysfunction is usually suspected in PCH[25], however the severe defects identified in *MINPP1* patient MRIs suggest major neurodegeneration at the level of these subcortical nuclei, a feature not typically associated with other PCH subtypes. These structures are well known to be primarily affected by metal ions accumulation and further investigation will be needed to determine how cation chelation could contribute to the disease pathogenesis. Nevertheless, our results reveal an unappreciated basic role for highly phosphorylated IPs in cellular homeostasis which is critical during neurodevelopment.

**SUPPLEMENTARY FIGURES AND LEGENDS**

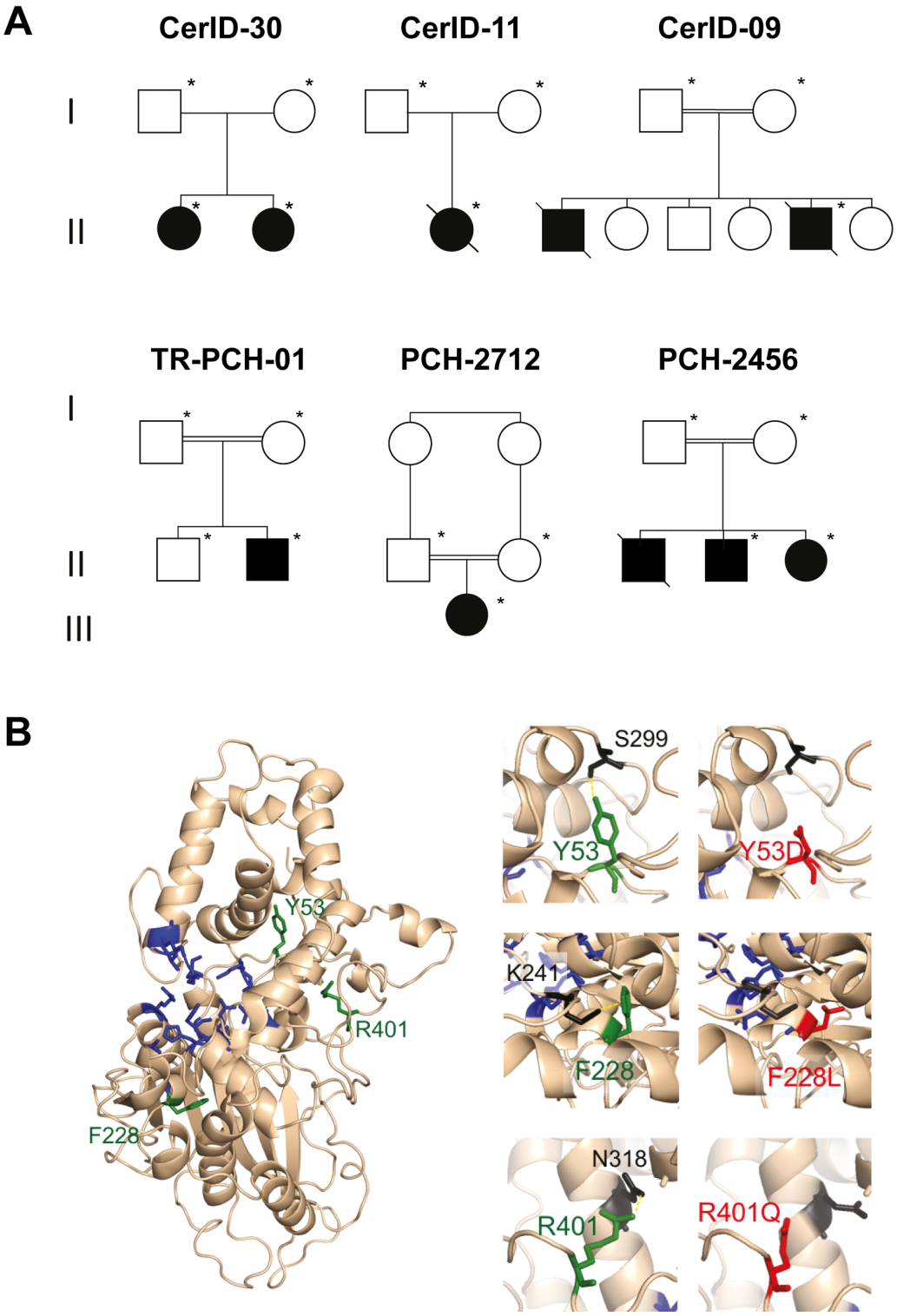


**Supplementary Figure 1. Family pedigrees and *in silico* prediction analysis of the missense *MINPP1* variants. (A)** Pedigrees of families with mutations in the *MINPP1* gene**.** Individuals subjected to Whole Exome Sequencing (WES) or Sanger Sequencing are indicated with asterisk. Additional DNA

samples for family CerID-09 could not be collected for segregation analysis. (**B**) Wildtype MINPP1 with amino acids involved in $IP_6$ binding are indicated in blue and amino acids mutated with missense variants are indicated in green. The Missense3D server predicted that all the three missense variants tested cause structural damage.

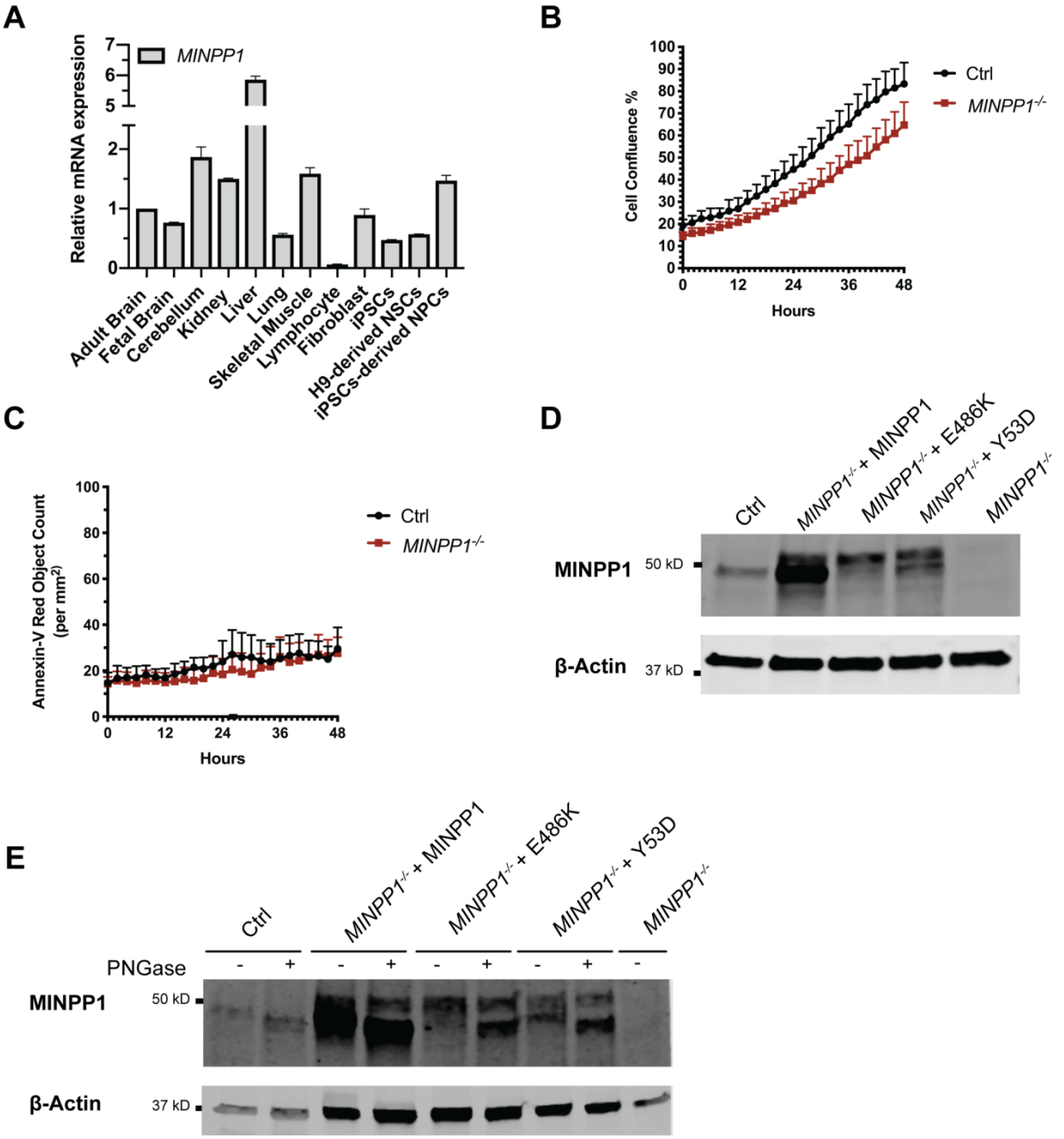


**Supplementary Figure 2: Expression profile of *MINPP1* in different human tissues and protein levels of MINPP1 variants and their corresponding glycosylation status in HEK293 cells. (A)**

Quantitative PCR analysis of human *MINPP1* expression, normalized with *ACTB*, in human cells and tissues. Abbreviations used: Neural Stem Cells (NSCs); Neuronal Progenitor Cells (NPCs) **(B)** Control and *MINPP1*$^{-/-}$ HEK293 were cultured for 48 hours in IncuCyte live-cell analysis system and cell confluence (%) was analysed in IncuCyte Zoom live-cell-imaging software. Graph shows the percentage of cell confluence (± s.d.) over time. **(C)** Control and *MINPP1*$^{-/-}$ HEK293 were cultured with Annexin-V containing growth media for 48 hours inside the IncuCyte live-cell analysis system, and images were captured with red fluorescence channel to detect Annexin-V positive cells. Graph shows the average ratio (±s.d.) of red cell object count per $mm^2$ (n=3, two-tailed student's t-test, not significant) **(D-E)** Western blot data showing the exogenous MINPP1 levels (D) and its glycosylated and deglycosylated forms (E) in *MINPP1*$^{-/-}$ HEK293 cells transiently transfected with plasmids encoding empty vector, wild type, Y53D or E486K variant MINPP1. MINPP1 is present in control HEK293 cells and absent in *MINPP1*$^{-/-}$ HEK293 cells. β-Actin shown as loading control.

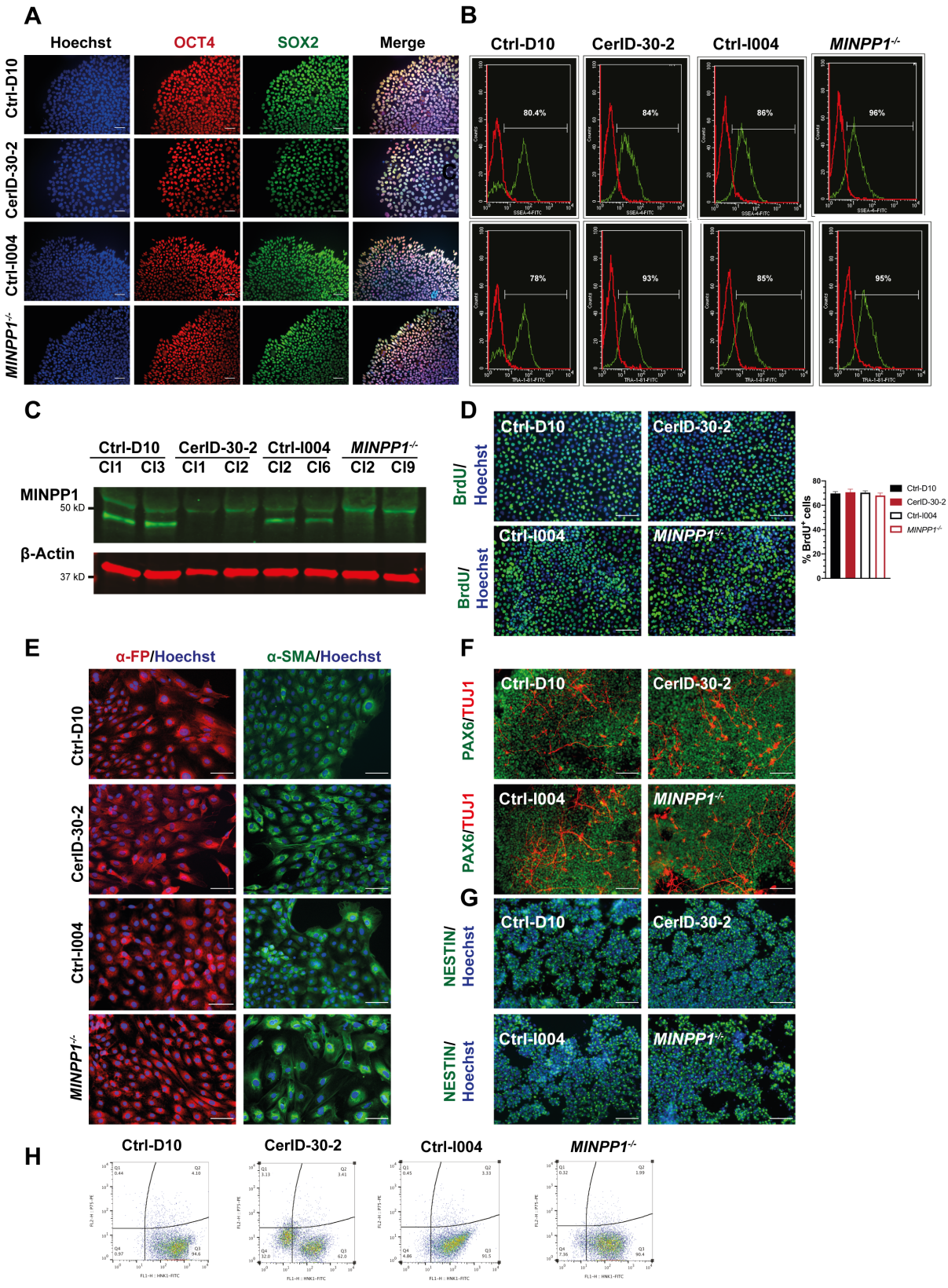


**Supplementary Figure 3. Characterization of patient-derived (CerID-30-2) and *MINPP1*$^{-/-}$ iPSCs and their neural derivatives. (A)** Immunofluorescence staining of embryonic stem cell markers OCT4 and SOX2 and **(B)** flow cytometer analysis of pluripotency markers SSEA-4 and TRA-1-81 in control

(Ctrl-D10 and Ctrl-I004), patient-derived (CerID-30-2), and *MINPP1*$^{-/-}$ iPSCs. **(C)** Western blot data showing the absence of MINPP1 in patient-derived CerID-30-2 and *MINPP1*$^{-/-}$ iPSCs. MINPP1 (48 kDa) is present in controls (Ctrl-D10 and Ctrl-I004) iPSC lines (lower band). β-actin is shown as loading control. **(D)** Representative images and quantification data of $BrdU^{+}$ staining assay in control (Ctrl-D10 and Ctrl-I004), patient-derived (CerID-30-2), and *MINPP1*$^{-/-}$ iPSCs. **(E)** Immunofluorescence staining of endoderm (alpha-Fetoprotein(AFP)) and mesoderm (smooth muscle actin (α-SMA)) markers following embryoid formation from control (Ctrl-D10 and Ctrl-I004), patient-derived (CerID-30-2), and *MINPP1*$^{-/-}$ iPSCs. **(F-G)** Representative immunofluorescence images of (**F**) PAX6 /TUJ1 and (**G**) NESTIN for control (Ctrl-D10 and Ctrl-I004), patient-derived (CerID-30-2) and *MINPP1*$^{-/-}$ iPSCs during neuronal differentiation at day 10 and day 14, respectively. **(H)** Flow cytometer analysis of P75 and HNK1 in control (Ctrl-D10 and Ctrl-I004), patient-derived (CerID-30-2) and *MINPP1*$^{-/-}$ neural rosette cultures. All scale bars correspond to 50 μm.

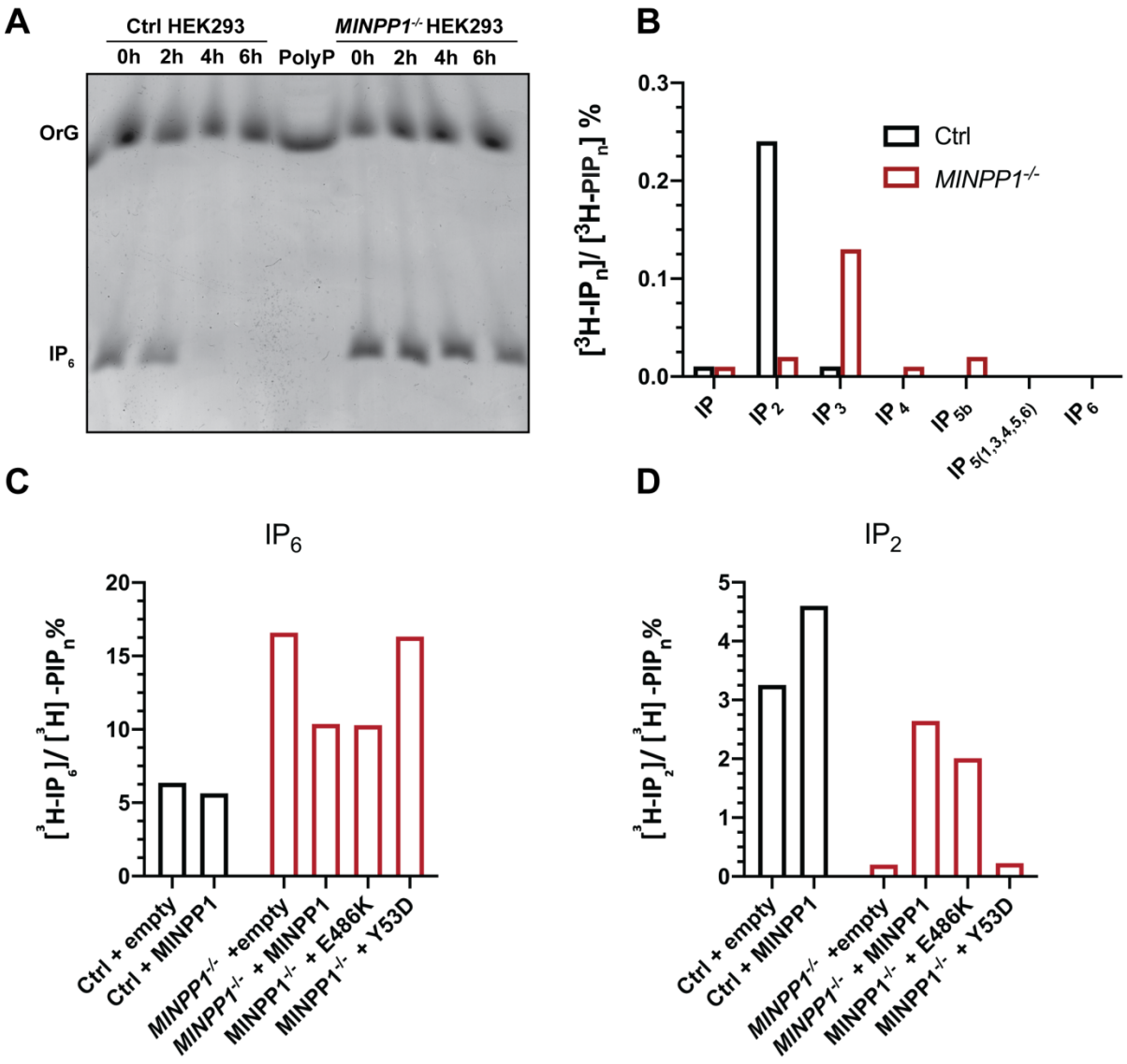


**Supplementary Figure 4. Phytase activity and SAX-HPLC analysis of extracellular and intracellular inositol phosphate levels.** (**A**) MINPP1 phytase activity in conditioned medium of *MINPP1*$^{-/-}$ HEK293 cells upon addition of 4 nmol of $IP_6$ and incubation at 37°C for the time period indicated above. The samples were then mixed with Orange G (OrG) loading dye and resolved by PAGE followed by toluidine blue staining. Gel image representative of two independent experiments. Polyphosphate (PolyP) is shown as size ladder. (**B**) SAX-HPLC analysis of inositol phosphate levels in cell culture media of [$^3$H]-inositol labeled control and *MINPP1*$^{-/-}$ HEK293 cells. **(C-D)** SAX-HPLC analysis of $IP_2$ and $IP_6$ levels in control and *MINPP1*$^{-/-}$ HEK293 cells transiently transfected with plasmids encoding empty vector, wildtype, Y53D or E486K variant MINPP1. The data is representative of two independent experiments. [$^3$H]-$IP_n$ levels are presented as percentage of total radioactivity in the

inositol-lipid fraction ([$^3$H]-PIP$_n$). Abbreviations used: IPn, inositol phosphates; PIPn, phosphatidyl inositol phosphates.

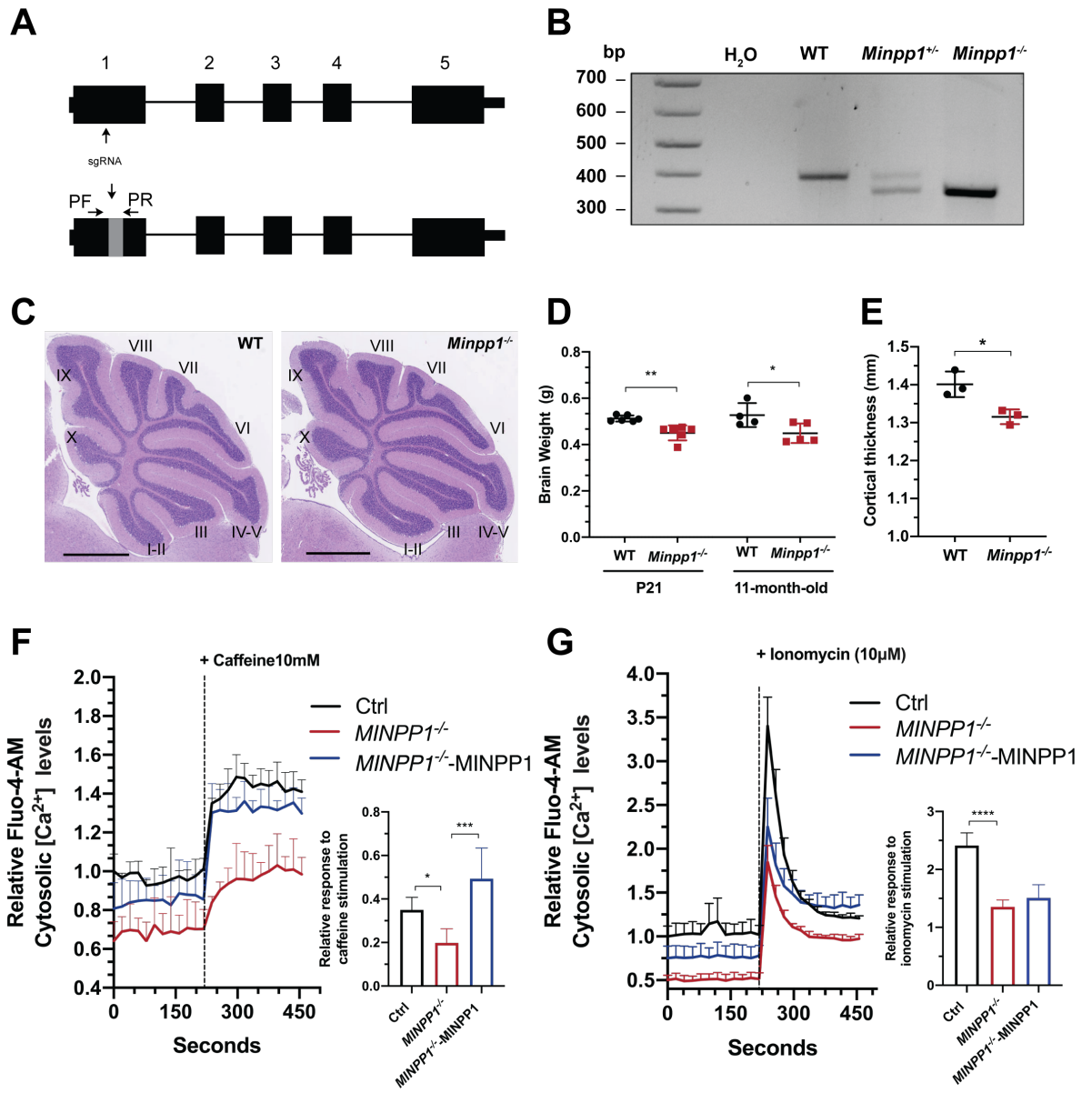


**Supplementary Figure 5: Generation and characterization of CRISPR-Cas9 Minpp1$^{-/-}$ mouse and Ca$^{2+}$ assays on HEK293 cell lines. (A)** Schema of the sgRNA targeting site and the location of PCR primers. Abbreviations used: Primer Forward (PF) and Primer Reverse (PR). (**B**) PCR based genotyping of *Minpp1*$^{-/-}$ mice indicated successful knockout alleles showing a 31 bp deletion and a smaller PCR product. (**C**) Representative images of hematoxylin-eosin (HE) staining on P21 sagittal slices of control and mutant cerebellum, scale bar 1 mm. (**D**) Quantification of total brain weight in grams (g) from P21 and 11-month old WT and *Minpp1*$^{-/-}$ mice. (N≥4 mice, Two-tailed student's t-test, * and ** indicate p

values $p<0.05$ and $p<0.01$, respectively). (**E**) Quantification of cortical thickness for the WT and *Minpp1*$^{-/-}$ cortex at P21 (N=3 mice, 30 sections per each mouse; Two-tailed Student's t-test, * indicates p value $p<0.05$). (**F-G**) Relative Fluo-4-AM cytosolic $Ca^{2+}$ levels in control, *MINPP1*$^{-/-}$ HEK293 and MINPP1 over-expression stable *MINPP1*$^{-/-}$ HEK293 cell lines (*MINPP1*$^{-/-}$-MINPP1) loaded either with 10 mM caffeine (**G**) or 10 µM ionomycin in the absence of extracellular $Ca^{2+}$. The dotted line indicates the addition of either caffeine (**F**) or ionomycin (**G**). Relative response after caffeine or ionomycin stimulation (peak) is represented graphically (inset). For all of the calcium assay experiments, the data are normalized to cell number with MTT colorimetric assay and presented as mean values relative to control baseline fluorescence intensity control ± s.d. (**F-G**) n=6, one-way ANOVA, Tukey's post hoc test, *, ***, **** indicate p values $p<0.05$, $p\leq 0.001$ and $p<0.0001$, respectively).

## ACKNOWLEDGMENTS

The project is funded by the French National Research Agency ANR-16-CE12- 0005-01 (VC), the Fondation pour la Recherche Médicale FRM-DEQ20160334938 (LC and VC) and FRM-FDT201904007935 (EU). This work was also supported by State funding from the Agence Nationale de la Recherche under "Investissements d'avenir" program (ANR-10-IAHU-01), the Fondation Bettencourt Schueller and the MSDAvenir fund (DEVO-DECODE project). A.S. and M.W. are supported by the Medical Research Council (MRC) awards (MC_UU_12018/4 and MC_UU_00012/4). We are grateful to families of patients for their participation and Dr B. Isidor for the clinical-follow up. We sincerely thank S. Jaalouk, V. Meneghini, F. Petit and A. Rotig for technical help and advice.

## AUTHOR CONTRIBUTIONS

Recruitment and evaluation of subjects: G.B., M.-T.V.-D., G.P., E.L., N.R., E.B., M.Z., M.T., F.M.S., D.M., F.G., A.M., N.B., N.B.-B., C.F. Genetic sequencing and interpretations: N.A.,V.S., C.B.-F., P.N., L.C., L.B., J.G.G., V.C. Inositol labelling and analysis: M.W. and A.S. iPSCs generation and characterization: E.U., D.M.-C., K.R., C.B., N.L. Mouse generation and characterization: K.R. and P.D. Neural differentiation and cell biology experiments: E.U. and K.R.

**COMPETING INTERESTS STATEMENT**

The authors declare no competing financial interests.

## REFERENCES


1. Irvine, R.F. & Schell, M.J. Back in the water: the return of the inositol phosphates. *Nat Rev Mol Cell Biol* **2**, 327-38 (2001).
2. Irvine, R.F. 20 years of Ins(1,4,5)P3, and 40 years before. *Nat Rev Mol Cell Biol* **4**, 586-90 (2003).
3. York, J.D. Regulation of nuclear processes by inositol polyphosphates. *Biochim Biophys Acta* **1761**, 552-9 (2006).
4. Raboy, V. myo-Inositol-1,2,3,4,5,6-hexakisphosphate. *Phytochemistry* **64**, 1033-43 (2003).
5. Shears, S.B. Assessing the omnipotence of inositol hexakisphosphate. *Cell Signal* **13**, 151-8 (2001).
6. Desfougeres, Y., Wilson, M.S.C., Laha, D., Miller, G.J. & Saiardi, A. ITPK1 mediates the lipid-independent synthesis of inositol phosphates controlled by metabolism. *Proc Natl Acad Sci U S A* (2019).
7. Wilson, M.S., Livermore, T.M. & Saiardi, A. Inositol pyrophosphates: between signalling and metabolism. *Biochem J* **452**, 369-79 (2013).
8. Chi, H. *et al.* Multiple inositol polyphosphate phosphatase: evolution as a distinct group within the histidine phosphatase family and chromosomal localization of the human and mouse genes to chromosomes 10q23 and 19. *Genomics* **56**, 324-36 (1999).
9. Craxton, A., Caffrey, J.J., Burkhart, W., Safrany, S.T. & Shears, S.B. Molecular cloning and expression of a rat hepatic multiple inositol polyphosphate phosphatase. *Biochem J* **328 ( Pt 1)**, 75-81 (1997).
10. Wilson, M.P. *et al.* Neural tube defects in mice with reduced levels of inositol 1,3,4-trisphosphate 5/6-kinase. *Proc Natl Acad Sci U S A* **106**, 9831-5 (2009).
11. Frederick, J.P. *et al.* An essential role for an inositol polyphosphate multikinase, Ipk2, in mouse embryogenesis and second messenger production. *Proc Natl Acad Sci U S A* **102**, 8454-9 (2005).
12. Hawkins, P.T. *et al.* Inhibition of iron-catalysed hydroxyl radical formation by inositol polyphosphates: a possible physiological function for myo-inositol hexakisphosphate. *Biochem J* **294 ( Pt 3)**, 929-34 (1993).
13. Poyner, D.R., Cooke, F., Hanley, M.R., Reynolds, D.J. & Hawkins, P.T. Characterization of metal ion-induced [3H]inositol hexakisphosphate binding to rat cerebellar membranes. *J Biol Chem* **268**, 1032-8 (1993).
14. Veiga, N. *et al.* The behaviour of myo-inositol hexakisphosphate in the presence of magnesium(II) and calcium(II): protein-free soluble InsP6 is limited to 49 microM under cytosolic/nuclear conditions. *J Inorg Biochem* **100**, 1800-10 (2006).
15. Brehm, M.A. & Windhorst, S. New options of cancer treatment employing InsP6. *Biochem Pharmacol* **163**, 206-214 (2019).
16. Irigoin, F. *et al.* Unique precipitation and exocytosis of a calcium salt of myo-inositol hexakisphosphate in larval Echinococcus granulosus. *J Cell Biochem* **93**, 1272-81 (2004).
17. Letcher, A.J., Schell, M.J. & Irvine, R.F. Do mammals make all their own inositol hexakisphosphate? *Biochem J* **416**, 263-70 (2008).
18. Wilson, M.S., Bulley, S.J., Pisani, F., Irvine, R.F. & Saiardi, A. A novel method for the purification of inositol phosphates from biological samples reveals that no phytate is present in human plasma or urine. *Open Biol* **5**, 150014 (2015).
19. Stuart, J.A., Anderson, K.L., French, P.J., Kirk, C.J. & Michell, R.H. The intracellular distribution of inositol polyphosphates in HL60 promyeloid cells. *Biochem J* **303 ( Pt 2)**, 517-25 (1994).

20. Otto, J.C., Kelly, P., Chiou, S.T. & York, J.D. Alterations in an inositol phosphate code through synergistic activation of a G protein and inositol phosphate kinases. *Proc Natl Acad Sci U S A* **104**, 15653-8 (2007).
21. Staiano, L., De Leo, M.G., Persico, M. & De Matteis, M.A. Mendelian disorders of PI metabolizing enzymes. *Biochim Biophys Acta* **1851**, 867-81 (2015).
22. Yousaf, R. *et al.* Mutations in Diphosphoinositol-Pentakisphosphate Kinase PPIP5K2 are associated with hearing loss in human and mouse. *PLoS Genet* **14**, e1007297 (2018).
23. Khaled, M.L. *et al.* PPIP5K2 and PCSK1 are Candidate Genetic Contributors to Familial Keratoconus. *Sci Rep* **9**, 19406 (2019).
24. Rusch, C.T., Bolsterli, B.K., Kottke, R., Steinfeld, R. & Boltshauser, E. Pontocerebellar Hypoplasia: a Pattern Recognition Approach. *Cerebellum* **19**, 569-582 (2020).
25. van Dijk, T., Baas, F., Barth, P.G. & Poll-The, B.T. What's new in pontocerebellar hypoplasia? An update on genes and subtypes. *Orphanet J Rare Dis* **13**, 92 (2018).
26. Chemin, J. *et al.* De novo mutation screening in childhood-onset cerebellar atrophy identifies gain-of-function mutations in the CACNA1G calcium channel gene. *Brain* **141**, 1998-2013 (2018).
27. Megahed, H. *et al.* Utility of whole exome sequencing for the early diagnosis of pediatric-onset cerebellar atrophy associated with developmental delay in an inbred population. *Orphanet J Rare Dis* **11**, 57 (2016).
28. Windhorst, S. *et al.* Tumour cells can employ extracellular Ins(1,2,3,4,5,6)P(6) and multiple inositol-polyphosphate phosphatase 1 (MINPP1) dephosphorylation to improve their proliferation. *Biochem J* **450**, 115-25 (2013).
29. Ali, N., Craxton, A. & Shears, S.B. Hepatic Ins(1,3,4,5)P4 3-phosphatase is compartmentalized inside endoplasmic reticulum. *J Biol Chem* **268**, 6161-7 (1993).
30. Nogimori, K. *et al.* Purification of an inositol (1,3,4,5)-tetrakisphosphate 3-phosphatase activity from rat liver and the evaluation of its substrate specificity. *J Biol Chem* **266**, 16499-506 (1991).
31. Chi, H. *et al.* Targeted deletion of Minpp1 provides new insight into the activity of multiple inositol polyphosphate phosphatase in vivo. *Mol Cell Biol* **20**, 6496-507 (2000).
32. Medina-Cano, D. *et al.* High N-glycan multiplicity is critical for neuronal adhesion and sensitizes the developing cerebellum to N-glycosylation defect. *Elife* **7**(2018).
33. Boissart, C. *et al.* Differentiation from human pluripotent stem cells of cortical neurons of the superficial layers amenable to psychiatric disease modeling and high-throughput drug screening. *Transl Psychiatry* **3**, e294 (2013).
34. Chambers, S.M. *et al.* Highly efficient neural conversion of human ES and iPS cells by dual inhibition of SMAD signaling. *Nat Biotechnol* **27**, 275-80 (2009).
35. Gerrard, L., Rodgers, L. & Cui, W. Differentiation of human embryonic stem cells to neural lineages in adherent culture by blocking bone morphogenetic protein signaling. *Stem Cells* **23**, 1234-41 (2005).
36. Cheng, Y.L. & Andrew, D.J. Extracellular Mipp1 Activity Confers Migratory Advantage to Epithelial Cells during Collective Migration. *Cell Rep* **13**, 2174-88 (2015).
37. Azevedo, C. & Saiardi, A. Extraction and analysis of soluble inositol polyphosphates from yeast. *Nat Protoc* **1**, 2416-22 (2006).
38. Saiardi, A. & Mudge, A.W. Lithium and fluoxetine regulate the rate of phosphoinositide synthesis in neurons: a new view of their mechanisms of action in bipolar disorder. *Transl Psychiatry* **8**, 175 (2018).
39. Cho, J. *et al.* Avian multiple inositol polyphosphate phosphatase is an active phytase that can be engineered to help ameliorate the planet's "phosphate crisis". *J Biotechnol* **126**, 248-59 (2006).
40. Riemer, J., Hoepken, H.H., Czerwinska, H., Robinson, S.R. & Dringen, R. Colorimetric ferrozine-based assay for the quantitation of iron in cultured cells. *Anal Biochem* **331**, 370-5 (2004).
41. Drecourt, A. *et al.* Impaired Transferrin Receptor Palmitoylation and Recycling in Neurodegeneration with Brain Iron Accumulation. *Am J Hum Genet* **102**, 266-277 (2018).
42. Hambidge, K.M. Micronutrient bioavailability: Dietary Reference Intakes and a future perspective. *Am J Clin Nutr* **91**, 1430s-1432s (2010).
43. Nielsen, A.V., Tetens, I. & Meyer, A.S. Potential of phytase-mediated iron release from cereal-based foods: a quantitative view. *Nutrients* **5**, 3074-98 (2013).

44. Rossi, D. *et al.* RyR1 and RyR3 isoforms provide distinct intracellular Ca2+ signals in HEK 293 cells. *J Cell Sci* **115**, 2497-504 (2002).
45. Muller, M.S., Obel, L.F., Waagepetersen, H.S., Schousboe, A. & Bak, L.K. Complex actions of ionomycin in cultured cerebellar astrocytes affecting both calcium-induced calcium release and store-operated calcium entry. *Neurochem Res* **38**, 1260-5 (2013).
46. Loss, O., Wu, C.T., Riccio, A. & Saiardi, A. Modulation of inositol polyphosphate levels regulates neuronal differentiation. *Mol Biol Cell* **24**, 2981-9 (2013).
47. Ryu, C. *et al.* STIM1 Regulates Somatic Ca(2+) Signals and Intrinsic Firing Properties of Cerebellar Purkinje Neurons. *J Neurosci* **37**, 8876-8894 (2017).
48. Betzer, C. & Jensen, P.H. Reduced Cytosolic Calcium as an Early Decisive Cellular State in Parkinson's Disease and Synucleinopathies. *Front Neurosci* **12**, 819 (2018).
49. Betzer, C. *et al.* Alpha-synuclein aggregates activate calcium pump SERCA leading to calcium dysregulation. *EMBO Rep* **19**(2018).
50. Lin, H.H. *et al.* Neuronatin promotes neural lineage in ESCs via Ca(2+) signaling. *Stem Cells* **28**, 1950-60 (2010).
51. Ringler, S.L., Aye, J., Byrne, E., Anderson, M. & Turner, C.P. Effects of disrupting calcium homeostasis on neuronal maturation: early inhibition and later recovery. *Cell Mol Neurobiol* **28**, 389-409 (2008).
52. West, A.E. *et al.* Calcium regulation of neuronal gene expression. *Proc Natl Acad Sci U S A* **98**, 11024-31 (2001).
53. Moreau, M. *et al.* Ca(2+) coding and decoding strategies for the specification of neural and renal precursor cells during development. *Cell Calcium* **59**, 75-83 (2016).
54. Yu, J. *et al.* Cytosolic multiple inositol polyphosphate phosphatase in the regulation of cytoplasmic free Ca2+ concentration. *J Biol Chem* **278**, 46210-8 (2003).
55. Akizu, N. *et al.* AMPD2 regulates GTP synthesis and is mutated in a potentially treatable neurodegenerative brainstem disorder. *Cell* **154**, 505-17 (2013).
56. Karaca, E. *et al.* Human CLP1 mutations alter tRNA biogenesis, affecting both peripheral and central nervous system function. *Cell* **157**, 636-50 (2014).
57. White, A.R., Kanninen, K.M. & Crouch, P.J. Editorial: Metals and neurodegeneration: restoring the balance. *Front Aging Neurosci* **7**, 127 (2015).
58. Levi, S. & Finazzi, D. Neurodegeneration with brain iron accumulation: update on pathogenic mechanisms. *Front Pharmacol* **5**, 99 (2014).
59. Di Meo, I. & Tiranti, V. Classification and molecular pathogenesis of NBIA syndromes. *Eur J Paediatr Neurol* **22**, 272-284 (2018).
60. Juneja, M. *et al.* A novel mutation in SLC39A14 causing hypermanganesemia associated with infantile onset dystonia. *J Gene Med* **20**, e3012 (2018).
61. Parmalee, N.L. & Aschner, M. Manganese and aging. *Neurotoxicology* **56**, 262-268 (2016).
62. Skjorringe, T., Moller, L.B. & Moos, T. Impairment of interrelated iron- and copper homeostatic mechanisms in brain contributes to the pathogenesis of neurodegenerative disorders. *Front Pharmacol* **3**, 169 (2012).
63. Bandmann, O., Weiss, K.H. & Kaler, S.G. Wilson's disease and other neurological copper disorders. *Lancet Neurol* **14**, 103-13 (2015).

## ONLINE METHODS

### Patients recruitment and investigation

The patients from families CerID-09, CerID-11 and CerID-30 included in this project were referred to the Departments of Pediatric Neurology, Genetics, Metabolism or Ophthalmology of the Necker Enfants Malades Hospital. Family TR-PCH-01 was recruited by the French Reference Centre for Cerebellar Malformations and Congenital Diseases at Trousseau Hospital. Patients from families PCH-2456 and PCH-2712 were referred for neurological or genetic assessment at the National Research Center in Cairo and Hacettepe University Medical Faculty Department of Pediatric Neurology in Turkey. Written informed consents have been obtained both from the participants and the legal representatives of the children. Details regarding sequencing, filtering and prioritization protocols for each family are outlined in Supplementary Note.

### Protein Multiple Sequence Alignment:

The following protein sequences are aligned through COBALT:Multiple Alignment tool: NP_004888.2 (H. Sapiens MINPP1), NP_034929.1 (M. musculus Minpp1), NP_062136.1 (R. norvegicus Minpp1), NP_957394.1 (D. Reiro minpp1b), NP_989975.1 (G. gallus MINPP1), XP_002935472.2 (X. tropicalis minpp1), XP_313302.4 (A. gambiae AGAP003555-PA), NP_563856.1 (A. thaliana histidine acid phosphatase family protein), NP_813655 (B. thetaiotaomicron BtMinpp)

### Maintenance and Culture of Human Induced Pluripotent Stem Cells (hiPSCs), Fibroblasts and HEK293 Cells

All human cell culture and storage protocols were performed with approval from French Research Ministry (DC 2015-2595, 09/05/2016) and all participants provided written consent. hiPSC lines Ctrl-D10 and CerID-30-2 were generated by Duke iPSC Share Resource Facility, using RNA-based reprogramming method. CerID-30-2 and Ctrl-D10 were derived from unrelated individuals. Ctrl-D10 iPSC line was derived from BJ fibroblasts of a non-disease affected male new born (ATCC cell line, CRL-2522). The control hiPSC line (IMAGINi004, referred to as Ctrl-I004 in this study) was generated by Imagine Institute iPSC Platform, using non-integrating Sendai virus approach (CytoTune-2.0). All hiPSC lines were shown to display embryonic pluripotency markers OCT4, SOX2, SSEA-4 and TRA-1-81(Supplementary Fig.3A-B). The absence of obvious chromosomal abnormalities was verified by CGH array 60K (data not shown). The differentiation into mesoderm and endoderm lineage following embryoid body formation was assessed as previously described[1]. Additionally, no obvious differences in proliferation and apoptosis were observed among all the iPSC lines. hiPSCs were maintained in vitronectin-coated (10 µg/ml; 07180, STEMCELL) 3.5 cm dishes (353001, Falcon) in complete mTeSR-

1 medium (STEMCELL, 85850) supplemented with 1% Penicillin-Streptomycin (PS) (15140122, Gibco) in a humidified incubator (5% $CO_2$, 37 °C). The media were replaced daily and iPSCs were mechanically passaged with ROCK inhibitor Y-27632 (10 μM; 72304, STEMCELL) every 7-8 days, with a 1:3 split ratio.

Human primary fibroblasts and HEK293T (HEK293) cells were cultured in Dulbecco's modified Eagle medium (DMEM) (11965092, Gibco) supplemented with 10% Fetal Bovine Serum (FBS) (16000044, Gibco) and 1% PS in a humidified incubator (5% $CO_2$, 37 °C).

**Generation of genome edited *MINPP1*$^{-/-}$ HEK293 and hiPSCs**

*MINPP1*$^{-/-}$ HEK293 and hiPSC lines were generated via a CRISPR-Cas9 genome editing strategy, as previously described[2]. Briefly, sgRNAs targeting the first exon of MINPP1 transcript variant 1 (NM_004897.5) were designed on CRISPOR website (http://crispor.tefor.net/) and further cloned into the pSpCas9(BB)-2A-GFP plasmid (PX458, 48138, Addgene). For the generation of *MINPP1*$^{-/-}$ HEK293 clones, transfection of pSpCas9(sgRNA)-2A-GFP into HEK293 cells was performed with Lipofectamine 2000 (11668019, Invitrogen), as per manufacturer's instructions (2.5 μg of DNA per well of a 6-well plate). Two days post-transfection, single GFP$^+$ HEK293 cells were sorted into 96 well plates by Fluorescence-activated cell sorting (FACS) (BD FACSAria II SORP, BD Biosciences). Indel mutations of clones were detected by Sanger sequencing, and target editing efficiency was assessed by TIDE analysis (https://tide-calculator.nki.nl/; data not shown).

For the generation of *MINPP1*$^{-/-}$ iPSCs clones, transfection of pSpCas9(sgRNA)-2A-GFP into hiPSC line (I004) was performed using Amaxa 4D-Nucleofector X-Unit (AAF-1002X, Lonza) according to manufacturer's instructions. Briefly, hiPSCs were pre-treated with Y-27632 (10 μM) for 1 hour and further dissociated into single cell suspension with Accutase (STEMCELL, 07920). 4 x$10^5$ iPSCs were nucleofected per 20 μl nucleocuvette strip, using P3 Primary Cell 4D X Kit S (V4XP-3032, Lonza), 1μg DNA per reaction, and the program CA-137. After nucleofection, iPSCs were seeded on vitronectin pre-coated 12-well plates and cultured in complete mTeSR-1 medium supplemented with Y-27632 (10 μM). Two days post-transfection, GFP$^+$ iPSCs were sorted by FACS and plated at low densities of 1-2x$10^4$ cells per 6cm dish (Falcon, 353037) in mTeSR-1 medium supplemented with Y-27632 (10 μM). After 12-16 days, a subset of individual colonies was processed for DNA extraction using Quick-DNA/RNA Miniprep Plus Kit (D7003, Zymo) and Sanger sequenced. Target editing efficiency was assessed by TIDE analysis (https://tide-calculator.nki.nl/; data not shown). After clonal selection and expansion, no unusual chromosomal abnormalities were detected by CGH array (60K, data not shown). Validation of *MINPP1*$^{-/-}$ iPSC clones were further assessed by the absence of MINPP1 and the presence of pluripotency markers OCT4 and SOX2 with western blot and immunofluorescence staining respectively (Supplementary Fig.3A, C).

**Generation of *Minpp1*$^{-/-}$ mice**

*Minpp1*$^{-/-}$ mice were generated with the aid of LEAT platform of Imagine Institute by using a CRISPR/Cas9 system. In this study, animals were used in compliance with the French Animal Care and Use Committee from the Paris Descartes University (APAFIS#961-201506231137361). Guide RNAs (sgRNAs) targeting the first exon of the gene were designed via the CRISPOR (http://crispor.tefor.net/). C57Bl/-J female mice (4 weeks old) were super ovulated by intraperitoneal injection of 5 IU PMSG (SYNCRO-PART® PMSG 600 UI, Ceva) followed by 5 IU hCG (Chorulon 1500 UI, Intervet) at an interval of 46-48 hours and mated with C57BL/6J male mice. The next day, zygotes were collected from the oviducts and exposed to hyaluronidase (H3884, Sigma-Aldrich) to remove the cumulus cells and then placed in M2 medium (M7167, Sigma-Aldrich) into a $CO_2$ incubator (5% $CO_2$, 37 °C). SgRNAs were hybridized with Cas9 (Wild type) protein and injected into the pronucleus of the C57Bl/6J zygotes. Surviving zygotes were placed in KSOM medium (MR-106-D, Merck-Millipore) and cultured overnight to two-cell stage and then transferred into the oviduct of B6CBAF1 pseudo-pregnant females. The generated knockouts were validated by Sanger sequencing combined with tide TIDE analysis (https://tide-calculator.nki.nl/; data not shown). All *Minpp1*$^{-/-}$ mice were backcrossed with C57BL/6J mice to remove potential off-targets. The *Minpp1*$^{-/-}$ offspring were identified by Polymerase Chain Reaction (PCR) genotyping (Supplementary Fig.5). Brain histological characterization was performed with standard hematoxylin/eosin staining.

**Generation of stable HEK293 cell lines**

HEK293 cells were transfected with either FLAG-HA-empty or FLAG-HA-MINPP1 plasmids by performing lipofection with the Lipofectamine 3000 reagent (Invitrogen, L3000015) as per manufacturer's instructions (2.5 µg of DNA per well of a 6-well plate und) under serum-free media. Six hours post-transfection, the media were replaced with normal HEK293 cell culture growth media (see above). Two days-post transfection, the cell culture media were replaced with the media supplemented with the selection antibiotic geneticin (0.6mg/ml, Life, 10131027) and continued to be replaced twice a week until the cells in the 6 well plate reach high confluence. At high confluence, the cells were passaged and continued to be cultured for two to three weeks with the cell culture media supplemented with the geneticin (0.6mg/ml). The selection of clones was assessed by checking the presence of MINPP1 with Western-blot.

**E14.5 Mouse Neural Progenitor Cell Culture**

Cerebral cortices (both halves) from E14.5 mice were dissected in Dulbecco Phospate Balanced Salt Solution (DPBS, 14190250, Gibco). All procedures were done at room temperature, unless otherwise stated. Cortices were then incubated for 15 minutes at 37 °C in neurocult basal medium (STEMCELL, 05700) with Trypsin (1/100, 25300062, Gibco) and DNaseI (1/1000, 79254, Qiagen). Next, neurocult basal medium with 10% FBS was added to the mixture to deactivate the Trypsin. The mixture was then

titurated with fire polished Pasteur pipettes to obtain a homogenous mixture of cells. The cells were then centrifuged for 5 minutes at 300xg, washed twice and finally resuspended in neurocult medium with proliferation supplement (STEMCELL, 05701), endothelial growth factor (EGF) (20 ng/ml, PHG0314, Gibco) and 1% PS. Cells were then plated on poly-L-lysine (0.01 mg/ml, P6282, Sigma) and laminin (10 µg/ml; Gibco, 23017015) pre-coated dishes. Cells were passaged post 5 days of culture. All experiments were performed before passage 3.

**Differentiation of hiPSCs into neural lineage**

hiPSCs were differentiated into neural lineage by following a published protocol[3]. In brief, hiPSCs were dissociated into small clumps with Accutase and seeded on polyornithine (0.1 mg/ml, P4957, Sigma) and laminin (4 µg/ml) pre-coated 4-well-plates (179820, Nunc) and cultured in mTSER supplemented with Y-27632 (10 µM). The day after, cell culture media were changed to N2B27 medium (1:1 mix of DMEM-F12 (31331093, Gibco) and Neural Basal Medium (1103049, Gibco)) supplemented with N2 (17502048, Gibco), B27 (17504044, Gibco), Noggin (100 ng/ml, 78060.1, STEMCELL), Y-27632 (10 µM) and 1% PS. The media were replaced every 3 days.

**Inositol Labelling and SAX-HPLC Analysis**

HEK293 cells and fibroblasts were plated at 10,000 cells/well on 6-well plates and radiolabeled for 5 days with 5 µCi/ml *myo*-[$^3$H]-inositol (1 mCi, NET114A001, Perkin Elmer) in inositol-free DMEM medium (DML13-500, Caisson) supplemented with dialyzed FBS (Gibco,26400-044) and 1%PS. One quarter of the media was replaced with fresh medium containing 5 µCi/ml [$^3$H]-inositol on day 2. For iPSCs and their day 7 neurally-differentiating counterparts, the inositol metabolic radiolabeling was performed for 3 days and inositol-free DMEM media were supplemented with either bFGF (10 ng/ml, PHG0264, Invitrogen) or Noggin (100 ng / ml, 78060.1, STEMCELL) respectively. The latter time point was chosen to analyze the inositol phosphate levels at day 10 differentiating stage, the time point corresponding to neuronal differentiation stage shortly after neural induction and before the observation of differences in the TUJ1/PAX6 cell populations between control and *MINPP1* mutant iPSCs (Supplementary Figure 3F). For in vitro overexpression studies, the inositol metabolic radiolabeling was performed for 3 days, followed by lipofectamine-based transfection into HEK293 cells in the presence of 5 µCi/ml *myo*-[$^3$H]-inositol. One day post-transfection, the inositol phosphates were extracted. Extraction of inositol phosphates was performed according to published protocol[4]. Briefly, cells were incubated on ice with 1 M perchloric acid and 5 mM EDTA for 10 minutes followed by the collection of extracts and an overnight neutralisation step with 1 M potassium carbonate. Inositol phosphates were then separated by strong anion-exchange high-performance liquid chromatography (SAX-HPLC). The peaks ([$^3$H]-$IP_n$) were identified based on comparison to standards according to a previously published study[4]. The radioactivity within each fraction was measured with a beta counter after addition of 4 ml of scintillation fluid (Ultima-Flo AP LCS-mixture; Packard).The data are

presented as percentage of total radioactivity in the inositol-lipid fraction, obtained by incubating the post-extraction cells with 0.1% NaOH and 0.1% SDS overnight at room temperature.

**Cloning of MINPP1 variants into plasmids**

The MINPP1 cDNA (transcript NM_004897.5) sequence was isolated by PCR from human brain cDNA. The PCR product was then ligated into the FLAG-HA-pcDNA3.1 vector (52535, Addgene) between XhoI and BamHI sites. FLAG-HA-pcDNA3.1 was a gift from Adam Antebi (Addgene plasmid # 52535; http://n2t.net/addgene:52535; RRID: Addgene_52535). The mutations c.157T>G and c.1456G>A were incorporated in to the wild type plasmid with QuickChange Lightning Site-Directed Mutagenesis Kit (210515, Agilent). One Shot TOP10 chemically competent *E. coli* (C404006, Invitrogen) were then transformed with the resulting plasmid and plated on ampicillin resistant agar plates. Plates were incubated at 37 °C overnight. Colony PCR was performed on plasmids by using T7 promoter/BGH-rev primers and clones were sequenced by Sanger sequencing to check sequence reliability.

**Transfection experiments for proliferation studies using HEK293 cells**

Transfection into HEK293 cells was performed using Amaxa 4D-Nucleofector X-Unit (AAF-1002X, Lonza) according to manufacturer's instructions. In brief, 2 x$10^5$ HEK293 cells were nucleofected per 20µl nucleocuvette strip, using P3 Primary Cell 4D X Kit S (V4XP-3032, Lonza), 1µg DNA per reaction, and the program CA-137.

**MTT Proliferation Assay**

Cells were cultured with Methylthiazolyldiphenyl-tetrazolium bromide (MTT) (0.5 mg/ml, M5655, Sigma) for 1.5 hours. Then, MTT and the cell culture medium were removed and 100% dimethyl sulfoxide (100 µl/well) was added to dissolve the formazan crystals. Next, the cell culture plate was left to shake for 15-30 minutes in the dark at room temperature, followed by transfer of the samples into flat-bottom 96-well microtiter plate (655101, Greiner). The optical density was read on a microplate reader at 560 nm (1681135, Biorad).

**Apoptosis Assay**

The apoptosis is measured using the Click-iT TUNEL Alexa Fluor 594 Imaging Assay (C10246, Thermofischer) according to manufacturer's instructions. For a positive control, cells are treated with tunicamycin (10 µg/ml, 3516/10, Biotechne) for 6 hours to induce apoptosis (data not shown). For quantification analysis, a minumum of 5 fields per replicate were analyzed in ImageJ. The percentage of TUNEL$^+$ cells were counted relative to the total number of Hoechst$^+$ cells per field which was comparable (i.e. Hoechst$^+$) between replicates and conditions.

**Quantification of free intracellular $Ca^{2+}$ levels**

Cells were plated at 25,000 cells/well on flat-bottom 96-well plates (Greiner, 655088). After 24 to 48 hours in culture, the cells were loaded with Fluo-4-AM (5 mM, F14201, Invitrogen) diluted in assay buffer (NaCl 140 mM, Glucose 11.5 mM, KCl 5.9 mM, $MgCl_2$ 1.4 mM, $NaH_2PO_4$ 1.2 mM, $NaHCO_3$ 5 mM, , HEPES 10 mM, pH 7.4) with or without $CaCl_2$ (1.8 mM) to a final concentration of 5 µM. After 30 minutes of incubation in a humidified incubator (5% $CO_2$, 37 °C), the loading medium was removed and the cells were washed twice with the assay buffer. Then, the cells were excited at 485nm and emission intensities was recorded at 535nm via a fluorometers (200ProTecan and Tristar LB941) in the presence of assay buffer. The measured fluorescence intensities were then normalised to cell number via MTT proliferation assay. For $Ca^{2+}$ stimulation experiments, Ionomycin (10 µM, I0634-1MG, Sigma) or Caffeine (10 mM, C0750, Sigma) were quickly added to the wells in the presence of assay buffer and fluorescence intensities were recorded every 30 seconds for a minimum of 10 minutes. All the $Ca^{2+}$ stimulation experiments were performed with early batch HEK293 cells[5].

**Quantification of intracellular total and free iron levels**

The total iron content was measured with a colorimetric ferrozine-based assay according to previous studies[6,7]. Briefly, cells were cultured on 6-well plate (92006, TPP) and incubated with or without ferric ammonium citrate (FAC) (100 µM, RES20400-A702X, Sigma) in serum-free DMEM for 48 hours. Then, the cells were lysed with NaOH (50 mM, 200µl/well) and 50 µl of the lysate was kept apart for protein quantification. The remaining cell lysate were mixed with equal volumes of 10 mM HCl and iron-releasing reagent (HCl 1.4 M, $KMnO_4$ 4.5%) and incubated for 2 hours at 60 °C. Once the samples reached room temperature, 30 µl of iron-detection reagent (6.5 mM ferrozine, 6.5 mM neocuproine, 2.5 M ammonium acetate, and 1 M ascorbic acid) was added to each sample. After 30 minutes of incubation at room temperature, the samples were transferred to flat-bottom 96-well microtiter plate (Greiner, 655101). The optical density was read on a microplate reader at 560 nm (Biorad, 1681135). FAC was used as reference standard.

The free iron levels ($Fe^{2+}$ and $Fe^{3+}$) were measured by using the Iron Assay Kit (Abcam, ab83366) according to manufacturer's instructions. In both iron-detection assays, the data are normalized against the protein levels, quantified via Pierce BCA Protein assay kit (23225, Thermo Scientific).

**Immunofluorescence**

Cells were fixed in cold 4% paraformaldehyde for 10 minutes followed by three washes of PBS and permeabilization in 0.25% PBS-Triton-X-100 for 10 minutes. Cells were blocked for 1 hour in 1% BSA and 22.52 mg/ml glycine diluted in 0.1% PBS-Tween-20 (PBST). Cells were then incubated overnight at 4 °C with the following primary antibodies diluted in 1% BSA/0.1% PBST: Anti-PAX6(1:400,

901301, BioLegend), Anti-TUBULIN β-3 (1:1000, 801201, BioLegend), Anti-OCT4 (1:100, sc-5279, Santa-Cruz), Anti-SOX2 (1:1000,AB5603, Millipore), Anti-NESTIN (1:200,N5413, Sigma). After 3 washes with 0.1% PBST, cells were incubated for 1 hour with Alexa-Fluor-coupled secondary antibodies (A21424, A-11034, Invitrogen) diluted 1:500 in 0.1% PBST. Following three washes with 0.1% PBST, cells were then incubated with Hoechst 33342 (H3570, Invitrogen) diluted 1:1000 in 0.1% PBST. After 10 minutes of incubation, cells were washed twice with 0.1% PBST and either kept in PBS or mounted with ProLong™ Diamond Antifade Mountant (P36965, Invitrogen). Images were acquired with CELENA-S Digital Imaging System (CS20001, Logos) and Zeiss Axioplan-2. For quantification analysis, a minumum of 10 fields per replicate were analyzed in ImageJ. The percentage of $PAX6^+$ , $TUJ1^+$ or $BrdU^+$ cells were counted relative to the total number of $Hoechst^+$ cells per field which was comparable (i.e. $Hoechst^+$) between replicates and conditions.

**Protein extraction and western blot analysis**

Protein extraction, quantification, separation in gel electrophoresis and transfer were performed as described previously[2]. Nitrocellulose membranes were blocked either in Odyssey-TM Blocking Buffer (927-50003, LICOR) or in 5% dry milk diluted in 0.2% PBST for 1 hour and further incubated overnight at 4 °C with the following primary antibodies diluted in either OdysseyTM Blocking Buffer or 2.5% dry milk diluted in 0.2% PBST: Anti-MINPP1 (1:2000, sc-10399, Santa-Cruz), Anti-β Actin (1:5000, AM4302, Invitrogen). After three washes with 0.2% PBST, the membranes were then incubated for 1 hour at room temperature with HRP (1:10000, sc-2314, sc-2020, Santa-Cruz) or IRDye-coupled (1:10000, 925-68070, 925-32211, LICOR) secondary antibodies. After three washes with 0.2% PBST, the membranes were developed either with HRP (ChemiDoc XRS, Biorad) or Odyssey CLx imaging system (LICOR).

**Statistics**

Data were analysed where appropriate with one-way analysis of variance (ANOVA), Two-tailed student's t-test and two-way ANOVA with GraphPad Prism 8. N and n values are detailed in figure legends. "N" refers to independent experiments or animals); "n" refers to technical replicates.

All the data are presented as mean ± the standard deviation (s.d.). Statistically significant differences are indicated on the figures by *p<0.05, **p<0.01, ***p<0.001, or ****p<0.0001.

**Data availability statement**

The HPLC results (Fig. 4) for the inositol metabolism are now provided as source data files. For the other datasets generated during and/or analysed during the current study are available from the corresponding author on reasonable request.

**Methods for Supplementary Figures:**

**Construction of human MINPP1 structural model:**

The human MINPP1 structure model was generated with the protein structure homology-modeling server Phyre V2.0 (PMID: 25950237) based on the D. castellii phytase structure (PDB: 2GFI) with 89% sequence coverage. The impact of the missense mutations involving amino-acids included in the MINPP1 structure (i.e. Tyr53, Arg401, Phe228) was evaluated using Missense3D (http://www.sbg.bio.ic.ac.uk/~missense3d/)[8]. All the structural figures were prepared with Pymol (http://www.pymol.org).

**RNA isolation, RT-qPCR and relative fold change expression analysis**

The total RNAs of the different tissues used in this study were ordered from Clontech Laboratories (USA); Human brain (636530); Human fetal brain (636526); Human cerebellum (636535); Human liver (636531); Human lung (636524); Human kidney (636529) and Human skeletal muscle (636534). Total RNA extraction was performed from cell culture pellet using TriZol (ThermoFischer, 15596026) according to the supplier's instructions. The purification of the RNA was done with the RNeasy Mini Kit (Qiagen, 74104). Reverse transcription of the total RNAs was performed using SuperScript II reverse transcriptase (ThermoFisher, 18064022) according to the manufacturer's recommendations. Quantitative PCR was performed with the SYBR Green PCR Master Mix reagent (ThermoFisher, 4364346) on an Applied Biosystems One Step Plus real-time PCR system (Applied Biosystems, 4376600.*ACTB* was chosen as a reference gene to normalize the results between different tissues and cell line. Primers used for qPCR were: CCCTTGCCATCCTAAAAGCC (Forward) and TGCTATCACCTCCCCTGTGT (Reverse) for *ACTB*; TGGACCTCCAACAGTTAATGATAA (Forward) and TGGCACTTGCAAAGTAGCTG (Reverse) for *MINPP1*. The relative expression of *MINPP1* was determined by the ΔΔCt method using the human brain as the reference tissue.

**Glycosylation Studies :**

The glycosylation status of different MINPP1 mutant forms is checked by following the previously described PnGase F protocol (P0704L, New England BioLabs) [2].

**Cell Proliferation and Apoptosis Assay with Incucyte-Live-Imaging System**

Cells were seeded on 96-well plate (4379, Essen Bioscience) and cultured with Annexin-V (1:200, 4641, Essen Bioscience) containing media inside the IncuCyte® Live Cell Analysis System (Essen Bioscience). Three images per well were taken with phase contrast and red fluorescence channels every 2 hours for a total of 48 hours, using 20x objective. Images were then analysed with Incucyte-Zoom software, by defining a mask with the basic analyzer. The same mask was applied to all time points.

**Differentiation of hiPSCs towards dorsal telencephalic progenitors**

hiPSCs were differentiated towards dorsal telencephalic lineage by following the protocol as previously described [2,9]. Briefly, hiPSCs were manually dissociated into big clumps and floated in non-coated dishes in neural induction media N2B27 (1:1 mix of DMEM-F12 (31331093, Gibco) and Neural Basal Medium (1103049, Gibco)) supplemented with N2 (07156, STEMCELL), NeuroCult SM1 without vitamin-A (05731, STEMCELL), bFGF (10 ng/ml, PHG0264, Invitrogen) and dual-SMAD inhibition small molecules SB431542 (20 µM, 72232, STEMCELL) and LDN193189 (HCl) (500 nM, 72146, STEMCELL). After 6 hours, embryoid body (EB)-like structures were seeded on polyornithine (0.1 mg/ml, P4957, Sigma) and laminin (4 µg/ml) pre-coated 3.5 cm dishes. The media were changed every 3 days. At day 12-15, the neural rosettes were manually or enzymatically passaged on to polyornithine-laminin-pre-coated dishes and cultured in N2B27 medium supplemented with bFGF (10 ng/ml), EGF (10 ng/ml, PHG0314, Invitrogen) and BDNF (20 ng/ml, 78005, STEMCELL). At confluence, cells were passaged with a density of $5x10^4/cm^2$ and the media was supplemented with Y-27632 (10µM) on the day of passage. Neuroectodermal origin of the emerging neural progenitor-like cells was assessed by HNK1/P75 Flow cytometry (Supplementary Fig.3H).

**BrdU Proliferation Assay**

Initially, the cells were incubated with 10 µM BrdU labelling solution (B5002-1G, Sigma) for 4 hours at 37 °C in a $CO_2$ incubator. The cells were further thoroughly washed thrice with PBS and fixed with 4% paraformaldehyde for 15 minutes. Permeabilization of the cells were performed using 0.25% PBS-Triton-X-100 for 10 minutes. After 3 washes with PBS, DNA hydrolysis was achieved by incubating the cells with 2 M HCL for 30 minutes at 37 °C. Further, the cells were neutralized with 0.1 M sodium borate buffer (pH 8.5) for 30 minutes at room temperature. Cells were thoroughly washed with PBS and immunostaining of the cells with BrdU antibody (1:250, ab6326, Abcam) was carried out as previously mentioned in the immunofluorescence section.

**Flow Cytometry**

Cells were fixed with 1% paraformaldehyde and cell suspensions in PBS were stained for 30 minutes with anti-SSEA-4-FITC (Miltenyi biotec 130–098-371), anti-TRA1-81-FITC (BD Biosciences, 560194), anti-HNK1-FITC (130-092-174, MiltenyiBiotec), anti-P75-APC (130-110-079, MiltenyiBiotec), REA control-FITC (130-113-449, MiltenyiBiotec), or REA Control -PE (130-113-450, MiltenyiBiotec) at 1/10 dilution. Prior to analysis, the samples were centrifuged and resuspended in PBS. The samples were then processed with FACSCalibur (BD Biosciences) and analyzed with FlowJo Software and BD CellQuest Pro software.

### *In vitro* phytase Assay

The *in vitro* phytase assay was performed as previously described[10]. Briefly, 4 nmol of $IP_6$ was added to 1 ml of conditioned media from Ctrl and *MINPP1*$^{-/-}$ HEK293 cells and further incubated for 0, 2, 4 and 6 hours at 37 °C. The samples were then mixed with Orange G loading dye and resolved by 35% PAGE followed by toluidine blue staining.

### Analysis of extracellular inositol phosphates

For analysis of extracellular inositol phosphates, cells were labelled for 5 days with [3H]-inositol as indicated above. Media were collected and centrifuged at 300xg for 5 minutes to remove cell contaminants. Perchloric acid was added to the supernatant to final 1 M. The acidified medium was incubated on ice for 10 minutes before centrifugation at 18,000 xg to remove precipitates. Inositol phosphates in the supernatant were then purified using titanium dioxide beads[11]. Briefly, 4 mg beads were added to the media extracts and the samples rotated at 4°C for 15 minutes. Beads were washed twice in 1 M perchloric acid, before elution with ammonium hydroxide. Radiolabeled inositol phosphates in the purified media extracts were separated by SAX-HPLC as before, and radioactivity in each fraction measured with a beta counter.

## REFERENCES


1. Menara, G., Lefort, N., Antignac, C. & Mollet, G. Generation of an induced pluripotent stem cell (iPSC) line (IMAGINi007) from a patient with steroid-resistant nephrotic syndrome carrying the homozygous p.R138Q mutation in the podocin-encoding NPHS2 gene. *Stem Cell Res* **46**, 101878 (2020).
2. Medina-Cano, D. *et al.* High N-glycan multiplicity is critical for neuronal adhesion and sensitizes the developing cerebellum to N-glycosylation defect. *Elife* **7**(2018).
3. Gerrard, L., Rodgers, L. & Cui, W. Differentiation of human embryonic stem cells to neural lineages in adherent culture by blocking bone morphogenetic protein signaling. *Stem Cells* **23**, 1234-41 (2005).
4. Azevedo, C. & Saiardi, A. Extraction and analysis of soluble inositol polyphosphates from yeast. *Nat Protoc* **1**, 2416-22 (2006).
5. Luo, D., Sun, H., Xiao, R.P. & Han, Q. Caffeine induced Ca2+ release and capacitative Ca2+ entry in human embryonic kidney (HEK293) cells. *Eur J Pharmacol* **509**, 109-15 (2005).
6. Drecourt, A. *et al.* Impaired Transferrin Receptor Palmitoylation and Recycling in Neurodegeneration with Brain Iron Accumulation. *Am J Hum Genet* **102**, 266-277 (2018).
7. Riemer, J., Hoepken, H.H., Czerwinska, H., Robinson, S.R. & Dringen, R. Colorimetric ferrozine-based assay for the quantitation of iron in cultured cells. *Anal Biochem* **331**, 370-5 (2004).
8. Ittisoponpisan, S. *et al.* Can Predicted Protein 3D Structures Provide Reliable Insights into whether Missense Variants Are Disease Associated? *J Mol Biol* **431**, 2197-2212 (2019).
9. Boissart, C. *et al.* Differentiation from human pluripotent stem cells of cortical neurons of the superficial layers amenable to psychiatric disease modeling and high-throughput drug screening. *Transl Psychiatry* **3**, e294 (2013).
10. Wilson, M.S., Bulley, S.J., Pisani, F., Irvine, R.F. & Saiardi, A. A novel method for the purification of inositol phosphates from biological samples reveals that no phytate is present in human plasma or urine. *Open Biol* **5**, 150014 (2015).

11. Wilson, M.S. & Saiardi, A. Inositol Phosphates Purification Using Titanium Dioxide Beads. *Bio Protoc* **8**(2018).

**Supplementary Note:**

**Detailed method for Sequencing, Variant Filtering and Prioritization**

**Families CerID-09, 11 and 30**

Genomic DNA was extracted from peripheral blood cells. As previously published (Chemin et al. Brain. 2018; Megahead et al. Orphanet J Rare Dis. 2016), Exome capture was performed with the the SureSelect Human All Exon kit (Agilent Technologies). Agilent Sure Select Human All Exon (54Mb Clinical Research Exome) libraries were prepared from 3µg of genomic DNA sheared with an Ultrasonicator (Covaris) as recommended by the manufacturer. Barcoded exome libraries were pooled and sequenced with a HiSeq2500 system (Illumina), generating paired-end reads. The mean depth of coverage of the exome libraries was greater than ~100-120X with >98 to 99% of the targeted exonic bases covered at least by 15 independent reads and >93 to 98% by at least 30 independent sequencing reads (98-99% at 15X and 93 to 98% at 30X). After demultiplexing, sequences were aligned to the reference human genome hg19 using the Burrows-Wheeler Aligner (BWA). Downstream processing was carried out with the Genome Analysis Toolkit (GATK), SAMtools and Picard, following documented best practices (http://www.broadinstitute.org/gatk/guide/topic?name=best-practices). Variant calls were made with the GATK HaplotypeCaller (V3.7). The annotation process was based on the latest release of the Ensembl database, Gnomad 2.1. Variants were annotated and analyzed using the Polyweb software interface designed by the Bioinformatics platform of University Paris Descartes. Variants were filtered to less than 1% minor allele frequency in population databases and with MAF <0.001 in our sequenced cohort that include more than 15000 exomes. Manual curation of the known PCH genes (for the gene list see Chemin et al. Brain 2018) was first performed to exclude a known genetic cause. Variants were then prioritized by the suspected mode of inheritance, OMIM status and *in silico* prediction tools (Mutation Taster (Schwarz et al. Nature Methods. 2014); SIFT and Polyphen (McLaren et al. Genome Biology. 2016); CADD score (Rentzsch et al. Nucleic Acids Res. 2018)). Candidate genes were correlated to the patient's phenotype, gene function and expression. Sanger sequencing of the patient and her parents was performed to confirm the variants and co-segregation using a 3500xl genetic analyzer (4405633; Applied Biosystems). For the family CerID-09, homozygous variants were identified in 31 genes. From these analyses, 3 genes with the predicted most likely pathogenic variants (*MINPP1*; *ZCCHC24* and *NKX1-2*) were further considered as candidates. For the family CerID-11, 4 variants were identified in 2 potential candidate genes with 2 heterozygous variants (*MINNP1* ; *KIAA1522*). For the family CerID-30, 21 variants were identified in 11 potential candidate genes including 6 genes with 2 or more heterozygous variants, and 5 genes with one homozygous variant. Two genes with most likely pathogenic variants were further explored: *MINPP1* and *MTFMT*. The involvement of MTFMT was excluded based on the absence of clinical correlations.

**Family TR-PCH-01**

Patient TR-PCH-01-1 was part of a replication cohort of 100 patients with congenital or early-onset cerebellar defects that includes 21 PCH cases. This cohort was investigated using a targeted gene panel. This panel includes 184 known genes involved in congenital cerebellar anomalies (list available upon request), and 13 candidate genes including *MINPP1*. Samples were prepared using Blood DNA and the SeqCap EZ Choice preparation kit (Roche) and sequenced on an Illumina MiSeq sequencer using 2 × 150 bp sequencing kits. The Basespace cloud computing platform (with BWA 2.1 and GATK Unified Genotyper 1.6) and the Variant Studio v.3.0 software provided by Illumina were used. Other known PCH genes were excluded for TR-PCH1-1. Pathogenicity of variants was ascertained according to the ACMG (American College of Medical Genetics) criteria. The segregation was confirmed by Sanger sequencing in the index case, both parents and unaffected sibling.

**Families PCH-2456 and PCH-2712**

Blood DNA was extracted using Qiagen reagents (Qiagen Inc., USA) and whole exome sequencing was performed on all affected family members using the Illumina HiSeq2500 which yields 100 bp paired-end reads covering 80% of the exome at 20X. GATK best practices pipeline was used for SNP and INDEL variant identification. Variants were prioritized by allele frequency (<0.1% MAF in our exome database of over 5000 individuals), conservation and predicted effect on protein function. The variants were predicted to be disease causing and were absent from 1000 Genomes, ExAC and gnomAD. Sanger sequencing confirmed segregation according to a strict recessive mode of inheritance in all genetically informative and available family members.


1. Chemin J, Siquier-Pernet K, Nicouleau M, Barcia G, Ahmad A, Medina-Cano D, Hanein S, Altin N, Hubert L, Bole-Feysot C, Fourage C, Nitschké P, Thevenon J, Rio M, Blanc P, Vidal C, Bahi-Buisson N, Desguerre I, Munnich A, Lyonnet S, Boddaert N, Fassi E, Shinawi M, Zimmerman H, Amiel J, Faivre L, Colleaux L, Lory P, Cantagrel V. De novo mutation screening in childhood-onset cerebellar atrophy identifies gain-of-function mutations in the CACNA1G calcium channel gene. Brain.2018 Jul 1;141(7):1998-2013**.**
2. Megahed H, Nicouleau M, Barcia G, Medina-Cano D, Siquier-Pernet K, Bole-Feysot C, Parisot M, Masson C, Nitschké P, Rio M, Bahi-Buisson N, Desguerre I, Munnich A, Boddaert N, Colleaux L, Cantagrel V. Utility of whole exome sequencing for the early diagnosis of pediatric-onset cerebellar atrophy associated with developmental delay in an inbred population. Orphanet J Rare Dis. 2016 May 4;11(1):57.
3. Schwarz JM, Cooper DN, Schuelke M, Seelow D. MutationTaster2: mutation prediction for the deep-sequencing age. Nat Methods. 2014 Apr;11(4):361-2.
4. McLaren W, Gil L, Hunt SE, Riat HS, Ritchie GR, Thormann A, Flicek P, Cunningham F. The Ensembl Variant Effect Predictor. Genome Biol. 2016 Jun 6;17(1):122.
5. Rentzsch P, Witten D, Cooper GM, Shendure J, Kircher M. CADD: predicting the deleteriousness of variants throughout the human genome. Nucleic Acids Res. 2019 Jan 8;47(D1):D886-D894.